Dipl.-Ing. Robert Triebl, BSc

Interplay of spin-orbit coupling and strong electronic correlations in multiorbital systems and topological insulators

DOCTORAL THESIS

For obtaining the academic degree of
Doktor der technischen Wissenschaften

Doctoral Program in Engineering Sciences
Doctoral School Physics

Graz University of Technology

Supervisor:
Assoc. Prof. Dipl.-Ing. Dr. Markus Aichhorn

Institute of Theoretical and Computational Physics

Graz, July 2018

AFFIDAVIT

I declare that I have authored this thesis independently, that I have not used other than the declared sources/resources, and that I have explicitly indicated all material which has been quoted either literally or by content from the sources used. The text document uploaded to TUGRAZonline is identical to the present doctoral thesis.

Date

Signature

Abstract

The discovery of topological insulators had a large impact on condensed matter physics as several potential applications have been suggested, and a deep understanding of many aspects is already achieved. However, how topological effects are influenced by many-body effects is still not clear, even new topological phases are proposed once correlations come into play. A bottleneck of several theoretical methods is the necessary correct treatment of spin-orbit coupling (SOC), which only recently became accessible for many methods designed to capture strong correlations. The goal of the present thesis is to analyze the interplay of SOC with strong correlations, with a focus on topological properties.

The influence of SOC onto the quasiparticle renormalization is analyzed by means of a three-band model with semicircular density of states using the dynamical mean-field theory (DMFT). It is shown that the impact of the SOC strongly depends on the filling. While for one and five electrons in the three bands the correlations are increased, they are decreased at half filling. The Hund's metal regime at a filling of two electrons is suppressed by the SOC. Furthermore, it is demonstrated that the effective SOC is enhanced by the correlations.

Regarding the topological aspects, topological insulators on the honeycomb lattice including interactions are analyzed. The phase diagram of the Kane-Mele-Hubbard Hamiltonian with an inversion-symmetry breaking term is calculated using the dynamical impurity approximation (DIA) and the topological Hamiltonian. Correlations stabilize the topological phase, until an antiferromagnetic moment destroys the topological distinctness. The results are compared to DIA calculations of a ribbon. There, gapless edge states are supposed to exist, but already small interactions lead to local antiferromagnetic moments that gap the edge states.

In physical realizations of the Kane-Mele model, the SOC is small. In order to describe a realistic topological insulator with a large gap, a two-orbital model of bismuthene on a substrate is used. Introducing correlations there, it is again demonstrated using DMFT that correlations increase the topological gap and thus stabilize the topological nontriviality, as long as no magnetic moment is present.

Kurzfassung

Die Entdeckung von topologischen Isolatoren hatte einen großen Einfluss auf die Physik der kondensierten Materie, da dadurch mehrere mögliche Anwendungen vorgeschlagen wurden und ein tiefes Verständnis vieler Aspekte erreicht werden konnte. Wie topologische Effekte jedoch durch Vielteilcheneffekte beeinflusst werden, ist noch nicht geklärt; es werden sogar neue topologische Phasen vorgeschlagen, wenn Korrelationen ins Spiel kommen. Ein problematischer Punkt mehrerer theoretischer Methoden ist die notwendige korrekte Behandlung der Spin-Bahn-Kopplung (SOC), die erst kürzlich für viele Methoden zugänglich wurde, die starke Korrelationen behandeln können. Das Ziel der vorliegenden Arbeit ist es, das Zusammenspiel von SOC mit starken Korrelationen zu analysieren, wobei der Fokus auf den topologischen Eigenschaften liegt.

Der Einfluss von SOC auf die Renormierung von Quasiteilchen wird mittels eines Dreibandmodells mit halbkreisförmiger Zustandsdichte mithilfe der Dynamischen Molekularfeldtheorie (DMFT) analysiert. Es wird gezeigt, dass der Einfluss der SOC stark von der Füllung abhängt. Während für ein und fünf Elektronen in den drei Bändern die Korrelationen erhöht sind, sind sie bei Halbfüllung verringert. Das Hund-Metall-Regime bei einer Füllung von zwei Elektronen wird durch die SOC unterdrückt. Darüber hinaus wird gezeigt, dass die effektive SOC durch die Korrelationen verstärkt wird.

In Bezug auf die topologischen Aspekte werden topologische Isolatoren auf dem Wabengitter einschließlich der Wechselwirkungen analysiert. Das Phasendiagramm des Kane-Mele-Hubbard-Modells, mit einem die Inversionssymmetrie brechenden Term, wird unter Verwendung der dynamischen Störstellenannäherung (DIA) und des topologischen Hamilton-Operators berechnet. Korrelationen stabilisieren die topologische Phase, bis ein antiferromagnetisches Moment die Topologie zerstört. Die Ergebnisse werden mit DIA-Berechnungen eines Streifens verglichen. Dort sollten zwar Randzustände ohne Bandlücke existieren, aber schon kleine Wechselwirkungen führen zu lokalen antiferromagnetischen Momenten, welche eine Bandlücke in den Randzuständen verursachen.

In physikalischen Realisierungen des Kane-Mele-Modells ist die SOC klein. Um einen realistischen topologischen Isolator mit einer großen Bandlücke zu beschreiben, wird ein Zweiorbitalmodell von Bismuthen auf einem Substrat verwendet. Indem man dort Korrelationen einführt, wird mit DMFT erneut gezeigt, dass diese die topologische Bandlücke vergrößern und somit die topologische Nichttrivalität stabilisieren, solange kein magnetisches Moment vorhanden ist.

Acknowledgments

Thank you, *Markus Aichhorn*, for the great supervision within the last years. I already appreciated your guidance while my master's studies, and I was happy that you gave me the opportunity to continue as a project assistant in your group. You always manage to achieve a very good atmosphere, without losing the focus on the important points. I am also grateful for all your advice, not only regarding physics.

Thank you, *Enrico Arrigoni*, for the official supervision of my thesis before the Markus's habilitation and for the simplification of the potential organizational difficulties that come along with a split supervision.

Thank you, *Jernej Mravlje*, for the time you took for discussions. You brought new perspectives into our common work and ensured with your personality a nice climate. Thank you, *all members of the TRIQS collaboration*, for providing tools that really simplify the research on interacting quantum systems. I enjoyed the discussions in Paris and many other places in the world on both physics and technical issues.

Thank you, *Manuel Zingl*, for all your help since I have started with the master's thesis. You were the first place to go when I tried my first mean-field, DFT, and DMFT calculations, and still helped with little problems when you were already in New York. Thank you, *Gernot Kraberger*, for all the advice in our daily work, especially for the programs, scripts, and commands you provided that enabled me to communicate with my computer properly.

Thank you, *Michael Rumetshofer*, for giving insights into probability theory and for pointing out when I was distracted too easily. Thank you, *Daniel Bauernfeind*, for all the discussions, from tensor products to bubbles in the stock market.

Thank you, *all members of the Institute of Theoretical and Computational Physics*, you provided an environment that made the physics building a place of well-being, even when physics was challenging. Thank you, *Brigitte Schwarz* and *Andreas Hirczy* for ensuring nearly frictionless operation of the institute.

Thank you, my dear parents, *Hannelore and Andreas Triebl*, for giving me the opportunity to do what I like, and for supporting all my decisions. Thank you, *Christoph and Andrea Triebl*, that I can always count on you.

Contents

1 Introduction

The goal of condensed matter physics is to understand the properties of existing materials, to capture the essential physical principals behind them, and, finally, to use the knowledge to produce new devices useful for the progress of mankind. Regarding the physical principles, the picture is clear: The only known fundamental interaction relevant for material science is the electromagnetic interaction, hence quantum electrodynamics is the theoretical framework that should, in principle, cover all physical effects of condensed matter. This theory exists since the 1940s and is still not proven wrong, hence the fundamental rules of material science are clearly set.

However, physics is not that easy, since it is impossible to treat all particles in a macroscopic object within quantum electrodynamics, or even with the usually chosen approximation, the Schrödinger equation. Depending on the scales one is looking at, different phenomena may emerge [1]. Once the sum is more than its parts, it is difficult to predict collective behavior. For the observation of new physical phenomena, usually, a good cooperation between many theoretical and experimental methods is necessary for success. In the last decades, this cooperation led to the discovery of a large variety of physical phenomena. Prominent examples of breakthroughs that even made the step to industry are the fabrication of the first transistor and the discovery of the giant magnetoresistance [2].

From a theorist's point of view, it is clear that capturing emergent phenomena is a goal that led to a plethora of theoretical and computational methods. From most general ab initio methods up to sophisticated models with the only intention to show a certain effect, and from one-electron hoppings up to continuous current densities – the toolbox in theoretical condensed matter physics is large, and often many viewpoints are needed to get a complete picture. The methods that might be useful to describe a certain phenomenon depends on its nature.

An interesting phenomenon are strong correlations of electrons. While the principle is simple – two electrons will repel each other – a detailed theoretical description is challenging. Since the movement of one electron influences all the other electrons around, correlations are the reason for many collective emergent phenomena, such as charge-density waves, magnetic order, or even superconductivity. One manifestation of strong correlations is the Mott insulator, which originates from a blocking of hoppings due to the electron repulsion.

While all theories based on bands fail to describe the Mott insulator, the dynamical mean-field theory (DMFT) [3–7] is well suited to describe the mass enhancement of the electrons due to correlations and also gives a correct description of the insulating regime. After applications to model systems such as the Hubbard model, it was later combined with the band-based density functional theory (DFT) [8, 9]. This is a nice example that the combination of several approaches is sometimes important, in this case even a direct merge instead of interpreting two complementary methods. While DFT works well do describe the band structure of weakly-correlated real materials but fails to capture Mott physics, DMFT is well suited for the Mott transition but needs the noninteracting band structure as an input. The combined DFT+DMFT method shows therefore good results for transport properties of correlated materials.

Another special kind of insulators are topological insulators [10–12]. The mathematical key concept is a nontrivial structure of the eigenfunctions in the Brillouin zone due to a band inversion. An important physical reason for a potential band inversion is the spin-orbit coupling (SOC), which is responsible for a nontrivial gap opening and spin-dependent edge channels. Thus topological insulators are closer related to ordinary band insulators than Mott insulators, but they were only discovered in 2005 [13–16], showing that also nowadays surprises in condensed matter physics are possible. Topological insulators are, due to the edge states, candidates for spintronic applications. Since the topological nature is encoded in the band structure, the search for interesting materials is mostly based on the DFT, leading to a classification of many materials into newly found topological classes, such as strong topological insulators or Weyl semimetals.

Once interactions are included, the understanding of different topological phases is not that detailed. In general, analyzing correlations in materials with strong SOC only recently gained importance, and already led to some interesting results. For example, correlated spin-orbital models are characterized by unusual exchange and are argued to lead to exotic phases such as spin-liquid ground states [17–23]. Another interesting example is the layered iridate $\mathrm{Sr_2IrO_4}$,where the interplay of SOC and correlations lead to an electronic structure similar to the one of layered cuprates and is argued to lead to high-temperature superconductivity [24–26]. Regarding topology, the strong correlations are supposed to lead to new topological phases [27, 28].

The goal of the present thesis is to further investigate the interplay of strong correlations and SOC, with a focus on topological insulators. In the chapters 2, 3, and 4, the basic concepts of strong correlations, SOC, and topological insulators are introduced. Since in case of many DFT+DMFT calculations an analytic continuation is necessary, the maximum entropy method and a generalization to offdiagonal spectral functions needed for many spin-orbit coupled materials is discussed in chapter 5. Chapter 6 focuses on the changes of the correlation strength in a three orbital model for all integer fillings as the SOC increases. It is shown that the interplay of Hund's rule coupling and SOC depends on the filling. For example, the Hund's tail present in case of a two electrons is suppressed by the SOC. The remainder of the thesis focuses on topological insulators on a honeycomb lattice. In chapter 7, the noninteracting models of graphene-like structures are introduced. The model for p_z orbitals including SOC, known as Kane-Mele model [13, 14], is the prototypical example of a topological insulator. The influence of correlations onto the magnetic and topological properties is analyzed in chapter 8. It turns out that the edge states, which would be topologically protected without magnetic moments, are gapped due to local spontaneous symmetry breaking. Finally, chapter 9 briefly discusses the physically more relevant model of a topological insulator based on the p_x and p_y orbitals.

2 Modeling of strongly correlated materials

The basic concept of *ab initio* electronic structure calculations is to solve the time-independent Schrödinger equation

$$H\left|\psi\right\rangle = E\left|\psi\right\rangle \tag{2.1}$$

with the full Hamiltonian containing both nuclei (with Greek indices) and electrons (with Latin indices) that reads in in real-space coordinates

$$\begin{aligned} H = &-\frac{\hbar^2}{2m_e}\sum_i \nabla_i^2 - \sum_\alpha \frac{\hbar^2}{2m_\alpha}\nabla_\alpha^2 + \sum_{i\neq j}\frac{e^2}{8\pi\epsilon_0\left|\boldsymbol{r}_i - \boldsymbol{r}_j\right|} \\ &- \sum_{i,\alpha}\frac{Z_\alpha e^2}{4\pi\epsilon_0\left|\boldsymbol{r}_i - \boldsymbol{r}_\alpha\right|} + \sum_{\alpha\neq\beta}\frac{Z_\alpha Z_\beta e^2}{8\pi\epsilon_0\left|\boldsymbol{r}_\alpha - \boldsymbol{r}_\beta\right|}. \end{aligned} \tag{2.2}$$

This problem is not solvable directly, as the dimensionality of the Hilbert space is too large for real materials. A reduction of the number of parameters is achieved by fixing the position of the nuclei, which is the so-called Born-Oppenheimer approximation. This is justified as the relative weight of nucleons and electrons is about 1823, causing a lot faster movement of the electrons.

With this approximation, the dimensionality of the problem is reduced to the electronic degrees of freedom only, as the Hamiltonian can be rewritten as

$$H = T + V + U = -\frac{\hbar^2}{2m_e}\sum_i \nabla_i^2 + \sum_i v(\boldsymbol{r}_i) + \sum_{i\neq j} u(\boldsymbol{r}_i, \boldsymbol{r}_j) \tag{2.3}$$

The exponential wall is, however, still present due to the interaction of the electrons. For example, a single bismuth atom with 83 electrons has $83 \times 3 = 249$ degrees of freedom. A many-body wave function depending on 249 variables is already impossible to store, solving the coupled differential equations cannot be considered. Further approximations are needed in order to achieve good results.

2.1 Weakly interacting models

2.1.1 Density functional theory

The most important method to calculate the electronic structure of real materials is the density functional theory (DFT). The Schrödinger equation solved in this framework contains no full electron-electron interaction term, but treats this effect via an effective one-particle potential. The only quantity of interest in order to determine this effective potential is the total electron density $n(\boldsymbol{r})$, which depends on only three variables, and not on $3 \times N$, where N is the total number of electrons, as the full many-body wave function $\Psi(\boldsymbol{r}_1, \ldots, \boldsymbol{r}_N)$. The density can be calculated from the wave function via

$$n(\boldsymbol{r}) = \int \prod_{i=2}^{N} \mathrm{d}^3 r_i \Psi^*(\boldsymbol{r}, \boldsymbol{r}_2, \ldots, \boldsymbol{r}_N) \Psi(\boldsymbol{r}, \boldsymbol{r}_2, \ldots, \boldsymbol{r}_N) \tag{2.4}$$

The theoretical backbone of the DFT are two theorems, called the Hohenberg-Kohn theorems. The first shows that the external potential $v(\boldsymbol{r})$ is a unique functional of the density $n(\boldsymbol{r})$, apart from a trivial constant [8]. As the external potential is the only variable input of the Schrödinger equation (2.1) with Hamiltonian (2.3) since the kinetic energy part is $p^2/2m$ and $u(\boldsymbol{r}_i, \boldsymbol{r}_j)$ is always given by the Coulomb repulsion, it also determines the many-body wave function of the ground state. Therefore, the functional $F[n] = T[n] + U[n]$ is a universal functional of the density that does not depend on the external potential. With that, one can define a functional

$$E_v[n] = \int \mathrm{d}^3 r \, v(\boldsymbol{r}) n(\boldsymbol{r}) + F[n]. \tag{2.5}$$

The second theorem shows that the ground-state density $n_0(\boldsymbol{r})$ minimizes $E_v[n]$, its value at n_0 is the ground-state energy of the total system [8].

As the exact form of $F[n]$ is unknown, the theory does, so far, not provide the ground state energy and the corresponding electron density. This can be achieved by mapping the interacting electron gas onto a noninteracting one, as proposed by Kohn and Sham [9], providing a set of equations that need to be solved self-consistently. The independent variables are then the non-interacting Kohn-Sham orbitals $|\psi_i\rangle$. Within this framework, the exact functional $F[n]$ is rewritten as [9]

$$F[n] = T[n] + U[n] = T_\mathrm{s}[n] + \frac{e^2}{2} \int \mathrm{d}^3 r \int \mathrm{d}^3 r' \frac{n(\boldsymbol{r}) n(\boldsymbol{r}')}{|\boldsymbol{r} - \boldsymbol{r}'|} + E_\mathrm{xc}[n]. \tag{2.6}$$

The first term, $T_\mathrm{s}[n]$, is the kinetic energy of the non-interacting Kohn-Sham particles. The second term is the Hartree part of the correlation energy of the electrons. The last term, $E_\mathrm{xc}[n]$, is the so-called exchange-correlation part of the functional, that is defined to cover all correlation effects except for the Hartree energy. The density is then the sum of one-particle densities of the Kohn-Sham orbitals, i.e.,

$$n(\boldsymbol{r}) = n_\mathrm{s}(\boldsymbol{r}) = \sum_i |\psi_i(\boldsymbol{r})| \,. \tag{2.7}$$

A variation of the functional $F[n[\psi_i, \psi_i^*]]$ with respect to ψ_i^* yields the Kohn-Sham equations

$$\left\{ -\frac{\hbar^2 \nabla^2}{2m_e} + v(\boldsymbol{r}) + e^2 \int \mathrm{d}^3 r' \frac{n(\boldsymbol{r}')}{|\boldsymbol{r} - \boldsymbol{r}'|} + \frac{\delta E_\mathrm{xc}[n(\boldsymbol{r})]}{\delta n(\boldsymbol{r})} \right\} \psi_i = \epsilon_i \psi_i. \tag{2.8}$$

Equations (2.7) and (2.8) need to be solved self-consistently in order to obtain the electron density.

So far, the formalism is exact, and would yield the correct ground-state density and the correct ground state energy, if the exact exchange-correlation functional was known. However, the exact exchange-correlation functional is not known, and approximations are needed in order to evaluate it. A popular choice is the local-density approximation (LDA) that depends only on the density via $E_{\mathrm{xc}}^{\mathrm{LDA}}[n(\boldsymbol{r})] = \int \mathrm{d}^3 r\, \epsilon_{\mathrm{xc}}[n(\boldsymbol{r})]\, n(\boldsymbol{r})$, where $\epsilon_{\mathrm{xc}}[n(\boldsymbol{r})]$ is the exchange-correlation energy per electron in a homogeneous electron gas. Another choice are flavors of the generalized-gradient approximation, where $\epsilon_{\mathrm{xc}}[n(\boldsymbol{r}), \nabla n(\boldsymbol{r})]$ depends on both the density as well as its gradient.

In the present thesis, only periodic crystals are considered. Since the translation operator commutes with the Hamiltonian and the momentum operator is the generator of translation, the momentum $\boldsymbol{k}/\hbar$ is a good quantum number. The Kohn-Sham Hamiltonian, which is the expression in the braces in Eq. (2.8), is therefore block diagonal in $\boldsymbol{k}$ with Bloch Hamiltonians $h_{\boldsymbol{k}}$, and the Kohn-Sham functions can be labeled by $\boldsymbol{k}$ and a band index ν. According to Bloch's theorem, they obey the relation

$$\psi_{\boldsymbol{k}\nu}(\boldsymbol{r}) = e^{\mathrm{i}\boldsymbol{k}\cdot\boldsymbol{r}} u_{\boldsymbol{k}\nu}(\boldsymbol{r}), \tag{2.9}$$

where $u_{\boldsymbol{k}\nu}(\boldsymbol{r})$ are lattice-periodic functions. They are updated in every step of the loop until self consistency is reached. Within DFT codes, it is important to express $u_{\boldsymbol{k}\nu}$ in a convenient basis to achieve a good precision in an affordable time. At the self-consistent point, the Bloch Hamiltonian $h_{\boldsymbol{k}}$ does not change with the iterations any more, and the final Kohn-Sham equation

$$h_{\boldsymbol{k}} \left| u_{\boldsymbol{k}\nu} \right\rangle = \epsilon_{\boldsymbol{k}\nu} \left| u_{\boldsymbol{k}\nu} \right\rangle \tag{2.10}$$

provides an effective one-particle Hamiltonian $h_{\boldsymbol{k}}$ and its associated bands $\epsilon_{\boldsymbol{k}\nu}$. Band structures obtained with DFT codes in such a way are nowadays a standard tool to analyze electronic properties of materials.

2.1.2 Wannier functions

Because of the periodicity of $u_{\boldsymbol{k}\nu}(\boldsymbol{r})$, the Bloch states $|\psi_{\boldsymbol{k}\nu}\rangle$ are fully delocalized in real space, in accordance with the fact that they are as localized as possible in reciprocal space. If one wants to visualize the atomic orbitals, a local, equivalent, basis has to be used. The most prominent local basis set are Wannier functions, that are defined as the Fourier transform of Bloch functions. This definition is, however, not unique, since any unitary transformation of the Bloch states does not change the space spanned by them. The general definition of a Wannier function at the real-space lattice vector $\boldsymbol{R}_i$ is thus

$$\left| w_{\boldsymbol{R}_i n} \right\rangle = \sum_{\boldsymbol{k}} e^{\mathrm{i}\boldsymbol{k}\cdot\boldsymbol{R}_i} \sum_{\nu} U_{\boldsymbol{k}}^{n\nu} \left| \psi_{\boldsymbol{k}\nu} \right\rangle . \tag{2.11}$$

Due to the orthogonality of the Bloch functions $\langle \psi_{\boldsymbol{k}\nu} | \, \psi_{\boldsymbol{k}'\nu'} \rangle = \delta_{\nu\nu'} \delta_{\boldsymbol{k}\boldsymbol{k}'}$ the Wannier functions are orthogonal as well, $\left\langle w_{\boldsymbol{R}_i n} \middle| \, w_{\boldsymbol{R}_j n'} \right\rangle = \delta_{ij} \delta_{nn'}$.

The freedom to choose the matrices $U_{\boldsymbol{k}}$ can be used to find the transformation that gives maximally localized Wannier functions, where the spread of the Wannier function at the origin $\boldsymbol{R}_i = 0$, defined as

$$\Omega = \sum_n \left[\left\langle w_{0n} \right| \boldsymbol{r}^2 \left| w_{0n} \right\rangle - \left\langle w_{0n} \right| \boldsymbol{r} \left| w_{0n} \right\rangle^2 \right] , \tag{2.12}$$

is minimized [29]. Here, $\boldsymbol{r}$ is the position operator. One program package that is able to calculate maximally localized Wannier functions is *Wannier90*, interfacing with many different DFT codes [30].

An alternative to maximally localized Wannier functions are projective Wannier functions [31–33]. Within this approach, the Bloch functions are projected onto local, usually atomic-like, functions $|\chi_n^{\alpha\sigma}\rangle$. Here, n denotes the orbital, α the atom and σ the spin. An expansion of these orbitals in terms of some Bloch functions within a selected energy window $\mathcal{W}$ reads

$$|\tilde{\chi}_{\boldsymbol{k}n}^{\alpha\sigma}\rangle = \sum_{\nu \in \mathcal{W}} \langle \psi_{\boldsymbol{k}\nu} | \, \chi_n^{\alpha\sigma} \rangle \, |\psi_{\boldsymbol{k}\nu}\rangle \, . \tag{2.13}$$

Note that the states $|\tilde{\chi}_{\boldsymbol{k}n}^{\alpha\sigma}\rangle$ are not orthogonal because the selection of an energy window truncates the Hilbert space. However, they can be orthonormalized via

$$|w_{\boldsymbol{k}n}^{\alpha\sigma}\rangle = \sum_{\alpha' n'} S_{nn'}^{\alpha\alpha'} \left| \tilde{\chi}_{\boldsymbol{k}n'}^{\alpha'\sigma} \right\rangle , \tag{2.14}$$

where $S \equiv O(\boldsymbol{k},\sigma)^{-1/2}$ and $O_{nn'}^{\alpha\alpha'}(\boldsymbol{k},\sigma) = \left\langle \tilde{\chi}_{\boldsymbol{k}n}^{\alpha\sigma} \middle| \, \tilde{\chi}_{\boldsymbol{k}n'}^{\alpha'\sigma} \right\rangle$. Detailed information on the influence of the orthogonalization can be found in the PhD thesis of Gernot Kraberger [34]. The projective functions $|w_{\boldsymbol{k}n}^{\alpha\sigma}\rangle$ can be transformed to real-space Wannier functions by a Fourier transformation $|w_{\boldsymbol{k}n}^{\alpha\sigma}\rangle = \sum_{\boldsymbol{R}} e^{\mathrm{i}\boldsymbol{k}\cdot\boldsymbol{R}} |w_{\boldsymbol{R}n}^{\alpha\sigma}\rangle$. In practice, it is useful to define projection operators

$$P^{\alpha\sigma}(\boldsymbol{k}) = \sum_n |w_{\boldsymbol{k}n}^{\alpha\sigma}\rangle \langle w_{\boldsymbol{k}n}^{\alpha\sigma}| \tag{2.15}$$

to transform objects from the Bloch basis to the Wannier basis. Their matrix elements are given by

$$P_{n\nu}^{\alpha\sigma}(\boldsymbol{k}) = \sum_{n'\alpha'} S_{nn'}^{\alpha\alpha'} \left\langle \tilde{\chi}_{n'}^{\alpha'\sigma} \middle| \, \psi_{\boldsymbol{k}\nu} \right\rangle . \tag{2.16}$$

For example, the Hamiltonian in reciprocal space reads in the projected Wannier basis

$$H_{nn'}^{\alpha\sigma}(\boldsymbol{k}) = \sum_{\nu \in \mathcal{W}} P_{n\nu}^{\alpha\sigma} \epsilon_{\boldsymbol{k}\nu} P_{n'\nu}^{\alpha\sigma\,*} . \tag{2.17}$$

The so-called hopping Hamiltonian $H_{nn'}^{\alpha\sigma}(\boldsymbol{R})$ is then obtained by a Fourier transformation of this Hamiltonian. Projecting the Bloch energies as in Eq. (2.17) works well for unitary projectors, but in case the number of local orbitals (index n) is smaller than the number of bands (index ν), the projector matrices $P^{\alpha\sigma}$ are not quadratic, and the eigenenergies of $H^{\alpha\sigma}$ do not represent the electronic energies.

2.2 Interaction Hamiltonians

In the previous section, Wannier functions $\left|w^{\sigma}_{\boldsymbol{R}_i n}\right\rangle$ have been introduced as a convenient basis for localized wave functions. In this basis, the noninteracting part of the Hamiltonian of a crystal is easily expressed in second quantization as

$$H_0 = \sum_{ij,nm,\sigma} t^{nm}_{ij} c^{\dagger}_{in\sigma} c_{jm\sigma} = \sum_{\boldsymbol{k},nm,\sigma} \epsilon^{nm}_{\boldsymbol{k}} c^{\dagger}_{\boldsymbol{k}n\sigma} c_{\boldsymbol{k}m\sigma}, \tag{2.18}$$

where $c^{\dagger}_{in\sigma}$ creates an electron in the Wannier orbital $\left|w^{\sigma}_{\boldsymbol{R}_i n}\right\rangle$, and $c^{\dagger}_{\boldsymbol{k}n\sigma}$ is its Fourier transform. The elements t^{nm}_{ij} express a hopping amplitude from orbital m of an atom at $\boldsymbol{R}_j$ to the orbital n of the atom at $\boldsymbol{R}_i$. Due to translation symmetry, its Fourier transform $\epsilon^{nm}_{\boldsymbol{k}}$ is diagonal in the reciprocal lattice number $\boldsymbol{k}$. Diagonalizing the matrix $\epsilon_{\boldsymbol{k}}$ results again in the Bloch eigenenergies $\epsilon_{\boldsymbol{k}\nu}$.

To obtain correlation effects beyond the effective one-particle picture, the repulsion of two electrons has to be included explicitly. A direct evaluation of the two-electron interaction in Eq. (2.2) in atomic units in the Wannier basis yealds an interaction Hamiltonian [35]

$$H_{\text{int}} = \sum_{\substack{ijkl\\mnop\\\sigma\sigma'}} (U_{\text{bare}})^{\sigma\sigma'}_{\substack{ijkl,\\mnop}} c^{\dagger}_{im\sigma} c^{\dagger}_{jn\sigma'} c_{lp\sigma'} c_{ko\sigma}, \tag{2.19}$$

where

$$(U_{\text{bare}})^{\sigma\sigma'}_{\substack{ijkl,\\mnop}} = \int \mathrm{d}^3 r \int \mathrm{d}^3 r' w^{\sigma *}_{im}(\boldsymbol{r}) w^{\sigma' *}_{jn}(\boldsymbol{r}') \frac{1}{|\boldsymbol{r}-\boldsymbol{r}'|} w^{\sigma'}_{lp}(\boldsymbol{r}') w^{\sigma}_{ko}(\boldsymbol{r}). \tag{2.20}$$

Here, the abbreviation $w^{\sigma}_{im}(\boldsymbol{r}) \equiv \left\langle \boldsymbol{r} \middle| w^{\sigma}_{\boldsymbol{R}_i m}\right\rangle$ is used. So far, the screening of the electronic interactions has not been considered yet. Doing so, the bare Coulomb interaction $V(\boldsymbol{r},\boldsymbol{r}') \propto 1/|\boldsymbol{r}-\boldsymbol{r}'|$ is reduced by the dielectric function ϵ and has thus to be replaced by the screened interaction

$$W(\boldsymbol{r},\boldsymbol{r}',\omega) = \frac{V(\boldsymbol{r},\boldsymbol{r}')}{\epsilon(\boldsymbol{r},\boldsymbol{r}',\omega)}. \tag{2.21}$$

Note that the interaction parameters U become frequency dependent due to the screening.

With the interaction Hamiltonian H_{int}, the dimensionality of the Hamiltonian grows again exponentially with system size, since a Fourier transformation to reciprocal space as in Eq. (2.18) does not lead to a block structure with block sizes of single unit cells any more. Therefore, approximations are needed in order to obtain solutions. An important approximation is to assume locality of the interaction term, i.e., $U_{ijkl} \propto \delta_{ij}\delta_{ik}\delta_{il}$. This assumption is especially valid in systems with a strong screening. The local interaction that has to be calculated is thus

$$U^{\sigma\sigma'}_{mnop}(\omega) = \int \mathrm{d}^3 r \int \mathrm{d}^3 r' w^{\sigma *}_{m}(\boldsymbol{r}) w^{\sigma' *}_{n}(\boldsymbol{r'}) W(\boldsymbol{r}, \boldsymbol{r'}, \omega) w^{\sigma'}_{p}(\boldsymbol{r'}) w^{\sigma}_{o}(\boldsymbol{r}). \tag{2.22}$$

There are ways to calculate these interactions from band theory, for example, the constrained random phase approximation (cRPA) [36, 37] or the constrained local density approximation (cLDA) [38]. In this thesis, the screening is assumed to be constant and the interaction terms $U^{\sigma\sigma'}_{mnop}$ rather seen as parameters instead of definite values that are a posteriori compared to experiments in order to see the validity of the chosen parameters. There are, however, symmetry reasons leading to constraints when choosing the entries of the tensor $U^{\sigma\sigma'}_{mnop}$. Usually, also additional symmetries, which are not fulfilled exactly by the crystal, are assumed in order to simplify the parametrization of the interaction tensor.

An important choice for $U^{\sigma\sigma'}_{mnop}$ is the Slater parametrization, that follows from the assumption of spherical symmetry. In that case, radial and angular parts of the atomic eigenfunctions separate, and the eigenfunctions are of the form

$$\psi_{nlm_l}(r, \theta, \phi) = R_{nl}(r) Y^{m_l}_{l}(\theta, \phi),$$

where $Y^{m_l}_{l}$ are the spherical harmonics. In other words, the assumption is that the angular dependence is the same as in an atom, but the radial dependence may not. For a given shell with angular momentum quantum number l, it is then easy to parametrize the interaction tensor in the spherical basis (orbital indices $mnop$ account for different m_l) in terms of Slater integrals [39, 40]

$$F^k = \int r^2 \mathrm{d}r \int r'^2 \mathrm{d}r' \frac{\min(r, r')^k}{\max(r, r')^{k+1}} R^2(r) R^2(r'). \tag{2.23}$$

It reads then

$$U_{mnop} = \sum_{k=0}^{2l} a_{kl}(m, n, o, p) F^k, \tag{2.24}$$

with the Racah-Wigner numbers [34]

$$\begin{aligned} a_{kl}(m, n, o, p) = (2l+1)^2 & \begin{pmatrix} l & k & l \\ 0 & 0 & 0 \end{pmatrix}^2 \times \\ & \sum_{q=0}^{k} (-1)^{m+n+q} \begin{pmatrix} l & k & l \\ -m & q & o \end{pmatrix} \begin{pmatrix} l & k & l \\ -n & -q & p \end{pmatrix}. \end{aligned} \tag{2.25}$$

When the spherical symmetry is lifted, also the symmetries of the interaction tensor are reduced, and the parametrization of the interaction tensor in the spherical basis in terms of Slater integrals as in Eq. (2.24) is not valid any more (even though often assumed, since it serves as a good approximation). If the localized Wannier orbitals have a cubic surrounding, it is more convenient to express the interaction Hamiltonian in a cubic basis rather than in the spherical basis. Since there is only one s orbital ($l = 0$), the transformation is trivial. For p orbitals ($l = 1$), a possible choice is

$$\begin{aligned} p_x &= Y_1^0 \\ p_y &= \frac{1}{\sqrt{2}}\left(Y_1^{-1} - Y_1^1\right) \\ p_z &= -\frac{\mathrm{i}}{\sqrt{2}}\left(Y_1^{-1} + Y_1^1\right), \end{aligned} \tag{2.26}$$

for d orbitals ($l = 2$) we can choose [40]

$$\begin{aligned} d_{z^2} &= Y_2^0 \\ d_{xz} &= \frac{1}{\sqrt{2}}\left(Y_2^{-1} - Y_2^1\right) \\ d_{yz} &= \frac{\mathrm{i}}{\sqrt{2}}\left(Y_2^{-1} + Y_2^1\right) \\ d_{xy} &= \frac{\mathrm{i}}{\sqrt{2}}\left(Y_2^{-2} - Y_2^2\right) \\ d_{x^2-y^2} &= \frac{1}{\sqrt{2}}\left(Y_2^{-2} + Y_2^2\right). \end{aligned} \tag{2.27}$$

In a spherical environment, all $Y_l^{m_l}$ are degenerate for the same l. Therefore, also the cubic harmonics are degenerate. They are, however, advantageous in a cubic (or octahedral) environment, since the crystal field possibly breaks the degeneracies. The cubic harmonics are in this case still eigenfunctions, whereas the spherical harmonics are not. For example, cubic symmetry splits the five d orbitals to two degenerate e_g and three degenerate t_{2g} orbitals. The two e_g orbitals are d_{z^2} and $d_{x^2-y^2}$, the other three belong to the t_{2g} manifold.

When the one-particle basis is changed with respect to a transformation matrix T, as for example from spherical to cubic, the interaction tensor has to be transformed according to

$$\tilde{U}_{m'n'o'p'} = \sum_{mnop} U_{mnop} T^*_{m'm} T^*_{n'n} T_{oo'} T_{pp'}, \tag{2.28}$$

The actual numbers in this tensor thus depend on the choice of the basis. Note that this is also true for the density-density entries. For example, one can assume that the interaction parameters behave as in a spherical surrounding to calculate the tensor entries in the spherical basis using the Slater parametrization (2.24), and transform the tensor then to the cubic basis. In the following, it will be discussed what the symmetries of the interaction tensor are for a given quantum number l in a cubic environment, and how the parametrization is related to the Slater form.

In case of an s orbital, the only unitary transformation in orbital space is a multiplication with a phase. The only entry in the interaction tensor is $U_{0000} = F_s^0 = U$. The local interaction Hamiltonian has therefore always the form

$$H_{\text{int}} = U n_{\uparrow} n_{\downarrow}. \tag{2.29}$$

The total interaction Hamiltonian is the sum over all local ones. The full Hamiltonian modeling a one-orbital material also includes the hopping (2.18), so that it has the famous Hubbard form [41]

$$H = \sum_{ij} t_{ij} c_i^{\dagger} c_j + U \sum_i n_{i\uparrow} n_{i\downarrow}. \tag{2.30}$$

For p electrons in a cubic basis (p_x, p_y, p_z), the three orbitals are equivalent since they are connected by a rotation in real space that is an element of the cubic group. Therefore, the three orbitals are degenerate; the cubic environment does not break degeneracies. As a consequence, the Slater parametrization is still valid. Looking at the interaction tensor in the cubic basis, there are only three different entries, namely $U_{mmmm} = F_p^0 + 4/25\, F_p^2$, $U_{mnmn} = F_p^0 - 2/25\, F_p^2$, and $U_{mnnm} = 3/25\, F_p^2$ for $m \neq n$. Instead of parametrizing these three values by the Slater integrals F_p^0 and F_p^2, one can also define directly the Coulomb interaction $U \equiv U_{mmmm}$ and the exchange interaction $J_{\text{H}} \equiv U_{mnnm}$ as parameters of the Slater Hamiltonian. With that, one finds $U' \equiv U_{mnmn} = U - 2J_{\text{H}}$. The Slater Hamiltonian for p orbitals has then the Kanamori form

$$\begin{aligned} H_{\text{int}} = U \sum_m n_{m\uparrow} n_{m\downarrow} + U' \sum_{m \neq n} n_{m\uparrow} n_{n\downarrow} + (U' - J_{\text{H}}) \sum_{m<n,\sigma} n_{m\sigma} n_{n\sigma} \\ + J_{\text{H}} \sum_{m \neq n} c_{m\uparrow}^{\dagger} c_{n\downarrow}^{\dagger} c_{m\downarrow} c_{n\uparrow} + J_{\text{H}} \sum_{m \neq n} c_{m\uparrow}^{\dagger} c_{m\downarrow}^{\dagger} c_{n\downarrow} c_{n\uparrow}. \end{aligned} \tag{2.31}$$

The first three terms are density-density interactions, the latter two are spin-flip and pair-hopping terms, respectively. Note that the definition of U and J_{H} here follow the Kanamori notation in cubic systems. As mentioned earlier, these values change in basis transformations. Another popular definition is the Slater parametrization suited for the rotationally invariant Hamiltonian (2.24). There, the definition of the interaction strength U^{S} and the Hund's coupling J_{H}^{S} differ from the Kanamori values U and J_{H}. The interaction strength is defined as $U^{\text{S}} \equiv F^0$; the definition of the other parameters, as for example J_{H}^{S}, depends on the magnetic quantum number l. In case of p orbitals one defines $J_{\text{H}p}^{\text{S}} \equiv 1/5\, F_p^2$ [35]. Therefore, the relations between Slater and Kanamori parameters are $J_{\text{H}p}^{\text{S}} = 5/3\, J_{\text{H}}$ and $U_p^{\text{S}} = U - 4/3\, J_{\text{H}}$.

In case of d orbitals in a cubic basis $(d_{xy}, d_{xz}, d_{yz}, d_{z^2}, d_{x^2-y^2})$, the five orbitals are not equivalent, but the three t_{2g} orbitals are. If one only considers these three t_{2g} orbitals, this part of the Slater Hamiltonian has again the Kanamori structure (2.31), but with the interaction parameters [42]

$$\begin{aligned} U &= F_d^0 + \frac{4}{49}F_d^2 + \frac{4}{49}F_d^4 \\ J_{\mathrm{H}} &= \frac{3}{49}F_d^2 + \frac{20}{441}F_d^4 \\ U' &= F_d^0 - \frac{2}{49}F_d^2 - \frac{4}{441}F_d^4 = U - 2J_{\mathrm{H}} \end{aligned} \tag{2.32}$$

The Slater parameters of the d shell are usually chosen as $U_d^{\mathrm{S}} = F_d^0$, $J_{Hd}^{\mathrm{S}} = 1/14\,(F_d^2 + F_d^4)$, and $F_d^4 = 0.625 F_d^2$ [35]. Together with Eq. (2.32), relations between the Kanamori and Slater parameters of the t_{2g} subsystem can be obtained. Interestingly, also the two-orbital Hamiltonian of isolated e_g orbitals has a Kanamori form. The Coulomb term U is the same as in case of the t_{2g} (2.32), but the Hund's coupling is given by $J_{\mathrm{H},e_g} = 4/49\,F_d^2 + 15/441\,F_d^4$.

So far, spherical symmetry was assumed in order to use the Slater form of the t_{2g} and the e_g part of the interaction Hamiltonian of d orbitals. Both of them are of Kanamori type with $U' = U - 2J_{\mathrm{H}}$. The respective interaction parameters U and J_{H} of the two Hamiltonians are related through the Slater integrals F_d^0, F_d^2, and F_d^4. These three, in principle independent, parameters are the only needed for a spherically symmetric d shell. If the symmetry is lowered by a cubic crystal field splitting called $10Dq$, 10 independent parameters are required to describe the full interaction Hamiltonian [40]. Looking now at the t_{2g} part of the Hamiltonian, it is still of Kanamori form (2.31), but with 3 instead of 2 independent parameters. As a consequence, U', U, and J_{H} are independent, when spherical symmetry is not required. In contrast, only two independent parameters are needed to describe the e_g Hamiltonian. Therefore, $U' = U - 2J_{\mathrm{H}}$ is still required in this case [40, 42]. The remaining $10 - 3 - 2 = 5$ independent parameters describe the coupling between e_g and t_{2g} orbitals.

Since the Kanamori Hamiltonian (2.31) represents the correct Hamiltonian for p, t_{2g}, and e_g orbitals in case of large $10Dq$, this model is further investigated here. Even though it is the most general form in a cubic surrounding, in some other models, as for example when a large spin-orbit coupling is involved (see Chapter 6), it is helpful to consider a generalization of the multi-orbital Kanamori Hamiltonian, where not only U, U' and Hund's coupling J_{H} are independent, but also the spin-flip and the pair-hopping amplitudes J_{SF} and J_{PH}. It reads then [42]

$$\begin{aligned} H_{\mathrm{GK}} = U \sum_m n_{m\uparrow} n_{m\downarrow} &+ U' \sum_{m \neq n} n_{m\uparrow} n_{n\downarrow} + (U' - J_{\mathrm{H}}) \sum_{m<n,\sigma} n_{m\sigma} n_{n\sigma} \\ &+ J_{\mathrm{SF}} \sum_{m\neq n} c_{m\uparrow}^\dagger c_{n\downarrow}^\dagger c_{m\downarrow} c_{n\uparrow} + J_{\mathrm{PH}} \sum_{m \neq n} c_{m\uparrow}^\dagger c_{m\downarrow}^\dagger c_{n\downarrow} c_{n\uparrow}. \end{aligned} \tag{2.33}$$

For a further interpretation of this Hamiltonian, it is helpful to rewrite it in terms of total charge N, total spin $\boldsymbol{S}$, and total orbital isospin. The first two are given by

$$N = \sum_{m\sigma} n_{m\sigma}, \qquad \boldsymbol{S} = \sum_{m,\sigma\sigma'} c^\dagger_{m\sigma} \boldsymbol{s}_{\sigma\sigma'} c_{m\sigma'}, \tag{2.34}$$

where $\boldsymbol{s}$ is the vector of the matrix representation of a single spin-1/2 electron. Usually, the prefactor $\hbar$ is absorbed in the energy units and the conventional spin basis is chosen, so that the representation reads $\boldsymbol{s} = \boldsymbol{\sigma}/2$, with Pauli matrices

$$\sigma_x = \begin{pmatrix} 0 & 1 \\ 1 & 0 \end{pmatrix} \quad \sigma_y = \begin{pmatrix} 0 & -\mathrm{i} \\ \mathrm{i} & 0 \end{pmatrix} \quad \sigma_z = \begin{pmatrix} 1 & 0 \\ 0 & -1 \end{pmatrix}. \tag{2.35}$$

The definition of the total orbital isospin depends on the number of considered orbitals, which makes a distinction necessary.

First, consider the case of two orbitals, where the isospin $\boldsymbol{T}$ is defined in analogy to the physical spin, just exchanging spin and orbital indices

$$\boldsymbol{T} = \frac{1}{2} \sum_{\sigma,mn} c^\dagger_{m\sigma} \boldsymbol{\sigma}_{mn} c_{n\sigma}. \tag{2.36}$$

The two-orbital generalized Kanamori Hamiltonian can then be rewritten as [42]

$$\begin{aligned} H_{\mathrm{GK}} = {} & \big(U + U' - J_{\mathrm{H}} + J_{\mathrm{SF}}\big) \frac{N(N-1)}{4} - \big(U - U' - J_{\mathrm{H}} + 3J_{\mathrm{SF}}\big) \frac{N}{4} \\ & + (J_{\mathrm{SF}} + J_{\mathrm{PH}}) T_x^2 + (J_{\mathrm{SF}} - J_{\mathrm{PH}}) T_y^2 + (U - U') T_z^2 \\ & + (J_{\mathrm{SF}} - J_{\mathrm{H}}) S_z^2. \end{aligned} \tag{2.37}$$

This Hamiltonian has the maximum charge, spin, and orbital symmetry $U(1)_C \otimes SU(2)_S \otimes SU(2)_O$ only if the parameters obey $J_{\mathrm{PH}} = 0$, $J_{\mathrm{SF}} = J_{\mathrm{H}}$ and $U' = U - J_{\mathrm{H}}$, resulting in [42]

$$\begin{aligned} & \left(U - \frac{1}{2} J_{\mathrm{H}}\right) \frac{N(N-1)}{2} - \frac{3}{4} J_{\mathrm{H}} N + J_{\mathrm{H}} \boldsymbol{T}^2 \\ = {} & \left(U - \frac{3}{2} J_{\mathrm{H}}\right) \frac{N(N-1)}{2} + \frac{3}{4} J_{\mathrm{H}} N - J_{\mathrm{H}} \boldsymbol{S}^2. \end{aligned} \tag{2.38}$$

This Hamiltonian maximizes the total spin S according to Hund's first rule and was originally introduced to describe magnetic impurities [42, 43]. It is, however, not compatible with the two-orbital Kanamori Hamiltonian (2.31) usually used to describe two p or d orbitals in a cubic environment. As mentioned before, for e_g orbitals, $J_{\mathrm{SF}} = J_{\mathrm{PH}} = J_{\mathrm{H}}$ and $U' = U - 2J_{\mathrm{H}}$ are required. Hamiltonian (2.37) reads in this case

$$H_{e_g} = (U - J_{\mathrm{H}}) \frac{N(N-1)}{2} - J_{\mathrm{H}} N + 2J_{\mathrm{H}} \left(\boldsymbol{T}^2 - T_y^2\right), \tag{2.39}$$

which is due to the T_y term not invariant under rotations in orbital space.

Table 2.1: Eigenenergies of the three-orbital Kanamori Hamiltonian (2.43) sorted by their quantum numbers. Fillings larger than $N = 3$ are added in brackets. The degeneracies are given by $(2S + 1)(2L + 1)$.

N	S	L	Degeneracy	Energy
0 [6]	0	0	1	0 $[15U - 30J_{\mathrm{H}}]$
1 [5]	1/2	1	6	0 $[10U - 20J_{\mathrm{H}}]$
2 [4]	1	1	9	$U - 3J_{\mathrm{H}}$ $[6U - 13J_{\mathrm{H}}]$
2 [4]	0	2	5	$U - J_{\mathrm{H}}$ $[6U - 11J_{\mathrm{H}}]$
2 [4]	0	0	1	$U + 2J_{\mathrm{H}}$ $[6U - 8J_{\mathrm{H}}]$
3	3/2	0	4	$3U - 9J_{\mathrm{H}}$
3	1/2	2	10	$3U - 6J_{\mathrm{H}}$
3	1/2	1	6	$3U - 4J_{\mathrm{H}}$

In case of three orbitals, an orbital isospin can be defined as

$$L_m = \mathrm{i} \sum_{\sigma,no} \varepsilon_{mno} c^\dagger_{n\sigma} c_{o\sigma}. \tag{2.40}$$

With this definition, the generalized Kanamori reads [42]

$$\begin{aligned} H_{\mathrm{GK}} = &\left(3U' - U\right) \frac{N(N-1)}{4} + \left(U - U' - J_{\mathrm{H}}\right) \frac{N}{4} + \left(U' - U\right) \boldsymbol{S}^2 \\ &+ \frac{1}{2} \left(U' - U + J_{\mathrm{H}}\right) \boldsymbol{L}^2 + \left(J_{\mathrm{SF}} - J_{\mathrm{H}}\right) \sum_{m \neq n} c^\dagger_{m\uparrow} c^\dagger_{n\downarrow} c_{m\downarrow} c_{n\uparrow} \\ &+ \left(U' - U + J_{\mathrm{H}} + J_{\mathrm{PH}}\right) \sum_{m \neq n} c^\dagger_{m\uparrow} c^\dagger_{m\downarrow} c_{n\downarrow} c_{n\uparrow} \end{aligned} \tag{2.41}$$

For a full $U(1)_C \otimes SU(2)_S \otimes SO(3)_O$ symmetry, the last two terms have to vanish, i.e., $J_{\mathrm{SF}} = J_{\mathrm{H}}$ and $J_{\mathrm{PH}} = U - U' - J_{\mathrm{H}}$, so that U, J_{H}, and U' are still free parameters. For example, the highly-symmetric solution with $U' = U - J_{\mathrm{H}}$ (corresponding to $J_{\mathrm{PH}} = 0$) yields

$$\left(U - \frac{3}{2} J_{\mathrm{H}}\right) \frac{N(N-1)}{2} - J_{\mathrm{H}} \boldsymbol{S}^2, \tag{2.42}$$

equivalent to the highly symmetric version of the two-orbital generalized Kanamori (2.38). The fact that the choice $U' = U - J_{\mathrm{H}}$ and $J_{\mathrm{PH}} = 0$ leads to a highly symmetric Hamiltonian that only depends on N^2, N, and $\boldsymbol{S}^2$ can be generalized to an arbitrary number of orbitals [42]. A vanishing pair hopping, however, is not possible for a physical t_{2g} Hamiltonian, which requires $J_{\mathrm{PH}} = J_{\mathrm{SF}} = J_{\mathrm{H}}$. In that case, $U' = U - 2J_{\mathrm{H}}$ is required (as in the Slater parametrization) in order to obtain the full symmetry. The t_{2g} Hamiltonian is then

$$H_{t_{2g}} = (U - 3J_{\mathrm{H}})\frac{N(N-1)}{2} + \frac{5}{2}J_{\mathrm{H}}N - 2J_{\mathrm{H}}\boldsymbol{S}^2 - \frac{J_{\mathrm{H}}}{2}\boldsymbol{L}^2. \tag{2.43}$$

In case U' differs from the symmetric value by $\Upsilon \equiv U' - U + 2J_{\mathrm{H}}$, the prefactors of the operators are modified, and an additional pair hopping term $\Upsilon \sum_{m\neq n} c^{\dagger}_{m\uparrow}c^{\dagger}_{m\downarrow}c_{n\downarrow}c_{n\uparrow}$ that breaks the symmetry is added. From Eq. (2.43), one can immediately read off the eigenenergies for a given filling N, once the eigenvalues of $\boldsymbol{S}^2$ and $\boldsymbol{L}^2$ are known. The first operator, $\boldsymbol{S}^2$, is by definition (2.34) the square of the total spin and has therefore the eigenvalue $S(S+1)$ where the possible values of S are given by the rules of coupling N different $s = 1/2$ particles. For example, in case of $N = 2$ one finds $S = 0, 1$. The second operator, $\boldsymbol{L}^2$, is equivalent to the sum of angular momenta with $l = 1$ and has eigenvalues $L(L+1)$ [40, 42]. This is expected since the three-orbital Kanamori Hamiltonian represents the interactions in p orbitals. It is, however, interesting, that this Hamiltonian is also a good choice for the t_{2g} subspace of the d orbitals that actually have $l = 2$. A closer look at this relation is given in section 3.3. With the eigenvalues of $\boldsymbol{S}^2$ and $\boldsymbol{L}^2$, the eigenenergies are known and displayed in table 2.1. Note that not all combinations of L and S are possible due to Pauli principle. From the eigenvalues, one sees that the Kanamori Hamiltonian intrinsically captures the first two Hund's rules, namely that first the total spin has to be maximized, then the total angular momentum. If $U' \neq U - 2J_{\mathrm{H}}$, some energies are shifted, but only the $L = 2$ levels split into 2 levels each, since the symmetry breaking additional pair hopping only acts in this subspace.

2.3 Dynamical mean-field theory

This section provides a basic introduction to the dynamical mean-field theory (DMFT), which is the most-used numerical method for obtaining the results of this thesis. Most derivations are left out here for the sake of brevity; they can be found, for example, in Ref. [5].

The goal of the DMFT is to solve model Hamiltonians of localized Wannier orbitals $H = H_0 + H_{\mathrm{int}}$ consisting of a noninteracting hopping part H_0 (see Eq. (2.18)) and a local interaction Hamiltonian H_{int} as introduced in the previous section. The basic idea is to map the full Hamiltonian H self-consistently onto an Anderson impurity model (AIM), which consists of a strongly correlated impurity coupled to a noninteracting bath. The Hamiltonian of the AIM is

$$\begin{aligned} H_{\mathrm{AIM}} = &\sum_{nm,\sigma} \epsilon^{nm}_{\mathrm{loc}} c^{\dagger}_{n\sigma}c_{m\sigma} + H_{\mathrm{int}} + \sum_{p,\sigma} \epsilon^{p}_{\mathrm{bath}} b^{\dagger}_{p\sigma}b_{p\sigma} \\ &+ \sum_{np,\sigma}\left(V_{np}c^{\dagger}_{n\sigma}b_{p\sigma} + V^{*}_{np}b^{\dagger}_{p\sigma}c_{n\sigma}\right). \end{aligned} \tag{2.44}$$

The first term describes the local noninteracting Hamiltonian on the impurity and is determined by the original hopping problem via

$$\epsilon_{\text{loc}}^{nm} = \frac{1}{N_k} \sum_{\boldsymbol{k}} \epsilon_{\boldsymbol{k}}^{nm}, \tag{2.45}$$

the second term is the interacting part. The third term is the Hamiltonian of the bath ($b^\dagger$ creates a particle in the bath), the last term couples the bath to the impurity. Note that the noninteracting part of the AIM described here does not contain terms that couple different spin species like $c_{n\sigma}^\dagger c_{m\sigma'}$. Such terms are, in general, needed if the SOC is included. However, for simplicity, it is assumed in this section that the spin species are not coupled and that they are identical.

The full noninteracting Hamilton matrix H_0^{AIM} consists of both impurity and bath, the impurity block and the bath block are coupled by the elements V_{np}. The noninteracting Green's function is given by

$$G_0^{\text{AIM}}(z) = \left(z - H_0^{\text{AIM}}\right)^{-1}, \tag{2.46}$$

where z is a complex frequency that is typically $z = \omega + \mathrm{i}0^+$ for the retarded Green's function, and $z = \mathrm{i}\omega_n$ for the Matsubara Green's function with fermionic Matsubara frequencies $\omega_n = (2n+1)\pi/\beta$ at inverse temperature β with $n \in \mathbb{N}$. Since H_0^{AIM} is not block diagonal, the impurity block and the bath block of $G_0^{\text{AIM}}(z)$ are coupled as well. However, it is possible to effectively integrate out the bath. The impurity part of $G_0^{\text{AIM}}(z)$, called $\mathcal{G}_0(z)$, can then be written as

$$\mathcal{G}_0(z) = \left(z - \epsilon_{\text{loc}} - \Delta(z)\right)^{-1}, \tag{2.47}$$

with a hybridization function matrix $\Delta(z)$, whose elements are

$$\Delta^{nm}(z) = \sum_p \frac{V_{np}^* V_{mp}}{z - \epsilon_{\text{bath}}^p} \tag{2.48}$$

Note that the inversion is a matrix inversion in the multi-orbital case since ϵ_{loc} and $\Delta(z)$ are matrices then. Given $\mathcal{G}_0(z)$ and H_{int}, an impurity solver can be used to calculate the interacting impurity Green's function $G_{\text{imp}}(z)$. The self-energy $\Sigma(z)$ is related to the Green's functions via the Dyson equation

$$G_{\text{imp}}^{-1}(z) = \mathcal{G}_0^{-1}(z) - \Sigma(z). \tag{2.49}$$

The correlation effects of H_{int} are thus encoded in $\Sigma(z)$.

The noninteracting Green's function of the full lattice model one originally wants to solve is

$$G_{\text{latt},\,0}(\boldsymbol{k}, z) = \left(z - \epsilon_{\boldsymbol{k}}^{nm} + \mu\right)^{-1}, \tag{2.50}$$

where the chemical potential μ has to be adjusted such that the interacting Green's function has the correct filling. Using the Dyson equation on the lattice, the interacting

Green's function is given by

$$G_{\text{latt}}(\boldsymbol{k},z) = \left(z - \epsilon_{\boldsymbol{k}}^{nm} + \mu - \Sigma(\boldsymbol{k},z)\right)^{-1}, \tag{2.51}$$

Within DMFT, the self-energy $\Sigma(\boldsymbol{k},z)$ is approximated by the local self-energy $\Sigma(z)$ of the AIM. However, the hybridization function $\Delta(z)$ optimally approximating the physical problem is not determined yet. Therefore, an additional constraint is needed in order to obtain the best $\Delta(z)$. In DMFT, the constraint is that the local Green's function G_{loc} has to be identical to the impurity Green's function

$$G_{\text{loc}}(z) = \frac{1}{N_k}\sum_{\boldsymbol{k}} G_{\text{latt}}(\boldsymbol{k},z) = G_{\text{imp}}(z). \tag{2.52}$$

This equation is called DMFT self-consistency condition and determines implicitly the AIM noninteracting Green's function and the hybridization function.

In practice, the self-consistency condition is solved in an iterative procedure. One starts with some initial self-energy and calculates the initial G_{latt} and G_{loc} using Eqs. (2.51) and (2.52). Using the self-consistency condition and the Dyson equation (2.49), $\mathcal{G}_0(z)$ is obtained. The AIM with this noninteracting Green's function is solved, yielding an impurity Green's function $G_{\text{imp}}(z)$ and an updated self-energy $\Sigma(z)$. With the new Σ, the next iteration can be started. The procedure is converged when $\Sigma(z)$ does not change with the iteration any more and when $G_{\text{loc}} = G_{\text{imp}}$.

2.3.1 DFT + DMFT

In case of real-material calculations, the noninteracting Hamiltonian has to be chosen realistically. Usually, this is done by a DFT calculation, followed by a Wannier projection onto a subset of orbitals that is believed to show interesting correlation physics. The interaction Hamiltonian is then defined in this Wannier basis and acts only on the subset of correlated orbitals. However, the correlations are also included to some extend in the exchange-correlation functional of DFT. Due to this so-called *double counting* of the correlation energy, the energy of the correlated orbitals has to be lowered by a double-counting correction to compensate for this effect.

Two important Wannier bases are maximally localized Wannier functions and projective Wannier functions, which are both explained in Sec. 2.1.2. Here, a way to combine DFT + DMFT is shown by means of the projection formalism, following Ref. [32]. In this case, the information how the correlated orbitals are related to the uncorrelated bands is encoded in the projectors $P_{n\nu}^{\alpha\sigma}(\boldsymbol{k})$. With them, one can transform quantities from the band basis to the basis of localized orbitals. Instead of performing the DMFT cycle in the Wannier basis with the downfolded Hamiltonian (2.17), one can rather stay in the Bloch basis and *upfold* the self-energy to the Bloch space

$$\Sigma_{\nu\nu'}^{\sigma}(\boldsymbol{k},z) = \sum_{\alpha}\sum_{nn'} P_{n\nu}^{\alpha\sigma *}(\boldsymbol{k}) \left[\Sigma_{nn'}^{\alpha\sigma}(z) - \Sigma_{nn'}^{\text{dc},\,\alpha\sigma}\right] P_{n'\nu'}^{\alpha\sigma}(\boldsymbol{k}), \tag{2.53}$$

where the double-counting correction Σ^{dc} is already subtracted. This upfolded self-energy as well as the Bloch energies $\epsilon_{\boldsymbol{k}\nu}$ are used to calculate the lattice Green's function with Eq. (2.51), which reads in the Bloch basis

$$G_{\mathrm{latt}}^{\sigma,\nu\nu'}(\boldsymbol{k},z) = \left[(z - \epsilon_{\boldsymbol{k}\nu} + \mu)\,\delta_{\nu\nu'} - \Sigma_{\nu\nu'}^{\sigma}(\boldsymbol{k},z)\right]^{-1}. \tag{2.54}$$

Since the local Green's function in the local Wannier basis is needed for the self-consistency cycle, the lattice Green's function has to be downfolded, which leads to the local Green's function

$$G_{\mathrm{loc}}^{\alpha\sigma,nn'}(z) = \sum_{\boldsymbol{k}} \sum_{\nu\nu'} P_{n\nu}^{\alpha\sigma}(\boldsymbol{k}) G_{\mathrm{latt}}^{\sigma,\nu\nu'}(\boldsymbol{k},z) P_{n'\nu'}^{\alpha\sigma *}(\boldsymbol{k}). \tag{2.55}$$

Using this local Green's function, the other DMFT steps can be performed. The chemical potential μ has to be adjusted such that the electron filling in the Bloch basis is correct. The double-counting correction $\Sigma_{nn'}^{\mathrm{dc},\,\alpha\sigma}$ should rectify the part of the correlation strength that is present in both DFT and DMFT. Many different approaches have been presented in literature, the method of choice depends on the problem [44–48].

2.3.2 Impurity solvers

How to solve the impurity model, i.e., calculate $G_{\mathrm{imp}}(z)$ given H_{AIM}, has not been discussed so far. Since this step is usually the most involved and time consuming part in a DMFT calculation, a short introduction is given here.

The first DMFT calculations [4] used the iterative perturbation theory [5, 49–54] as a solver, which is a computationally inexpensive, but approximate approach. Another approach that is frequently used is exact diagonalization [5, 55]. There, the AIM is restricted to a finite number of bath sites, such that the dimesion of H_{AIM} small enough that it can be diagonalized. Due to the truncation of the AIM, not all hybridization functions $\Delta(z)$ can be displayed. Usually, the parameters of the truncated AIM are chosen by a fit of Δ, leading to a systematic error due to the discretization. An advantage of this method is the access to real-frequency properties without analytic continuation. This is also true for methods based on the density matrix renormalization group and tensor networks [56–58], which can achieve a lot better spectral resolution than exact diagonlization, since more bath sites are included in the AIM. Other approaches include the non-crossing approximation [59], slave bosons [60], numerical renormalization group [61], and Quantum Monte Carlo methods. The Quantum Monte Carlo methods are a large class of important impurity solvers that need to be discussed in more detail. For DMFT calculations, the Hirsch-Fye algorithm [62] was the first method used [63–65]. A drawback of this method is the discretization of imaginary time steps, constituting a systematic error. This error can be avoided by another class of algorithms, called Continuous Time Quantum Monte Carlo (CTQMC) [66], which does not rely on a discretization of imaginary time τ. CTQMC is based on an expansion of the partition function $\mathcal{Z} = \mathrm{Tr}\ e^{-\beta H}$. For this reason, the Hamiltonian of the AIM is split into two parts $H_{\mathrm{AIM}} = H_{\mathrm{A}} + H_{\mathrm{B}}$, and $\mathcal{Z}$ is then expanded in powers of H_{B}. The choice of

H_B marks different flavors of CTQMC, prominent examples are the interaction expansion (CTINT) [67] and the hybridization expansion (CTHYB) [68, 69], which is briefly discussed here, since it is extensively used in this thesis.

Continuous-time Quantum Monte Carlo in hybridization expansion (CTHYB)

The following discussion on the CTHYB solver is based on Emanuel Gull's thesis [70] and review paper [66].

In the hybridization expansion, the part the partition function is expanded in is the hybridization term of the AIM $H_\mathrm{B} = H_\mathrm{hyb}$. The static part H_A is the rest, consisting of the local Hamiltonian of the impurity including the interaction terms, and the local Hamiltonian of the bath. Therefore, this Hamiltonian is called here H_lb. The partition function can then be written as

$$\mathcal{Z} = \mathrm{Tr}\, e^{-\beta H_\mathrm{AIM}} = \mathrm{Tr}\left[e^{-\beta H_\mathrm{lb}} T_\tau e^{-\int_0^\beta \mathrm{d}\tau\, H_\mathrm{hyb}(\tau)}\right], \tag{2.56}$$

where T_τ is the imaginary time-ordering operator and

$$H_\mathrm{hyb}(\tau) = e^{\tau H_\mathrm{lb}} H_\mathrm{hyb} e^{-\tau H_\mathrm{lb}} \tag{2.57}$$

the time-dependent hybridization Hamiltonian in interaction representation. Expansion in a power series in H_hyb yields

$$\mathcal{Z} = \sum_{q=0}^{\infty} \int_0^\beta \mathrm{d}\tau_1 \cdots \int_{\tau_q - 1}^\beta \mathrm{d}\tau_q \; \mathrm{Tr}\left[e^{-\beta H_\mathrm{lb}} H_\mathrm{hyb}(\tau_q) \cdots H_\mathrm{hyb}(\tau_1)\right]. \tag{2.58}$$

One can then write the Hamiltonians explicitly as their creation and annihilation operators and split off the parts containing only operators that act on the bath. The bath partition function can be calculated exactly, and one obtains

$$\begin{aligned} \mathcal{Z} =& \mathcal{Z}_\mathrm{bath} \sum_{q=0}^{\infty} \int \mathrm{d}\tau_1 \mathrm{d}\tau_1' \cdots \mathrm{d}\tau_q \mathrm{d}\tau_q' \\ & \times \mathrm{Tr}_\mathrm{imp}\left[e^{-H_\mathrm{loc}} T_\tau c(\tau_q) c^\dagger(\tau_q') \cdots c(\tau_1) c^\dagger(\tau_1')\right] \det \Delta. \end{aligned} \tag{2.59}$$

Thus, all the information about the influence of the bath onto the impurity is encoded in the determinant of the hybridization function. In CTHYB, Eq. (2.59) is estimated using importance sampling. Each set of imaginary times $\tau_1, \dots, \tau_q, \tau_1', \dots, \tau_q'$ defines a configuration; within this configuration space, a Markov chain Monte Carlo is performed.

As in other flavors of Quantum Monte Carlo, it cannot be guarantied that each contribution to the partition function is positive, hindering to interpret the contributions as probabilities, which is needed for the Monte Carlo. This is the so-called *sign problem*, leading to worse statistics. In some cases, it is not possible to perform the Monte Carlo in sizable time.

3 Spin-orbit coupling

3.1 Basics of relativistic quantum mechanics

So far, non-relativistic quantum mechanics has been used, so that all results are based on the Schrödinger equation. The energy-momentum relation of the Schrödinger equation, however, $E = p^2/2m$, whereas the correct relation from Einstein's special theory of relativity is

$$E^2 = m^2c^4 + c^2p^2. \tag{3.1}$$

The fact that the relation is quadratic in E was causing difficulties in the physical interpretation in the early days of quantum mechanics. Paul Dirac had the idea to write down a relation that is linear in the operators, i.e., $E = c\boldsymbol{\alpha}\cdot\boldsymbol{p} + \beta mc^2$, leading to the Dirac equation

$$\mathrm{i}\hbar\frac{\partial\psi}{\partial t} = -\mathrm{i}c\sum_i \alpha_i\frac{\partial\psi}{\partial x_i}\psi + \beta mc^2 = H\psi. \tag{3.2}$$

The correct dispersion (3.1) is only fulfilled if the quantities α_i and β obey the relations

$$\begin{aligned} \alpha_i\alpha_j + \alpha_j\alpha_i &= 2\delta_{ij} \\ \alpha_i\beta + \beta\alpha_i &= 0 \\ \beta^2 &= 1 \end{aligned} \tag{3.3}$$

Obviously, α_i and β cannot be ordinary numbers since they would not anticommute. It it possible to represent them as matrices, though, where 4 × 4 objects are the smallest possible. One frequently used representation is the Dirac representation

$$\alpha_i = \begin{pmatrix} 0 & \sigma_i \\ \sigma_i & 0 \end{pmatrix} \qquad \beta = \begin{pmatrix} \mathbb{1} & 0 \\ 0 & -\mathbb{1} \end{pmatrix}, \tag{3.4}$$

where σ_i are the Pauli matrices (2.35), and $\mathbb{1}$ is the 2 × 2 unit matrix.

How the Dirac equation is related to the Schrödinger equation and how its four components can be interpreted is best seen in the non-relativistic limit. This paragraph presents important results from Ref. [71], leaving out many steps of the actual calculation. Considering the Dirac equation with an electromagnetic potential $A^\mu = (\Phi, \boldsymbol{A})$, the momentum has to be replaced by $p^\mu \to p^\mu - e/cA^\mu$, so that the Dirac equation (3.2) reads

$$\mathrm{i}\hbar\frac{\partial\psi}{\partial t} = \left[c\boldsymbol{\alpha}\cdot\left(\boldsymbol{p} - \frac{e}{c}\boldsymbol{A}\right) + \beta mc^2 + e\Phi\right]\psi \tag{3.5}$$

In the non-relativistic limit, it is convenient to write the four-component vector ψ as two

two-component vectors ϕ and χ via

$$\psi = e^{-\mathrm{i}\frac{mc^2}{\hbar}t} \begin{pmatrix} \phi \\ \chi \end{pmatrix}, \tag{3.6}$$

since then the approximation

$$\chi \approx \frac{\boldsymbol{\sigma} \cdot (\boldsymbol{p} - (e/c)\boldsymbol{A})}{2mc} \phi \tag{3.7}$$

holds. The so-called small component χ is thus by a factor $\sim v/c$ smaller than the large component ϕ. With that, one finally arrives at the Pauli equation

$$\mathrm{i}\hbar \frac{\partial \phi}{\partial t} = \left[\frac{(\boldsymbol{p} - (e/c)\boldsymbol{A})^2}{2m} - \frac{e\hbar}{2mc} \boldsymbol{\sigma} \cdot \boldsymbol{B} + e\Phi \right] \phi \tag{3.8}$$

describing the physics of the large component.

To interpret the result, it is helpful to analyze the pysical meaning of $\boldsymbol{\sigma}$ by calculating some commutation relation, as done for example in [72]. With $\boldsymbol{l} = \boldsymbol{r} \times \boldsymbol{p}$, one finds

$$[H, l_z] = -\mathrm{i}\hbar c(-\alpha_1 p_y + \alpha_2 p_x) = -\mathrm{i}\hbar c(\boldsymbol{\alpha} \times \boldsymbol{p})_z. \tag{3.9}$$

The orbital angular momentum is thus not a conserved quantity in the Dirac equation, in contrast to non-relativistic quantum mechanics. Defining the operators

$$s_i \equiv \frac{\hbar}{2} \begin{pmatrix} \sigma_i & 0 \\ 0 & \sigma_i \end{pmatrix}, \tag{3.10}$$

the commutators are

$$[s_i, s_j] = \mathrm{i}\hbar \varepsilon_{ijk} s_k \tag{3.11}$$

and the eigenvalues of $\boldsymbol{s}^2$ are $3/4\,\hbar^2 = s(s+1)\hbar^2$. Therefore, $\boldsymbol{s}$ is the smallest possible angular momentum with $s = 1/2$. The commutator with the Dirac Hamiltonian H is

$$[H, s_z] = \mathrm{i}\hbar c(-\alpha_1 p_y + \alpha_2 p_x) = \mathrm{i}\hbar c(\boldsymbol{\alpha} \times \boldsymbol{p})_z. \tag{3.12}$$

Combining equations (3.9) and (3.12) and defining $j_z = l_z + s_z$, one finds $[H, j_z] = 0$. In analogy, one can get the same results for j_x and j_y, yielding

$$[H, j_i] = [H, \boldsymbol{j}^2] = 0 \tag{3.13}$$

for an angular momentum $\boldsymbol{j} = \boldsymbol{l} + \boldsymbol{s}$. The interpretation of these results is that $\boldsymbol{j}$ is the total relativistic angular momentum, which is conserved. The angular momentum $\boldsymbol{s}$ does not originate from the movement of the electron and is therefore an intrinsic angular momentum called *spin*.

With the definition of the angular momenta $\boldsymbol{l}$ and $\boldsymbol{s}$, the Pauli equation (3.8) can be reduced by assuming a weak uniform magnetic field $\boldsymbol{B}$, where only first order terms are kept, to

$$i\hbar\frac{\partial\phi}{\partial t} = \left[\frac{\boldsymbol{p}^2}{2m} - \frac{e}{2mc}(\boldsymbol{l} + 2\boldsymbol{s}) \cdot \boldsymbol{B}\right]\phi. \tag{3.14}$$

This equation is similar to its nonrelativistic equivalent, with the difference that the magnetic field also couples to an intrinsically appearing spin by $(e/2mc)g_s\boldsymbol{s}$ with a Landé factor of $g_s = 2$. To conclude, we have seen that the Dirac equation allows in the non-relativistic limit within the standard Dirac representation (3.4) to interpret the four components as the spin-up and spin-down components of a large and and a small part, respectively. Note that the assignment might be different in other representations. The spin quantities that pop up have to be treated with the Pauli equation (3.8) and are not explainable from non-relativistic quantum mechanics.

3.2 Relativistic origin of the spin-orbit coupling

3.2.1 The weakly relativistic limit

In the last section, the relativistic appearance of spin has been discussed. In the non-relativistic limit, this spin-components enter physically only as a Zeemann splitting (3.14) when a magnetic field is present. In this section it is shown that relaxing the limit to a weakly relativistic approximation will lead to a coupling of the internal spin with the orbital angular momentum, next to some shifts of energy levels.

Starting point is again the Dirac equation (3.5), but for simplicity this time only the static form $H\psi = E\psi$ is considered. Furthermore, the vector potential $\boldsymbol{A}$ is assumed to be zero and the scalar potential to be of the form $e\Phi = v(\boldsymbol{r}) \propto 1/r$. The Dirac equation is then

$$H\psi = \left[c\,\boldsymbol{\alpha}\cdot\boldsymbol{p} + \beta mc^2 + v(\boldsymbol{r})\right]\psi = \tilde{E}\psi \tag{3.15}$$

As in the non-relativistic approximation, it is useful to split the four-index object ψ into a large and a small component via

$$\psi = \begin{pmatrix}\phi\\ \chi\end{pmatrix}. \tag{3.16}$$

Note that the time dependence present in (3.6) is dropped since we are interested in the time-independent solution. The resulting two coupled equations are

$$\begin{aligned} c\,(\boldsymbol{\sigma}\cdot\boldsymbol{p})\,\chi &= [E - v(\boldsymbol{r})]\phi \\ c\,(\boldsymbol{\sigma}\cdot\boldsymbol{p})\,\phi &= [E - v(\boldsymbol{r}) + 2mc^2]\chi, \end{aligned} \tag{3.17}$$

where we defined $E = \tilde{E} - mc^2$, the energy on top of the rest energy mc^2. Substituting one equation into the other yields

$$\frac{1}{2m}(\boldsymbol{\sigma}\cdot\boldsymbol{p})K(\boldsymbol{\sigma}\cdot\boldsymbol{p})\,\phi + v(\boldsymbol{r})\phi = E\phi \tag{3.18}$$

for the large component, with

$$K \equiv \left[1 + \frac{E - v(\boldsymbol{r})}{2mc^2}\right]^{-1}. \tag{3.19}$$

Note that the momenta p_i do not commute with K, as it depends on position $\boldsymbol{r}$. The entries of the Pauli matrices, however, are numbers and commute, therefore, with K and p_i. Using the relation $\sigma_i \sigma_j = \delta_{ij}\mathbb{1} + \mathrm{i}\varepsilon_{ijk}\sigma_k$ and the Einstein sum convention, one obtains

$$(\boldsymbol{\sigma} \cdot \boldsymbol{p})K(\boldsymbol{\sigma} \cdot \boldsymbol{p}) = \sigma_i p_i K \sigma_j p_j = p_i K \sigma_i \sigma_j p_j = p_i K p_i \mathbb{1} + \mathrm{i}\sigma_k \varepsilon_{ijk} p_i K p_j,$$

hence Eq. (3.18) can be rewritten as

$$\left[\frac{1}{2m}\boldsymbol{p}K \cdot \boldsymbol{p} + \frac{\mathrm{i}}{2m}\boldsymbol{\sigma} \cdot (\boldsymbol{p}K \times \boldsymbol{p}) + v(\boldsymbol{r})\right]\phi = E\phi \tag{3.20}$$

The first term is the so-called scalar relativistic term since it is proportional to the unit matrix and hence not spin-dependent, whereas the second is the spin-orbit coupling (SOC).

In most applications, K (defined in Eq. (3.19)) is approximated. It is, however, not necessary to use the same approximation at both appearances of K in Eq. (3.20). For example, most DFT codes leave out the SOC, but keep a scalar relativist term since modifications in that part do not increase the complexity significantly. Here, we want to treat both on equal footing. Since $mc^2 \gg E - v(\boldsymbol{r})$, K can be expanded in $\frac{E - v(\boldsymbol{r})}{2mc^2}$. The crudest approximation is zeroth order, so that $K \approx 1$. This is equivalent to the non-relativistic limit that led to the Pauli equation (3.8) in the previous section. Since we are dealing here with the time-independent Dirac equation without an external vector potential, Eq. (3.20) reduces in this limit to the ordinary Schrödinger equation

$$\left[\frac{\boldsymbol{p}^2}{2m} + v(\boldsymbol{r})\right]\phi = E\phi.$$

Note that the SOC vanishes completely because of $\boldsymbol{p} \times \boldsymbol{p} = 0$. In order to obtain an effect of the SOC, K needs to be different from 1. Therefore, K has to be expanded at least to first order

$$K = \left[1 + \frac{E - v(\boldsymbol{r})}{2mc^2}\right]^{-1} \approx 1 - \frac{E - v(\boldsymbol{r})}{2mc^2}. \tag{3.21}$$

In this weakly relativistic approximation, the eigenvalue equation (3.20) reads

$$\left[\frac{\boldsymbol{p}^2}{2m} - \frac{1}{4m^2c^2}\left[\boldsymbol{p}(E - v(\boldsymbol{r})) \cdot \boldsymbol{p}\right] + \frac{\mathrm{i}}{4m^2c^2}\boldsymbol{\sigma} \cdot (\boldsymbol{p}v(\boldsymbol{r}) \times \boldsymbol{p})\right]\phi = [E - v(\boldsymbol{r})]\phi \tag{3.22}$$

Note that the energy E still appears in this Hamiltonian. The equation can be solved iteratively when replacing $E - v(\boldsymbol{r})$ with the whole operator on the left. Neglecting all terms $\propto 1/c^4$ or higher, the series ends after the first iteration and we can use

$E - v(\boldsymbol{r}) \approx \boldsymbol{p}^2/2m$ on the left hand side of the equation. However, the commutator $[\boldsymbol{p}, v(\boldsymbol{r})] = -\mathrm{i}\hbar\nabla v(\boldsymbol{r}) \neq 0$, so it does make a difference if $E - v(\boldsymbol{r})$ is replaced by $\boldsymbol{p}^2/2m$ in a term $\boldsymbol{p}(E - v(\boldsymbol{r})) \cdot \boldsymbol{p}$, or $(E - v(\boldsymbol{r}))\boldsymbol{p} \cdot \boldsymbol{p}$, or $\boldsymbol{p} \cdot \boldsymbol{p}(E - v(\boldsymbol{r}))$. Here, we symmetrize the term before replacing it, i.e.,

$$\begin{aligned}\boldsymbol{p}(E - v(\boldsymbol{r})) \cdot \boldsymbol{p} &= \frac{1}{2}\left[\boldsymbol{p} \cdot \boldsymbol{p}(E - v(\boldsymbol{r})) + \mathrm{i}\hbar\boldsymbol{p} \cdot \nabla v + (E - v(\boldsymbol{r}))\boldsymbol{p} \cdot \boldsymbol{p} + \mathrm{i}\hbar\nabla v \cdot \boldsymbol{p}\right] \\ &\approx \frac{\boldsymbol{p}^4}{2m} + \frac{\mathrm{i}\hbar}{2}[\nabla v, \boldsymbol{p}] = \frac{\boldsymbol{p}^4}{2m} - \frac{\hbar^2}{2}\nabla^2 v(\boldsymbol{r})\end{aligned}$$

Using the commutation relations also in the SOC term, equation (3.22) is of the form

$$\left[\frac{\boldsymbol{p}^2}{2m} + v(r) - \frac{\boldsymbol{p}^4}{8m^3c^2} + \frac{\hbar^2}{8m^2c^2}\nabla^2 v(\boldsymbol{r}) + \frac{\hbar}{4m^2c^2}\boldsymbol{\sigma} \cdot (\nabla v(\boldsymbol{r}) \times \boldsymbol{p})\right]\phi = E\phi \tag{3.23}$$

3.2.2 Fine structure levels of the hydrogen-like atom

In an hydrogen-like atom, the potential is of the special form $v(r) = Z\hbar c\alpha_{\mathrm{F}}/r$. As in all spherically symmetric potentials $v(\boldsymbol{r}) = v(r)$, one can rewrite Eq. (3.23) in terms of spin $\boldsymbol{s} = \boldsymbol{\sigma}\hbar/2$ and orbital angular momentum $\boldsymbol{l} = \boldsymbol{r} \times \boldsymbol{p}$. With a fine structure constant $\alpha_{\mathrm{F}} = e^2/(4\pi\epsilon_0\hbar c)$, it reads then

$$\left[\frac{\boldsymbol{p}^2}{2m} + \frac{Z\hbar c\alpha_{\mathrm{F}}}{r} - \frac{\boldsymbol{p}^4}{8m^3c^2} + \frac{Z\alpha_{\mathrm{F}}\pi\hbar^3}{2m^2c}\delta(r) + \frac{Z\alpha_{\mathrm{F}}\hbar}{2m^2c}\frac{1}{r^3}(\boldsymbol{l} \cdot \boldsymbol{s})\right]\phi = E\phi. \tag{3.24}$$

The first two terms correspond again to the Schrödinger equation. The third term proportional to $\boldsymbol{p}^4$ is called mass term and is easily understood from an expansion of the relativistic energy momentum relation $E(p)$. The fourth term is the Darwin correction. Since it is proportional to $\delta(r)$, it only affects the s orbitals. For all other orbitals, $\phi(0) = 0$ holds and the Darwin contribution vanishes. The last term is the SOC.

Without the relativistic corrections, the Hamiltonian commutes with the components of the orbital angular momentum $\boldsymbol{l}$. Therefore, the eigenfunctions in real space separate into a radial and an orbital part

$$\langle \boldsymbol{r} | \phi \rangle = \phi(\boldsymbol{r}) = R_{nl}(r) Y_l^{m_l}(\theta, \varphi) = \langle r, \theta, \varphi | n, l, m_l \rangle ,$$

and the eigenfunctions can be labeled by a radial (principal) quantum number n and two orbital quantum numbers, l and m_l, obeying $\boldsymbol{l}^2 |n, l, m_l\rangle = \hbar^2 l(l+1) |n, l, m_l\rangle$ and $l_z |n, l, m_l\rangle = m_l |n, l, m_l\rangle$. Because of the conservation of the angular momentum, the eigenenergies cannot depend on m_l. Due to an additional conserved quantity of the $1/r$ potential, called Runge-Lenz vector, also the different l are degenerate. The eigenvalues are

$$E_n = -\frac{Z^2\alpha_{\mathrm{F}}^2 mc^2}{2n^2}. \tag{3.25}$$

In this considerations, the spin does not appear. To get from Schrödinger to Pauli equation, it has to be included ad hoc. The eigenvalues are known from the usual

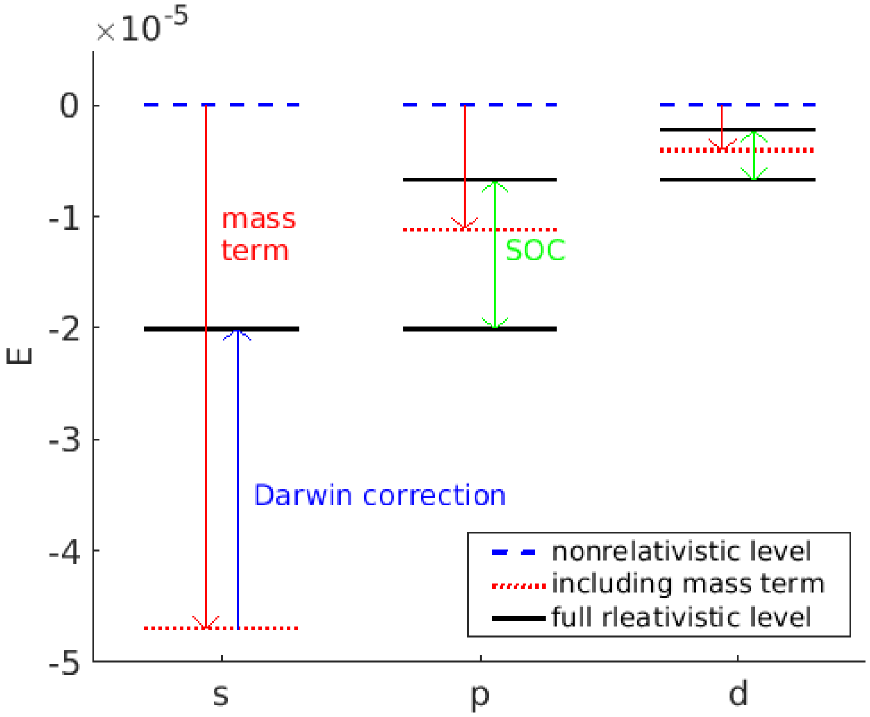

Figure 3.1: Fine-structure levels of the third shell ($n = 3$) of hydrogen. The energy is given in eV and relative to the non-relativistic level.

relations of angular momentum, i.e, $\boldsymbol{s}^2 |s, m_s\rangle = \hbar^2 s(s+1) |s, m_s\rangle$ and $s_z |s, m_s\rangle = \hbar m_s |s, m_s\rangle$ with $s = 1/2$ and $m_s = \pm 1/2$. The total eigenfunctions of the hydrogen-like atom without relativistic corrections are then $|n, l, m_l\rangle \otimes |s, m_s\rangle$ with eigenvalues given by Eq. (3.25).

Including the weakly relativistic corrections, the energy levels shift because of scalar relativistic mass and Darwin terms. The SOC leads to and additional splitting. Now, the strength of the splitting is considered. The spin-orbit term is of the form

$$H_{\mathrm{SO}} = \lambda(r) \boldsymbol{l} \cdot \boldsymbol{s}, \tag{3.26}$$

with a coupling parameter that is for a hydrogen-like Hamiltonian of the form

$$\lambda(r) = \frac{\hbar^2}{2m^2c^2} \frac{1}{r} \frac{\mathrm{d}v}{\mathrm{d}r} = \frac{Z\alpha_{\mathrm{F}}\hbar}{2m^2c} \frac{1}{r^3}, \tag{3.27}$$

where the first expression is true for a general spherically symmetric potential and the second in the special case of a hydrogen-like atom. Due to its dependence on r it will change the atomic eigenfunctions. However, a good approximation of the energy shift can be found in perturbation theory by calculating the expectation value [73, 74]

$$\left\langle \frac{1}{r^3} \right\rangle = \left\langle nlm_l \middle| \frac{1}{r^3} \middle| nlm_l \right\rangle = \int \mathrm{d}r\, r^2 R_{nl}^2(r) \frac{1}{r^3} = \left(\frac{Zmc\alpha_\mathrm{F}}{n\hbar} \right)^3 \frac{1}{l \left(l + \frac{1}{2}\right) (l+1)}, \tag{3.28}$$

which is valid for all $l \neq 0$. The expectation value of $\boldsymbol{l} \cdot \boldsymbol{s}$ can be evaluated using the total angular momentum $\boldsymbol{j}$. In section 3.1 it was shown that the total angular momentum $\boldsymbol{j} = \boldsymbol{l} + \boldsymbol{s}$ commutes with the Dirac Hamiltonian. The eigenvalues $\hbar^2 j(j+1)$ of $\boldsymbol{j}^2$ are thus good quantum numbers, where j can take the values $l \pm 1/2$. The expectation value is therefore [74]

$$\langle \boldsymbol{l} \cdot \boldsymbol{s} \rangle = \frac{1}{2} \left\langle \boldsymbol{j}^2 - \boldsymbol{l}^2 - \boldsymbol{s}^2 \right\rangle = \frac{\hbar^2}{2} \left[j(j+1) - l(l+1) - \frac{3}{4} \right] \tag{3.29}$$

for $l \neq 0$ and $\langle \boldsymbol{l} \cdot \boldsymbol{s} \rangle = 0$ for $l = 0$. Hence, the eigenvalues of the spin-orbit operator are in first order perturbation theory [74]

$$\langle H_\mathrm{SO} \rangle = \frac{Z^4 \alpha_\mathrm{F}^4 mc^2}{4n^3} \frac{j(j+1) - l(l+1) - 3/4}{l(l+1/2)(l+1)}. \tag{3.30}$$

Notably, it grows with the fourth power of the atom number Z and is thus strong for heavy elements. If the two scalar relativistic terms are included as well, one obtains a simple expression for the fine structure correction that is valid for all quantum numbers n, j, and l, where $j = 1/2$ for $l = 0$ and $j = l \pm 1/2$ else:

$$\langle H_\mathrm{mass} + H_\mathrm{Darwin} + H_\mathrm{SO} \rangle = -\frac{Z^4 \alpha_\mathrm{F}^4 mc^2}{2n^3} \left(\frac{1}{j + \frac{1}{2}} - \frac{3}{4n} \right). \tag{3.31}$$

This energy corrections are shown for hydrogen ($Z = 1$) in Fig. 3.1.

To obtain the correct fine structure, one can also solve the Dirac equation exactly, which is a bit more involved than the weakly relativistic approximation used here. The resulting atomic energies are

$$E_{nj} = -mc^2 \left[1 - \left(1 + \left[\frac{Z\alpha_\mathrm{F}}{n - j - \frac{1}{2} + \sqrt{\left(j + \frac{1}{2}\right)^2 - Z^2 \alpha_\mathrm{F}^2}} \right]^2 \right)^{-1/2} \right]. \tag{3.32}$$

Expanding this expression in $Z\alpha_\mathrm{F}$ yields in zeroth order the nonrelativistic eigenenergies (3.25) and in first order the correction (3.31).

3.3 SOC in p and d orbitals

In the last section, it has been shown that the relativistic effects can be approximated by scalar shifts in the energy and an additional spin-orbit coupling

$$H_{\mathrm{SO}} = \lambda\, \boldsymbol{l} \cdot \boldsymbol{s} = \lambda \left(l_x s_x + l_y s_y + l_z s_z \right) . \tag{3.33}$$

The s_i operators act only on spin space, whereas the l_i act only in orbital space, so $l_i s_i$ may also be written as $l_i \otimes s_i$. Since both l_i and s_i are single-particle operators, their direct product is one as well. The operators can therefore be expanded as $\boldsymbol{l} = \sum_{nm} c_n^\dagger \boldsymbol{l}_{nm} c_m$, where n and m are orbital indices, and $\boldsymbol{s} = \sum_{\sigma\sigma'} c_\sigma^\dagger \boldsymbol{s}_{\sigma\sigma'} c_\sigma'$, where σ and σ' are spin indices. Note that the same symbols $\boldsymbol{l}$ and $\boldsymbol{s}$, respectively, are used for both the operators as well as their matrix representations.

The irreducible representations of the spin operators are of dimension 2 and are independent of l. They are chosen here as $\boldsymbol{s} = \hbar \boldsymbol{\sigma}/2$, where $\boldsymbol{\sigma}$ are the usual Pauli matrices (2.35). As mentioned in the previous section, the spin-orbit coupling is only present for $l \geq 1$. A possible representation of the $l = 1$ orbitals in the spherical basis ($m_l = -1$, $m_l = 0$, $m_l = 1$) is easily obtained from the well-known relations

$$\begin{aligned} l_z \left| l, m_l \right\rangle &= \hbar m_l \left| l, m_l \right\rangle \\ l_\pm \left| l, m_l \right\rangle &= \hbar \sqrt{l(l+1) - m_l(m_l \pm 1)} \left| l, m_l \pm 1 \right\rangle , \end{aligned} \tag{3.34}$$

where $l_\pm = l_x \pm \mathrm{i} l_y$ are the so-called ladder operators. The matrices read

$$l_x = \frac{\hbar}{\sqrt{2}} \begin{pmatrix} 0 & 1 & 0 \\ 1 & 0 & 1 \\ 0 & 1 & 0 \end{pmatrix} \quad l_y = \frac{\hbar}{\sqrt{2}} \begin{pmatrix} 0 & \mathrm{i} & 0 \\ -\mathrm{i} & 0 & \mathrm{i} \\ 0 & -\mathrm{i} & 0 \end{pmatrix} \quad l_z = \hbar \begin{pmatrix} -1 & 0 & 0 \\ 0 & 0 & 0 \\ 0 & 0 & 1 \end{pmatrix} . \tag{3.35}$$

This representation can be transformed to a cubic basis (p_x, p_y, p_z) using transformation (2.26),

$$l_x = \hbar \begin{pmatrix} 0 & 0 & 0 \\ 0 & 0 & -\mathrm{i} \\ 0 & \mathrm{i} & 0 \end{pmatrix} \quad l_y = \hbar \begin{pmatrix} 0 & 0 & \mathrm{i} \\ 0 & 0 & 0 \\ -\mathrm{i} & 0 & 0 \end{pmatrix} \quad l_z = \hbar \begin{pmatrix} 0 & -\mathrm{i} & 0 \\ \mathrm{i} & 0 & 0 \\ 0 & 0 & 0 \end{pmatrix} . \tag{3.36}$$

The spin-orbit operator of p orbitals in a cubic basis ($p_x^\uparrow$, $p_y^\uparrow$, $p_z^\uparrow$, $p_x^\downarrow$, $p_y^\downarrow$, $p_z^\downarrow$) is therefore

$$\boldsymbol{l} \cdot \boldsymbol{s} = \frac{\hbar^2}{2} \begin{pmatrix} 0 & -\mathrm{i} & 0 & 0 & 0 & 1 \\ \mathrm{i} & 0 & 0 & 0 & 0 & -\mathrm{i} \\ 0 & 0 & 0 & -1 & \mathrm{i} & 0 \\ 0 & 0 & -1 & 0 & \mathrm{i} & 0 \\ 0 & 0 & -\mathrm{i} & -\mathrm{i} & 0 & 0 \\ 1 & \mathrm{i} & 0 & 0 & 0 & 0 \end{pmatrix} \tag{3.37}$$

From now on, the prefactor $\hbar$ will be dropped, since it just scales every angular momentum operator. This corresponds to a change to atomic units. As described in detail in the sections 3.1 and 3.2.2, the components of the total angular momentum $\boldsymbol{j} = \boldsymbol{l} + \boldsymbol{s}$ commute with the full Dirac Hamiltonian, and, hence, also with the spin-orbit operator. Therefore, using the eigenfunctions of $\boldsymbol{j}^2$ and j_z with eigenvalues $\boldsymbol{j}^2 \left|j, m_j\right\rangle = j(j+1) \left|j, m_j\right\rangle$ and $j_z \left|j, m_j\right\rangle = m_j \left|j, m_j\right\rangle$ as basis functions, H_{SO} has to be diagonal. This basis is called j basis. The relation between $\left|j, m_j\right\rangle$ and the cubic basis vectors $\left|l, m_l\right\rangle \otimes \left|s, m_s\right\rangle$ are obtained from the usual rules of adding angular momenta, leading to the Clebsch-Gordan coefficients

$$\begin{aligned}
\left|j = \frac{3}{2}, m_j = \frac{3}{2}\right\rangle &= \left|m_l = 1, m_s = \frac{1}{2}\right\rangle \\
\left|j = \frac{3}{2}, m_j = \frac{1}{2}\right\rangle &= \sqrt{\frac{1}{3}} \left|m_l = 1, m_s = -\frac{1}{2}\right\rangle + \sqrt{\frac{2}{3}} \left|m_l = 0, m_s = \frac{1}{2}\right\rangle \\
\left|j = \frac{1}{2}, m_j = \frac{1}{2}\right\rangle &= \sqrt{\frac{2}{3}} \left|m_l = 1, m_s = -\frac{1}{2}\right\rangle - \sqrt{\frac{1}{3}} \left|m_l = 0, m_s = \frac{1}{2}\right\rangle \\
\left|j = \frac{3}{2}, m_j = -\frac{3}{2}\right\rangle &= \left|m_l = -1, m_s = -\frac{1}{2}\right\rangle \\
\left|j = \frac{3}{2}, m_j = -\frac{1}{2}\right\rangle &= \sqrt{\frac{1}{3}} \left|m_l = -1, m_s = \frac{1}{2}\right\rangle + \sqrt{\frac{2}{3}} \left|m_l = 0, m_s = -\frac{1}{2}\right\rangle \\
\left|j = \frac{1}{2}, m_j = -\frac{1}{2}\right\rangle &= \sqrt{\frac{2}{3}} \left|m_l = -1, m_s = \frac{1}{2}\right\rangle - \sqrt{\frac{1}{3}} \left|m_l = 0, m_s = -\frac{1}{2}\right\rangle
\end{aligned} \tag{3.38}$$

Here, $l = 1$ and $s = 1/2$ is not written explicitly for brevity. Using transformation (2.26), the $l = 1$ orbitals can be expressed in terms of the cubic harmonics. For convenience, arrows are used to label $m_s = \pm 1/2$.

$$\begin{aligned}
\left|j = \frac{3}{2}, m_j = \frac{3}{2}\right\rangle &= -\frac{1}{\sqrt{2}} \left|p_x^{\uparrow}\right\rangle + \frac{\mathrm{i}}{\sqrt{2}} \left|p_y^{\uparrow}\right\rangle \\
\left|j = \frac{3}{2}, m_j = \frac{1}{2}\right\rangle &= \frac{2}{\sqrt{6}} \left|p_z^{\uparrow}\right\rangle - \frac{1}{\sqrt{6}} \left|p_x^{\downarrow}\right\rangle + \frac{\mathrm{i}}{\sqrt{6}} \left|p_y^{\downarrow}\right\rangle \\
\left|j = \frac{1}{2}, m_j = \frac{1}{2}\right\rangle &= -\frac{1}{\sqrt{3}} \left|p_z^{\uparrow}\right\rangle - \frac{1}{\sqrt{3}} \left|p_x^{\downarrow}\right\rangle + \frac{\mathrm{i}}{\sqrt{3}} \left|p_y^{\downarrow}\right\rangle \\
\left|j = \frac{3}{2}, m_j = -\frac{1}{2}\right\rangle &= \frac{2}{\sqrt{6}} \left|p_z^{\downarrow}\right\rangle + \frac{1}{\sqrt{6}} \left|p_x^{\uparrow}\right\rangle + \frac{\mathrm{i}}{\sqrt{6}} \left|p_y^{\uparrow}\right\rangle \\
\left|j = \frac{1}{2}, m_j = -\frac{1}{2}\right\rangle &= \frac{1}{\sqrt{3}} \left|p_z^{\downarrow}\right\rangle - \frac{1}{\sqrt{3}} \left|p_x^{\uparrow}\right\rangle - \frac{\mathrm{i}}{\sqrt{3}} \left|p_y^{\uparrow}\right\rangle \\
\left|j = \frac{3}{2}, m_j = -\frac{3}{2}\right\rangle &= \frac{1}{\sqrt{2}} \left|p_x^{\downarrow}\right\rangle + \frac{\mathrm{i}}{\sqrt{2}} \left|p_y^{\downarrow}\right\rangle
\end{aligned} \tag{3.39}$$

With this transformation, the spin-orbit matrix (3.37) is brought from the cubic p basis to j basis. It is then diagonal with elements $1/2$ for the four $j = 3/2$ orbitals and -1 in case of the two $j = 1/2$ orbitals, since

$$\boldsymbol{l} \cdot \boldsymbol{s} = \frac{1}{2}\left(\boldsymbol{j}^2 - \boldsymbol{l}^2 - \boldsymbol{s}^2\right) = \frac{1}{2}\left(j(j+1) - 2 - \frac{3}{4}\right). \tag{3.40}$$

Therefore, the SOC splits the (including spin) six p orbitals by an energy $\Delta E_{\mathrm{SO}} = 3/2\ \lambda$ into two $j = 1/2$ orbitals lower in energy and four $j = 3/2$ orbitals.

Similarly, using relations (3.34) for $l = 2$ and the transformation (2.27), one obtains a matrix representation of the angular momentum operators for d orbitals in a cubic basis (d_{yz}, d_{xz}, d_{xy}, d_{z^2}, $d_{x^2-y^2}$) [40]

$$\begin{aligned}
l_x &= \left(\begin{array}{ccc|cc} 0 & 0 & 0 & -\sqrt{3}\mathrm{i} & -\mathrm{i} \\ 0 & 0 & \mathrm{i} & 0 & 0 \\ 0 & -\mathrm{i} & 0 & 0 & 0 \\ \hline \sqrt{3}\mathrm{i} & 0 & 0 & 0 & 0 \\ \mathrm{i} & 0 & 0 & 0 & 0 \end{array}\right) \\
l_y &= \left(\begin{array}{ccc|cc} 0 & 0 & -\mathrm{i} & 0 & 0 \\ 0 & 0 & 0 & \sqrt{3}\mathrm{i} & -\mathrm{i} \\ \mathrm{i} & 0 & 0 & 0 & 0 \\ \hline 0 & -\sqrt{3}\mathrm{i} & 0 & 0 & 0 \\ 0 & \mathrm{i} & 0 & 0 & 0 \end{array}\right) \\
l_z &= \left(\begin{array}{ccc|cc} 0 & \mathrm{i} & 0 & 0 & 0 \\ -\mathrm{i} & 0 & 0 & 0 & 0 \\ 0 & 0 & 0 & 0 & 2\mathrm{i} \\ \hline 0 & 0 & 0 & 0 & 0 \\ 0 & 0 & -2\mathrm{i} & 0 & 0 \end{array}\right).
\end{aligned} \tag{3.41}$$

The lines indicate the blocks of t_{2g} and e_g orbitals. With that, the matrix of the SOC is found, that can again be transformed to j basis. Here, j can take the values $j = 3/2$ and $j = 5/2$. The eigenenergies of $H_{\mathrm{SO}} = \lambda \boldsymbol{l} \cdot \boldsymbol{s}$ are then $-3/2\ \lambda$ ($j = 3/2$) and λ ($j = 5/2$).

If a cubic crystal field is applied, the t_{2g} and e_g orbitals are split by $10Dq$. In that case, the Hamiltonian has three distinct energy levels. The diagonalization is easily done in the limit $10Dq \gg \lambda$, since then the e_g and t_{2g} blocks can be considered as decoupled. The e_g blocks of the angular momentum operators (3.41) have no entries. Therefore, the SOC does not influence the two e_g orbitals in this limit, the angular momentum is completely quenched. The t_{2g} blocks, on the other hand, have in our chosen basis ordering exactly the same form as the matrix representations of $\boldsymbol{l}$ of the p orbitals; they differ only by a minus sign. Therefore,

$$\boldsymbol{l}(t_{2g}) \mathrel{\widehat{=}} -\boldsymbol{l}(p), \tag{3.42}$$

which is called *T-P correspondence* [40]. As a consequence, the t_{2g} orbitals have an effective angular momentum of $l_{\mathrm{eff}} = 1$ due to a partially quenching of the $l = 2$ orbitals. Since the spin-orbit operator is linear in the orbital angular momentum, it also acquires a minus sign, but is the same apart from that, $H_{\mathrm{SO}}(t_{2g}) = \lambda\, \boldsymbol{l}_{\mathrm{eff}}\cdot\boldsymbol{s} \mathrel{\widehat{=}} -\lambda\, \boldsymbol{l}_p\cdot\boldsymbol{s} = -H_{\mathrm{SO}}(p)$. Its matrix representation in the basis $(d^{\uparrow}_{yz},\, d^{\uparrow}_{xz},\, d^{\uparrow}_{xy},\, d^{\downarrow}_{yz},\, d^{\downarrow}_{xz},\, d^{\downarrow}_{xy})$ and its eigenvectors can therefore be copied from Eqs. (3.37) and (3.39) and read

$$\boldsymbol{l}_{\mathrm{eff}}\cdot\boldsymbol{s} = \frac{1}{2}\begin{pmatrix} 0 & \mathrm{i} & 0 & 0 & 0 & -1 \\ -\mathrm{i} & 0 & 0 & 0 & 0 & \mathrm{i} \\ 0 & 0 & 0 & 1 & -\mathrm{i} & 0 \\ 0 & 0 & 1 & 0 & -\mathrm{i} & 0 \\ 0 & 0 & \mathrm{i} & \mathrm{i} & 0 & 0 \\ -1 & -\mathrm{i} & 0 & 0 & 0 & 0 \end{pmatrix} \tag{3.43}$$

$$\begin{aligned}
\left|j_{\mathrm{eff}} = \frac{3}{2}, m_j = \frac{3}{2}\right\rangle &= -\frac{1}{\sqrt{2}}\left|d^{\uparrow}_{yz}\right\rangle + \frac{\mathrm{i}}{\sqrt{2}}\left|d^{\uparrow}_{xz}\right\rangle \\
\left|j_{\mathrm{eff}} = \frac{3}{2}, m_j = \frac{1}{2}\right\rangle &= \frac{2}{\sqrt{6}}\left|d^{\uparrow}_{xy}\right\rangle - \frac{1}{\sqrt{6}}\left|d^{\downarrow}_{yz}\right\rangle + \frac{\mathrm{i}}{\sqrt{6}}\left|d^{\downarrow}_{xz}\right\rangle \\
\left|j_{\mathrm{eff}} = \frac{1}{2}, m_j = \frac{1}{2}\right\rangle &= -\frac{1}{\sqrt{3}}\left|d^{\uparrow}_{xy}\right\rangle - \frac{1}{\sqrt{3}}\left|d^{\downarrow}_{yz}\right\rangle + \frac{\mathrm{i}}{\sqrt{3}}\left|d^{\downarrow}_{xz}\right\rangle \\
\left|j_{\mathrm{eff}} = \frac{3}{2}, m_j = -\frac{1}{2}\right\rangle &= \frac{2}{\sqrt{6}}\left|d^{\downarrow}_{xy}\right\rangle + \frac{1}{\sqrt{6}}\left|d^{\uparrow}_{yz}\right\rangle + \frac{\mathrm{i}}{\sqrt{6}}\left|d^{\uparrow}_{xz}\right\rangle \\
\left|j_{\mathrm{eff}} = \frac{1}{2}, m_j = -\frac{1}{2}\right\rangle &= \frac{1}{\sqrt{3}}\left|d^{\downarrow}_{xy}\right\rangle - \frac{1}{\sqrt{3}}\left|d^{\uparrow}_{yz}\right\rangle - \frac{\mathrm{i}}{\sqrt{3}}\left|d^{\uparrow}_{xz}\right\rangle \\
\left|j_{\mathrm{eff}} = \frac{3}{2}, m_j = -\frac{3}{2}\right\rangle &= \frac{1}{\sqrt{2}}\left|d^{\downarrow}_{yz}\right\rangle + \frac{\mathrm{i}}{\sqrt{2}}\left|d^{\downarrow}_{xz}\right\rangle
\end{aligned} \tag{3.44}$$

The subscript “eff” is used here to denote that the functions are only related to effective angular momenta. As a consequence of the minus sign in the T-P equivalence, the $j_{\mathrm{eff}} = 3/2$ orbitals are lower in energy with an eigenvalue of $-\lambda/2$, the eigenenergy of the $j_{\mathrm{eff}} = 1/2$ orbitals is λ.

3.4 LS (Russel-Saunders) and jj coupling

According to Hund’s first two rules, the ground state of an atom is determined by 1.) maximization of the total spin S and 2.) maximization of the total angular momentum L. This behavior is encoded in the respective interaction Hamiltonian. In this thesis, the focus is on the t_{2g} orbitals, where the interaction can be described by a Kanamori Hamiltonian. Its properties as well as the eigenenergies depending on S and L are discussed in section 2.2. In this section, a Kanamori Hamiltonian with $U' = U - 2J_{\mathrm{H}}$ is again assumed. When SOC is present, the one-particle energy levels split, hence some degeneracies are lifted. Furthermore, $\boldsymbol{S}$ and $\boldsymbol{L}$ do not commute with the Hamiltonian any more, hence, their eigenvalues are not good quantum numbers. Only the total angular momentum $\boldsymbol{J}$, which is the sum of spin and orbital angular momenta of all electrons, commutes with the Hamiltonian, so only J and M_J are suited to label eigenstates. Because of the conservation of angular momentum, eigenstates with different M_J have to be degenerate if the number of electrons N and J are the same. The actual eigenvalues and eigenvectors can be calculated numerically by diagonalizing the total Hamiltonian

$$H = H_{\text{I}} + H_{\text{SO}}, \tag{3.45}$$

where, in the cubic basis, H_{I} is the Kanamori Hamiltonian (2.31) consisting of two-particle terms, and H_{SO} the one-particle spin-orbit coupling

$$H_{\text{SO}} = \lambda \sum_{\alpha\beta} (\boldsymbol{l}_{\text{eff}} \cdot \boldsymbol{s})_{\alpha\beta} c^{\dagger}_{\alpha} c_{\beta}. \tag{3.46}$$

Here, α and β are combined indices containing both spin and orbital index $\alpha = (m, \sigma)$, and $(\boldsymbol{l}_{\text{eff}} \cdot \boldsymbol{s})_{\alpha\beta}$ are the matrix elements written explicitly in Eq. (3.43). For p orbitals, the Hamiltonian looks exactly the same when λ is replaced by $-\lambda$.

In the limit of small and large SOC, approximate solutions can be found. In atomic physics, these limits are usually viewed as different ways to couple the angular momenta $\boldsymbol{s}_i$ and $\boldsymbol{l}_i$. If the SOC λ is small compared to Hund's coupling J_{H}, there is a strong tendency that the spins of different electrons are aligned, since the total spin has to be maximized first (Hund's rules). Therefore, it is assumed that the spins of the individual atoms couple first to a total spin $\boldsymbol{S} = \sum_i \boldsymbol{s}_i$, and the orbital angular momenta couple to a total angular momentum $\boldsymbol{L} = \sum_i \boldsymbol{l}_i$, just as in the case without SOC described in section 2.2. The total angular momentum is in this picture then obtained by coupling these two as $\boldsymbol{J} = \boldsymbol{L} + \boldsymbol{S}$. Therefore, this coupling scheme is called LS coupling or Russel-Saunders coupling. If the SOC is large, i.e., $\lambda \gg J_{\text{H}}$, the coupling of intrinsic and orbital angular momenta of the respective electrons is dominant. Therefore, first they couple to an angular momentum $\boldsymbol{j}_i$ of electron i, which then couple to a total angular momentum $\boldsymbol{J} = \sum_i \boldsymbol{j}_i$. This regime is hence called jj coupling.

Let us first discuss the limit of a small SOC, i.e., the LS coupling regime. Since the coupling of the spins $\boldsymbol{S} = \sum_i \boldsymbol{s}_i$ and the coupling of the orbital angular momenta $\boldsymbol{L} = \sum_i \boldsymbol{l}_i$ is dominant, S and L are still good quantum numbers. Additional atomic quantum numbers are M_S and M_L (note that all of them are degenerate without SOC), but they are not good quantum numbers if SOC is present. In first order perturbation theory, the energy correction of a state with N electrons, spin S and angular momentum L due to SOC is calculated by diagonalizing

$$H^{SL}_{M_S M_L, M'_S M'_L} = \left\langle NSLM_S M_L \middle| \sum_{i=1}^{N} \lambda\, \boldsymbol{l}_i \cdot \boldsymbol{s}_i \middle| NSLM'_S M'_L \right\rangle. \tag{3.47}$$

To calculate how the one-particle operator $\boldsymbol{l}_i \cdot \boldsymbol{s}_i$ acts on the many-body state $|NSLM_S M_L\rangle$, one can express the latter as linear combinations of direct products of one-electron functions with spin $s_i = 1/2$ and $l_i = 1$ via Clebsch-Gordan coefficients. Finally, products of one-particle terms $\langle l = 1, m_l|\, \boldsymbol{l}\, |l = 1, m'_l\rangle$ and $\langle s = 1/2, m_s|\, \boldsymbol{s}\, |s = 1/2, m'_s\rangle$ need to be evaluated; their values are given in (3.35) and (2.35). Since the total angular momentum $\boldsymbol{J} = \boldsymbol{S} + \boldsymbol{L}$ commutes with the full Hamiltonian, the matrix (3.47) is diagonal when moving from the basis $|NSLM_SM_L\rangle$ to the J basis $|NSLJM_J\rangle$ via another set of Clebsch-Gordan coefficients. Following this procedure, it turns out that it is possible to give for each filling N a closed expression depending on $\boldsymbol{L}$ and $\boldsymbol{S}$ that is usually used to formulate the SOC in the LS coupling regime,

$$H_{\mathrm{SO}} \approx \zeta(N)\, \boldsymbol{L} \cdot \boldsymbol{S}. \tag{3.48}$$

Note that the LS coupling constant ζ depends on the number of electrons. A detailled, more general derivation of this expression using elements of group theory and the Wigner-Eckart theorem can be found in Ref. [40]. In case of t_{2g} orbitals, the LS coupling constants are $\zeta(N=1)=\lambda$ and $\zeta(N=2)=\lambda/2$. Replacing electrons with holes, one has $\zeta(N=5)=-\lambda$ and $\zeta(N=3)=-\lambda/2$. For $N=3$, the linear term vanishes. In case of p orbitals, an additional minus sign appears due to the minus in the T-P equivalence. To calculate the energies, $\boldsymbol{L}\cdot\boldsymbol{S}$ is evaluated using the total angular momentum $\boldsymbol{J}=\boldsymbol{S}+\boldsymbol{L}$ via

$$\boldsymbol{L}\cdot\boldsymbol{S} = \frac{1}{2}\left(\boldsymbol{J}^2 - \boldsymbol{L}^2 - \boldsymbol{S}^2\right) = \frac{1}{2}\left(J(J+1) - L(L+1) - S(S+1)\right), \tag{3.49}$$

where J can take the values $J = L+S, L+S-1, \ldots, |L-S|$.

In the jj coupling regime, where the SOC is large compared to Hund's coupling, the Kanamori Hamiltonian (2.43) except the term depending on U can be viewed as the perturbation. The unperturbed eigenstates are then the Slater determinants of the eigenfunctions of the operator $\boldsymbol{l}\cdot\boldsymbol{s}$ given in equation (3.44). The coarse structure of the energy levels is then given by the number of particles in the $j=3/2$ orbitals $N_{3/2}$ and the number of electrons in the $j=1/2$ orbitals $N_{1/2}=N-N_{3/2}$. The energy splitting of this is then calculated from diagonalizing

$$\left\langle j_1 m_{j1}, \ldots, j_N m_{jN} \middle| -2J_{\mathrm{H}}\boldsymbol{S}^2 - \frac{J_{\mathrm{H}}}{2}\boldsymbol{L}^2 \middle| j_1 m'_{j1}, \ldots, j_N m'_{jN} \right\rangle. \tag{3.50}$$

The Slater determinants $|j_1 m_{j1}, j_2 m_{j2}, \ldots, j_N m_{jN}\rangle$ consist of direct products $\bigotimes_{i=1}^{N} |j_i, (m_j)_i\rangle$, that can be further decoupled to terms $|l_i, (m_l)_i\rangle \otimes |s_i, (m_s)_i\rangle$, using the Clebsch-Gordan coefficients of Eq. (3.38). Using $\boldsymbol{S}^2 = \left(\sum_i \boldsymbol{s}_i\right)^2$ and $\boldsymbol{L}^2 = \left(\sum_i \boldsymbol{l}_i\right)^2$, one finally arrives again at simple one-particle matrix elements of $\boldsymbol{s}$ and $\boldsymbol{l}$. Again, knowing that J and M_J are good quantum numbers, the matrix is diagonal in the basis $|J, M_J, j_1, \ldots, j_N\rangle$. Another way to calculate the splitting is to transform the interaction Hamiltonian H_{I} into the one-particle j basis in which H_{SO} is diagonal. The energy splitting for a given particle distribution $N_{3/2}$ and $N_{1/2}$ can then be found by looking at the respective particle sectors of H_{I}. For two electrons in t_{2g} orbitals, for example, both of them will occupy $j=3/2$ orbitals, hence all terms in H_{I} containing a creation or annihilation operator in the $j=1/2$ orbitals can be dropped, and only a half filled $j=3/2$ Hamiltonian needs to be considered. This special case is analyzed in detail in Chapter 6.

3.5 Spin-orbit coupling in DFT+DMFT

3.5.1 Spin-orbit coupling in crystals

In the previous sections, the spin-orbit Hamiltonian was assumed to be of the form $\lambda\,\boldsymbol{l}\cdot\boldsymbol{s}$ with a constant λ. In case of a hydrogen-like atom, the parameter can be calculated from Eqs. (3.27) and (3.28). For a more general atom, the appearance of many electrons may be modeled with an effective, screened potential $v(r)$ that differs from the $1/r$ potential of the hydrogen-like atom, but still preserves radial symmetry. In this case, the first equality of Eq. (3.27) is still valid, and λ can be calculated approximately from $\left\langle\frac{1}{r}\frac{\mathrm{d}v}{\mathrm{d}r}\right\rangle$. For atoms, the SOC is thus well captured by a constant prefactor λ. Its value for many atoms can be found in Ref. [75].

In crystals, however, is the local potential $v(\boldsymbol{r})$ not radially symmetric any more. As a result, the possible splitting of the bands due to the SOC will depend on $\boldsymbol{k}$, the SOC is not a purely local effect. However, the bands will still be two-fold degenerate, if the crystal has a center of inversion [73, 76–79], as explained in the following. The weakly relativistic Hamiltonian (3.23) commutes with the time-reversal operator Θ. Due to Kramer's theorem, the time-reversed Bloch functions have the same energy, i.e., $E^{\sigma}(\boldsymbol{k}) = E^{-\sigma}(-\boldsymbol{k})$. In case of an inversion center, one has $E^{\sigma}(\boldsymbol{k}) = E^{\sigma}(-\boldsymbol{k})$. Hence, if both time-reversal symmetry and inversion symmetry are present, the relation $E^{\sigma}(\boldsymbol{k}) = E^{-\sigma}(\boldsymbol{k})$ holds. Thus, the SOC may break some degeneracies of the bands since it is a $\boldsymbol{k}$-dependent energy correction, but the spin degeneracy is still present. If inversion symmetry is broken in the bulk crystal, the resulting splitting of the bands of different spin is called *Dresselhaus splitting*. Furthermore, also the surface or any other confining potential breaks the inversion symmetry. The symmetry breaking part of the potential (e.g. the surface potential) can be written in first approximation as an electric field $e\,\boldsymbol{r}\cdot\boldsymbol{E}$. The resulting correction of the Hamiltonian due to the SOC is the *Rashba Hamiltonian* [73, 80]

$$H_{\mathrm{R}} = \frac{\alpha_{\mathrm{R}}}{\hbar}\boldsymbol{\sigma}\cdot(\boldsymbol{k}\times\boldsymbol{E}) \tag{3.51}$$

with a *Rashba coupling* α_{R}. The according splitting of the bands is called *Rashba splitting*.

In addition to the non-locality of the spin-orbit effects, also the basis of the local functions has to be kept in mind when a DMFT calculation is set up. When using a Wannier basis, the matrix representation of the SOC in that basis is, in general, not known. In an LDA+DMFT calculation, one thus has to be careful at which stage of the calculation the SOC is included, since after the construction of Wannier orbitals, it is not obvious how the SOC is represented best.

3.5.2 Implementation of the spin-orbit coupling in Wien2k

One way to circumvent this problem is to include the SOC already in the DFT calculation, since then no additional term has to be introduced in the (already relativistic) Wannier basis. The all-electron code Wien2k [81], for example, includes the scalar relativistic terms by default, and allows to include the SOC on top of that. The latter is done using the so-called *second variational treatment* [82–84]. Within this perturbative approach, the SOC operator is evaluated in the scalar-relativistic basis, where spin is still a good quantum number, and subsequently diagonalized. The advantage of this approximation is that the matrix dimension is kept small, as only a limited number of the low lying eigenfunctions is usually used [83].

3.5.3 Introducing the spin-orbit coupling in the Wannier basis

For a physical interpretation of DMFT results, it is often helpful to reduce the Hamiltonian to a minimal model capturing the basic effects. In case of the SOC, the minimal model is the atomic term $H_{\mathrm{SO}} = \lambda \boldsymbol{l} \cdot \boldsymbol{s}$, which is legitimate to assume if the quantum number l of the local basis is known, since the SOC is of atomic origin. The value of λ for a compound can be estimated in first approximation by its atomic value. In order to account for the lattice effects, a DFT calculation including the SOC can be used (see last section). To obtain the local parameter λ, one can, for instance, use the splitting of the bands at the Γ point. The way chosen in this thesis is to fit the local Hamiltonian H_{loc}: First, the DFT code Wien2k [81] is used to calculate the band structure with and without the SOC. Second, a maximally localized Wannier basis is constructed for both DFT calculations using Wannier90 [30]. In the Wannier basis, the local Hamiltonian is calculated. Third, λ is obtained by fitting the local Hamiltonian with SOC, i.e., minimizing

$$\sum_{\alpha\beta} \left[\left| (H_{\mathrm{loc}}^{\text{with SOC}})_{\alpha\beta} \right| - \left| (H_{\mathrm{loc}}^{\text{without SOC}})_{\alpha\beta} + \lambda (\boldsymbol{l} \cdot \boldsymbol{s})_{\alpha\beta} \right| \right]^2 , \tag{3.52}$$

where $(\cdot)_{\alpha\beta}$ denotes the matrix representation with combined spin-orbital indices α and β, and $H_{\mathrm{loc}} = \sum_{\boldsymbol{k}} H(\boldsymbol{k})/N_k$. If the projection is only onto orbitals of a certain quantum number l, the operator $\boldsymbol{l} \cdot \boldsymbol{s}$ is well defined. However, for this approach, not only the operator, but also its matrix representation in the Wannier basis has to be known. Here, it is assumed that it is identical to the matrix representation in the basis of the atomic orbitals that are used as a seed for the Wannier optimization. This assumption can only be justified a posteriori in case the fit is a good approximation to $H_{\mathrm{loc}}^{\text{with SOC}}$. Since it is always possible to acquire a phase in the process of maximal localization, the absolute value of the respective local Hamiltonians is taken in Eq. (3.52). An example for the t_{2g} orbitals of $\mathrm{Sr_2RuO_4}$ is shown in Fig. 3.2. In this material, the spherical symmetry is broken into an e_g and a t_{2g} block by an octahedral crystal field. The t_{2g} orbitals are further split by both a tetragonal crystal field and the SOC. To obtain the matrix representation of the $\boldsymbol{l} \cdot \boldsymbol{s}$ operator, the T-P correspondence is used (see Eq. (3.43) and Sec. 3.3). Since the band structure in Fig. 3.2 shows that the bands are approximated well, this example shows that both T-P correspondence and the fit method are suited to describe the SOC in $\mathrm{Sr_2RuO_4}$.

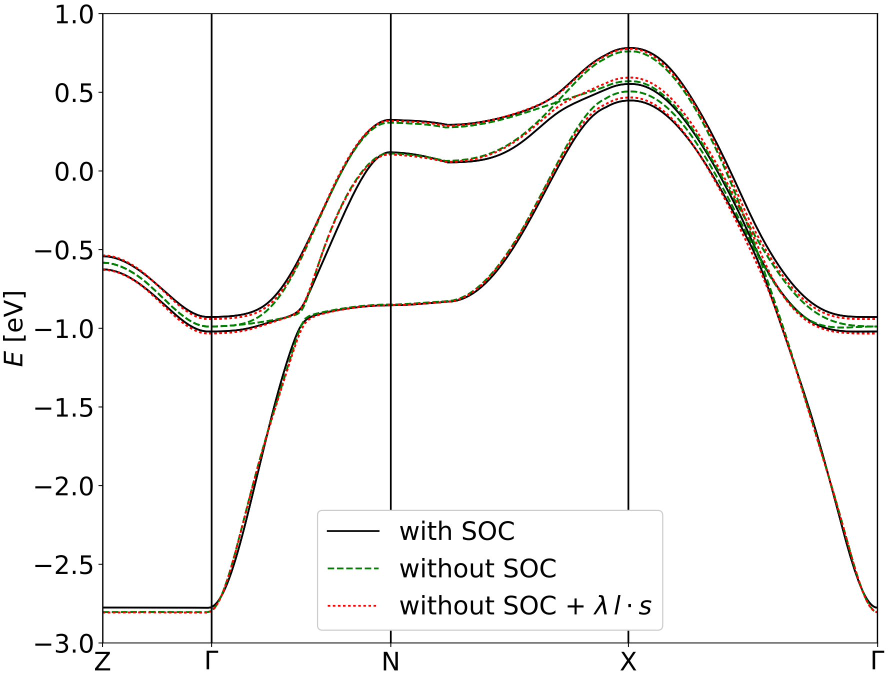

Figure 3.2: Bandstructure of Sr_2RuO_4, $\lambda = 94$ meV

4 Topological Insulators

4.1 Mathematical basics of topology

The usual picture shown in talks when topological insulators are introduced, is a mug that transforms into a doughnut. These continuous deformations are indeed key for a physical understanding of topological insulators, but in order to put it on a more rigorous footing, first, the basic mathematical concepts are introduced, starting with the meaning of the word "topology".

Definition [85, 86]: Let X be any set and $\mathfrak{T} = \{U_i | i \in I\}$ a collection, finite or infinite, of subsets of X. The pair $(X, \mathfrak{T})$ is a *topological space* if $\mathfrak{T}$ satisfies the following relations:

- $\emptyset \in \mathfrak{T}$, $X \in \mathfrak{T}$
- Any finite or infinite subcollection $\{U_j | j \in J\}$, where J is a part of the index set I, satisfies $\bigcup_{j\in J} U_j \in \mathfrak{T}$
- Any finite subcollection $\{U_k | k \in K\}$, where K is a finite part of the index set I, satisfies $\bigcap_{k\in K} U_k \in \mathfrak{T}$

The members U_i of $\mathfrak{T}$ are called *open sets*, and collection $\mathfrak{T}$ is said to give a *topology* to X. Often, one uses only X to denote the topological space and does not explicitly write $\mathfrak{T}$, but implicitly adds it to the symbol X.

Examples that trivially fulfill these three constraints are $\mathfrak{T} = \{\emptyset, X\}$, called *trivial topology*, and if $\mathfrak{T}$ is a collection of all subsets, called the *discrete topology.* Another important example is the *usual topology* of the real numbers $X = \mathbb{R}$, where the open sets U_i are open intervals (a, b) and their unions [85]. The definition of a topological space given here is very general, since it does not have to be continuous or equipped with a metric. In order to classify now geometrical objects, for example, one needs some equivalence relation to say whether or not two objects are equal or different from each other. Various equivalence relations appear in many fields of mathematics. In case of Euclidean geometry, for example, similarity serves as an equivalence relation, so that two triangles are similar if the corresponding angles are the same. In the field of topology, a not so stringent definition is chosen, so that a mug and a doughnut are still equivalent, as mentioned in the example before. The way to go is via smooth transformations, since a surface can be smoothly changed as long as no hole is teared into it or closed. In a mathematical language, one needs two more definitions to rigorously describe that behavior.

Definition [85]: X and Y are topological spaces. A map $f : X \to Y$ is *continuous* if the inverse image of an open set in Y is an open set in X.

This definition reduces to the usual definitions of continuity for real valued functions $f : \mathbb{R} \to \mathbb{R}$ if the usual topology is used [85, 86]. In order that two objects are equivalent, this mapping needs to be invertible, leading to the definition of homeomorphisms

Definition [85]: X and Y are topological spaces. A map $f : X \to Y$ is a *homeomorphism* if it is continuous and if it has an inverse $f^{-1} : Y \to X$ that is also continuous. If a homeomorphism between X and Y exists, these two topological spaces are said to be *homeomorphic.*

The homeomorphism relation fulfills the rules of a general equivalence relation [85] and serves here as a formal way to classify topological spaces. *Topological invariants* are numbers related to topological spaces that do not change under a homeomorphism. Therefore, they are a useful tool to distinguish different equivalence classes. However, from its definition follows that two topological spaces with different topological invariants are for sure in different equivalence classes, but not that two topological spaces with the same topological invariant belong to the same equivalence class since a mapping may not exist.

A famous topological invariant is the Euler characteristics χ. It is defined for a polyhedron K as

$$\begin{aligned}\chi(K) = (&\text{number of vertices in } K) - (\text{number of edges in } K) \\ &+ (\text{number of faces in } K).\end{aligned} \tag{4.1}$$

For a cube, it is $\chi = 8 - 12 + 6 = 2$. Imagine now to insert another vertex in the middle of some face. One generates then one additional vertex, four new edges, and four faces, whereas one face gets removed. Therefore, the change in the Euler characteristics is $\Delta\chi = 1 - 4 + 3 = 0$. This is quite general, since inserting a vertex in a face surrounded by N_e edges changes the number of vertices by $+1$, the number of edges by N_e and the number of faces by $N_e - 1$. In analogy, removing one vertex does not change χ, hence removing or inserting any number of vertices leaves the Euler characteristics invariant. With this argument it is plausible, even though no explicit proof is given here, that any convex polyhedron has the Euler characteristics $\chi = 2$. This is known as Euler's polyhedron formula. The Euler characteristics can be generalized to any compact, connected 3D object X, meaning that in contrast to a polyhedron K it may also have curved elements in its surface. If a polyhedron K is homeomorphic to X, one defines $\chi(X) = \chi(K)$. The question now may arise if this definition is unique, or if it is possible that there are polyhedrons K_1 and K_2 with different χ, which are both homeomorphic to χ. The answer is given by the theorem of Poincaré-Alexander, stating that $\chi(X)$ is independent of K as long as K is homeomorphic to X [85]. This theorem is a generalization of Euler's theorem and shows that the Euler characteristics serves as a topological invariant to classify the homeotopy classes of 3D geometrical objects. For example, a sphere has $\chi = 2$, a torus $\chi = 0$. Mug and doughnut from the introductory example are homeomorphic to a torus, and have, therefore, also the Euler characteristics $\chi = 2$.

4.2 Geometry in curved space

As tearing a hole or closing one are the only non-homeomorphic transformations, the Euler characteristics is also related to the number of holes. In order to give a solid definition of the number of holes, usually the 2D surface of the 3D object is considered. A geometric quantity for the number of holes of a connected, orientable surface is the *genus* g, which is defined as the maximum number of cuttings along non-intersecting closed simple curves that leave the surface still connected. It is related to the Euler characteristics via

$$\chi = 2 - 2g. \tag{4.2}$$

By introducing the 2D surface of the 3D object, already a next important step in the mathematical description of objects has been taken. Note that the surface covers already the whole topological information. Without looking at the 3D object globally, it should thus be possible to calculate the genus from the local properties of all points of the 2D surface. However, when doing so, one needs the surface to be smooth at every point, so that one knows how neighboring points on the surface are related. Mathematically, one defines for this purpose the *manifold*. The correct definition is given for example in Refs. [85, 86], but for the purpose here it is enough to view it as a topological space that is locally at every point Euclidean, or in other words, there exists a local environment of every point within the n-dimensional manifold that is homeomorphic to the Euclidean space $\mathbb{R}^n$. A cube does not fulfill these requirements because of the edges, but a sphere and a torus, for example, do. In this sense, one can look at closed surfaces like a torus or a sphere as two-dimensional differentiable manifolds without any boundary.

The question is now if the information of all local quantities such as derivatives at every point are enough to determine global quantities such as the genus. This question is answered in the wide field of Riemannian geometry, where a *metric* $g_{\mu\nu}$ is defined on the manifold. The concepts of Riemannian geometry are important in many fields of physics, from field theories in curved geometry, as for example electrodynamics in a toroidal geometry, up to the theory of general relativity. With the metric tensor, also the line element $\mathrm{d}s^2 = \sum_{\mu\nu} g_{\mu\nu}\mathrm{d}x^\mu \mathrm{d}x^\nu$ is defined and distances can be measured. It also provides the rules how a vector is parallely transported along the surface. In $\mathbb{R}^2$, the coordinates of a vector simply do not change during a parallel transport, but as soon as the manifold is curved, this is not the case. In general, the *connection* specifies how tensors are transported along a curve [85]. For example, if a vector is moved on a sphere, the direction of the vector changes, depending on the chosen path. The *curvature* calculated from the connection is a measure how much the manifold differs from $\mathbb{R}^n$, and measures the differences of a vector that is parallely transported on two different infinitesimal paths [85]. In general, curvatures are tensorial object, but in the case of a 2D surface embedded in $\mathbb{R}^3$ considered here, a suitable curvature is the scalar Gaussian curvature K. It can be calculated by $K = \kappa_1\kappa_2$ with the principal curvatures κ_1 and κ_2, which in turn are best visualized as the inverse radii of ellipsoids or hyperboloids locally approximating the manifold. In case of a sphere with radius R, for example, one has $\kappa_1 = \kappa_2 = 1/R$ and $K = 1/R^2$. Going back to the question raised at the beginning

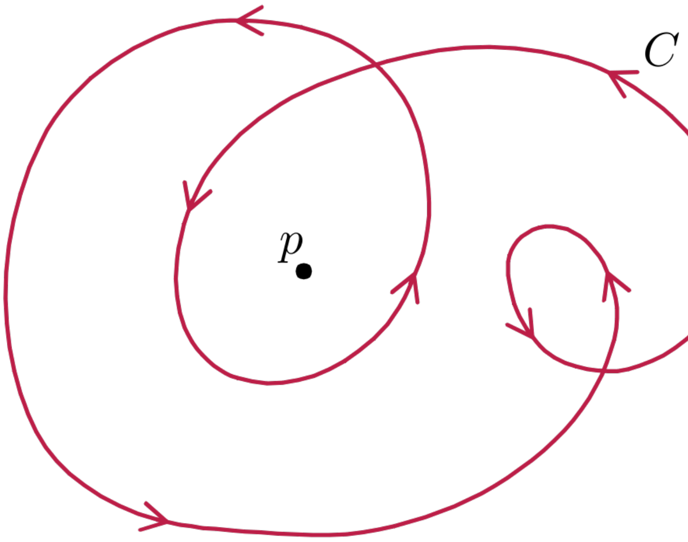

Figure 4.1: The winding number of curve C around point p is given by the number it travels counterclockwise around it. Here, $W(C) = 2$. Graphic taken from [87].

of this paragraph whether local quantities are enough to determine global invariants, it can now be answered by the Gauß-Bonnet theorem, which reads for smooth closed 2D manifolds embedded in a 3D space [86]

$$\int_M K \mathrm{d}A = 2\pi\chi(M). \tag{4.3}$$

Thus, one can indeed obtain the topological information from a 3D object (number of holes) from local properties of the 2D surface (curvature). The integral is quantized, any smooth deformation does not change its value. When a hole is created or closed, i.e., the genus changes by one, the curvature diverges at this point and the integral is not defined. Hence, only a non-continuous transformation can change the invariants χ and g, so they are suited to label the homeomorphic classes.

4.3 Winding numbers and Skyrmions

4.3.1 Theory

In the previous sections, the Euler invariant and its relation to curvature has been introduced. Another famous example to determine a global, integer topological invariant is the winding number of a closed 1D curve embedded in a 2D space $\mathbb{R}^2$. For any closed, smooth curve C (a 1D differential manifold) parametriced in cartesian coordinates $x(t)$ and $y(t)$, one can intuitively determine how often it winds around the origin using the polar angle φ,

$$\begin{aligned}W(C) &= \frac{1}{2\pi}\Delta\varphi = \frac{1}{2\pi}\int_C \mathrm{d}\varphi = \frac{1}{2\pi}\int_C \mathrm{d}t\left(\frac{\partial\varphi}{\partial x}\frac{\mathrm{d}x}{\mathrm{d}t} + \frac{\partial\varphi}{\partial y}\frac{\mathrm{d}y}{\mathrm{d}t}\right)\\ &= \frac{1}{2\pi}\int_C \mathrm{d}t\frac{1}{x^2+y^2}\left(x\dot{y} - y\dot{x}\right).\end{aligned} \tag{4.4}$$

The winding number is integer, since for closed curves the change of the angle $\Delta\varphi$ has to be a multiple of 2π. An example is given in Fig. 4.1. In case of smooth transformations of the curve, the winding number only changes when the curve is moved over the origin, so when there is a t such that $\boldsymbol{x}(t) = \boldsymbol{O}$. In this case, the denominator becomes 0, the integrand diverges and the winding number is not defined. If one normalizes the radius of the curve $C(\boldsymbol{x} = [x, y])$, i.e., projects it to the unit circle $\mathcal{S}^1$ via

$$\frac{\boldsymbol{x}(t)}{|\boldsymbol{x}(t)|} = \boldsymbol{u}\left(e^{2\pi\mathrm{i}t}\right),$$

then one simply has

$$W(C) = \frac{1}{2\pi}\int_C \mathrm{d}t\left(u_1\dot{u}_2 - u_2\dot{u}_1\right). \tag{4.5}$$

Note that by writing the winding number in this way it only depends on the mapping $\boldsymbol{u}(t)$, which is actually a circle map $\boldsymbol{u} : \mathcal{S}^1 \to \mathcal{S}^1$. In this view, the winding number is equivalent to the so-called *degree* of a map $\deg(\boldsymbol{u}) = W(C)$. The degree can be generalized from smooth mappings of one dimensional circles $\mathcal{S}^1$ to smooth mappings of n dimensional spheres $\mathcal{S}^n$, i.e., $\boldsymbol{u} : \mathcal{S}^n \to \mathcal{S}^n$. Within this generalization, it can be viewed as [88]

$$\deg(\boldsymbol{u}) = \frac{\text{oriented area of } \boldsymbol{u}(\mathcal{S}^n)}{\text{area of } \mathcal{S}^n}, \tag{4.6}$$

and takes the simple form [88]

$$\deg(\boldsymbol{u}) = \frac{1}{\text{area of } \mathcal{S}^n}\int_{\mathcal{S}^n} \mathrm{d}^N t \det\left(\boldsymbol{u}\Big|\frac{\partial\boldsymbol{u}}{\partial t_1}\Big|\dots\Big|\frac{\partial\boldsymbol{u}}{\partial t_n}\right). \tag{4.7}$$

Therefore, only the determinant of a matrix with column vectors $\boldsymbol{u}$ and its derivatives is important for the degree. In case of a one dimensional mapping from a circle to a circle, it obviously reduces to Eq. (4.5), in case of a two dimensional mapping it reads

$$\deg(\boldsymbol{u}) = \frac{1}{4\pi}\int \mathrm{d}^2 t\, \boldsymbol{u}\cdot\left(\frac{\partial\boldsymbol{u}}{\partial t_1}\times\frac{\partial\boldsymbol{u}}{\partial t_2}\right). \tag{4.8}$$

To give an example, assume that the surface of the sphere is parametrized by the usual spherical coordinates $\boldsymbol{t} = (\theta, \varphi)$. In case of the identity mapping, which reads in karthesian coordinates $\boldsymbol{u}_1(\theta, \varphi) = (\sin\theta\cos\varphi, \sin\theta\sin\varphi, \cos\theta)$, the integrand of Eq. (4.8) is 1, wherefore also $\deg(\boldsymbol{u}_1) = 1$ follows. This makes sense since the identitiy mapping $\boldsymbol{u}_1(\theta, \varphi)$ covers the whole sphere once, wherefore the oriented area of $\boldsymbol{u}_1$ is identical to the one of the sphere. If one chooses the mapping $\boldsymbol{u}_2(\theta,\varphi) = (\sin\theta\cos 2\varphi, \sin\theta\sin 2\varphi, \cos\theta)$, the whole sphere is covered twice and $\deg(\boldsymbol{u}_2) = 2$. In case of another mapping $\boldsymbol{u}_3(\theta,\varphi) = (\sin\theta\cos\varphi, \sin\theta\sin\varphi, (\cos\theta)^2)$, only the upper hemisphere is covered twice, but the orientation of the surface is different for $\theta < \pi$ and $\theta > \pi$, so that the winding number is $\deg(\boldsymbol{u}_3) = 0$. In general, since the mapping $\boldsymbol{u}$ is smooth, $\boldsymbol{u}(\theta,\varphi) = \boldsymbol{u}(\theta + 2\pi, \varphi) = \boldsymbol{u}(\theta, \varphi + 2\pi)$. Therefore, when $\boldsymbol{u}$ is tracked on the sphere, it always has to come back to the same point, which means that it is not possible to cover only parts of the sphere with only positive orientation. As a consequence, either the whole sphere is covered or nothing of it, hence the degree has to be integer, similar to the winding number in 1D. To conclude, for 1D and 2D, the degree has been geometrically argued to be integer valued. Altough it is not obvious from Eq. (4.7), one can indeed algebraically proof that the degree is an integer for all dimensions n [89]. This integer is a topological invariant since it cannot be changed by a smooth transformation. For example, in case of $n = 1$, it was mentioned before that the winding number only changes when the curve moves through the origin. When the curve is projected to the unit circle, this corresponds to a discontinuity in $\boldsymbol{u}$; hence for two functions $\boldsymbol{u}_1$ and $\boldsymbol{u}_2$ with different degrees, no continuous transformation exists. In fact, this is generalized to degrees of all dimensions, and can furthermore be inverted in a sense that if the degree is the same, the functions belong to the same equivalence class

$$\boldsymbol{u}_1 \sim \boldsymbol{u}_2 \Leftrightarrow \deg(\boldsymbol{u}_1) = \deg(\boldsymbol{u}_2). \tag{4.9}$$

This statement is known as Hopf theorem [88].

4.3.2 Magnetic topological defects

Physical examples of winding numbers can be found in magnetic structures, where many different topological defects can be found. One example that became famous due to a Nobel price in Physics in 2016 are vortices in the xy model. Kosterlitz and Thouless got the prize for the discovery of the topological phase transition in this model together with Haldane, who got it for his work on the model named after him that is described in section 4.7.1. A vortex is a point-like topological defect in a 2D vector field on a 2D manifold. When the vectors are normalized on each point, they are characterized by their polar angle $\theta(\boldsymbol{x})$. If the field is continuous everywhere except at the point-like defect that acts as a singularity in the field, the change of θ along a closed curve has to be a multiple on 2π. In fact, it is a winding number as described previously. Due to the continuity of θ, the actual integration path is not important, as long as it is a continuous curve around the singularity. In physics, this kind of winding number is called *vortex number* v defined by

$$v \equiv W(C) = \frac{1}{2\pi}\oint_C \nabla\theta \cdot \mathrm{d}\boldsymbol{x}. \tag{4.10}$$

Note that the definition is identical to the winding number in Eq. (4.5). A singularity with a vortex number $v = 1$ is called vortex, one with a vortex number $v = -1$ antivortex. The vortex number is topologically protected, the total vortex number within a region

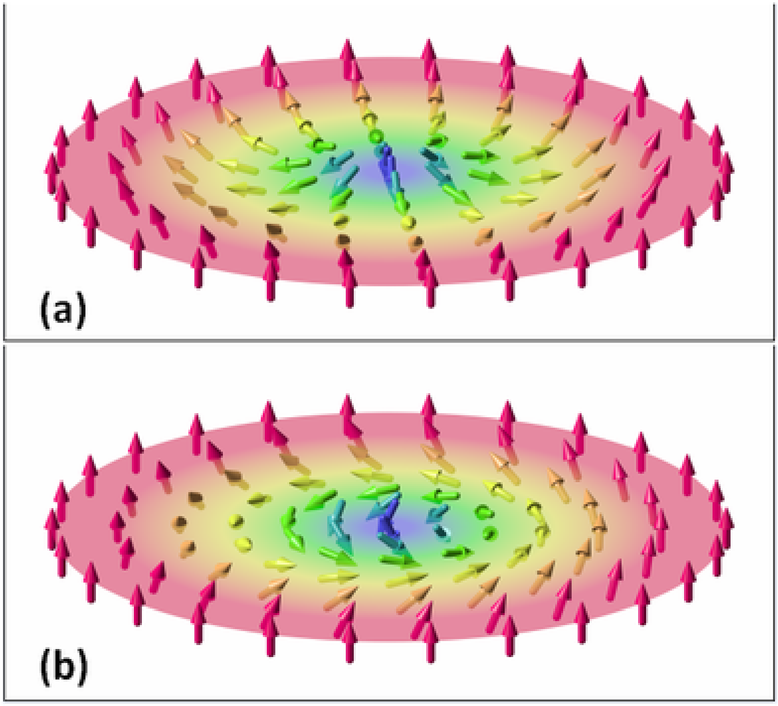

Figure 4.2: The vector field of two, two-dimensional magnetic skyrmions: a) a hedgehog skyrmion and b) a spiral skyrmion [90]

in space cannot change as long as no singularity leaves or enters the region. Locally, a vortex number can only change when two singularities combine at some point or if one point splits into two singularities. One example for the former case is the annihilation of a vortex and an antivortex. Since the xy model is a model of classical angular momenta on a lattice, the continuum model of a vortex is only an approximation. It can then be defined for the plaquette i, j as the sum of the changes $\Delta\theta$ of the angels of the four vectors at the corners of the plaquette. Note that this numerical vortex number is not strictly quantized. If the energy fluctuations are large enough, a vortex or antivortex could be created or annihilated.

A second important topological defect is the skyrmion. It was originally proposed by Tony Skyrme as a model for nucleons [91], and became popular in solid state physics as certain geometries of 3D magnetic moments on a 2D surface. Note that these magnetic skyrmions are in contrast to vortices not point-like singularities, but extended objects. Examples are shown in Fig. 4.2. In case of a 3D vector field of normalized magnetic moments $\boldsymbol{m}(\boldsymbol{x})$ on a 2D plane $\mathbb{R}^2$, the *skyrmion number* w can be defined by mapping the plane $\mathbb{R}^2$ onto a sphere $\mathcal{S}^2$ via a stereographic projection, since then the degree of $\boldsymbol{m}$ is defined as [92]

$$w \equiv \deg(\boldsymbol{m}) = \frac{1}{4\pi} \int \mathrm{d}^2x \, \boldsymbol{m} \cdot \left(\frac{\partial \boldsymbol{m}}{\partial x_1} \times \frac{\partial \boldsymbol{m}}{\partial x_2} \right) . \tag{4.11}$$

Since the degree is quantized, the skyrmion number w is a topologically protected integer. Similar as a vortex, in can only change if two non-trivial objects merge. Again, it should be noted that in solids, the vector field is not continuous, but the magnetic moments are arranged on a lattice. Therefore, the skyrmion number is not exactly quantized and skyrmions may form and disappear due to thermal fluctuations.

4.4 Bundles

The last concept needed to give a glance onto the mathematical backbone of topological insulators are *fiber bundles*. The correct definition is rather lengthy and technical since it involves various terms that need to be defined. However, the concept of bundles is important for the foundation of topology and also interesting for physicist in order to get a deeper view beyond the applications. Therefore, the terminology is introduced here on the basis of the Möbius strip. A geometrical interpretation of the Möbius strip is as follows: If one takes a rectangular shaped strip of paper and glues the ends together without twisting, such that it has the shape of the side area of a cylinder, it is called trivial strip. It is an oriented surface with an inner and an outer side. If one twists the paper strip once before gluing the ends, one gets the topologically non-trivial Möbius strip. It has only one side, and one has to go around the circle twice in order to reach a point again (see Fig. 4.3). The topology of the strip is analyzed by the way the strip is mapped onto a circle. In this context, the paper strip is called *total space*. Each horizontal line segment is a *fiber*, and the circle is the *base space*. The *projection* Π maps each fiber in the total space to a point in the base space (see Fig. 4.3). The *fiber bundle* is the whole object, including the total space, the base space, the fiber, the mapping, and some structure group that is left out here [86]. The point is now that in case of an ordinary strip, it is possible to smoothly map each fiber to a point on the circle and invert the mapping as well. In case of the Möbius strip, on the other hand, one can define such a map in the open interval $(0, 2\pi)$ on the circle, but when one moves across the point $0 = 2\pi$ the fiber is inverted, with the consequence that the function is not smooth at this point. In other words, the ordinary strip is a direct product of the circle $\mathcal{S}^1$ with a line segment L, i.e., $T = \mathcal{S}^1 \otimes L$. In case of the Möbius strip, this is not possible. Note that each segment of the Möbius strip is a direct product of a segment of the circle, but as soon as the circle closes, the product breaks down. So far, the bundle has been introduced on the example of paper strips with periodic boundary conditions, where the strip itself is the total space, a circle is the base space, and horizontal line segments are the fibers. The name "fiber" induces that it has to be some onedimensional segment, but this is not true. The concept of a fiber bundle is a lot more general. A prominent example of a bundle, where the fiber is a whole vectorspace (called *vector bundle*), is the tangent space of a manifold. The base space is then some differentiable n dimensional manifold (e.g. a sphere, then $n = 2$). The fibers are the tangent spaces, i.e., the n dimensional vector spaces spanned by the tangent vectors at each point of the manifold (e.g. a tangent plane attached to some point of the sphere). The total space is the unity of all tangent spaces.

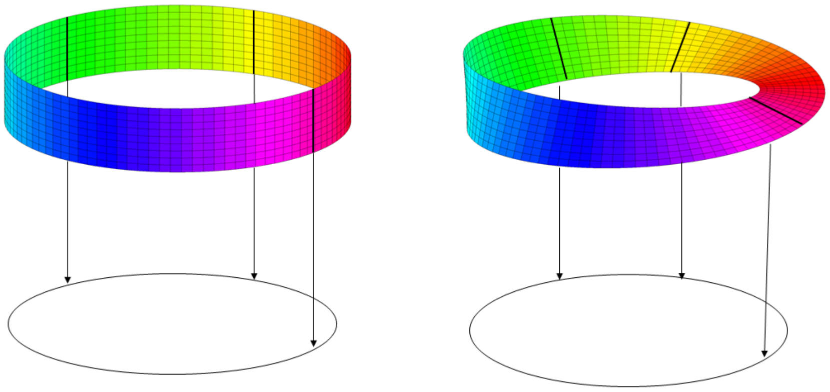

Figure 4.3: Trivial paper strip (left) and nontrivial Möbius strip (right) as an example for fiber bundles. The base space is in both cases a circle. Each line segment (the fiber) is mapped onto a point of the circle.

In physics, eigenstates are a nice example for bundles. Let $H(\boldsymbol{a})$ be a Hamiltonian that depends on some parameters a_i. The nth eigenstate of H is called $|n, \boldsymbol{a}\rangle$ and is assumed not to be degenerate for any parameters $\boldsymbol{a}$, which means that level crossings are prohibited. Then, an eigenstate $|n, \boldsymbol{a}\rangle$ cannot be distinguished from another state $e^{\mathrm{i}\phi} |n, \boldsymbol{a}\rangle$ that differs from the original state by a phase ϕ. Hence, at each point $\boldsymbol{a}$ in parameter space, the nth eigenstate has a $U(1)$ degree of freedom. For a given n, all of these eigenstates form a bundle. The base space is the parameter space $\boldsymbol{a}$, the fiber at some point $\boldsymbol{a}_0$ of it is the one-dimensional space $e^{\mathrm{i}\phi} |n, \boldsymbol{a}_0\rangle$, and the total space is the unity of all those fibers for all parameters $\boldsymbol{a}$.

For a certain kind of bundles, the *principal bundles*[1], one can define a connection and a curvature, similar to the connection and the curvature of a Riemannian manifold described in section 4.2. In case of a manifold M, the connection basically describes how the tangent space changes when one moves from point $P \in M$ to P' along a curve γ. It describes, therefore, the geometry of the manifold. The connection of the bundle P may not be confused with the geometrical, Riemannian connection of its base manifold M, since it does not describe the local topology of the surface, but the local topology of the bundle living on top of it. For example, in case of the eigenstates with the freedom of the phase ϕ, the connection of the bundle describes how the phase ϕ changes as the parameters $\boldsymbol{a}$ change, and not how the different points $\boldsymbol{a}$ are related.

---

[1] For a definition see, e.g, [85]. An example for a principle bundle is the eigenstate bundle $e^{\mathrm{i}\phi} |n, \boldsymbol{a}\rangle$.

4.5 Berry phase

In the previous section, it has been mentioned that eigenstates are the bundles relevant in quantum mechanics, with the phase as a fiber. In order to derive the related connection and curvature, changes of the phase have to be analyzed once the parameters vary within the base manifold. Historically, it was common believe in early times of quantum mechanics, that the phase of states has no physical meaning. However, Berry has shown in 1984 that a geometric phase, which may has observable effects, appears if a system is transformed adiabatically in a cyclical manner [93].

The derivation given here is following the review of Yoichi Ando [11] and the lecture notes of Yuriy Mokrousov [94]. Given a Hamiltonian H that depends on a set of parameters $\boldsymbol{a}$ changing cyclically over time t, the equation for the eigenvectors $|n, \boldsymbol{a}(t)\rangle$ reads

$$H[\boldsymbol{a}(t)]\,|n, \boldsymbol{a}(t)\rangle = E_n[\boldsymbol{a}(t)]\,|n, \boldsymbol{a}(t)\rangle \,. \tag{4.12}$$

The focus here is on the time evolution of a certain state $|\psi_n(t)\rangle$, which is an eigenstate at time $t = 0$, i.e., $|\psi_n(t = 0)\rangle \equiv |n, \boldsymbol{a}(0)\rangle$. It is assumed that it is at no point $\boldsymbol{a}$ in the manifold degenerate with another eigenstate. The state evolves in time obeying the time-dependent Schrödinger equation

$$H[\boldsymbol{a}(t)]\,|\psi_n(t)\rangle = \mathrm{i}\hbar \frac{\partial}{\partial t}\,|\psi_n(t)\rangle \,. \tag{4.13}$$

In case the Hamiltonians at different times commute, $|\psi_n(t)\rangle$ remains an eigenstate and only picks up a trivial phase called dynamical phase factor

$$\theta_n(t) = -\frac{1}{\hbar}\int_0^t \mathrm{d}t'\; E_n[\boldsymbol{a}(t')]. \tag{4.14}$$

If the Hamiltonians at different times do not commute, $|\psi_n(t)\rangle$ is not an eigenstate any more and has, in principle, to be expanded in the eigenstates at time t,

$$|\psi_n(t)\rangle = \sum_m c_{nm}(t)\,|m, \boldsymbol{a}(t)\rangle \,. \tag{4.15}$$

However, for states well separated in energy and a Hamiltonian that varies slowly compared to the internal time scales, the adiabatic approximation is valid, stating that the overlap to other states is suppressed and $c_{nm}(t) \propto \delta_{nm}$ holds [94]. Therefore, the solution can be expressed just in terms of the nth eigenstate of the explicitly time dependent Hamiltonian in equation (4.12)

$$|\psi_n(t)\rangle = \exp\left\{\frac{\mathrm{i}}{\hbar}\int_0^t \mathrm{d}t'\,\left(\mathrm{i}\hbar\,\dot{\boldsymbol{a}}(t')\,\langle n, \boldsymbol{a}(t')|\,\nabla_{\boldsymbol{a}}\,|n, \boldsymbol{a}(t')\rangle - E_n[\boldsymbol{a}(t')]\right)\right\}|n, \boldsymbol{a}(t)\rangle \tag{4.16}$$

which can be shown by inserting the solution (4.16) in the Schrödinger equation (4.13) [11].

Thus, if the parameters $\boldsymbol{a}$ change adiabatically, a phase factor consisting of two terms appears. The second term gives the expected dynamical phase factor θ_n (see Eq. (4.14)).

The first phase in equation (4.16) is nontrivial and is called *Berry phase* γ_n, if the parameters $\boldsymbol{a}$ describe a closed path C as time evolves from 0 to a period T:

$$\begin{aligned}\gamma_n[C] &\equiv \mathrm{i}\int_0^T \mathrm{d}t\, \dot{\boldsymbol{a}}(t)\cdot \langle n,\boldsymbol{a}(t)|\,\nabla_{\boldsymbol{a}}\,|n,\boldsymbol{a}(t)\rangle \\ &= \mathrm{i}\oint_C \mathrm{d}\boldsymbol{a}\cdot\langle n,\boldsymbol{a}|\,\nabla_{\boldsymbol{a}}\,|n,\boldsymbol{a}\rangle = \mathrm{i}\oint_C \mathrm{d}\boldsymbol{a}\cdot \boldsymbol{A}^n(\boldsymbol{a}) = \mathrm{i}\oint_C A^n(\boldsymbol{a})\end{aligned} \tag{4.17}$$

where we introduced the Berry connection

$$\boldsymbol{A}^n(\boldsymbol{a}) \equiv \langle n,\boldsymbol{a}|\,\nabla_{\boldsymbol{a}}\,|n,\boldsymbol{a}\rangle \tag{4.18}$$

and its connection form[2]

$$A^n(\boldsymbol{a}) \equiv \mathrm{d}\boldsymbol{a}\cdot\boldsymbol{A}^n(\boldsymbol{a}) = \sum_i A_i^n(\boldsymbol{a})\,\mathrm{d}a_i \tag{4.19}$$

The Berry phase is a phase factor additional to the dynamical one accumulated by following a closed path in parameter space $\boldsymbol{a}$. It is important to note that it does not change by a simple gauge transformation

$$|n,\boldsymbol{a}\rangle \to |n,\boldsymbol{a}\rangle' = e^{\mathrm{i}\phi_n(\boldsymbol{a})}\,|n,\boldsymbol{a}\rangle\,, \tag{4.20}$$

as shown easily. The corresponding connection is

$$\boldsymbol{A}'^n = \boldsymbol{A}^n - \nabla_{\boldsymbol{a}}\phi, \quad A'^n = A^n - \mathrm{d}\phi \tag{4.21}$$

Thus, the change of the Berry phase is $\oint \mathrm{d}\phi = 0$, since the path is closed. Note the similarities between the Berry connection and the vector potential in electrodynamics, which behaves similarly under a gauge transformation. Furthermore, just as the electromagnetic field tensor is defined as the exterior derivative of the vector potential, the Berry curvature is defined as the exterior derivative of the Berry connection form[3]

$$F^n(\boldsymbol{a}) \equiv \mathrm{d}A^n(\boldsymbol{a}) = \frac{1}{2}\sum_{ij} F_{ij}^n\,\mathrm{d}a_i\wedge\mathrm{d}a_j \tag{4.22}$$

with components [94]

$$F_{ij}^n(\boldsymbol{a}) \equiv \frac{\partial A_j^n}{\partial a_i} - \frac{\partial A_i^n}{\partial a_j} = -2\mathrm{Im}\left\langle \frac{\partial}{\partial a_i}(n,\boldsymbol{a})\right|\left.\frac{\partial}{\partial a_j}(n,\boldsymbol{a})\right\rangle \tag{4.23}$$

---

[2] Sometimes, the Berry connection form is also just called Berry connection. For a mathematical definition of a *form*, or, more generally, an *n-form*, see, e.g, [85].

[3] A few remarks on mathematical details taken from Ref. [85]: F^n is a two-form, where the wedge product $\mathrm{d}a_i\wedge\mathrm{d}a_j$ is the totally antisymmetric tensor $\mathrm{d}a_i\wedge\mathrm{d}a_j = \mathrm{d}a_i\otimes\mathrm{d}a_j - \mathrm{d}a_j\otimes\mathrm{d}a_i$. The Berry curvature is actually a field strength and not a curvature, but can be derived from a closely related curvature.

Using the generalized Stoke's theorem, the Berry phase can be written in terms of the curvature

$$\gamma_n[C] = \mathrm{i} \oint_C A^n = \mathrm{i} \int_S \mathrm{d}A^n = \mathrm{i} \int_S F^n, \tag{4.24}$$

where S is a surface with boundary C. In physics, the manifold M is often part of $\mathbb{R}^3$ (or $\mathbb{R}^2$). The curvature tensor can then be expressed as a curvature vector $\boldsymbol{F}^n$ with components [94]

$$(\boldsymbol{F}^n)_i \equiv \frac{1}{2} \sum_{jk} \epsilon_{ijk} F^n_{jk}, \tag{4.25}$$

which is related to the connection via

$$\boldsymbol{F}^n = \nabla_{\boldsymbol{a}} \times \boldsymbol{A}^n \tag{4.26}$$

In this special case, Stoke's theorem reads

$$\gamma_n[C] = \mathrm{i} \oint_C \mathrm{d}\boldsymbol{a} \cdot \boldsymbol{A}^n(\boldsymbol{a}) = \mathrm{i} \int_S \mathrm{d}^2\boldsymbol{a} \cdot \boldsymbol{F}^n(\boldsymbol{a}). \tag{4.27}$$

In electrodynamics, the equivalent to the curvature vector is the magnetic field. Therefore, the Berry phase is formally related to a magnetic flux through a surface S.

If the eigenstates with eigenenergy E_n are not separated, but N-fold degenerate at some point $\boldsymbol{a}$, i.e., the N different states $|n, \alpha, \boldsymbol{a}\rangle$ have the same eigenenergy, they do not only have the $U(1)$ phase freedom, but the freedom of any $U(N)$ unitary transformation U^N. Possible gauge transformations are then

$$|n, \alpha, \boldsymbol{a}\rangle \rightarrow |n, \alpha, \boldsymbol{a}\rangle' = \sum_\beta U^N_{\alpha\beta} |n, \beta, \boldsymbol{a}\rangle. \tag{4.28}$$

As a consequence, the Berry phase is no longer only a phase, but matrix valued, with a matrix valued Berry connection

$$[\boldsymbol{A}^n(\boldsymbol{a})]_{\alpha\beta} \equiv \langle n, \alpha, \boldsymbol{a}| \nabla_{\boldsymbol{a}} |n, \beta, \boldsymbol{a}\rangle. \tag{4.29}$$

Since the elements of the connection A^n_i are now matrices, they do not commute. Therefore, it is a *non-abelian* connection. The non-abelian Berry curvature is then

$$F^n(\boldsymbol{a}) \equiv \mathrm{d}A^n(\boldsymbol{a}) + A^n(\boldsymbol{a}) \wedge A^n(\boldsymbol{a}) = \frac{1}{2} \sum_{ij} F^n_{ij} \, \mathrm{d}a_i \wedge \mathrm{d}a_j \tag{4.30}$$

with elements

$$F^n_{ij}(\boldsymbol{a}) \equiv \frac{\partial A^n_j}{\partial a_i} - \frac{\partial A^n_i}{\partial a_j} + \left[A^n_i, A^n_j\right]. \tag{4.31}$$

In the abelian case, the commutator and the wedge produce $A^n \wedge A^n$ vanish, and Eqs. (4.22) and (4.23) are restored.

4.6 Chern numbers

A very important quantity in the field of topological insulators is the Chern number. This concept is very general; in fact, Chern numbers can be defined for any complex vector bundle. The *total Chern class* of a complex vector bundle with field stregth F (e.g. the Berry curvature) is [85]

$$c(F) \equiv \det\left(\mathbb{1} + \frac{\mathrm{i}F}{2\pi}\right) = \sum_j c_j(F). \tag{4.32}$$

The term $c_j(F)$ is the jth *Chern class* and is obtained by ordering the terms in Eq. (4.32) by degree – it is of degree $2j$. Note that in an D-dimensional manifold M, all Chern classes with $2j > D$ vanish [85]. In general, the first three Chern classes are [85, 89]

$$\begin{aligned} c_0(F) &= 1 \\ c_1(F) &= \frac{\mathrm{i}}{2\pi}\mathrm{Tr}F \\ c_2(F) &= -\frac{1}{8\pi^2}\left[\mathrm{Tr}F \wedge \mathrm{Tr}F - \mathrm{Tr}(F \wedge F)\right]. \end{aligned} \tag{4.33}$$

In the special case when the base manifold M is an oriented compact manifold of even dimension $D = 2j$, one can integrate the Chern class over the whole manifold to obtain the *Chern number* [89]

$$C = \int_M c_j(F) \tag{4.34}$$

One important example is the Berry phase of the $U(1)$ bundle of the nth non-degenerate eigenstate discussed before, when the manifold of the parameter space is a two-dimensional surface. Using Eqs. (4.24) and (4.33), the first Chern number is

$$C = \int_M c_1(F) = \frac{\mathrm{i}}{2\pi}\int_M F^n = \frac{1}{2\pi}\gamma_n \tag{4.35}$$

Therefore, the first Chern number is directly related to the Berry phase. Since the integral is over the full manifold, the Berry phase has to be a multiple of 2π, and the Chern number is therefore integer.

4.7 Invariants describing topological insulators

4.7.1 First Chern number and the quantum Hall effect

In the band structure theory, the eigenstates are the Bloch functions $|u_{n\boldsymbol{k}}\rangle$, which are parametrized by the momentum $\boldsymbol{k}$. Therefore, the base space manifold is the Brillouin zone. For a two-dimensional system, it has the topology of a torus, which is an oriented surface. Therefore, for a band n without degeneracies, a first Chern number as introduced in the last section is defined (cf. Eqs. (4.27) and (4.35)), called in this context

Chern topological invariant, via

$$C_n \equiv \frac{1}{2\pi}\mathrm{i}\int_{BZ} \mathrm{d}^2\boldsymbol{k}\cdot\boldsymbol{F}^n(\boldsymbol{k}) = \frac{1}{2\pi}\mathrm{i}\oint_{\partial BZ} \mathrm{d}\boldsymbol{k}\cdot\boldsymbol{A}^n(\boldsymbol{k}), \tag{4.36}$$

with the Berry connection $\boldsymbol{A}^n(\boldsymbol{k}) = \langle u_{n\boldsymbol{k}}|\,\nabla_{\boldsymbol{k}}\,|u_{n\boldsymbol{k}}\rangle$ and the Berry curvature vector $\boldsymbol{F}^n(\boldsymbol{k}) = \nabla_{\boldsymbol{k}}\times\boldsymbol{A}^n(\boldsymbol{k})$. The simplest physical models consist of two bands, one occupied and one unoccupied band separated by a gap, described by a two-by-two Bloch Hamiltonian $H(\boldsymbol{k})$. Any matrix of dimension two can be expanded in the Pauli matrices (2.35) and the unit matrix as

$$H(\boldsymbol{k}) = \epsilon(\boldsymbol{k})\mathbb{1} + \boldsymbol{h}(\boldsymbol{k})\cdot\boldsymbol{\sigma}, \tag{4.37}$$

where $\boldsymbol{\sigma}$ is the vector of Pauli matrices. It can be shown that the Chern number C_n defined by Eq. (4.36) of the lower band of a Hamiltonian (4.37) can be calculated easily via [95, 96]

$$C_n = \frac{1}{4\pi}\int \mathrm{d}^2k \left[\frac{\partial\hat{\boldsymbol{h}}(\boldsymbol{k})}{\partial k_x}\times\frac{\partial\hat{\boldsymbol{h}}(\boldsymbol{k})}{\partial k_y}\right]\cdot\hat{\boldsymbol{h}}(\boldsymbol{k}). \tag{4.38}$$

The hat denotes the normalized vector $\hat{\boldsymbol{h}} = \boldsymbol{h}/\,|\boldsymbol{h}|$. The right hand side of this expression is a two-dimensional winding number as defined in Eq. (4.8). According to Hopf theorem explained in Sec. 4.3.1, it can thus be used as an invariant to distinguish the equivalence classes, and any smooth transformation of $\hat{\boldsymbol{h}}(\boldsymbol{k})$ does not change C_n. The only way to change the winding number by a smooth transformation of $\boldsymbol{h}(\boldsymbol{k})$ is therefore in case $\boldsymbol{h}(\boldsymbol{k}) = 0$ at some point in the Brillouin zone, since then $\hat{\boldsymbol{h}}(\boldsymbol{k})$ is not defined. For a Hamiltonian (4.37), this corresponds to a crossing of the bands. If one assumes that the minimum of the upper band is larger than or equal to the maximum of the lower band for all $\boldsymbol{k}$, the lower band is totally occupied, whereas the upper is empty. Then, the Chern number (4.38) is the total Chern number of the occupied states, and a band crossing is equivalent to a closing of the gap. Therefore, for a single band of an insulator, the Chern topological invariant is, mathematically speaking, both a first Chern number, as well as a winding number. It can only change when the gap to some other band is closed.

In case of many occupied bands that are possibly degenerate, the non-abelian Berry curvature (4.31) has to be used in principle. The Chern class is proportional to $\operatorname{Tr} F$ (see Eq. (4.32)), where the trace is over all occupied bands in order to obtain the Chern number of the electrons. However, since the trace of the commutator vanishes, it does not matter whether the non-abelian or the abelian curvature (4.23) is used to calculate the total Chern invariant. Therefore, one can formally still use this definition (4.38) of the Chern invariant for each band n with the abelian Berry curvature independent of degeneracies, but it is not necessarily uniquely defined, as it can depend on gauge. The trace corresponding to the total Chern invariant is then the sum of Chern invariants related to occupied bands

$$C = \sum_{n\ \text{occupied}} C_n. \tag{4.39}$$

and is a uniquely defined integer if the gap between filled and empty bands remains finite [10, 97],

The first physical appearence of this invariant was in Ref. [98], where Thouless, Kohmoto, Nightingale, and den Nijs showed theoretically that the Hall conductance is quantized as

$$\sigma_{xy} = p\frac{e^2}{h} \tag{4.40}$$

with an integer-valued TKNN invariant p, after it has been observed experimentally two years before [99]. The TKNN invariant is now understood as the Chern invariant of the occupied bands, i.e., $p = C$ [11, 100]. The physical origin of the nontrivial topology in case of the quantum Hall effect is the large magnetic field. However, it is also possible to obtain a nontrivial Chern invariant from the intrinsic structure of the bands, which is called *anomalous quantum Hall effect.* An insulator showing this effect is called a *Chern insulator*, since its total Chern number is different from zero. The most prominent example of a Chern insulator is the Haldane model, where the magnetic flux of the ordinary quantum Hall effect is mimicked by a complex nearest neighbor hopping on a spinless honeycomb lattice [101] (see also chapter 7).

4.7.2 $\mathbb{Z}_2$ classifications of time-reversal symmetry breaking topological insulators

Both magnetic flux and complex hopping, which are needed in the examples above in order to obtain a nontrivial Chern number, break time-reversal symmetry. In fact, for time-reversal symmetric systems, the first Chern number is always zero [100]. It is, however, still possible in the symmetric case to classify nontrivial topology, but different topological invariants have to be used. In case of time-reversal symmetry breaking 2D quantum Hall states, the total first Chern number $C \in \mathbb{Z}$ is the relevant invariant. In contrast, for time-reversal symmetric 2D systems, another invariant $\nu \in \mathbb{Z}_2$ is usually used. In the following, the most important approaches to define the $\mathbb{Z}_2$ invariant are described.

One rather simple way to generalize the approach described so far is to define a Chern invariant for each spin. This is only possible when spin is a good quantum number, so that each band can be classified as ↑ or ↓ band. The total Chern number is then $C = C^{\uparrow} + C^{\downarrow}$, and a spin Chern number can be defined as [12, 102, 103]

$$C_{\mathrm{S}} = (C^{\uparrow} - C^{\downarrow})/2. \tag{4.41}$$

With that, the $\mathbb{Z}_2$ invariant is defined as $\nu_{\mathrm{S}} = C_{\mathrm{S}} \mod 2$, and takes on the values 0,1 [10, 12]. The only constraint for this definition is that the spin-up and the spin-down block are not coupled. If this constraint is fulfilled, $C^{\uparrow}$ and $C^{\downarrow}$ are, in principle, independent, hence also C and C_{S} can take any value. If furthermore time-reversal symmetry is obeyed, $C^{\uparrow} = -C^{\downarrow}$, so that C_{S} is the only possibility for nontriviality. Since the spin Chern number is related to the spin Hall conductivity $\sigma^{\mathrm{s}}_{xy} = (\sigma^{\uparrow}_{xy} - \sigma^{\downarrow}_{xy})/2$, systems with trivial Chern number C, but nontrivial $\mathbb{Z}_2$ invariant ν_{S} are called *quantum spin Hall insulators.*

Prominent examples are the Kane-Mele model without Rashba coupling [13, 14], which basically consists of one Haldane model for each spin species, and the BHZ model [15] for the HgTe/CdTe quantum well, which led to the first experimental observation of the quantum spin Hall effect [16].

In case the spin species are coupled, the spin Chern number is not well defined and other definitions have to be used. The definition of the $\mathbb{Z}_2$ invariant for 2D systmes by Fu and Kane [104] is directly based on the time-reversal symmetry, which is reviewed here briefly. Starting point in this approach is the charge polarization of a 1D system

$$P_\rho \equiv \sum_n \langle w_{0n}| X |w_{0n}\rangle = \frac{\mathrm{i}}{2\pi} \sum_n \int_{-\pi}^{\pi} \mathrm{d}k \, \left\langle u_{nk} \middle| \frac{\partial}{\partial k} \middle| u_{nk} \right\rangle \tag{4.42}$$

with the Bloch functions $|u_{nk}\rangle$ (see Eq. (2.9)) and Wannier functions $|w_{xn}\rangle$ (see Eq. (2.11)). Note that the integrand is the 1D Berry connection. While Bloch and Wannier functions depend on the gauge, the charge polarization is invariant up to a lattice constant. If the system is time-reversal symmetric and no degeneracies are present except for the Kramers degeneracy forced by the time-reversal symmetry, the $2N$ eigenstates may be divided into N Kramers pairs related via

$$\begin{aligned} \left|u^{\mathrm{I}}_{-k\alpha}\right\rangle &= -e^{\mathrm{i}\chi_{k\alpha}} \Theta \left|u^{\mathrm{II}}_{k\alpha}\right\rangle \\ \left|u^{\mathrm{II}}_{-k\alpha}\right\rangle &= e^{\mathrm{i}\chi_{-k\alpha}} \Theta \left|u^{\mathrm{I}}_{k\alpha}\right\rangle , \end{aligned} \tag{4.43}$$

where Θ is the time-reversal operator, $\alpha = 1, \dots, N$, and $\chi_{k\alpha}$ some phase relating the Kramers partners. Similar as the Chern number is split into a spin-up and a spin-down part in the last paragraph, one can split the charge polarization into a part I and a part II, i.e., $P_\rho = P^{\mathrm{I}} + P^{\mathrm{II}}$. The difference between these two is the *time-reversal polarization*

$$P_\theta = P^{\mathrm{I}} - P^{\mathrm{II}} \tag{4.44}$$

To obtain a 2D $\mathbb{Z}_2$ invariant, the Hamiltonian needs to depend continuously on a periodic pumping parameter t with the constraints

$$\begin{aligned} H[t+T] &= H[t] \\ H[-t] &= \Theta H[t] \Theta^{-1}. \end{aligned} \tag{4.45}$$

With the second constraint, it is assured that the Hamiltonian is time reversal invariant at two distinct points $t_1 = 0$ and $t_2 = T/2$. Therefore, the time-reversal polarization is defined at these two points. It is not gauge invariant, but the difference is, and serves as the invariant

$$\nu \equiv P_\theta(T/2) - P_\theta(0) \mod 2. \tag{4.46}$$

The $\mathbb{Z}_2$ invariant can be calculated using the $U(2N)$ matrix relating time-reversed wave functions

$$M_{mn}(k) \equiv \langle u_{-km}| \Theta |u_{kn}\rangle . \tag{4.47}$$

Note that the matrix elements are gauge dependent. Because of Eq. (4.43), M is an antisymmetric matrix at the time-reversal invariant momenta $k = 0$ and $k = \pi$, hence a Pfaffian is defined. The time-reversal polarization can be written as

$$(-1)^{P_\theta} = \frac{\sqrt{\det M(0)}}{\operatorname{Pf} M(0)} \frac{\sqrt{\det M(\pi)}}{\operatorname{Pf} M(\pi)}. \tag{4.48}$$

In case of a 2D topological insulator with rectangular unit cell, k_x is the momentum k of the 1D system, whereas k_y serves as the pumping parameter t (or vice versa). Using Eqs. (4.46) and (4.48), the Fu-Kane invariant can be written as

$$(-1)^{\nu} = \prod_{i=1}^{4} \frac{\sqrt{\det M(\mathbf{\Gamma}_i)}}{\operatorname{Pf} M(\mathbf{\Gamma}_i)}, \tag{4.49}$$

where $\mathbf{\Gamma}_i$ are the four time-reversal invariant momenta (TRIM) $\mathbf{\Gamma}_1 = (0,0)$, $\mathbf{\Gamma}_2 = (0,\pi)$, $\mathbf{\Gamma}_3 = (\pi,0)$, and $\mathbf{\Gamma}_4 = (\pi,\pi)$. In contrast to the spin Chern number, this invariant can be trivially generalized to 3D topological insulators, where the strong topological $\mathbb{Z}_2$ invariant ν_0 is the product of the eight TRIM. Note that even though Eq. (4.49) suggests that information about the Bloch functions is only needed at the TRIM, the gauge at the points in between the TRIM is also of importance since the branches of the square root needs to be chosen such that $\sqrt{\det M(\boldsymbol{k})}$ evolves continuously. The correct gauge is only redundant in case of an inversion-symmetric unit cell, because then

$$\frac{\sqrt{\det M(\mathbf{\Gamma}_i)}}{\operatorname{Pf} M(\mathbf{\Gamma}_i)} = \prod_{m=1}^{N} \xi_{2m}(\mathbf{\Gamma}_i), \tag{4.50}$$

where $\xi_{2m}(\mathbf{\Gamma}_i)$ is the eigenvalue of the parity operator of the $2m$th occupied band. It has the same value as its Kramers degenerate partner $\xi_{2m-1}(\mathbf{\Gamma}_i)$ [105]. In all other cases, the evolution of the square root has to be done carefully. One way to find a smooth gauge is to use maximally localized Wannier funcions [29, 106]. Details of this approach are explained in the author's master's thesis [107].

4.7.3 Second Chern number and dimensional reduction

In the investigation of the Fu-Kane invariant for 2D topological insulators, a 1D system is the starting point, and the second dimension is created by a pumping parameter. The 3D topological insulators can be classified by a generalization of the 2D case. However, it is also possible to obtain 2D and 3D invariants from a 4D topological insulator by reducing the number of parameters, as sketched in the following. A detailed description can be found in Ref. [108]. In case of a 4D insulator, the relevant Chern number is the second Chern number $C_2 \in \mathbb{Z}$, which is the integral over the second Chern class, see Sec. 4.6. The integral over the four-dimensional Brillouin zone is

$$C_2 = \frac{1}{32\pi^2} \int \mathrm{d}^4 k \sum_{ijkl} \epsilon_{ijkl} \operatorname{Tr}\left[F_{ij} F_{kl}\right] \tag{4.51}$$

with the non-abelian Berry curvature matrices

$$F_{ij}(\boldsymbol{k}) = \frac{\partial A_j}{\partial k_i} - \frac{\partial A_i}{\partial k_j} + \mathrm{i}\,[A_i, A_j]\,, \tag{4.52}$$

where the Berry connection matrices A_i have the elements

$$A_i^{mn}(\boldsymbol{k}) = -\mathrm{i}\left\langle u_{m\boldsymbol{k}} \middle| \frac{\partial}{\partial k_i} \middle| u_{n\boldsymbol{k}} \right\rangle. \tag{4.53}$$

The trace is over all occupied bands[4]. In contrast to the 2D quantum Hall stated described by the first Chern number, breaking time-reversal symmetry is not required for a nontrivial second Chern number. Therefore, the 4D topological insulator is the fundamental time-reversal invariant insulator.

The invariants from time-reversal invariant Hamiltonians of lower dimension can be obtained by dimensional reduction, which means that the parameters k_i that are not needed are replaced by nonphysical parameters θ_i. In case of a 3D Bloch Hamiltonians, a topological classification is possible by interpolating between two Hamiltonians $H_1(\boldsymbol{k})$ and $H_2(\boldsymbol{k})$ using an additional parameter θ, satisfying

$$\begin{aligned} H(\boldsymbol{k}, \theta = 0) &= H(\boldsymbol{k}, \theta = 2\pi) \\ H(\boldsymbol{k}, \theta = 0) &= H_1(\boldsymbol{k}) \\ H(\boldsymbol{k}, \theta = \pi) &= H_2(\boldsymbol{k}) \\ \Theta^\dagger H(-\boldsymbol{k}, -\theta)\Theta &= H^{\mathrm{T}}(\boldsymbol{k}, \theta) \end{aligned} \tag{4.54}$$

Furthermore, $H(\boldsymbol{k}, \theta)$ needs to be gapped for any θ. Since the interpolation is periodic, a second Chern number in the $(\boldsymbol{k}, \theta)$ space is defined. One can show [108] that the *relative second Chern parity*

$$N_3[H_1(\boldsymbol{k}), H_2(\boldsymbol{k})] = (-1)^{C_2[H(\boldsymbol{k},\theta)]} \tag{4.55}$$

is well defined for gapped, time-reversal invariant Hamiltonians H_1 and H_2. The topology is then defined by comparing to the vacuum Hamiltonian H_0. If $N_3[H(\boldsymbol{k}), H_0] = 1$, then $H(\boldsymbol{k})$ is trivial, if $N_3[H(\boldsymbol{k}), H_0] = -1$, it is nontrivial. Therefore, the Chern parity is a $\mathbb{Z}_2$ classification. Physically, the second Chern parity is related to the magnetoelectric polarization [100, 108, 109]

$$P_3 = \frac{1}{16\pi^2} \int \mathrm{d}^3k \sum_{ijk} \epsilon_{ijk}\, \mathrm{Tr}\left\{ \left[F_{ij} - \frac{2}{3}\mathrm{i} A_i A_j \right] A_k \right\}. \tag{4.56}$$

If $P_3 = 0$, the insulator is trivial, if $P_3 = 1/2$, it is nontrivial [108]. The relation between the second Chern number of a 4D insulator and the magnetoelectric polarization of a

---

[4] Note that a matrix product occurs in the trace. Thus, the commutator $[A_i, A_j]$ influences the result, and the non-abelian curvature has to be used. Therefore, in contrast to the first Chern number (see Eqs. (4.36) and (4.39)), it is not possible to write the second Chern number as a sum of terms that only depend on the connection of one single band.

3D insulator is analogous to the relation of the first Chern number of a 2D insulator and the charge polarization (4.42) of a 1D insulator. In Ref. [109], it is shown that the classification of a 3D insulator using P_3 is equivalent to the Fu-Kane classification of a strong topological insulator. Thus, the $\mathbb{Z}_2$ index ν_0 is related to the dimensional reduction of the second Chern number. The $\mathbb{Z}_2$ invariant of a 2D topological insulator is obtained by another dimensional reduction [108].

4.7.4 Topology in interacting systems

In the previous section, several topological invariants are introduced. Due to dimensional reduction, also the $\mathbb{Z}_2$ invariants are related to either first or second Chern number, meaning that these quantities are key for a topological classification of insulators. Their definitions (4.36), (4.39), and (4.51) are based on the Berry connection, which in turn is calculated using the Bloch functions $|u_{n\boldsymbol{k}}\rangle$. Therefore, the definitions cannot be used for interacting systems, since then one-electron wave functions are not defined. However, the Chern numbers can also be formulated in terms of Green's functions [110–114]. The first Chern number reads in terms of the Matsubara Green's function [114]

$$C = \frac{1}{24\pi^2} \int \mathrm{d}k_0 \int \mathrm{d}^2k \sum_{\mu,\nu,\rho=0}^{3} \epsilon_{\mu\nu\rho} \operatorname{Tr}\left[G\frac{\partial G^{-1}}{\partial k_\mu} G\frac{\partial G^{-1}}{\partial k_\nu} G\frac{\partial G^{-1}}{\partial k_\rho}\right], \tag{4.57}$$

where k_0 is the Matsubara frequency $k_0 \equiv \mathrm{i}\omega_n$. A similar expression is also possible for the second Chern number by just increasing the number of dimensions from two to four [114]

$$\begin{aligned} C_2 =& \frac{1}{480\pi^3} \int \mathrm{d}k_0 \int \mathrm{d}^4k \sum_{\mu,\nu,\rho,\sigma,\tau=0}^{3} \epsilon_{\mu\nu\rho\sigma\tau} \\ & \times \operatorname{Tr}\left[G\frac{\partial G^{-1}}{\partial k_\mu} G\frac{\partial G^{-1}}{\partial k_\nu} G\frac{\partial G^{-1}}{\partial k_\rho} G\frac{\partial G^{-1}}{\partial k_\sigma} G\frac{\partial G^{-1}}{\partial k_\tau}\right]. \end{aligned} \tag{4.58}$$

For noninteracting systems, the two expressions (4.57) and (4.58) reduce to the first and second Chern numbers (4.39) and (4.51) of the Bloch vector bundle. However, since the definitions (4.57) and (4.58) are based on Green's functions, they can also be used as a generalization to interacting systems. The question is, whether these two expressions are still Chern numbers of a vector bundle in the mathematical sense, and if so, what the bundle is. Zhong Wang and his coworkers showed that C and C_2 defined above in terms of Green's functions are indeed Chern numbers [115–117]. The associated vector bundle is the set of eigenvectors of the Green's function at zero frequency

$$G^{-1}(\omega = 0, \boldsymbol{k})\,|\alpha(\omega = 0, \boldsymbol{k})\rangle = \mu_\alpha(\omega = 0, \boldsymbol{k})\,|\alpha(\omega = 0, \boldsymbol{k})\rangle\,. \tag{4.59}$$

For a noninteracting system, $G^{-1}(\omega = 0, \boldsymbol{k}) = H(\boldsymbol{k})$, hence $|\alpha(\omega = 0, \boldsymbol{k})\rangle = |u_{n\boldsymbol{k}}\rangle$, and the Chern numbers are those of an ordinary Bloch bundle. Therefore, the Green's function approach serves indeed as a generalization to the Chern numbers calculated from Bloch bands, with the bundle $|\alpha(\omega = 0, \boldsymbol{k})\rangle$.

Hence, the topological properties of an interacting system are the same as for an artificial noninteracting Bloch Hamiltonian that is minus the inverse Green's function at $\omega = 0$. This defines the so called *topological Hamiltonian* [117]

$$H_{\mathrm{t}}(\boldsymbol{k}) = -G^{-1}(\omega = 0, \boldsymbol{k}). \tag{4.60}$$

Thus, all topological properties are encoded in an artificial system. Since this is interactionless, all methods described in the previous sections can be used to calculate both Chern invariants as well as $\mathbb{Z}_2$ invariants, since they are related to the Chern numbers by dimensional reduction. However, it is prudent to mention that only the topological properties are encoded in $H_{\mathrm{t}}(\boldsymbol{k})$, it is not suitable to use it for estimates of any other quantities.

5 The maximum entropy method for distributions with positive and negative values

Within many methods, as for example CTQMC (see Sec. 2.3.2), the Green's function is calculated on the imaginary frequency axis, whereas results on the real axis are needed for many physical interpretations. However, since the Green's function is analytic in the whole complex plane except for the poles, $G(\omega)$ can be obtained from its Matsubara counterpart $G(\mathrm{i}\omega_n)$ via analytic continuation. For all complex arguments z, the Green's function can be expressed in terms of the spectral function $A(\omega)$ via

$$G(z) = \int \mathrm{d}\omega' \frac{A(\omega')}{z - \omega'}. \tag{5.1}$$

This relation is also valid in the multi-orbital case, when G and A are matrices. In this chapter, an element-wise view is used, so that G and A denote a certain element (either diagonal or off-diagonal) of the respective matrices. Because of Eq. (5.1), the Matsubara Green's function ($z = \mathrm{i}\omega_n$) as well as the retarded Green's function ($z = \omega + \mathrm{i}0^+$) can be calculated easily once the spectral function is known. The inverse operation, i.e., calculating $A(\omega)$ from $G(\mathrm{i}\omega_n)$, is not straight forward, as can be seen by the following considerations. Using a Fourier transformation, the relation between the spectral function and the Green's function of imaginary time $G(\tau)$ is

$$G(\tau) = \int \mathrm{d}\omega \frac{e^{-\omega\tau}}{1 + e^{-\omega\beta}} A(\omega). \tag{5.2}$$

For discrete ω and τ meshes, this equation is a matrix multiplication

$$\boldsymbol{G} = K\boldsymbol{A} \tag{5.3}$$

with the elements $G_i = G(\tau_i)$, $A_j = A(\omega_j)$, and a Kernel

$$K_{ij} = \frac{e^{-\omega_j \tau_i}}{1 + e^{-\omega_j \beta}} \Delta\omega_j.$$

Due to the exponential behavior of the Kernel, the condition number of the matrix K is large. Thus, calculating directly the inverse $\boldsymbol{A} = K^{-1}\boldsymbol{G}$ is an *ill-posed* problem and therefore numerically challenging or even impossible.

The task of an analytic continuation under these ill-posed conditions is to find an approximate spectral function $\boldsymbol{A}$ with a reconstruction $\tilde{\boldsymbol{G}} = K\boldsymbol{A}$ that captures the physically relevant features, but does not follow the noise. In case of non-negative spectral functions $A(\omega)$, several methods exist to perform that task, as for example series expansions (e.g. the Padé method [118–120]), information-theoretical approaches such as the maximum entropy method (MEM) [121–124] and stochastic methods [125–129]. However, the Green's function is, in general, matrix valued, and when the SOC is included, finite off-diagonal elements persist. The norm of off-diagonal elements $\int \mathrm{d}\omega A(\omega)$ is zero, hence $A(\omega)$ is negative at some frequencies.

Gernot Kraberger, Manuel Zingl, Markus Aichhorn, and the author published a generalization to the MEM, working for matrix-valued Green's functions and self-energies [130]. Gernot Kraberger devised the idea of the positive-negative entropy, which was further developed by the author and put on a probabilistic footing. This theoretical investigation is described in this chapter. It should be noted that the positive-negative entropy has been also carried out in the field of astrophysics [131, 132]. However, some aspects, such as the parametrization in the singular-value basis, are not considered in these publications, and other aspects, such as the derivation of the integration measure when using the positive-negative entropy, are done in a different fashion. Therefore, the full investigation is summarized here.

5.1 Theoretical basics of the maximum entropy method

The probability density of a certain spectral function $\boldsymbol{A}$ given $\boldsymbol{G}$ is

$$p(\boldsymbol{A}|\boldsymbol{G}) = \frac{1}{Z} p(\boldsymbol{G}|\boldsymbol{A}) p(\boldsymbol{A}) \tag{5.4}$$

with a normalization Z. To express the likelihood, the uncertainty of $G(\tau)$ has to be known. If, as usual, a Gaussian distribution is assumed, one has

$$p(\boldsymbol{G}|\boldsymbol{A}) \propto e^{-\chi^2/2} \tag{5.5}$$

with a misfit

$$\chi^2 = \sum_i \frac{\left(\tilde{G}_i - G_i\right)^2}{\sigma_i^2}, \tag{5.6}$$

and the reconstruction $\tilde{\boldsymbol{G}} = K\boldsymbol{A}$. The parameters σ_i^2 are variances of the probability distributions of G at the points τ_i. If the values of the Green's function at different values of τ are correlated, the misfit has to be generalized to $\chi^2 = (K\boldsymbol{A} - \boldsymbol{G})^{\mathrm{T}} C^{-1} (K\boldsymbol{A} - \boldsymbol{G})$ with a covariance matrix C.

The difficult part is to assign a prior distribution $p(\boldsymbol{A})$. John Skilling showed in his famous work [133] that, based on some general axioms, the prior for non-negative spectral functions maximizes the entropy

$$S(A, D) = \int \mathrm{d}\omega \left(A(\omega) - D(\omega) - A(\omega) \log \frac{A(\omega)}{D(\omega)} \right), \tag{5.7}$$

with a so-called *default model* $D(\omega)$ that includes the knowledge one has about the spectral function. In case no information is present, it has to be chosen constant within a frequency range. The full form of $p(\boldsymbol{A})$ is still missing, though, as well as the integration measure $m(\boldsymbol{A})$ for integrals over A, needed to calculate the probability that $\boldsymbol{A}$ is in some domain I via

$$P(\boldsymbol{A} \in I) = \int_I \mathrm{d}^{N_\omega} A \; m(\boldsymbol{A})\, p(\boldsymbol{A}), \tag{5.8}$$

where $\mathrm{d}^{N_\omega} A$ is the volume element in the space of spectral functions with a dimension equal to the number of ω points N_ω. In Ref. [133], Skilling also showed how these quantities look like by using a special example, which is also described here in the following, since it helps to visualize the origin of the entropic term (5.7). Next to the already introduced discretization of the ω axis $\omega \to \omega_i$, the A axis is discretized as well:

$$A(\omega_i) \equiv A_i \to n_i \quad \text{with} \quad A_i \approx n_i \Delta A \tag{5.9}$$

and $n_i \in \mathbb{N}$. The assumption is now that units of ΔA are randomly distributed on the different slots ω_i with the constraint that on average μ_i units are placed. Usually, an imaginary monkey is instructed to fulfill that task. The distribution for that process is a Poisson distribution

$$P(n_i|\mu_i) = \frac{\mu_i^{n_i}}{n_i!} e^{-\mu_i}. \tag{5.10}$$

Since the process is independent for each slot, the total probability is the product of the individual probabilities. Using Stirling's formula $n_i! \approx \sqrt{2\pi n_i}\, n_i^{n_i} e^{n_i}$ valid for large n_i, one obtains

$$P(\boldsymbol{n}|\boldsymbol{\mu}) = \frac{1}{\prod_i \sqrt{2\pi n_i}} e^{\sum_i n_i - \mu_i - n_i \log(n_i/\mu_i)} \tag{5.11}$$

Resubstituting $n_i = A_i/\Delta A$ and $\mu_i = D_i/\Delta A$ leads to

$$P(\boldsymbol{A}|\boldsymbol{D}, \Delta A) = \left(\frac{\Delta A}{2\pi}\right)^{N_\omega/2} \frac{1}{\prod_i \sqrt{A_i}}\, e^{\frac{1}{\Delta A}\sum_i A_i - D_i - A_i \log \frac{A_i}{D_i}}, \tag{5.12}$$

where N_ω is the number of ω points. This is the probability of a spectrum $\boldsymbol{A}$, where each A_i is discretized in units of ΔA. In order to write it for continuous A_i, one cannot formulate a probability of a certain function, but has to look at the probability that the function is within some domain I.

$$\begin{aligned} P(\boldsymbol{A} \in I|\boldsymbol{D}, \Delta A) &= \sum_{\boldsymbol{A} \in I} P(\boldsymbol{A}|\boldsymbol{D}, \Delta A) \approx \int_I \frac{\mathrm{d}^{N_\omega} A}{\Delta A^{N_\omega}}\; P(\boldsymbol{A}|\boldsymbol{D}, \Delta A) \\ &= \int_I \frac{\mathrm{d}^{N_\omega} A}{\Delta A^{N_\omega}} \left(\frac{\Delta A}{2\pi}\right)^{N_\omega/2} \frac{1}{\prod_j \sqrt{A_j}}\, e^{\frac{1}{\Delta A}\sum_i A_i - D_i - A_i \log \frac{A_i}{D_i}} \\ &= \frac{1}{(2\pi \Delta A)^{N_\omega/2}} \int_I \frac{\mathrm{d}^{N_\omega} A}{\prod_j \sqrt{A_j}}\, e^{\frac{1}{\Delta A} S} \end{aligned} \tag{5.13}$$

with

$$S = \sum_i S_i = \sum_i A_i - D_i - A_i \log \frac{A_i}{D_i}. \tag{5.14}$$

Writing the entropy in the continuous form, this entropy coincides, up to a factor $\Delta\omega$, to the entropy in Eq. (5.7). Hence, the exponential part of $P(\boldsymbol{A}|\boldsymbol{D}, \Delta A)$ fulfills the properties the universal prior has to fulfill. However, also a prefactor $1/\sqrt{A_i}$ appears. In Ref. [133], the conclusion of this result is that the only consistent way is to put it into the measure, so that

$$m(\boldsymbol{A}) = \frac{1}{\prod_j \sqrt{A_j}}. \tag{5.15}$$

The probability distribution function reads then

$$p(\boldsymbol{A}|\boldsymbol{D}, \Delta A) = \frac{1}{(2\pi\Delta A)^{N_\omega/2}}\, e^{\frac{1}{\Delta A} S}. \tag{5.16}$$

Since the factor $1/\Delta A$ in front of S in the exponential is not defined, it is a so-called *hyper parameter* that needs to be adjusted correctly. Usually, it is dubbed $\alpha \equiv 1/\Delta A$. Using Eqs. (5.4), (5.5), and (5.16), the probability distribution of a spectrum $\boldsymbol{A}$ for given α, data $\boldsymbol{G}$, and default model $\boldsymbol{D}$ is

$$p(\boldsymbol{A}|\boldsymbol{G}, \alpha, \boldsymbol{D}) = \frac{1}{Z(\alpha)} e^{-\frac{1}{2}\chi^2(\boldsymbol{A},\boldsymbol{G}) + \alpha S(\boldsymbol{A},\boldsymbol{D})}, \tag{5.17}$$

according probabilities are obtained from integrals of the form

$$P(\boldsymbol{A} \in I|\boldsymbol{G}, \alpha, \boldsymbol{D}) = \int_I \frac{\mathrm{d}^{N_\omega} A}{\prod_j \sqrt{A_j}}\, p(\boldsymbol{A}|\boldsymbol{G}, \alpha, \boldsymbol{D}) \tag{5.18}$$

The highest probability for a given α is thus achieved by a maximization of

$$Q = -\frac{1}{2}\chi^2 + \alpha S. \tag{5.19}$$

Step one of all MEM is thus to maximize Q as a function of α. Step two is to use that information to obtain a final spectrum. The way to do that is one of the key decisions of a maximum entropy calculation.

5.2 Entropy of two independent variables

In the previous section, a positive distribution is assumed. Offdiagonal elements of spectral functions do not have this constraint. To get a more general function out of positive functions, one could subtract two positive functions which are independent, or one can consider the phase and the absolute value as independent. All of these are just assumptions, since no rigorous way is known to derive a general entropy as Skilling did. However, there is an argument for subtracting two positive functions: If a spectral function has no offdiagonal elements, one could create some by a unitary transformation. In this special case, the offdiagonal elements are linear combinations of independent positive functions $A(\omega) = \sum_n a_n A_n(\omega)$. If two positive functions A_1 and A_2 are added, the resulting function $A' = A_1 + A_2$ is again positive. The entropy of the resulting sum A' of the independent positive functions should thus have the same entropy $S(A')$ given in Eq. (5.7). If two positive functions are subtracted, i.e., $A'' = A_1 - A_2$, the resulting entropy is different, since A'' is possibly negative for some frequencies. For the example of the linear combination of positive functions $A = \sum_n a_n A_n$, one can, therefore, just sum up all parts with positive coefficients $A^+ = \sum_{a_n>0} a_n A_n$ and with negative coefficients $A^- = -\sum_{a_n<0} a_n A_n$. The entropies $S(A^+)$ and $S(A^-)$ are then the usual entropies of Eq. (5.7). The entropy of $A = A^+ - A^-$, though, is the entropy of a function that originates from the subtraction of two positive functions, which will be derived in the following. Here, only this approach is considered.

5.2.1 Probabilities with several monkeys

The previous section, the MEM is introduced using a monkey putting balls of size ΔA into boxes. If a linear combination of positive functions is considered, this is equivalent to several monkeys putting different types of balls into boxes. Each monkey corresponds to one spectral function A_n. Here, the focus is on two special cases of linear combinations: adding and subtracting two functions. As the probability distributions for all boxes i are equivalent, the index is not written here explicitly. Consider first two monkeys with balls of the same sign and mean values μ_1 and μ_2, which corresponds to adding two positive functions. The according probabilities for each monkey to put n balls into the slot are $P_1(n_1|\mu_1)$ and $P_2(n_2|\mu_2)$, where both are Poisson distributions (5.10). Several different numbers of balls n_1 thrown in by monkey 1 and numbers of balls n_2 thrown in by monkey 2 lead to the same sum $N = n_1 + n_2$. The probability that in total N balls are in a slot is

$$P(N|\mu_1, \mu_2) = \sum_n P_1(n|\mu_1) P_2(N - n|\mu_2). \tag{5.20}$$

This is the convolution of two Poisson distributions and is again a Poisson distribution with mean value $\mu = \mu_1 + \mu_2$, as easy to show. This is consistent with the previously mentioned statement that the sum of two positive functions is again a positive function, wherefore the probability distribution has to be of the same form. In case of two monkeys with balls of opposite sign, one obtains

$$P^{\pm}(N|\mu_1, \mu_2) = \sum_n P_1(n|\mu_1) P_2(n - N|\mu_2). \tag{5.21}$$

This distribution is called Skellam distribution [134] and is the one that should be used for functions that can be both positive and negative [132].

5.2.2 Entropies for sums and differences of non-negative functions

Looking at probabilities has the problem that it is not obvious which part of P is put into the measure, and which into the probability density has to be optimized (see Eq.(5.20)). The strategy chosen here is simply to add two entropies, since entropies are extrinsic quantities [135, 136]. The idea is to describe a function that is given by the difference of two non-negative functions $A^+(\omega)$ and $A^-(\omega)$, i.e., $A(\omega) = A^+(\omega) - A^-(\omega)$. However, it is also interesting to look at the sum of these two functions $B = A^+ + A^-$, especially for consistency reasons, since B is again a non-negative function, for which the ordinary entropy should be correct. The probabilities and entropies of A^+ and A^- are assumed to be independent. The entropy of one lattice point i is thus, dropping again the indices, the sum of the entropies of A^+ and A^-,

$$\begin{aligned} S(A^+, A^-) &= S(A^+) + S(A^-) \\ &= A^+ - D^+ - A^+ \log \frac{A^+}{D^+} + A^- - D^- - A^- \log \frac{A^-}{D^-}. \end{aligned} \tag{5.22}$$

The total entropy for vectors $\boldsymbol{A}^+$, $\boldsymbol{A}^-$ is the sum of the entropies at each ω point, i.e., $S(\boldsymbol{A}^+, \boldsymbol{A}^-) = \sum_i S(A_i^+, A_i^-)$. This entropy has two parameters, A^+ and A^-, that have to be optimized instead of only one, which is the case in ordinary MEM. Note that also two default models are needed here. Next to the entropy corresponding to the prior distribution, also a misfit $\chi^2(A^+, A^-)$ needs to be given. The maximum entropy solution is then to maximize $Q(A^+, A^-) = -\chi^2/2 + \alpha S$ with respect to both A^+ and A^-. However, if one has some χ^2 that depends on one parameter only, for example on $B = A^+ + A^-$ or $A = A^+ - A^-$, the maximization of Q with respect to the other parameter is trivial, since it is equivalent to maximize the entropy only, which can be done analytically.

The cases where the relevant parameter is either $B = A^+ + A^-$ or $A = A^+ - A^-$ can be treated simultaneously by the coordinate transformation of $S(A^+, A^-)$ to $S(A, B)$

$$\begin{aligned} B &= A^+ + A^- \qquad & A &= A^+ - A^- \\ A^+ &= (B + A)/2 \qquad & A^- &= (B - A)/2, \end{aligned} \tag{5.23}$$

leading to

$$S(A, B) = B - (D^+ + D^-) - \frac{B + A}{2} \log \frac{B + A}{2D^+} - \frac{B - A}{2} \log \frac{B - A}{2D^-}. \tag{5.24}$$

The entropy for a function B, which originates from adding two positive functions, is denote here as $S^+(B)$. It is obtained from the condition $\frac{\partial S}{\partial A} = 0$, which leads to

$$A^+ D^- = A^- D^+ \Leftrightarrow A = B \frac{D^+ - D^-}{D^+ + D^-}, \tag{5.25}$$

$$S^+(B) = B - (D^+ + D^-) - B \log \frac{B}{D^+ + D^-}. \tag{5.26}$$

This is the same expression as for a single distribution, with the sum of D^+ and D^- as default model $S^+(B, D^+, D^-) = S(B, D = D^+ + D^-)$. This is expected, since convolving two Poisson distributions with mean values μ_1 and μ_2 gives another Poisson distribution with mean value $\mu = \mu_1 + \mu_2$ (see last section). Default model and mean value are related via $D = \mu \Delta A$. Thus, it is proved that maximum entropy is consistent regarding the decomposition of a non-negative function into many non-negative functions. The entropy for a function A, which originates from the difference of two positive functions, is called $S^\pm(A)$. It is obtained from the condition $\frac{\partial S^\pm}{\partial B} = 0$, which leads to

$$A^+A^- = D^+D^- \Leftrightarrow B = \sqrt{A^2 + 4D^+D^-} \tag{5.27}$$

$$S^\pm(A) = \sqrt{A^2 + 4D^+D^-} - (D^+ + D^-) - A \log \frac{\sqrt{A^2 + 4D^+D^-} + A}{2D^+} \tag{5.28}$$

This entropy is qualitatively different to the ordinary entropy (5.7) that is also valid for the sum of two positive functions. The entropy $S^\pm$ is symmetric around zero if $D^+ = D^-$ and is thus suited for spectral functions that are possibly positive and negative in some frequency intervals [130–132]. If $D^- = 0$ is chosen, it reduces to the ordinary entropy, since this corresponds to a spectrum that cannot be negative.

Given now the misfit $\chi^2(\boldsymbol{A})$ and the entropy $S(\boldsymbol{A})$ or $S^\pm(\boldsymbol{A})$ (depending on whether the spectral function $\boldsymbol{A}$ is strictly non-negative or possibly both positive and negative), two tasks have to be done in order to get the optimal spectrum: First, optimize Q for given values of α with respect to the spectral function, and second, determine the best hyper parameter α.

5.3 Optimization of Q

The condition for maximizing Q given α is $\partial Q / \partial A_i = 0$, or, equivalently, $\alpha \partial S / \partial A_i = \frac{1}{2} \partial \chi^2 / \partial A_i$. For the ordinary entropy $S(\boldsymbol{A}) = S^+(\boldsymbol{A}) = \sum_i \left(A_i - D_i - A_i \log \frac{A_i}{D_i} \right)$ and the misfit $\chi^2 = \sum_j (\tilde{G}_j - G_j)^2 / \sigma_j^2$ (with the reconstruction $\tilde{G}_j = \sum_i K_{ji} A_i$), the derivatives read [137]

$$\begin{aligned} \frac{\partial S}{\partial A_i} &= -\log \frac{A_i}{D_i} \\ \frac{\partial \chi^2}{\partial A_i} &= \sum_j \frac{\partial \chi^2}{\partial \tilde{G}_j} \frac{\partial \tilde{G}_j}{\partial A_i} = \sum_j \frac{\partial \chi^2}{\partial \tilde{G}_j} K_{ji} \end{aligned} \tag{5.29}$$

The stationarity condition is thus in vector notation

$$-2\alpha \log \frac{\boldsymbol{A}}{\boldsymbol{D}} = K^{\mathrm{T}} \frac{\partial \chi^2}{\partial \tilde{\boldsymbol{G}}} \tag{5.30}$$

Bryan suggested to reduce the space by a singular value decomposition (SVD) of the Kernel $K = U\Xi V^{\mathrm{T}}$ via the ansatz [137]

$$A_i = D_i e^{\sum_j V_{ij} u_j}, \tag{5.31}$$

which is in vector notation

$$\boldsymbol{A} = \boldsymbol{D} e^{V\boldsymbol{u}}. \tag{5.32}$$

Plugging this into the maximization condition, the matrix V stands on the very left on both sides of the equal sign. Therefore, the condition is already fulfilled in the much smaller singular space when dropping the matrix V on both sides:

$$-2\alpha \boldsymbol{u} = \Xi U^{\mathrm{T}} \frac{\partial \chi^2}{\partial \tilde{\boldsymbol{G}}} \tag{5.33}$$

This equation has to be solved numerically. The advantage of parametrization (5.31) is that the equation, which has to be solved, is in the space of relevant singular values, which is much smaller than the original space, where every point of the ω grid constitutes a dimension.

In case of the entropy $S^{\pm}(\boldsymbol{A})$, another parametrization is needed to reduce the space. The derivative of the entropy is

$$\frac{\partial S^{\pm}}{\partial A_i} = -\log \frac{A_i + \sqrt{A_i^2 + 4D_i^+ D_i^-}}{2D_i^+} = -\log \frac{A_i^+}{D_i^+},$$

so that the maximization condition becomes in vector notation

$$-2\alpha \log \frac{\boldsymbol{A}^+}{\boldsymbol{D}^+} = K^{\mathrm{T}} \frac{\partial \chi^2}{\partial \tilde{\boldsymbol{G}}} \tag{5.34}$$

The left hand side of the last expression is written as a function of $\boldsymbol{A}^+$, the right hand side is a function of $\boldsymbol{A}$ since usually $\chi^2 = (K\boldsymbol{A} - \boldsymbol{G})^{\mathrm{T}} C^{-1} (K\boldsymbol{A} - \boldsymbol{G})$. However, due to equation (5.27), one of the three quantities $\boldsymbol{A}^+, \boldsymbol{A}^-, \boldsymbol{A}$ is enough to determine the other two:

$$A_i^- = \frac{D_i^+ D_i^-}{A_i^+} \tag{5.35}$$

$$A_i = A_i^+ - A_i^- = A_i^+ - \frac{D_i^+ D_i^-}{A_i^+} \tag{5.36}$$

$$A_i^+ = \frac{\sqrt{A_i^2 + 4D_i^+ D_i^-} + A_i}{2} \tag{5.37}$$

$$A_i^- = \frac{\sqrt{A_i^2 + 4D_i^+ D_i^-} - A_i}{2} \tag{5.38}$$

If one wants to do the optimization in the smaller SVD space, one of the three quantities has to be expressed in terms of some parameters $\boldsymbol{u}$. Due to equation (5.34) – notice here the similarity to equation (5.30) – one can take

$$\boldsymbol{A}^{+} = \boldsymbol{D}^{+} e^{V\boldsymbol{u}} \tag{5.39}$$

$$\boldsymbol{A}^{-} = \boldsymbol{D}^{-} e^{-V\boldsymbol{u}} \tag{5.40}$$

$$\boldsymbol{A} = \boldsymbol{D}^{+} e^{V\boldsymbol{u}} - \boldsymbol{D}^{-} e^{-V\boldsymbol{u}} \tag{5.41}$$

With that, the maximization condition takes the same form as in case of the usual entropy

$$-2\alpha\boldsymbol{u} = \Xi U^{\mathrm{T}} \frac{\partial \chi^2}{\partial \tilde{\boldsymbol{G}}}. \tag{5.42}$$

5.4 Probability of α

Many methods exist to determine the best value of α once the functions $\boldsymbol{A}_\alpha^*$ that optimize $Q_\alpha(\boldsymbol{A})$ have been found. One possibility is the so-called *classic* MEM, which is based on the probabilistic picture [138]. In case of the usual entropy $S(\boldsymbol{A})$, the correct probability density for α is obtained by a marginalization over the spectrum, using its probability density (5.17) and the measure (5.15)

$$\begin{aligned} p(\alpha|\boldsymbol{G}) = \frac{p(\boldsymbol{G}|\alpha)p(\alpha)}{p(\boldsymbol{G})} &\propto \int \frac{\mathrm{d}^{N_\omega}A}{\prod_j \sqrt{A_j}}\, p(\boldsymbol{G}|\boldsymbol{A},\alpha)p(\boldsymbol{A}|\alpha)p(\alpha) \\ &= \int \frac{\mathrm{d}^{N_\omega}A}{\prod_j \sqrt{A_j}}\, Z_{\chi^2}^{-1} e^{-\frac{1}{2}\chi^2(\boldsymbol{G},\boldsymbol{A})}\, Z_S^{-1} e^{\alpha S(\boldsymbol{A})} p(\alpha) \\ &= \frac{p(\alpha)}{Z_{\chi^2} Z_S(\alpha)} \int \frac{\mathrm{d}^{N_\omega}A}{\prod_j \sqrt{A_j}}\, e^{-\frac{1}{2}\chi^2(\boldsymbol{G},\boldsymbol{A})+\alpha S(\boldsymbol{A})} \\ &= \frac{p(\alpha) Z_Q(\alpha)}{Z_{\chi^2} Z_S(\alpha)} \end{aligned} \tag{5.43}$$

Note that $Z_S(\alpha)$ depends on α but Z_{χ^2} does not. Therefore, it is important to calculate the former properly when looking for the maximum of $p(\alpha|\boldsymbol{G})$, whereas the latter is just a normalization constant. For the prior distribution $p(\alpha)$, usually Jeffrey's prior $1/\alpha$ is assumed, as α is scale invariant. What is missing to evaluate $p(\alpha|\boldsymbol{G})$ are the two integrals

$$Z_S(\alpha) = \int \frac{\mathrm{d}^{N_\omega}A}{\prod_j \sqrt{A_j}}\, e^{\alpha S(\boldsymbol{A})} \tag{5.44}$$

$$Z_Q(\alpha) = \int \frac{\mathrm{d}^{N_\omega}A}{\prod_j \sqrt{A_j}}\, e^{-\frac{1}{2}\chi^2(\boldsymbol{G},\boldsymbol{A})+\alpha S(\boldsymbol{A})} \tag{5.45}$$

The integrals over A can be approximated by expanding the exponents to second order in A around their maxima (called steepest decent approximation):

$$\int \mathrm{d}^N x \; e^{\Phi(\boldsymbol{x})} \mu(\boldsymbol{x}) \approx \mu(\boldsymbol{x}^*) e^{\Phi(\boldsymbol{x}^*)} (2\pi)^{N/2} |H|^{-1/2} \tag{5.46}$$

where $\boldsymbol{x}^*$ maximizes $\Phi(\boldsymbol{x})$,

$$H_{ij} = \frac{\partial^2}{\partial x_i \partial x_j} \Phi \Big|_{\boldsymbol{x}^*} \tag{5.47}$$

is the Hessian at this point, and $|H|$ its determinant. In case of Z_S,

$$\frac{\partial^2 S}{\partial A_i \partial A_j} = -\frac{1}{A_i} \delta_{ij}. \tag{5.48}$$

Note that the measure is identical to the square root of the Hessian. The approximative value of the integral is thus [138]

$$Z_S(\alpha) = \left(\frac{2\pi}{\alpha} \right)^{N_\omega/2} \tag{5.49}$$

The same normalization has been obtained by writing the discrete sum of the Poisson distribution as an integral (5.13), since both the discretization and steepest descent approximation are exact in the limit of large α. With the second derivative of Q,

$$H_{ij} = -\frac{\partial^2 Q}{\partial A_i \partial A_j} \Big|_{\boldsymbol{A}^*} = (K^{\mathrm{T}} C^{-1} K)_{ij} + \frac{\alpha}{A_i^*} \delta_{ij}, \tag{5.50}$$

the second integral reads [138]

$$Z_Q(\alpha) = |H|^{-1/2} \frac{(2\pi)^{N_\omega/2}}{\prod_i \sqrt{A_i^*}} e^{-\frac{1}{2}\chi^2(\boldsymbol{A}^*) + \alpha S(\boldsymbol{A}^*)}. \tag{5.51}$$

$\boldsymbol{A}^*$ is the spectrum that optimizes $Q = -\chi^2/2 + \alpha S$ for a given value of α.

In case of the positive-negative entropy $S^{\pm}$, the according measure $m^{\pm}(\boldsymbol{A})$ needs to be calculated. In Ref. [132], this is done by approximating the Skellam distribution. Here, the measure of $\boldsymbol{A}^+$ and $\boldsymbol{A}^-$ are used, as well as a steepest decent approximation. Since $\boldsymbol{A}^+$ and $\boldsymbol{A}^-$ are independent functions, one has to marginalize over both in order to obtain the correct probability distribution for α.

$$\begin{aligned} Z_Q &= \int \frac{\mathrm{d}^{N_\omega} A^+}{\prod_i \sqrt{A_i^+}} \frac{\mathrm{d}^{N_\omega} A^-}{\prod_j \sqrt{A_j^-}} e^{-\frac{1}{2}\chi^2 + \alpha S} \\ &= \int \frac{\mathrm{d}^{N_\omega} A \; \mathrm{d}^{N_\omega} B}{\prod_i \sqrt{B_i^2 - A_i^2}} e^{-\frac{1}{2}\chi^2 + \alpha S} \end{aligned} \tag{5.52}$$

First, the case that χ^2 only depends on $\boldsymbol{B} = \boldsymbol{A}^+ + \boldsymbol{A}^-$ is analyzed, which is used in this chapter to show the consistency of assuming two independent spectral functions that can be added or subtracted. For $S(\boldsymbol{A}, \boldsymbol{B})$ it has already been mentioned that the maximum is at $A_i^* = B_i \frac{D_i^+ - D_i^-}{D_i^+ + D_i^-}$ (Eq. (5.25)) and that $S^\pm(\boldsymbol{A}^*, \boldsymbol{B}) = S^+(\boldsymbol{B})$. The second derivative is

$$\frac{\partial^2 S(\boldsymbol{A}, \boldsymbol{B})}{\partial A_i \partial A_j} = -\frac{B_i}{B_i^2 - A_i^2} \delta_{ij} \tag{5.53}$$

Using the steepest decent approximation for the integral over A, one obtains therefore

$$Z_Q = \left(\frac{2\pi}{\alpha} \right)^{N_\omega/2} \int \frac{\mathrm{d}^{N_\omega} B}{\prod_i \sqrt{B_i}} \, e^{-\frac{1}{2}\chi^2(\boldsymbol{B}) + \alpha S^+(\boldsymbol{B})} \tag{5.54}$$

The integral has the same form as Z_Q for the ordinary entropy $S(\boldsymbol{B})$ (Eq. (5.45)), except for the prefactor, which cancels with Z_S. Therefore, assuming that the spectral function $\boldsymbol{B}$ is a sum of two independent spectral functions gives the same distribution $p(\alpha|\boldsymbol{G})$ as in the ordinary case, when $\boldsymbol{B}$ is just assumed to be a non-negative function, showing again the consistency of the splitting into two functions. If, on the other hand, a misfit χ^2 is assumed that only depends on $\boldsymbol{A} = \boldsymbol{A}^+ - \boldsymbol{A}^-$, the entropy is maximized for $B_i^* = \sqrt{A_i^2 + D_i^+ D_i^-}$ (Eq. (5.27)) and its second derivative is

$$\frac{\partial^2 S(\boldsymbol{A}, \boldsymbol{B})}{\partial B_i \partial B_j} = -\frac{A_i}{A_i^2 - B_i^2} \delta_{ij}, \tag{5.55}$$

so that the integral becomes in the steepest decent approximation

$$\begin{aligned} Z_Q &= \left(\frac{2\pi}{\alpha} \right)^{N_\omega/2} \int \frac{\mathrm{d}^{N_\omega} A}{\prod_i \sqrt{B_i^*}} \, e^{-\frac{1}{2}\chi^2(\boldsymbol{A}) + \alpha S(\boldsymbol{A}, \boldsymbol{B}^*)} \\ &= \left(\frac{2\pi}{\alpha} \right)^{N_\omega/2} \int \frac{\mathrm{d}^{N_\omega} A}{\prod_i \sqrt[4]{A_i^2 + 4 D_i^+ D_i^-}} \, e^{-\frac{1}{2}\chi^2(\boldsymbol{A}) + \alpha S^\pm(\boldsymbol{A})} \end{aligned} \tag{5.56}$$

The expression looks similar as the one for the sum $\boldsymbol{B}$, but with a different entropy $S^\pm$ instead of the ordinary entropy S, and with a different measure

$$m^\pm(\boldsymbol{A}) = \frac{1}{\prod_i \sqrt[4]{A_i^2 + 4 D_i^+ D_i^-}}. \tag{5.57}$$

Note that the metric tensor is again the second derivative of the entropy. In contrast to the ordinary metric, it does depend on the default models. For $D_i^- = 0$, which forces the spectral function to be non-negative at this frequency, the measure reduces to the ordinary measure. When the integral (5.56) is evaluated again in the steepest decent approximation, one obtains

$$Z_Q^{\pm}(\alpha) = |H^{\pm}|^{-1/2} \frac{(2\pi)^{N_\omega/2}}{\prod_i \sqrt[4]{A_i^{*2} + 4D_i^{+}D_i^{-}}} e^{-\frac{1}{2}\chi^2(\boldsymbol{A}^*) + \alpha S^{\pm}(\boldsymbol{A}^*)}, \tag{5.58}$$

with

$$H_{ij}^{\pm} = -\frac{\partial^2 Q^{\pm}}{\partial A_i \partial A_j}\bigg|_{\boldsymbol{A}^*} = (K^{\mathrm{T}} C^{-1} K)_{ij} + \frac{\alpha}{\sqrt{A_i^{*2} + 4D_i^{+}D_i^{-}}} \delta_{ij}, \tag{5.59}$$

and $\boldsymbol{A}^*$ maximizing $Q^{\pm} = -\chi^2/2 + \alpha S^{\pm}$ for a given value of α.

6 Interplay of spin-orbit coupling and strong correlations in multi-orbital systems

This chapter originates from a project with Jernej Mravlje, Markus Aichhorn, Gernot Kraberger, and the author, with the aim to understand the influence of spin-orbit coupling onto the correlation strength. The collaboration led to a publication, which is in preparation. In order to allow for a self-contained description, the whole paper is included here in its entirety.

Abstract

We investigate the influence of spin-orbit coupling λ in strongly-correlated multi-orbital systems that we describe by a three-orbital Hubbard-Kanamori model on a Bethe lattice. We solve the problem at all integer fillings N with the dynamical mean-field theory using the continuous-time hybridization expansion Monte Carlo solver. We investigate how the quasiparticle renormalization Z varies with the strength of spin-orbit coupling. For all fillings except $N = 2$, the behavior of Z on λ can be understood in terms of the atomic Hamiltonian (the atomic charge gap) and the spin-orbit induced changes of orbital degeneracies and polarizations in the j-basis. At $N = 2$, λ increases Z at small U but suppresses it at large U, thus eliminating the characteristic Hund's metal tail in $Z(U)$. We also compare the effects of the spin-orbit coupling to the effects of a tetragonal crystal field. Although this crystal field also lifts the orbital degeneracy, its effects are different, which can be understood in terms of the different form of the interaction Hamiltonian expressed in the respective diagonal single-particle bases.

6.1 Introduction

Strongly-correlated electronic systems with sizable spin-orbit coupling (SOC) are a subject of intense current interest. We stress a few aspects: (i) In the limit of strong interactions, the associated "spin" models are characterized by unusual exchange and are argued to lead to exotic phases such as spin-liquid ground states [17–23, 139–143]. (ii) The electronic structure of layered iridate Sr_2IrO_4, which features both SOC and sizeable electronic repulsion, is (at low energies) similar to the one of layered cuprates and is argued to lead to high-temperature superconductivity [24–26]. (iii) In Sr_2RuO_4, a compound in which the correlations are driven by the Hund's rule coupling, the SOC affects the Fermi surface [144, 145]. Furthermore, the SOC plays a key role in the ongoing discussion on the superconducting order parameter [146, 147]. (iv) Last, but not least, the development and improvement of multi-orbital dynamical mean-field theory (DMFT) techniques (also driven by the interest in multi-orbital compounds following the discovery of superconductivity in pnictides) has lead to a detailed and to a large extent even quantitative understanding of several correlated multi-orbital materials. Particular emphasis has been put to the importance of the Hund's rule coupling for electronic correlations [42, 148, 149]. A question, that is imminent in this respect, is how this picture is affected by the SOC.

Let us first summarize the key results for the three-orbital models without SOC. The overall behavior was in part understood in terms of the atomic criterion, comparing the atomic charge gap Δ_{at} to the kinetic energy. This criterion failed for occupancy $N = 2$, where the additional suppression of the coherence scale is important [42, 148, 149]. This suppression coincides with the slowing down of the spin fluctuations [150] and was explained from the perspective of the impurity model that is influenced by a reduction of the spin-spin Kondo coupling due to virtual fluctuations to a high-spin multiplet at half-filling [151–154]. The occurrence of strong correlations at $N = 2$ for moderate interactions was also interpreted (in the context of iron-based superconductors) as a consequence of the proximity to a half-filled (in our case $N = 3$) Mott insulating state [155–158], for which the critical interaction is very small due to the Hund's rule coupling. The compounds characterized by the behavior discussed above were dubbed Hund's metals.

In each case, the SOC modifies all aspects of this picture. First, the local Hamiltonian changes, and as a result also the atomic charge gap changes. Second, the SOC reduces the ground state degeneracy and hence the kinetic energy. Therefore, both the qualitative picture inferred from the atomic criterion, as well as quantitative results, can be expected to be strongly affected by the SOC.

In this work, we use multi-orbital DMFT to investigate the role of SOC in a three-orbital model with semicircular non-interacting density of states and Kanamori interactions. We are particularly interested in the electronic correlations, and aim to establish the key properties that control their strength, similarly to what has been achieved for the materials without SOC in earlier work. For this purpose, we calculate the quasiparticle residue Z and investigate its behavior as a function of interaction parameters and SOC for different electron occupancies. We find rich behavior where depending on the occupancy and the interaction strength the SOC increases or suppresses Z. Partly, this is understood in terms of the influence of the SOC on the atomic charge gap Δ_{at} and the associated critical Hubbard interaction for the metal to insulator transition [149]. In the Hund's metals regime, where the SOC leads to a disappearance of characteristic Hund's metal tail, this criterion fails. We interpret the behavior in terms of the suppression of the half-filled Mott insulating state in the phase diagram instead.

Earlier DMFT work investigated some aspects of the SOC, for instance different magnetic ground states at certain electron fillings [159–161]. Zhang *et al.* successfully applied DMFT to Sr_2RuO_4 and pointed out an increase of the effective SOC by correlations [144], discussed also in LDA+U [162] and slave-boson/Gutzwiller approaches [163, 164]. Kim *et al.* also investigated Sr_2RuO_4 and reconciled the Hund's metal picture with the presence of SOC in this compound [145, 165]. Finally, in an important work Kim *et al.* looked at the semicircular model, as in the present work, but did not systematically investigate the evolution of the quasiparticle residue [166].

This paper is structured as follows. In Sec. 6.2, we start by describing the model and methods. In Sec. 6.3 we give a qualitative discussion of the expected behavior in terms of the atomic problem. In Sec. 6.4 we show the results of the DMFT calculations, and put them into context of real materials. We end with our conclusions in Sec. 6.5.

6.2 Model and method

We consider a three-orbital problem with the (non-interacting) semicircular density of states $\rho(\epsilon) = \frac{2}{\pi D^2}\sqrt{D^2 - \epsilon^2}$. We use the half-bandwidth D as the energy unit. The atomic interaction is described in terms of the Kanamori Hamiltonian,

$$\begin{aligned} H_{\mathrm{I}} = &\sum_i U n_{i\uparrow} n_{i\downarrow} + U' \sum_{i \neq j} n_{i\uparrow} n_{j\downarrow} + (U' - J_{\mathrm{H}}) \sum_{i<j,\sigma} n_{i\sigma} n_{j\sigma} \\ &+ J_{\mathrm{H}} \sum_{i \neq j} c^\dagger_{i\uparrow} c^\dagger_{j\downarrow} c_{i\downarrow} c_{j\uparrow} + J_{\mathrm{H}} \sum_{i \neq j} c^\dagger_{i\uparrow} c^\dagger_{i\downarrow} c_{j\downarrow} c_{j\uparrow}, \end{aligned} \tag{6.1}$$

where $c^\dagger_{i\sigma}$ creates an electron in orbital i with spin σ. We set $U' = U - 2J_{\mathrm{H}}$ to make the Hamiltonian rotationally invariant in orbital space. One can express H_{I} in terms of the total number of electrons $N = \sum_{i\sigma} n_{i\sigma}$, the total spin $\boldsymbol{S} = \frac{1}{2}\sum_i \sum_{\sigma\sigma'} c^\dagger_{i\sigma} \boldsymbol{\tau}_{\sigma\sigma'} c_{i\sigma'}$, where $\boldsymbol{\tau}$ is the vector of Pauli matrices, and the total orbital isospin $\boldsymbol{L}$ with components $L_i = \mathrm{i} \sum_{jk\sigma} \epsilon_{ijk} c^\dagger_{j\sigma} c_{k\sigma}$,

$$H_{\mathrm{I}} = (U - 3J_{\mathrm{H}}) \frac{N(N-1)}{2} + \frac{5}{2} J_{\mathrm{H}} N - 2J_{\mathrm{H}} \boldsymbol{S}^2 - \frac{J_{\mathrm{H}}}{2} \boldsymbol{L}^2. \tag{6.2}$$

The first two Hund's rules are manifest in this form. The effects of spin-orbit coupling are, in general, described by the one-particle operator $H_\lambda = \lambda\, \boldsymbol{l} \cdot \boldsymbol{s} = \sum_i l_i \otimes s_i$, where $\boldsymbol{l}$ and $\boldsymbol{s}$ are the orbital angular momentum and the spin of the respective electron. Our three-orbital model is motivated by cases where the e_g-t_{2g} crystal-field splitting within the d-manifold of a material is strong. Therefore, one retains only the three t_{2g} orbitals. The matrix representations of the $l = 2$ operators l_x, l_y, and l_z in the cubic basis within the t_{2g} subspace are up to a sign equal to the ones for the $l = 1$ operators in cubic basis, which is called TP-correspondence [40, 167]. Therefore, the SOC operator reads

$$H_\lambda = \lambda\, \boldsymbol{l}_{t_{2g}} \cdot \boldsymbol{s} = -\lambda\, \boldsymbol{l}_p \cdot \boldsymbol{s} = -\lambda/2(\boldsymbol{j}^2_{\mathrm{eff}} - \boldsymbol{l}^2_p - \boldsymbol{s}^2), \tag{6.3}$$

where $\boldsymbol{l}_p$ are generators of the $l = 1$ orbital angular momentum and $\boldsymbol{j}_{\mathrm{eff}}$ is the effective total one-particle angular momentum $\boldsymbol{j}_{\mathrm{eff}} = \boldsymbol{l}_p + \boldsymbol{s}$. In order to keep the notation light, we will drop the index "eff" in the following, and denote the total angular momentum by $\boldsymbol{j}$. With the eigenvalues $l_p = 1$ and $s = 1/2$ ($\hbar = 1$), j can be $1/2$ or $3/2$ and $m_j = -j, -j+1, \ldots, +j$. The eigenvalues of H_λ are thus $-\lambda/2$ for $j = 3/2$ and λ for $j = 1/2$, leading to a spin-orbit splitting of $\frac{3}{2}\lambda$. Note that in contrast to p orbitals, the

$j = 3/2$ band is lower in energy because of the minus sign in the TP-correspondence. Therefore, the non-interacting electronic structure consists of four degenerate $j = 3/2$ bands and two degenerate $j = 1/2$ bands, the latter higher in energy.

The full problem is solved by the DMFT [3, 5] method, where the Hamiltonian is mapped self-consistently to an Anderson impurity model, assuming a local self-energy Σ. This impurity problem is solved by the continuous-time quantum Monte Carlo hybridization expansion method [68]. We performed the calculations using the TRIQS package [168, 169]. In the j-basis, which is defined to diagonalize the local Hamiltonian H_λ, also the hybridization is diagonal, hence one can use real-valued imaginary-time Green's functions for the calculations. This is convenient because it reduces the fermionic sign problem and makes the calculations feasible [159, 166]. However, the sign problem still remains a limiting factor for large Hund's couplings and small temperatures. All results reported in this paper were calculated at an inverse temperature $\beta D = 80$.

All calculations are done in the paramagnetic state, as we focus on the effect of the SOC in the correlated metallic regime. Note that different kinds of insulating states occur because antiferromagnetic and excitonic order parameters do not vanish in some parameter regimes [22, 160, 170–172].

6.3 Crystal field analogy and the atomic problem

In the j-basis, the non-interacting density of states consist of two semicircular parts split by $\frac{3}{2}\lambda$, where the $j = 3/2$ part is four-fold, the $j = 1/2$ part two-fold degenerate. Such a density of states also arises in the case of a tetragonal crystal field, but, obviously, the eigenstates differ in the two situations; the SOC and tetragonal crystal field cannot be simultaneously diagonalized.

It is instructive to rewrite the Kanamori Hamiltonian to the j-basis,

$$H_\mathrm{I} = \sum_{ijkl} U_{ijkl} c_i^\dagger c_j^\dagger c_l c_k = \sum_{\alpha\beta\gamma\delta} \tilde{U}_{\alpha\beta\gamma\delta} d_\alpha^\dagger d_\beta^\dagger d_\delta d_\gamma \tag{6.4}$$

with

$$\tilde{U}_{\alpha\beta\gamma\delta} = \sum_{ijkl} U_{ijkl} A_{\alpha i}^* A_{\beta j}^* A_{k\gamma} A_{l\delta}, \tag{6.5}$$

where A is the unitary transformation between the cubic t_{2g} and the j-basis [173]. The Latin indices are combined indices of orbital and spin, the Greek indices are combined indices of j and m_j. As the Kanamori Hamiltonian is invariant under this transformation for $J_\mathrm{H} = 0$ (seen easily from Eq. (6.2)), the result of the crystal-field splitting and the SOC is identical in this case.

On the other hand, for a finite Hund's coupling the crystal field and SOC lead to different results. The transformed Hamiltonian in j-basis differs from its form in cubic basis (6.1). We can split it into a pure $j = 1/2$ part, a pure $j = 3/2$ part, and a part that mixes the $j = 1/2$ and $j = 3/2$ parts,

$$H_\mathrm{I} = H_{j=\frac{1}{2}} + H_{j=\frac{3}{2}} + H_\mathrm{mix}. \tag{6.6}$$

The first two terms read

$$H_{j=\frac{1}{2}} = \left(U - \frac{4}{3}J_{\mathrm{H}}\right) n_{\frac{1}{2},\frac{1}{2}} n_{\frac{1}{2},-\frac{1}{2}}, \tag{6.7}$$

$$\begin{aligned} H_{j=\frac{3}{2}} = {} & (U - J_{\mathrm{H}}) \left(n_{\frac{3}{2},\frac{3}{2}} n_{\frac{3}{2},-\frac{3}{2}} + n_{\frac{3}{2},\frac{1}{2}} n_{\frac{3}{2},-\frac{1}{2}}\right) \\ & + \left(U - \frac{7}{3}J_{\mathrm{H}}\right) \left(n_{\frac{3}{2},-\frac{3}{2}} n_{\frac{3}{2},-\frac{1}{2}} + n_{\frac{3}{2},\frac{3}{2}} n_{\frac{3}{2},\frac{1}{2}}\right) \\ & + \left(U - \frac{7}{3}J_{\mathrm{H}}\right) \left(n_{\frac{3}{2},-\frac{3}{2}} n_{\frac{3}{2},\frac{1}{2}} + n_{\frac{3}{2},\frac{3}{2}} n_{\frac{3}{2},-\frac{1}{2}}\right) \\ & + \frac{4}{3}J_{\mathrm{H}} \left(d^{\dagger}_{\frac{3}{2},-\frac{3}{2}} d^{\dagger}_{\frac{3}{2},\frac{3}{2}} d_{\frac{3}{2},-\frac{1}{2}} d_{\frac{3}{2},\frac{1}{2}} + d^{\dagger}_{\frac{3}{2},-\frac{1}{2}} d^{\dagger}_{\frac{3}{2},\frac{1}{2}} d_{\frac{3}{2},-\frac{3}{2}} d_{\frac{3}{2},\frac{3}{2}}\right), \end{aligned} \tag{6.8}$$

the density-density part of H_{mix} is

$$\begin{aligned} H_{\text{mix, dd}} = {} & \left(U - \frac{5}{3}J_{\mathrm{H}}\right) \left(n_{\frac{1}{2},\frac{1}{2}} n_{\frac{3}{2},\frac{3}{2}} + n_{\frac{1}{2},-\frac{1}{2}} n_{\frac{3}{2},-\frac{3}{2}}\right) \\ & + (U - 2J_{\mathrm{H}}) \left(n_{\frac{1}{2},\frac{1}{2}} n_{\frac{3}{2},\frac{1}{2}} + n_{\frac{1}{2},-\frac{1}{2}} n_{\frac{3}{2},-\frac{1}{2}}\right) \\ & + \left(U - \frac{7}{3}J_{\mathrm{H}}\right) \left(n_{\frac{1}{2},\frac{1}{2}} n_{\frac{3}{2},-\frac{1}{2}} + n_{\frac{1}{2},-\frac{1}{2}} n_{\frac{3}{2},\frac{1}{2}}\right) \\ & + \left(U - \frac{8}{3}J_{\mathrm{H}}\right) \left(n_{\frac{1}{2},\frac{1}{2}} n_{\frac{3}{2},-\frac{3}{2}} + n_{\frac{1}{2},-\frac{1}{2}} n_{\frac{3}{2},\frac{3}{2}}\right). \end{aligned}$$

H_{mix} contains 30 more terms that are not shown here. The convention is that $n_{\frac{1}{2},\frac{1}{2}}$, for example, means $n_{j=\frac{1}{2},m_j=\frac{1}{2}}$. $H_{j=\frac{1}{2}}$ is a one-band Hubbard Hamiltonian with an effective interaction $U_{\mathrm{eff}} = U - 4/3\,J_{\mathrm{H}}$. For the density-density part of $H_{j=\frac{3}{2}}$, one observes that the terms with the same $|m_j|$'s have prefactors $U - J_{\mathrm{H}}$, terms with different $|m_j|$'s have prefactor $U - 7/3J_{\mathrm{H}}$. If one uses $|m_j|$ as the orbital index and the sign of m_j as the spin, the density-density part of this Hamiltonian is similar to the density-density part of a two-band Kanamori Hamiltonian, but with different prefactors. Importantly, there is only one kind of prefactor for inter-orbital interactions, namely $U - 7/3J_{\mathrm{H}}$, instead of $U - 2J$ and $U - 3J$ in Eq. (6.1). This influences the electronic correlations, as we will see below in the case of $N = 2$. Following this interpretation of the m_j's, the last two terms are pair-hopping like expressions with an effective strength of $4/3\,J_{\mathrm{H}}$. A detailed analysis of this Hamiltonian can be found in Sec. 6.6.

The atomic Hamiltonian $H_{\mathrm{loc}} = H_{\mathrm{I}} + H_{\lambda}$ can be used to estimate the correlation strength by calculating the atomic charge gap

$$\Delta_{\mathrm{at}} = E_0(N+1) + E_0(N-1) - 2E_0(N), \tag{6.9}$$

where $E_0(N)$ is the ground state of a system with N electrons [42]. According to the Mott-Hubbard criterion, the metal-insulator transition takes place at a critical Hubbard interaction $U = U_{\mathrm{c}}$ when the charge gap equals the kinetic energy.

Table 6.1: Comparison of the atomic charge gap Δ_{at} obtained from a spin-orbit coupling λ or a tetragonal crystal-field splitting Δ_{cf} in the limit $\lambda, \Delta_{\mathrm{cf}} \ll J_{\mathrm{H}}$.

N	SOC	crystal field
1	$U - 3J_{\mathrm{H}} + 1/2\,\lambda$	$U - 3J_{\mathrm{H}}$
2	$U - 3J_{\mathrm{H}} + 1/2\,\lambda$	$U - 3J_{\mathrm{H}} + 3/2\,\Delta_{\mathrm{cf}}$
3	$U + 2J_{\mathrm{H}} - 3/2\,\lambda$	$U + 2J_{\mathrm{H}} - 3/2\,\Delta_{\mathrm{cf}}$
4	$U - 3J_{\mathrm{H}} + \lambda$	$U - 3J_{\mathrm{H}}$
5	$U - 3J_{\mathrm{H}} + \lambda$	$U - 3J_{\mathrm{H}} + 3/2\,\Delta_{\mathrm{cf}}$

Table 6.2: Comparison of the atomic charge gap Δ_{at} obtained from a spin-orbit coupling λ or a tetragonal crystal-field splitting Δ_{cf} in the limit $\lambda, \Delta_{\mathrm{cf}} \gg J_{\mathrm{H}}$.

N	SOC	crystal field
1	$U - 7/3\,J_{\mathrm{H}}$	$U - 3J_{\mathrm{H}}$
2	$U - J_{\mathrm{H}}$	$U + J_{\mathrm{H}}$
3	$U - 7/3\,J_{\mathrm{H}}$	$U - 3J_{\mathrm{H}}$
4	$U - 3J_{\mathrm{H}} + 3/2\,\lambda$	$U - 5J_{\mathrm{H}} + 3/2\,\Delta_{\mathrm{cf}}$
5	$U - 4/3\,J_{\mathrm{H}}$	U

The ground state energies and the atomic charge gaps for a Kanamori Hamiltonian with spin-orbit coupling have been already analyzed in the supplementary material of Ref. [166]. Here, we briefly recapitulate certain limits and compare them to the case of a tetragonal crystal field splitting. The SOC lowers the energy of the $j = 3/2$ bands by $\lambda/2$ and increases the energy of the $j = 1/2$ orbitals by λ. Therefore, the crystal-field splitting parameter Δ_{cf} is chosen such that it increases the on-site energy of one orbital by Δ_{cf}, and that it lowers the energy of the other two by $\Delta_{\mathrm{cf}}/2$ in accordance with the effect of λ. Physically, this crystal field corresponds to a tetragonal tensile distortion in z direction. Both λ and Δ_{cf} are supposed to be positive; a negative sign would correspond to a particle-hole transformation.

We start with a discussion of the crystal-field splitting [174–177]. For fillings $N = 1$, 2, and 5, the ground state does not change with the crystal-field splitting. For $N = 3$ and $N = 4$, there is a level crossing with a transition from a high-spin to a low-spin state (e.g., from $|\uparrow, \uparrow, \uparrow\rangle$ to $|\uparrow\downarrow, \uparrow, 0\rangle$), which is responsible for differences in the atomic charge gap for small and large Δ_{cf}. The respective values for the charge gap in the limits of small and large Δ_{cf} are listed in tables 6.1 and 6.2. Note that in the large Δ_{cf} limit, the relevant Hamiltonian is a two-orbital one for fillings $N = 1, 2$, and 3, and a one-orbital one for $N = 5$. For the Kanamori Hamiltonian with ν orbitals, the charge gap depends on the relative filling; at half-filling it is $\Delta_{\mathrm{at}} = U + (\nu - 1)J_{\mathrm{H}}$, otherwise $U - 3J_{\mathrm{H}}$. The filling $N = 4$ is special as an electron can only be added by paying additionally crystal-field splitting energy.

We now turn to the discussion of SOC. Note that the limits $\lambda \ll J_{\mathrm{H}}$ and $\lambda \gg J_{\mathrm{H}}$ correspond to the LS and jj coupling scheme, respectively. A look at tables 6.1, 6.2 reveals that practically all entries are different from the corresponding crystal-field ones. The values for a large SOC can be obtained from the Hamiltonian expressed in the j-basis discussed above. For $N = 5$, where the effective model is a single-orbital model, the interaction parameter is $U - \frac{4}{3}J_{\mathrm{H}}$, as seen from Eq. (6.7), in contrast to the crystal field result, where one obtains simply U. In case of $N = 2$, it is interesting to note that the dependence of the charge gap on J_{H} is different in sign for SOC and crystal field. This follows from Eq. (6.8), which does not favor the alignment of the angular momenta j_z of the respective orbitals (see also Sec. 6.6) . This opposite behavior is also reflected in the full DMFT solution, as we discuss below. We will see that for $N = 2$, there are parameter regimes, where the correlation strength increases with crystal-field splitting, but decreases with SOC.

6.4 DMFT results

We now turn to the DMFT results. We focus on the interplay between the SOC and electronic correlations, which we follow by calculating the Matsubara self-energies. Due to the symmetry, the Green's functions and the self-energies are diagonal in the j-basis with two independent components $\Sigma_{1/2}$ and $\Sigma_{3/2}$.

Fig. 6.1 displays the calculated self-energies for the case of one electron. One can see that due to the SOC $|\mathrm{Im}\Sigma_{3/2}|$ is larger and its slope at low energies that determines the quasiparticle residue

$$Z_\nu = \lim_{\mathrm{i}\omega_n \to 0} \left[1 - \frac{\partial \mathrm{Im}\Sigma_\nu(\mathrm{i}\omega_n)}{\partial \mathrm{i}\omega_n} \right]^{-1}. \tag{6.10}$$

is larger. The origin of that is discussed below, where we investigate the evolution of Z_ν with λ for all integer occupancies, but let us first discuss the other part of the interplay, namely the influence of the electronic correlations on the SOC.

6.4.1 Influence of electronic correlations on the SOC

For this purpose it is convenient to introduce the average self-energy

$$\Sigma_{\mathrm{a}} = \frac{2}{3}\Sigma_{\frac{3}{2}} + \frac{1}{3}\Sigma_{\frac{1}{2}} \tag{6.11}$$

and the difference

$$\Sigma_{\mathrm{d}} = \Sigma_{\frac{1}{2}} - \Sigma_{\frac{3}{2}}. \tag{6.12}$$

In terms of $\Sigma_{\mathrm{a,d}}$ the self-energy matrix can be written in the form

$$\Sigma = \Sigma_{\mathrm{a}}\mathbb{1} + \frac{2}{3}\Sigma_{\mathrm{d}}\boldsymbol{l} \cdot \boldsymbol{s}, \tag{6.13}$$

which holds in any basis (see Sec. 6.7). This form is also convenient as one can directly see that Σ_d determines the influence of electronic correlations on the physics of SOC. In particular, the real part $\mathrm{Re}\Sigma_\mathrm{d}(\omega)$ can be used to define the effective spin-orbit constant

$$\lambda_\mathrm{eff}(\omega) = \lambda + \frac{2}{3}\,\Sigma_\mathrm{d}(\omega). \tag{6.14}$$

For all cases we looked at, we find that the real part of $\Sigma_\mathrm{d}(\mathrm{i}\omega_n)$ is positive for all ω_n as long as both orbitals are metallic, thus correlations always increase the SOC. This is discussed further in Sec. 6.7.

6.4.2 Influence of SOC on electronic correlations: One and five electrons

In the remainder of the paper we investigate how the SOC influences the electronic correlations, which is followed by calculating the j-orbital occupations and the quasiparticle residues Z_ν. These are calculated by fitting six lowest frequency points of Matsubara self-energies to a 4th order polynomial.

Without SOC, one electron and one hole (five electrons) in the system are equivalent due to the particle-hole symmetry, but the SOC breaks this symmetry. For large λ, only the $j = 3/2$ ($j = 1/2$) orbitals are partially occupied for $N = 1$ ($N = 5$). Hence, these are more interesting regarding electronic correlations. In Fig. 6.2, we show how the fillings and the quasiparticle weights of these orbitals change when the SOC is increased. Furthermore, the atomic charge gap is plotted.

The change in orbital polarization influences the correlation strength. This is best seen for $J_\mathrm{H} = 0$, since then the effective repulsion is simply U, independent of the SOC. The quasiparticle weight of the relevant orbitals is reduced by the SOC as the polarization increases, which is shown in Fig. 6.2 for $U = 3$ (circles). The reduction is weak for $N = 1$ but strong for $N = 5$, which is due to the lower kinetic energy of one hole in one $j = 1/2$ orbital compared to the energy of one electron in two $j = 3/2$ orbitals. In the case of $U = 3$ and $J_\mathrm{H} = 0$ displayed in Fig. 6.2, even a metal-insulator transition takes place.

The Hund's coupling reduces the correlation strength (stars, crosses). This happens for two reasons: J_H reduces the polarization, and it decreases the atomic charge gap. The latter is expected for $N = 1$, where the effective number of orbitals reduces with increasing λ from three to two. In this case, a finite exchange interaction J_H leads to a reduction of the repulsion between electrons in different orbitals.

Interestingly, J_H also decreases the strength of correlations for $N = 5$ in the limit of large λ, altough the effective number of orbitals is one and inter-orbital effects are thus suppressed. However, the transformation from the cubic Kanamori Hamiltonian to its j-basis equivalent mixes inter- and intra-orbital interactions, so that the effective $j = 1/2$ interaction strength is $U - 4/3\,J_\mathrm{H}$, as explained in Sec. 6.3. In contrast, in case of a large tetragonal crystal-field splitting, the atomic charge gap is indeed simply given by U for $N = 5$.

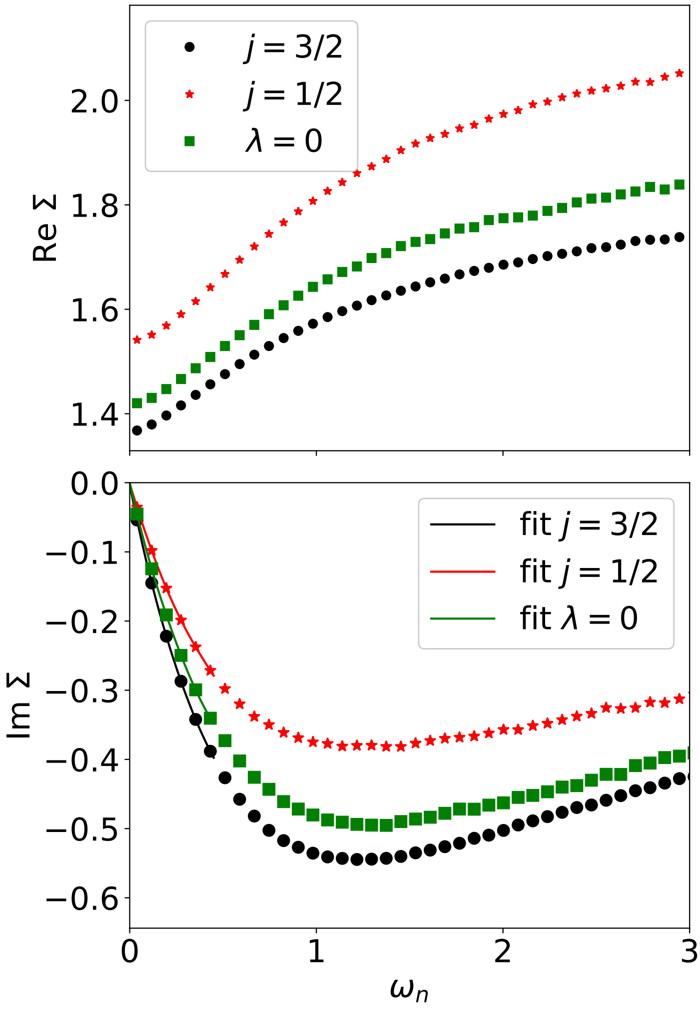

Figure 6.1: Real (top) and imaginary (bottom) part of the self-energy for the parameters $N = 1$, $\lambda = 0.1$, $U = 3$, and $J_{\mathrm{H}} = 0.1\,U$. The green squares display the results without SOC for comparison. The lines show a polynomial fit of degree four through the first six Matsubara frequencies.

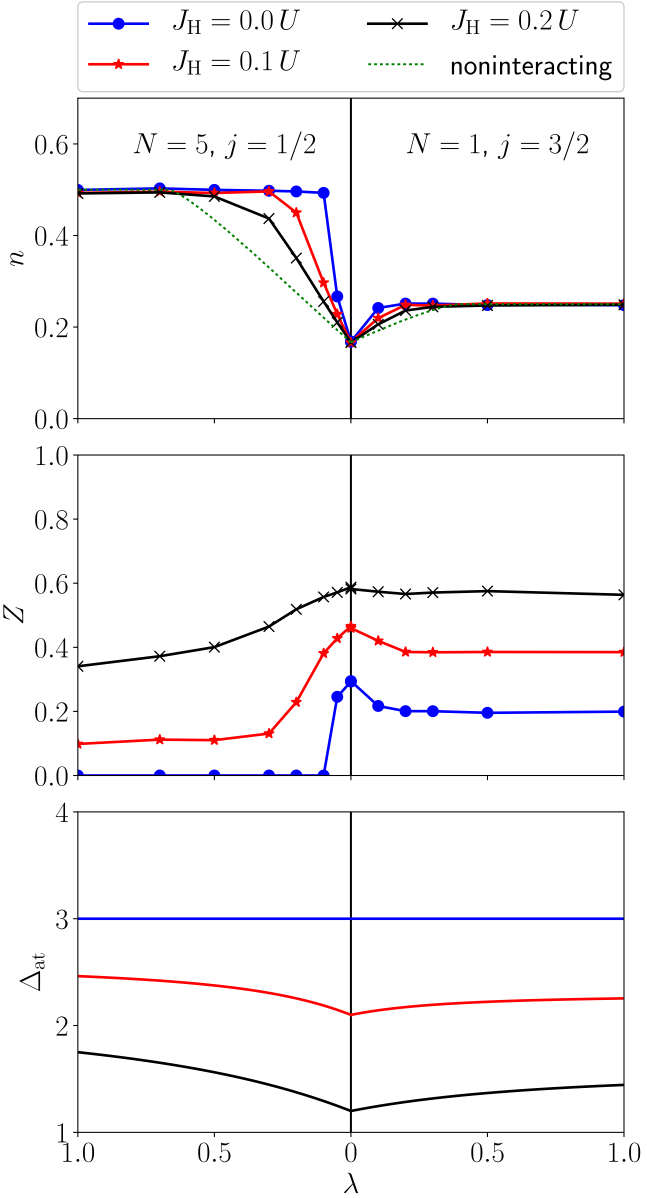

Figure 6.2: Influence of the spin-orbit coupling for a filling of $N = 1$ (right column) and $N = 5$ (left column) for $U = 3$. The top panel shows for $N = 1$ the electron density of the $j = 3/2$ orbital, for $N = 5$ the hole density of the $j = 1/2$ orbital to allow for a better comparability. The green dotted line displays the repective noninteracing results. The middle panel shows the quasi-particle weight Z of the respective orbitals, and the bottom panel the atomic charge gap Δ_{at}.

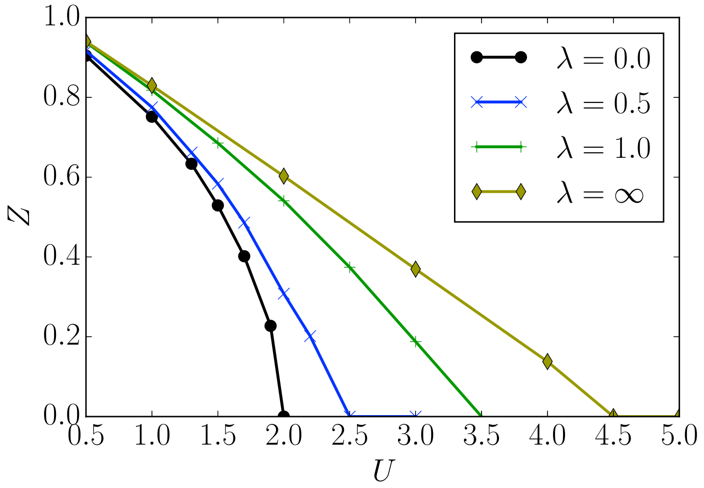

Figure 6.3: Quasiparticle weight Z of the $j = 3/2$ orbital as a function of U for $J_\mathrm{H} = 0.1\,U$ and a total filling of $N = 3$.

6.4.3 Half filling

In Fig. 6.3 we display the quasiparticle weight of the $j = 3/2$ orbitals (again, the $j = 1/2$ are emptied out with SOC and are therefore not discussed here) at $N = 3$ for several λ. One can see that λ strongly increases U_c and changes the behavior drastically. To understand why this occurs, first recall that at $\lambda = 0$, Hund's coupling strongly reduces the kinetic energy since it enforces the high-spin ground state [148]. Hence, the Hund's coupling leads to a drastic reduction of the critical interaction strength [149]. This causes a steep descent of Z as a function of U when the critical U is approached (see Fig. 6.3 for $\lambda = 0$ and $J_\mathrm{H} = 0.1U$).

As λ is large, this physics does not apply any more. The filling of the $j = 3/2$ orbitals increase to three electrons in two orbitals. Since the Hamiltonian of the $j = 3/2$ orbitals alone is particle-hole symmetric, this large λ limit shows identical physics to the large λ limit in case of $N = 1$. As described above in section 6.4.2, this $\lambda \to \infty$ system is characterized by an increase of Z with increasing J_H. This is opposite to the half-filled $N = 3$ case at $\lambda = 0$, where Z decreases with J_H.

In Fig. 6.4, we show how the polarization, the quasiparticle weight, and the atomic charge gap vary with λ. We find that Z increases for physically relevant Hund's couplings (e.g., $J_\mathrm{H} = 0.1U$, $J_\mathrm{H} = 0.2U$). Furthermore, the qualitative difference of the small and large λ limits discussed above results in crossings of the $Z(\lambda)$ curves for different Hund's couplings (see middle panel of Fig. 6.4). These crossings are already expected from the atomic charge gap, which is $U + 2J_\mathrm{H}$ for $\lambda = 0$ and drops to $U - 7/3J_\mathrm{H}$ for $\lambda \to \infty$, as shown in the tables 6.1 and 6.2 as well as in the lower panel of Fig. 6.4.

The results in Fig. 6.4 show SOC can strongly modify the correlation strength. One needs to notice, though, that these changes occur over a quite large range of λ, for

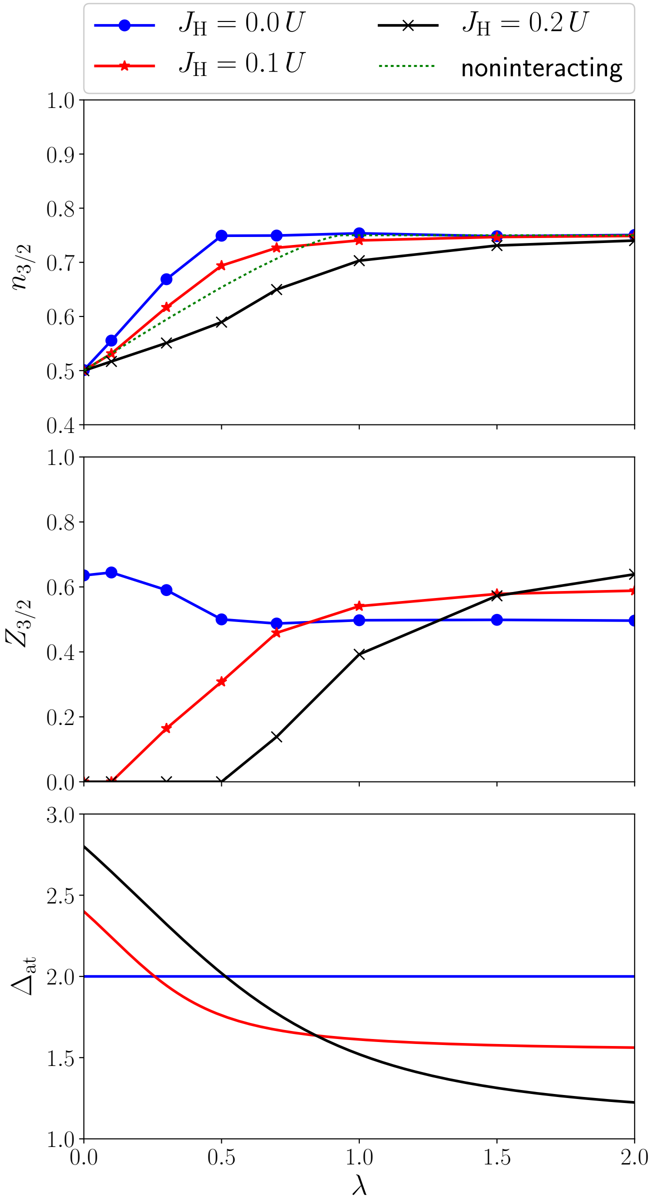

Figure 6.4: Filling of the $j = 3/2$ orbital, quasi-particle weight of the electrons in this orbital, and the atomic charge gap as a function of spin-orbit coupling λ for $N = 3$ and $U = 2$.

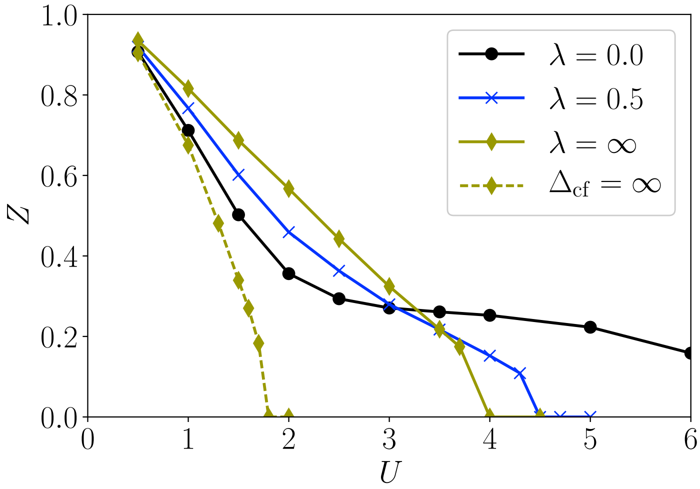

Figure 6.5: Quasiparticle weight Z of the $j = 3/2$ orbital as a function of U for $J_{\mathrm{H}} = 0.2\,U$ and $N = 2$. The dashed line shows the corresponding Z of the d_{xz} orbital in case of an infinite tetragonal crystal field splitting.

instance, full polarization is reached at $\lambda \approx 1$, whereas it occurs at $\lambda \approx 0.3$ in the case of $N = 1$ and $U = 3$ (compare Fig. 6.4 with Fig. 6.2).

6.4.4 Two electrons

We now discuss the interesting case of two electrons. In absence of SOC, this is the case of a Hund's metal. Fig. 6.5 shows the dependence of Z on U for several values of λ and $J_{\mathrm{H}}/U = 0.2$. The data at small λ exhibit a tail with small Z, which is characteristic for the Hund's metal regime. The SOC has a drastic effect here; increasing λ suppresses the Hund's metal behavior and leads to a featureless, almost linear, approach of Z towards 0 with increasing U. Interestingly, the influence of λ on Z is opposite at small U where increasing λ increases Z, thus making the system less correlated, and at a high U, where Z diminishes with λ and hence correlations become stronger.

The latter behavior is easy to understand. A strong SOC reduces the number of relevant orbitals from three to two, and leads to the increase of the atomic charge gap from $U - 3J_{\mathrm{H}}$ to $U - J_{\mathrm{H}}$ (see Fig. 6.7 and Sec. 6.3). Both the reduction of the kinetic energy due to the reduced degeneracy and the increase of the atomic charge gap with λ contribute to a smaller critical U, which is indeed seen on the plot. We want to note here that the reduction of the critical U is even stronger for the crystal-field case (shown as a dashed line in the figure), since there the corresponding atomic gap is larger ($U + J_{\mathrm{H}}$, see Sec. 6.3).

We turn now to the small-U regime where the SOC reduces the electronic correlations. One can rationalize this from a scenario that pictures Hund's metals as doped Mott insulators at half filling [155–158]. Fig. 6.6 presents the values of U where a Mott

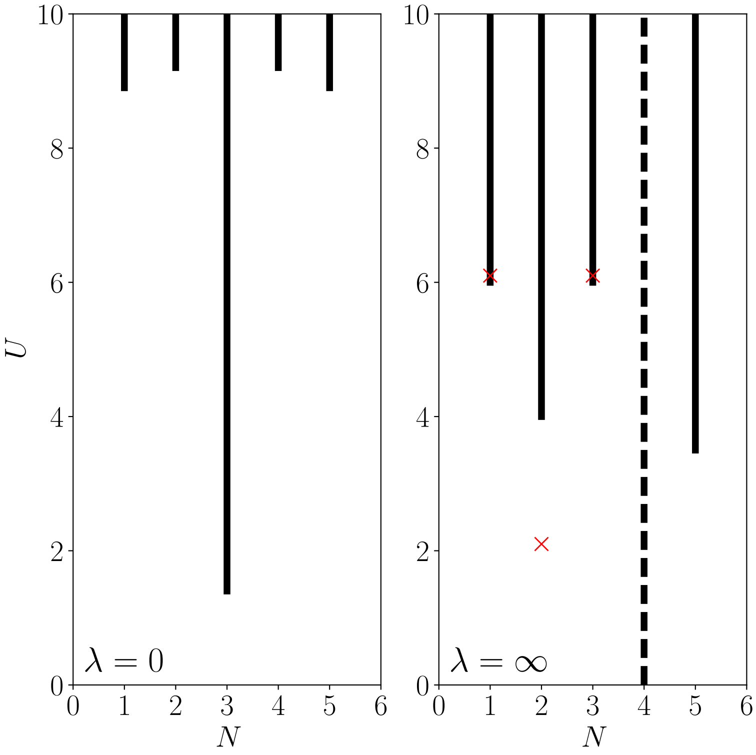

Figure 6.6: The Mott insulator occurs for values of U indicated by bars for a Hund's coupling of $J_{\mathrm{H}} = 0.2U$. The left picture shows the case without SOC, the right with an infinite SOC. Note that in the latter case no Mott insulator occurs for $N = 4$ since this case is a band insulator. The critical values for $\lambda = 0$ are taken from Ref. [149]. The red crosses indicate the critical U in case a tetragonal crystal field is applied instead of the SOC. For $N = 2$, the value can also be extracted from Fig. 6.5.

insulator occurs. In this picture, the correlations for small interactions at $N = 2$ are due to proximity to a half-filled insulating state. For interaction parameters U and J_H that lead to a Mott insulator at half filling, doping with holes leads to a metallic state with low quasiparticle weight. This low-Z region lasts to doping concentrations of more than one hole per atom, as can be seen from Fig. 2 in Ref. [149]. As a result, for an interaction U in between the critical values for two and three electrons $U_\mathrm{c}(N = 2) < U < U_\mathrm{c}(N = 3)$, the quasiparticle weight is small, but not zero. As one increases λ, the critical U at $N = 3$ increases strongly, and the insulating state appears only for large values of U. Consequently, the $N = 2$ state cannot be viewed as a doped $N = 3$ Mott insulator any more. In fact, for a large SOC, the critical interaction strength U_c for a Hund's coupling of $J_\mathrm{H}/U = 0.2$ is lowest for $N = 2$, as displayed in Fig. 6.6. As a consequence, the Hund's tail disappears, as highlighted in Fig. 6.5, and the quasiparticle weight increases with SOC in case of a small U and large Hund's couplings (see middle panel of Fig. 6.7). In passing we note that the DMFT self-consistency is essential to account for the increase of Z in the small U regime. Calculations for an impurity model found a suppression of the Kondo temperature (and hence suppression of Z) with increased λ [165], which is different from what we find in the DMFT results here.

In Fig. 6.7, we also compare the SOC to a tetragonal crystal field. One sees that the crystal field always increases the correlation strength. To understand this it is convenient to recall that atomic gaps are different, and as a result, also the critical U's are different. For an infinite crystal field, they are marked with crosses in Fig. 6.6. In particular, the critical interaction at $N = 2$ in case of an infinite crystal field is only slightly larger than the critical interaction at $N = 3$ without any splitting. Therefore, Hund's metals with interactions in the range $U_\mathrm{c}(N = 2) < U < U_\mathrm{c}(N = 3)$ become insulating as Δ_cf increases, in contrast to the SOC case. Another difference is the ground state degeneracy, which is three for the $S = 1$ ground state of the two-orbital Kanamori and five in case of the $J = 2$ ground state of $H_{j=3/2}$, see Sec. 6.6, which also points to a weaker correlations in the SOC case.

Another interesting observation from Fig. 6.7 is that the quasiparticle weight is almost independent of Hund's coupling in the limit of large λ for $U = 2$. In Fig. 6.8, we show that the weak dependence on J_H is also apparent for other values of U, and only becomes significant when the Hund's coupling is exceeding $J_\mathrm{H} > 0.2U$. However, since the atomic gap does depend on J_H, the position of the Hubbard bands are different, even though Z is the same, as shown in the inset of Fig. 6.8.

6.4.5 Four electrons

The filling of four electrons is special because strong SOC leads to a band insulator with fully occupied $j = 3/2$ orbitals and empty $j = 1/2$ orbitals, with no renormalization $Z = 1$ for both orbitals in the large λ regime.

The second panel of Fig. 6.9 shows the quasiparticle renormalization of both orbitals in the metallic phase as a function of λ. One can see that $Z_{3/2}$ is hardly affected, and $Z_{1/2}$ increases only slightly for the given parameters $U = 2$ and $J_\mathrm{H} = 0.2U$, indicating that the orbital polarization has only a weak influence onto the correlation strength,

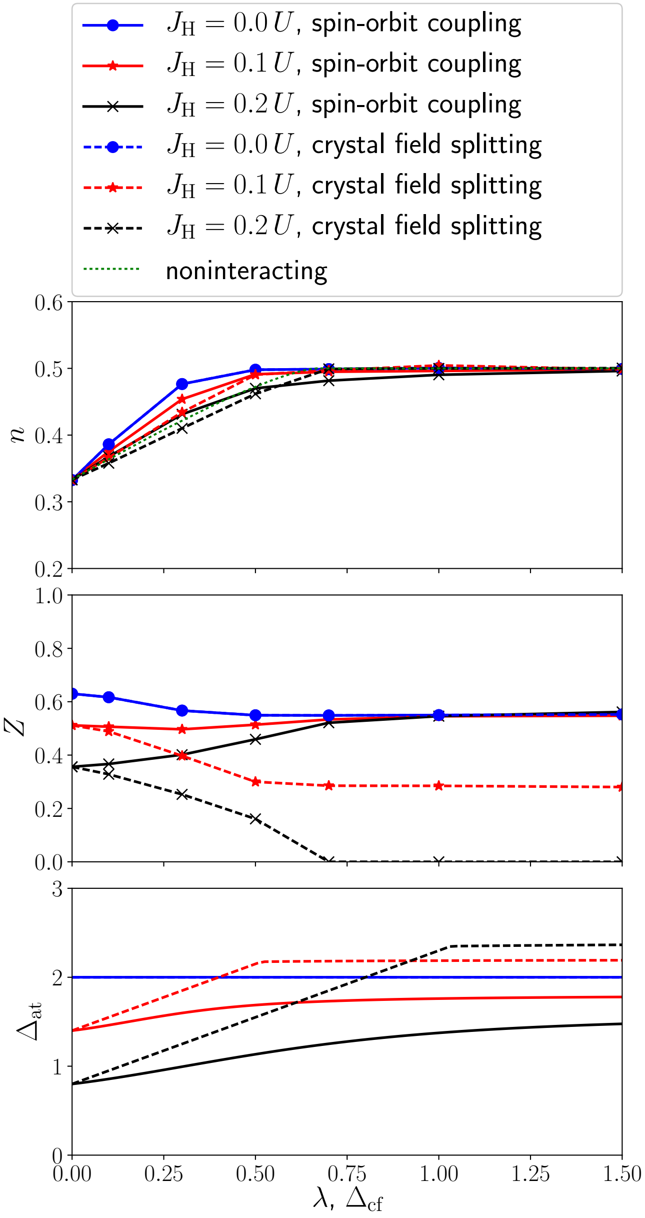

Figure 6.7: Filling of the orbitals, quasi-particle weight of the electrons in this orbital, and the atomic charge gap for $N = 2$ and $U = 2$. Solid lines correspond to the SOC case, and $j = 3/2$ quantities are plotted as function of λ. Dashed lines are results for crystal-field splitting, where we plot $d_{xz/yz}$ quantities as function of Δ_cf.

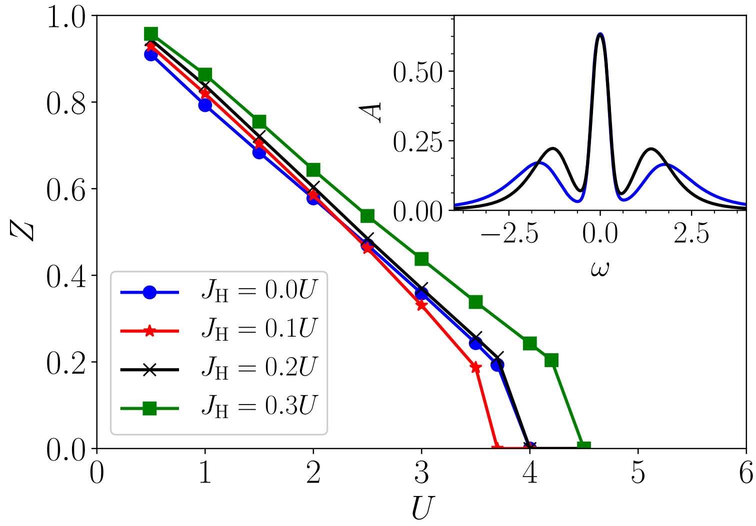

Figure 6.8: Quasiparticle weight Z of the $j = 3/2$ orbital as a function of U for $\lambda \to \infty$ and a total filling of $N = 2$. The inset shows the respective impurity spectral functions for $U = 3$ and $J_{\mathrm{H}} = 0$ (blue) and $J_{\mathrm{H}} = 0.2U$ (black). As the Hund's coupling J_{H} increases, the quasiparticle weight (= area of the quasiparticle peak) stays the same, whereas the position of the Hubbard bands changes due to different charge gaps. To obtain the spectral functions, imaginary-time data has been analytically continued using a maximum entropy method [178] with an alternative evidence approximation [179] and the preblur formalism [180].

unless in close vicinity to the metal-insulator transition.

A comparison to the crystal-field results shows two major differences: First, the orbital polarization is smaller in the case of the crystal field, as compared to the SOC case, and a larger value of crystal field splitting is needed to reach a band insulator. The reason for this is a larger atomic gap in the SOC case (see lower panel in Fig. 6.9 and Tab. 6.1, 6.2). Second, the quasiparticle renormalization of the d_{xy} orbital is lowest when its filling is around 1/2. This enhancement of correlation effects at half filling is absent for the $j = 1/2$ orbital.

6.4.6 Discussion

It is interesting to discuss our results in the context of real materials and consider which parameter regimes are realized (see also Refs. [166, 167]). One can first recall the atomic values ξ for the SOC that roughly increases with the fourth power of the atomic number. ξ takes small values in $3d$ (Mn: 0.04 eV, Co: 0.07 eV), intermediate values in $4d$ (Ru: 0.13 eV, Rh: 0.16 eV) and reaches considerable strength in $5d$ (Os: 0.42 eV, Ir: 0.48 eV) atoms [75]. These atomic values are representative also for the values of SOC found in corresponding oxides. Roughly, one can take that $J_{\mathrm{H}}/U = 0.1$, and values of U that diminish from 4 eV(in $3d$), 3 eV ($4d$), 2 eV ($5d$). Finally, the bandwidth will vary from case to case, since it depends the most on structural details among all the microscopic parameters. As a rule of thumb, however, it increases giving values of half-bandwidth from D=1 eV($3d$), 1.5 eV($4d$), 2 eV($5d$). These all are of course only rough estimates, meant to indicate trends.

The clear-cut case with strong influence of SOC are $5d$ oxides at $N = 5$. In iridates, λ/D ranges from 0.26 in $\mathrm{Sr_2IrO_3}$ up to 2.0 in $\mathrm{Na_2IrO_3}$ due to the small bandwidth in this compound [166]. Inspecting now Fig. 6.2, one sees that the SOC leads to a strong orbital polarization and strongly affects the correlations at those values of λ/D. Actually, the sensitivity to SOC at $N = 5$ is so strong that one can expect significant impact also in $4d^5$ compounds, like rhodates, too, although λ is by a factor of 3 smaller there. Indeed, the enhancement of correlations has been observed in a material-realistic DMFT study of $\mathrm{Sr_2RhO_4}$ [167, 181]. Rather small SOC leads also to a large polarization in the particle-hole transformed counterpart $N = 1$ (with potentially important consequences for the magnetic ordering [182]), but the increase of the quasiparticle renormalization is weak, see Fig. 6.2.

Opposite to the $N = 1$ and $N = 5$ cases, the SOC at $N = 3$ makes the electronic correlations weaker. Also in contrast to the former two cases, the effect of SOC on polarization and quasiparticle renormalization becomes pronounced only at larger values of λ. From Fig. 6.4 we can infer that for full polarization $\lambda/D > 0.5$ is necessary. As a consequence, for λ/D smaller than 0.2, which would be the case for many $4d$ materials, the effect of SOC on correlations is rather small. However, for larger values, such as in double perovskites (e.g. $\mathrm{Sr_2ScOsO_6}$), quite a substantial reduction of correlations can occur with SOC [183].

For the filling $N = 2$, we show in Fig. 6.5 a systematic suppression of the Janus-faced behavior with SOC, making the Hund's tail disappear.

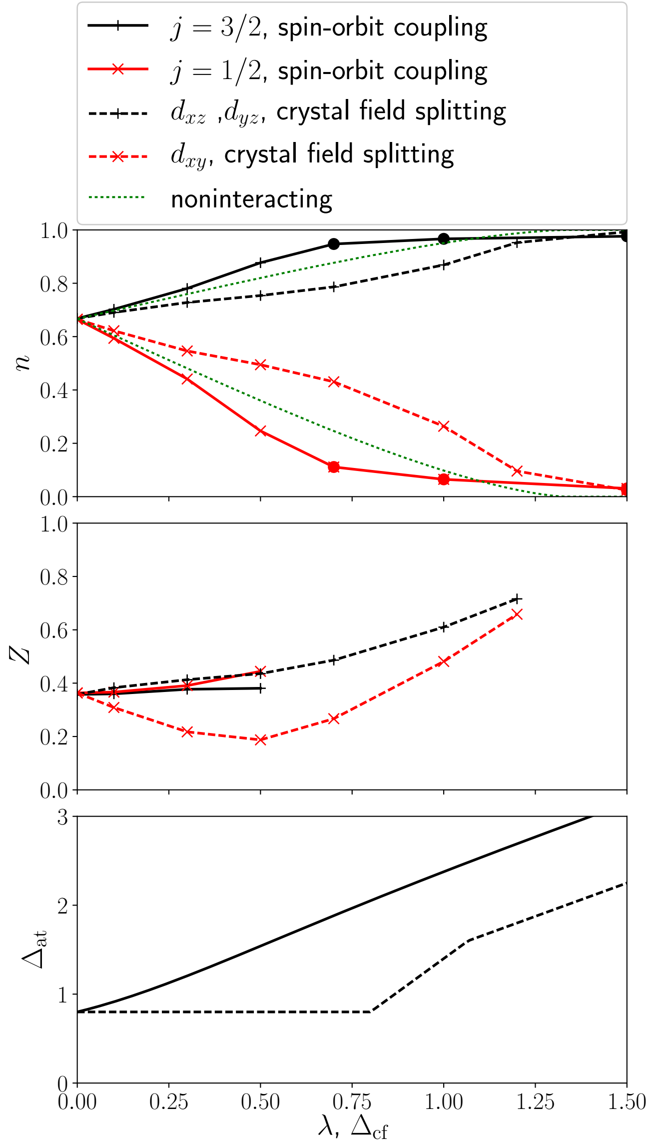

Figure 6.9: Filling, quasiparticle renormalization, and atomic charge gap of the orbitals as a function of spin-orbit coupling (full lines) and crystal field splitting (dashed lines) for $N = 4$, $U = 2$, $J_{\mathrm{H}} = 0.2\,U$. Full dots indicate insulating phases. In case of SOC, all calculations with $\lambda \geq 0.7$ are insulating, whereas in case of a crystal field only the last point shown ($\Delta_{\mathrm{cf}} = 1.5$) is insulating. The green dotted lines shows the orbital fillings in the noninteracting case. Then, crystal field and SOC are equivalent.

This effect is already sizable for $\lambda/D \approx 0.5$ and should, hence, be present in many $5d$ systems. Indeed, it has been seen in calculations for the $5d^2$ compound Sr_2MgOsO_6 [183]. For a smaller SOC of $\lambda/D \approx 0.1$, which is a good estimate for many $4d$ materials, we do not find a substantial change of Z (see, for example, Fig. 6.7). Therefore, we think the SOC only weakly affects the correlation strength in materials with $4d^2$ configuration, such as Sr_2MoO_4 [184–186].

For $N = 4$, our model calculations predict that the SOC affects the correlation strength only a little provided it is small enough to remain in the metallic phase. If it exceeds a certain magnitude, though, a metal-insulator transition occurs. The critical λ decreases with increasing U. Examples for this behavior are on the one hand Sr_2RuO_4 ($\lambda = 0.10\,\mathrm{eV}$), where the quasiparticle renormalization hardly changes as the SOC is turned on [145], and, on the other hand, $NaIrO_3$ ($\lambda = 0.33\,\mathrm{eV}$), where the interplay of SOC and U leads to an insulating state [187].

6.5 Conclusion

In this paper we investigated the influence of the SOC on the quasiparticle renormalization Z in a three-orbital model on a Bethe lattice within DMFT. Depending on the filling of the orbitals (and for $N = 2$ also the interaction strength), the SOC can decrease or increase the strength of correlations. The behavior can be understood in terms of the SOC induced changes of the effective degeneracy, the fillings of the relevant orbitals, and the interaction matrix elements in the low energy subspace.

The spin-orbital polarization leads to an increase of correlation strength for $N = 1, 5$ with particularly strong effect in for $N = 5$ where a half-filled single band problem is realized, relevant for iridate compounds. For the nominally half-filled case $N = 3$, the opposite trend is observed. Here, turning on SOC makes the system less correlated, and the critical interaction strength U_c for a Mott transition is reduced. For the $N = 2$ Hund's metallic phase, the influence of SOC is more involved. We find there are two regimes as function of U with opposite effect of SOC. For small U, the inclusion of SOC increase Z, whereas for large U it decreases Z, and in turn also the critical interaction U_c decreases. As a result, the so-called Hund's tail with small quasi-particle renormalization for a large region of interaction values, disappears.

We also considered the effects of the electronic correlations on SOC and found that in cases where the system remains metallic, correlations always enhance the effective SOC.

6.6 Atomic Hamiltonian in the limit of small and large spin-orbit couplings

The full local Hamiltonian reads (see also Eq. (6.2))

$$\begin{aligned} H_\mathrm{loc} &= H_\mathrm{I} + H_\lambda + H_\epsilon \\ &= (U - 3J_\mathrm{H})\frac{N(N-1)}{2} + \left(\frac{5}{2}J_\mathrm{H} + \epsilon\right)N - 2J_\mathrm{H}\boldsymbol{S}^2 - \frac{J_\mathrm{H}}{2}\boldsymbol{L}^2 + \lambda\,\boldsymbol{l}_{t_{2g}} \cdot \boldsymbol{s} \end{aligned} \tag{6.15}$$

Table 6.3: Eigenenergies of the Hamiltonian $H_{j=\frac{3}{2}}$ of the $j = 3/2$ orbitals, Eq. (6.8)

N	J	$E_{j=3/2}$
0	0	0
1	3/2	ϵ
2	2	$2\epsilon + U - 7/3\, J_{\mathrm{H}}$
2	0	$2\epsilon + U + 1/3\, J_{\mathrm{H}}$
3	3/2	$3\epsilon + 3U - 17/3\, J_{\mathrm{H}}$
4	0	$4\epsilon + 6U - 34/3\, J_{\mathrm{H}}$

with an SOC λ and an on-site energy ϵ. Note that this Hamiltonian contains both two-particle terms like N^2, $\boldsymbol{L}^2$, and $\boldsymbol{S}^2$, as well as one-particle terms like N and $\boldsymbol{l}_{t_{2g}} \cdot \boldsymbol{s}$. For $\lambda = 0$, the total spin S and the total orbital angular momentum L are good quantum numbers and determine together with the total number of electrons N the eigenenergies. As λ is finite, the energy levels split according to their total angular momentum J. For example, the nine-fold degenerate $S = 1$, $L = 1$ ground state in the $N = 2$ sector splits into a $J = 2$, a $J = 1$, and a $J = 0$ sector. The respective degeneracies are $2J + 1$. The total angular momentum J is for all values of λ a good quantum number, in contrast to the total spin S and the total orbital angular momentum L.

For a small SOC ($\lambda \ll J_{\mathrm{H}}$), one can use first-order perturbation theory in order to calculate the level splitting due to the SOC. In this approximation, the spin-orbit term is approximated by $C\lambda \boldsymbol{L} \cdot \boldsymbol{S}$. The constant C depends on the number of electrons and is C=1,1/2 for 1 and 2 electrons, and C=-1,-1/2 for one and two holes. For three electrons, L =0, and the first-order perturbation theory gives no energy correction. Since the total angular momentum is approximated by $\boldsymbol{J} = \boldsymbol{L} + \boldsymbol{S}$, this regime is known as LS-coupling regime.

In the limit of large SOC ($\lambda \gg J_{\mathrm{H}}$), the spin-orbit term is the dominant term that is solved exactly, whereas $\boldsymbol{S}^2$ and $\boldsymbol{L}^2$ may be treated perturbatively. The many-body eigenstates of the unperturbed system are then the Slater determinants of $j = 1/2$ and $j = 3/2$ one-electron states. Following Eq. (6.3), the matrix elements of $\lambda\, \boldsymbol{l}_{t_{2g}} \cdot \boldsymbol{s}$ depend in this unperturbed eigenbasis only on the number of electrons in the $j = 3/2$ and the $j = 1/2$ orbitals. The total angular momentum is $\boldsymbol{J} = \sum_i \boldsymbol{j}_i$, therefore, this regime is the jj-coupling regime. For fillings $N \leq 4$, only the $j = 3/2$ orbitals are occupied in the ground state. The spin-orbit term is then proportional to the particle number N and can be absorbed in the one-electron energy ϵ.

Calculating the matrix elements of $\boldsymbol{S}^2$ and $\boldsymbol{L}^2$ for Slater determinants with different N and J using Clebsch-Gordan coefficients, one can find the eigenenergies of the Hamiltonian in the jj coupling regime. This approach is equivalent to looking for the eigenvalues of $H_{j=\frac{3}{2}}$ presented in Eq. (6.8) in the main text, where all contributions of the $j = 1/2$ orbitals are neglected. The eigenenergies of $H_{j=\frac{3}{2}}$, including an on-site energy ϵ, are shown in table 6.3.

form if one assigns the absolute value of m_j as orbitals and its sign as spin, e.g.,

Table 6.4: Full list of quantum numbers and eigenenergies in the two-particle sector of a two-orbital system. We compare energies E_{e_g} of an ordinary Kanamori Hamiltonian for e_g orbitals with energies $E_{j=3/2}$ for the effective $j = 3/2$ Hamiltonian stemming from a large SOC in t_{2g} orbitals.

N	T	T_y	$\tilde{S}$	$\tilde{S}_z$	E_{e_g}	$E_{j=3/2}$
2	0	0	1	-1	$U - 3J_{\mathrm{H}}$	$U - 7/3\, J_{\mathrm{H}}$
2	0	0	1	0	$U - 3J_{\mathrm{H}}$	$U - 7/3\, J_{\mathrm{H}}$
2	0	0	1	1	$U - 3J_{\mathrm{H}}$	$U - 7/3\, J_{\mathrm{H}}$
2	1	-1	0	0	$U - J_{\mathrm{H}}$	$U - 7/3\, J_{\mathrm{H}}$
2	1	0	0	0	$U + J_{\mathrm{H}}$	$U + 1/3\, J_{\mathrm{H}}$
2	1	1	0	0	$U - J_{\mathrm{H}}$	$U - 7/3\, J_{\mathrm{H}}$

$d_{\frac{3}{2},\frac{1}{2}} \mapsto c_{1\uparrow}$ and $d_{\frac{3}{2},-\frac{3}{2}} \mapsto c_{2\downarrow}$. It reads then

$$H_{j=\frac{3}{2}} = \left(U - \frac{5}{3}J_{\mathrm{H}}\right)\frac{N(N-1)}{2} - \frac{1}{3}J_{\mathrm{H}}N + \frac{4}{3}J_{\mathrm{H}}\left(\boldsymbol{T}^2 - 2T_y^2\right) \tag{6.16}$$

with a total spin

$$\tilde{\boldsymbol{S}} = \frac{1}{2}\sum_i \sum_{\sigma\sigma'} c_{i\sigma}^{\dagger} \boldsymbol{\tau}_{\sigma\sigma'} c_{i\sigma'} \tag{6.17}$$

and the two-orbital isospin

$$\boldsymbol{T} = \frac{1}{2}\sum_{\sigma} \sum_{ij} c_{i\sigma}^{\dagger} \boldsymbol{\tau}_{ij} c_{j\sigma} \tag{6.18}$$

Note that $\tilde{\boldsymbol{S}}$ is not a physical spin, since it stems from mapping the sign of m_j to an artificial spin.

Hamiltonian (6.16) has the structure of a generalized Kanamori Hamiltonian, where the spin-flip and pair-hopping parameters J_{SF} and J_{PH} are not restricted to be equal to the Hund's coupling J_{H} as in the ordinary Kanamori Hamiltonian (6.1). It terms of $\boldsymbol{T}$ and $\tilde{\boldsymbol{S}}$, the generalized Kanamori Hamiltonian reads [42]

$$\begin{aligned} H_{\mathrm{GK}} &= \left(U + U' - J_{\mathrm{H}} + J_{\mathrm{SF}}\right)\frac{N(N-1)}{4} - \left(U - U' - J_{\mathrm{H}} + 3J_{\mathrm{SF}}\right)\frac{N}{4} \\ &\quad + (J_{\mathrm{SF}} + J_{\mathrm{PH}})T_x^2 + (J_{\mathrm{SF}} - J_{\mathrm{PH}})T_y^2 + (U - U')T_z^2 + (J_{\mathrm{SF}} - J_{\mathrm{H}})\,\tilde{S}_z^2. \end{aligned} \tag{6.19}$$

In order that $H_{j=\frac{3}{2}}$ fits the structure of the generalized Hamiltonian, one has to replace the parameters of H_{GK} by $U \mapsto U - J_{\mathrm{H}}$, $J_{\mathrm{H}} \mapsto 0$, $J_{\mathrm{SF}} \mapsto 0$, $J_{\mathrm{PH}} \mapsto \frac{4}{3}J_{\mathrm{H}}$, and $U' \mapsto U - \frac{7}{3}J_{\mathrm{H}}$.

Hamiltonian (6.19) with the parameters of the usual Kanamori Hamiltonian, $U' = U - 2J_{\mathrm{H}}$, $J_{\mathrm{SF}} = J_{\mathrm{PH}} = J_{\mathrm{H}}$, is the symmetric form of the two-band Hamiltonian describing

e_g bands [42]

$$H_{e_g} = (U - J_{\mathrm{H}})\frac{N(N-1)}{2} - J_{\mathrm{H}}N + 2J_{\mathrm{H}}\left(\boldsymbol{T}^2 - T_y^2\right). \tag{6.20}$$

While $H_{j=\frac{3}{2}}$ is the Hamiltonian relevant for the two $j = 3/2$ orbitals of a three orbital system with infinite SOC, H_{e_g} is its counterpart describing the d_{xz} and d_{yx} orbitals when the tetragonal crystal field splitting is infinite. The difference between these two operators is thus responsible for the qualitative different behavior of crystal field and SOC in case of a filling of $N = 2$ (see Sec. 6.4.4). The operators (6.16) and (6.16) are of similar form, but have different prefactors.

A complete set of commuting operators for both Hamiltonians is N, $\boldsymbol{T}^2$, T_y, $\tilde{\boldsymbol{S}}^2$ and $\tilde{S}_z$. The full list of quantum numbers and the eigenenergies of the two operators is shown in Tab. 6.4 for $N = 2$. For the $j = 3/2$ orbitals, one sees that due to the prefactors, the $\tilde{S} = 1$ ground state is degenerate with two $\tilde{S} = 0$ states. This is related to the fact that spin-flip and Hund's coupling terms vanish in the related generalized Kanamori Hamiltonian so that the relative orientation of pseudo-spins of two electrons in different orbitals has no influence on the energy. The physical reason for this is that all five states belong to the $J = 2$ ground state manifold that is found in the picture of jj coupling and therefore have to be degenerate. As a consequence, charge fluctuations to different values of pseudospin S are for large Hund's couplings still possible, in contrast to an ordinary Kanamori Hamiltonian, where J_{H} splits energy levels of different spin.

6.7 Effective spin-orbit coupling

The operator of the SOC (6.3) leads to off-diagonal elements in the noninteracting Hamiltonian in the cubic basis. If both interactions and SOC are present, the self-energy will have off-diagonal elements as well, changing the effective strength λ_{eff} of the SOC.

The structure of the off-diagonal elements can be understood in case of our degenerate three-orbital model system using simple analytical considerations. In the j-basis, both the local Hamiltonian and the hybridization function are diagonal, hence Σ is diagonal as well, with different values for the $j = 3/2$ and the $j = 1/2$ orbitals. This diagonal matrix can be split into a term proportional to the unit matrix and a term proportional to the matrix representation of the $\boldsymbol{l}_{t_{2g}} \cdot \boldsymbol{s}$ operator, which is diagonal in j-basis with elements -0.5 in case of $j = 3/2$, and 1 in case of $j = 1/2$. Therefore,

$$\Sigma = \Sigma_{\mathrm{a}}\mathbb{1} + \frac{2}{3}\Sigma_{\mathrm{d}}\boldsymbol{l}_{t_{2g}} \cdot \boldsymbol{s} \tag{6.21}$$

with an average self-energy

$$\Sigma_{\mathrm{a}} = \frac{2}{3}\Sigma_{\frac{3}{2}} + \frac{1}{3}\Sigma_{\frac{1}{2}} \tag{6.22}$$

and the difference

$$\Sigma_{\mathrm{d}} = \Sigma_{\frac{1}{2}} - \Sigma_{\frac{3}{2}}. \tag{6.23}$$

The effective SOC is thus

$$\lambda_{\mathrm{eff}}(\omega) = \lambda + \frac{2}{3}\,\Sigma_{\mathrm{d}}(\omega) \tag{6.24}$$

and is, in principle, dependent on the frequency. In the cubic basis, the diagonal elements of the self-energy are given by Σ_{a}, the off-diagonal elements up to a phase by $2/3\,\Sigma_{\mathrm{d}}$.

For large frequencies, the values of Σ_{d} are given by the Hartree-Fock values. Using Eq. (6.6), the Hartree-Fock values in j-basis are

$$\Sigma^{\mathrm{HF}}_{\frac{1}{2}} = \left\langle \frac{\partial H_{\mathrm{I}}}{\partial n_{\frac{1}{2},\frac{1}{2}}} \right\rangle = \left(U - \frac{4}{3}J_{\mathrm{H}}\right) n_{\frac{1}{2}} + \left(4U - \frac{26}{3}J_{\mathrm{H}}\right) n_{\frac{3}{2}} \tag{6.25}$$

$$\Sigma^{\mathrm{HF}}_{\frac{3}{2}} = \left\langle \frac{\partial H_{\mathrm{I}}}{\partial n_{\frac{3}{2},\frac{3}{2}}} \right\rangle = \left(2U - \frac{13}{3}J_{\mathrm{H}}\right) n_{\frac{1}{2}} + \left(3U - \frac{17}{3}J_{\mathrm{H}}\right) n_{\frac{3}{2}}, \tag{6.26}$$

hence the at $\omega \to \infty$

$$\Sigma^{\mathrm{HF}}_{\mathrm{d}} = (U - 3J_{\mathrm{H}})\left(n_{\frac{3}{2}} - n_{\frac{1}{2}}\right) \tag{6.27}$$

The effective SOC for large frequencies is therefore determined by an effective correlation strength $U-3J_{\mathrm{H}}$ and the orbital polarization. Since the $j = 3/2$ orbital is lower in energy, its occupation is higher, and $\Sigma^{\mathrm{HF}}_{\mathrm{d}}$ is always positive as long as the effective interaction is repulsive. As a consequence, the correlations always enhance the correlation strength at large frequencies.

At low frequencies and temperatures, assuming a metal, the values of Σ are related to electronic occupancies, too. Namely, $j = 1/2$ and $j = 3/2$ problems are independent and the corresponding Fermi surface must, by Luttinger theorem, contain the correct number of electrons. At the Fermi surface, $\mu + \epsilon_k - \Sigma = 0$, which can be used to relate the difference of ϵ_k to the difference of Σ. Assuming that the electronic density of states is a constant ρ independent of energy (square shaped function), the result is $\Sigma_{\mathrm{d}}(0) = 1/\rho\left(n_{3/2} - n_{1/2}\right) - 3/2\lambda$. In general, $\Sigma_{\mathrm{d}}(0)$ depends on the density of states, the SOC, and the orbital polarization, but not explicitly on the interaction parameters U and J_{H}. Since the Hartree-Fock value does depend on the interaction parameters, the large frequency and small frequency values of Σ_{d} can be quite different, as shown in Fig. 6.10. In contrast to the Hartree-Fock value valid at large frequencies, $\Sigma_{\mathrm{d}}(\omega = 0)$ cannot be calculated exactly. However, in all metallic DMFT calculation performed, we verified numerically that $\Sigma_{\mathrm{d}}(\omega = 0)$ is positive, hence the effective SOC is also increased for low frequencies [163]. The results for $U = 2$, $J_{\mathrm{H}} = 0.1\,U$ are shown in Fig. 6.11.

In the case of Sr_2RuO_4, the DMFT work of Ref. [145] and Ref. [144] found that the real part of Σ_{d} was to a good approximation a constant and the imaginary part to a good approximation 0 (strictly, there are additional complications, as the system only has cubic symmetry). We reproduce this result in a DMFT calculation with parameters $N = 4$, $U = 2$, $J_{\mathrm{H}} = 0.2\,U$, and $\lambda = 0.1$, which correspond approximately to the vales in Sr_2RuO_4. However, if the parameters are changed, for example to a Hund's coupling of $J_{\mathrm{H}} = 0.1\,U$, the off-diagonal elements of Σ start to show a more pronounced frequency dependence, as shown in Fig. 6.10. The reason for this is the strong direct dependence

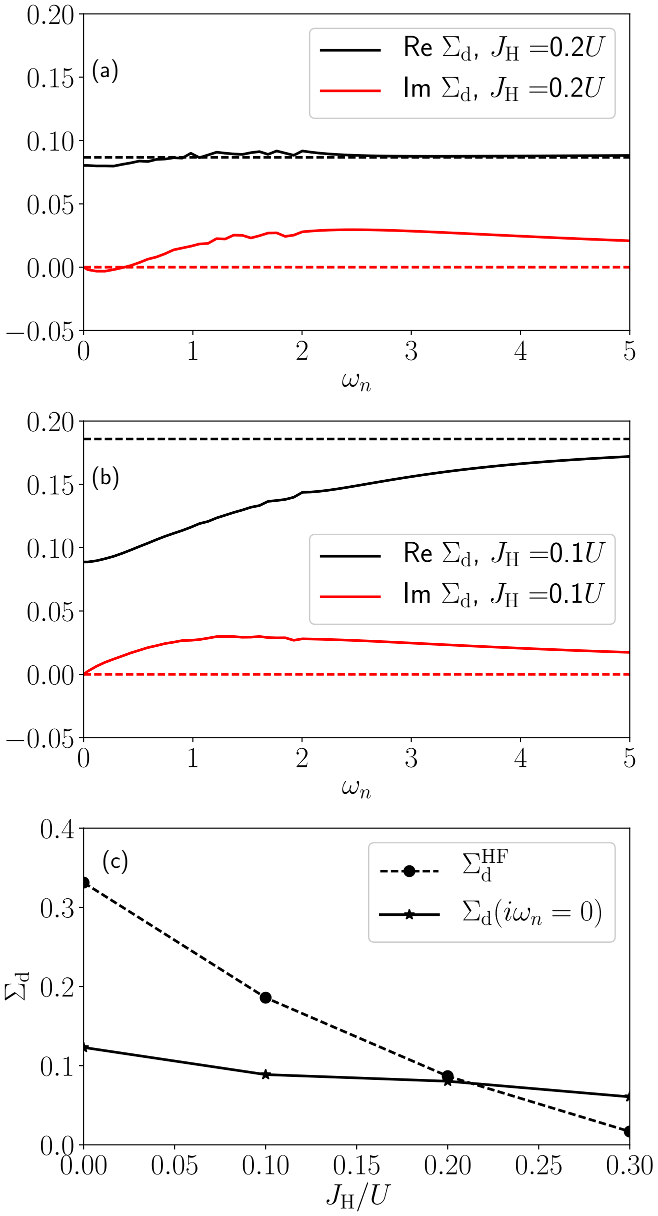

Figure 6.10: Difference of the self-energies $\Sigma_\mathrm{d} = \Sigma_{\frac{1}{2}} - \Sigma_{\frac{3}{2}}$ for $N = 4$, $\lambda = 0.1$, and $U = 2$. Subplots (a) and (b) show Σ_d as a function of Matsubara frequencies ω_n for Hund's couplings $J_\mathrm{H} = 0.2\,U$ and $J_\mathrm{H} = 0.1\,U$, respectively. The dashed lines are the respective Hartree-Fock values. Subplot (c) shows the Hartree-Fock values corresponding to $\Sigma_\mathrm{d}(\mathrm{i}\omega_n \to \infty)$ (dashed) and $\Sigma_\mathrm{d}(\mathrm{i}\omega_n \to 0)$ (full line) as a function of J_H. While the Hartree-Fock value strongly decreases with J_H, $\Sigma_\mathrm{d}(\mathrm{i}\omega \to 0)$ is hardly influenced.

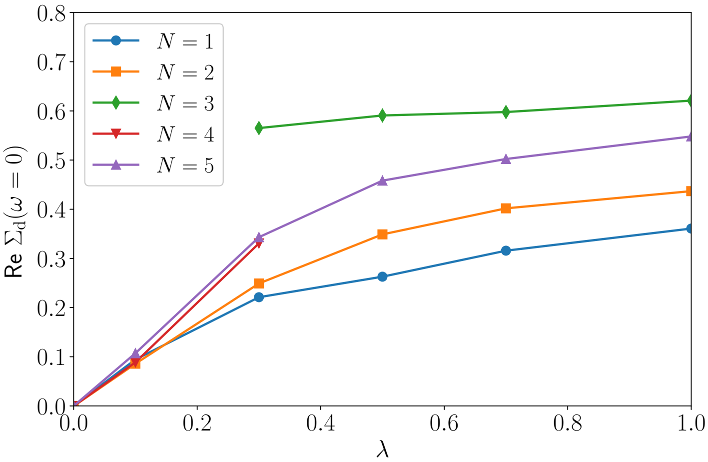

Figure 6.11: Increase of the first Matsubara self-energy $\Sigma_\mathrm{d}(\mathrm{i}\omega_0) \approx \Sigma_\mathrm{d}(\omega = 0)$ with the SOC for $U = 2$, $J_\mathrm{H} = 0.1\,U$, and all integer fillings. For $N = 3$ and $\lambda < 0.3$, the system is a Mott insulator, and for $N = 4$ and $\lambda > 0.3$ a band insulator. The data points are not shown for these parameters, since the chemical potential (and with that $\Sigma(\omega = 0)$) is not well defined.

of λ_eff on the interaction parameters in the Hartree-Fock limit, which is not present at low frequencies. It the lower panel of Fig. 6.10, one sees that the Hartree-Fock value strongly decreases with the Hund's coupling, whereas static value at $\omega = 0$ only changes slightly.

7 Topological insulators on the honeycomb lattice

The first example for a phase transition from a topologically trivial to a non-trivial band insulator without external magnetic field as described in section 4.7.1 was found by Haldane, wherefore he received the Nobel prize together with Kosterlitz and Thouless (see section 4.3.2). The Haldane model is based on a one-band honeycomb lattice with a nearest neighbor hopping, which is equivalent to the most simplistic tight-binding model of graphene. The topological transition to a Chern insulator comes now into play via a complex next-nearest neighbor hopping that introduces local magnetic fluxes and thus breaks time-reversal symmetry (c.f. Sec. 4.7.1). Furthermore, Haldane considered an energy difference between the two sublattices A and B of the honeycomb lattice. The total Hamiltonian reads [101]

$$H_{\text{Haldane}} = -t \sum_{\langle i,j \rangle} c_i^\dagger c_j - t' \sum_{\langle\langle i,j \rangle\rangle} e^{\mathrm{i}\nu_{ij}\phi} c_i^\dagger c_j + \lambda_\nu \sum_i \xi_i c_i^\dagger c_i, \tag{7.1}$$

where $\langle \cdot, \cdot \rangle$ denotes nearest neighbor sites and $\langle\langle \cdot, \cdot \rangle\rangle$ next-nearest neighbor sites, and $\xi_i = 1$ for $i \in A$ and $\xi_i = -1$ for $i \in B$. The prefactor ν_{ij} of the phase ϕ is defined such that it is $\nu_{ij} = -1$ if a left turn is performed when hopping to the next-nearest neighbor, and $\nu_{ij} = 1$ in case of a right turn. Details to this Hamiltonian as well as the full phase diagram can be found, for example, in the master's thesis of the author [107].

7.1 Band structure of graphene-like structures

The tight-binding model on the honeycomb lattice shows Dirac cones in the dispersion relation, which are crucial for the topological characteristic of the Haldane model. The bands around the Fermi level forming the Dirac cones in graphene stem from the p_z orbitals, but it is also possible to obtain a Dirac cone from the p_x and p_y orbitals when the p_z orbitals are shifted in energy. Furthermore, the p_x and p_y orbitals are strongly hybridized with the s orbitals. Therefore, in the tight-binding model for graphene presented here, all orbitals of the $2s$ and $2p$ shell are included.

On the level of molecular orbitals, the energy levels of graphene can be understood in terms of hybrid orbitals. A linear combination of the $2s$ orbital with various numbers of $2p$ orbitals leads to different geometrical structures. Combining it with one p orbital results in the sp^1 hybrid orbital linear in shape, a combination with two to the sp^2 hybrid orbitals with a triangular shape, and a combination with all three to the tetragonal sp^3 orbitals. In case of planar graphene, the sp^2 hybridization is the relevant one. The parametrization of the hybrid orbitals in terms of the cubic harmonics is given by [188]

$$\begin{aligned}
\left|sp_1^2\right\rangle &= \frac{1}{\sqrt{3}}\left|2s\right\rangle - \sqrt{\frac{2}{3}}\left|2p_y\right\rangle \\
\left|sp_2^2\right\rangle &= \frac{1}{\sqrt{3}}\left|2s\right\rangle + \sqrt{\frac{2}{3}}\left(\frac{\sqrt{3}}{2}\left|2p_x\right\rangle + \frac{1}{2}\left|2p_y\right\rangle\right) \\
\left|sp_3^2\right\rangle &= -\frac{1}{\sqrt{3}}\left|2s\right\rangle + \sqrt{\frac{2}{3}}\left(-\frac{\sqrt{3}}{2}\left|2p_x\right\rangle + \frac{1}{2}\left|2p_y\right\rangle\right)
\end{aligned} \tag{7.2}$$

The lobes of the three orbitals are separated by an angle of 120 degrees, leading to a maximal overlap with the hybrid orbitals of the neighboring atoms in a triangular geometry. This is the reason why the honeycomb lattice is the optimal geometry for two-dimensional carbon. Due to the overlap, the atomic hybrid orbitals form a bonding σ and an antibonding σ^* molecular orbital. The remaining p_z orbitals do not hybridize with the s orbitals, they form a delocalized bonding π and an antibonding π^* orbital. Since the overlap of the p_z orbitals sticking out of the plane is a lot smaller then the overlap of the hybrid sp^2 orbitals, the energy splitting of the π and π^* orbitals is smaller than the energy splitting of the σ and σ^* orbitals. Due to the four electrons of carbon in the second shell, the bonding σ orbital is filled by three electrons, and the remaining electron in the conjugated π system determines the physics near the Fermi energy.

From this simple atomic/molecular picture it is clear that the p_z orbital is the most important one for the low energy physics. They are, however, surrounded by the σ bands from the hybrid sp^2 orbitals. A better description including a $\boldsymbol{k}$-dependence is achieved by a tight-binding approximation. As a basis, the cubic $2s, 2p_x, 2p_y, 2p_z$ basis is usually chosen. Note that the honeycomb lattice has two atoms in the unit cell, each belonging to one of the sublattices A and B. The Bloch Hamiltonian has therefore for each spin species the block structure

$$H^{\uparrow\uparrow}(\boldsymbol{k}) = H^{\downarrow\downarrow}(\boldsymbol{k}) = \begin{pmatrix} H_{AA} & H_{AB} \\ H_{BA} & H_{BB} \end{pmatrix}, \tag{7.3}$$

with $H_{AA} = H_{BB}$ in graphene due to the symmetry of A and B sites. Since all the nearest neighbors of an atom in sublattice A are in sublattice B, the matrices H_{AA} and H_{BB} contain only the on-site energies of the respective orbitals in the simplest nearest neighbor tight-binding approximations. In pure graphene, the on-site levels of the p orbitals are degenerate. Setting the energy zero-point to this level, the matrices simply read $H_{AA} = H_{BB} = \mathrm{diag}(\epsilon_s, 0, 0, 0)$. For the block H_{AB}, symmetry considerations can be used to determine its structure. Since the p_z orbital is antisymmetric in z and all other orbitals are symmetric, the full Bloch Hamiltonian spits into a π and a σ block. If one furthermore uses the fact that the s orbitals are even and the p orbitals odd, the total Bloch Hamiltonian has the form

$$H_{AB}(\boldsymbol{k}) = \begin{pmatrix} h_{ss} & h_{sx} & h_{sy} & 0 \\ -h_{sx} & h_{xx} & h_{xy} & 0 \\ -h_{sy} & h_{xy} & h_{yy} & 0 \\ 0 & 0 & 0 & h_{zz} \end{pmatrix} \tag{7.4}$$

If the unit cell is defined such that the reciprocal lattice vectors are $\boldsymbol{b}_1 = (2\pi, 2\pi/\sqrt{3})$ and $\boldsymbol{b}_2 = (0, 4\pi/\sqrt{3})$, the matrix elements are given by [188–191]

$$\begin{aligned}
h_{ss}(\boldsymbol{k}) &= V_s \left[\exp\left(-\mathrm{i}\frac{k_y}{\sqrt{3}}\right) + 2\exp\left(\mathrm{i}\frac{k_y}{2\sqrt{3}}\right)\cos\left(\frac{k_x}{2}\right)\right] \\
h_{sx}(\boldsymbol{k}) &= V_{sp}\,\mathrm{i}\sqrt{3}\exp\left(\mathrm{i}\frac{k_y}{2\sqrt{3}}\right)\sin\left(\frac{k_x}{2}\right) \\
h_{sy}(\boldsymbol{k}) &= V_{sp}\left[\exp\left(-\mathrm{i}\frac{k_y}{\sqrt{3}}\right) - \exp\left(\mathrm{i}\frac{k_y}{2\sqrt{3}}\right)\cos\left(\frac{k_x}{2}\right)\right] \\
h_{xx}(\boldsymbol{k}) &= V_{p\pi}\exp\left(-\mathrm{i}\frac{k_y}{\sqrt{3}}\right) + \frac{1}{2}\left(-3V_{p\sigma} + V_{p\pi}\right)\exp\left(\mathrm{i}\frac{k_y}{2\sqrt{3}}\right)\cos\left(\frac{k_x}{2}\right) \\
h_{yy}(\boldsymbol{k}) &= -V_{p\sigma}\exp\left(-\mathrm{i}\frac{k_y}{\sqrt{3}}\right) + \frac{1}{2}\left(3V_{p\pi} - V_{p\sigma}\right)\exp\left(\mathrm{i}\frac{k_y}{2\sqrt{3}}\right)\cos\left(\frac{k_x}{2}\right) \\
h_{xy}(\boldsymbol{k}) &= \frac{\mathrm{i}\sqrt{3}}{2}\left(V_{p\sigma} + V_{p\pi}\right)\exp\left(\mathrm{i}\frac{k_y}{2\sqrt{3}}\right)\sin\left(\frac{k_x}{2}\right) \\
h_{zz}(\boldsymbol{k}) &= V_{p\pi}\left[\exp\left(-\mathrm{i}\frac{k_y}{\sqrt{3}}\right) + 2\exp\left(\mathrm{i}\frac{k_y}{2\sqrt{3}}\right)\cos\left(\frac{k_x}{2}\right)\right]
\end{aligned} \tag{7.5}$$

The hopping parameters needed are the hopping strength of the s orbitals V_s, the hopping in the p orbitals for both σ and π bonds $V_{p\sigma}$ and $V_{p\pi}$, and the hybridization of s and p orbitals V_{sp}. If one also considers that the orbitals on different site have a finite overlap $S_{ij} = \langle\psi_i|\,\psi_j\rangle \neq 0$ so that the overlap matrix S is not the unit matrix, also the strength of the overlaps W_s, $W_{p\sigma}$ and $W_{p\pi}$, and W_{sp} have to be considered. The matrix elements S_{ij} have the same $\boldsymbol{k}$-dependence as the matrix elements of Hamiltonian (7.5), but different prefactors W_i instead of V_i. The full parameter list for graphene is given in table 7.1 (see also [189]). The band energies are obtained via the general eigenvalue equation $H(\boldsymbol{k})\,|\psi\rangle = E(\boldsymbol{k})S\,|\psi\rangle$, and are plotted for the parameters in table 7.1 in Fig. 7.1. The hybrid orbitals form three filled σ orbitals and three empty σ^* orbitals, separated by a gap of about 6 eV. The π and π^* bands stemming from the p_z orbitals, on the other hand, do not open a gap, but form a Dirac cone. They are therefore determining the transport properties.

7.2 Spin-orbit coupling

Including a local, atomic spin-orbit coupling (SOC) of the form $\lambda\,\boldsymbol{l}\cdot\boldsymbol{s}$ as introduced in chapter 3, the local blocks of the Hamiltonian, i.e., H_{AA} and H_{BB}, are affected. The

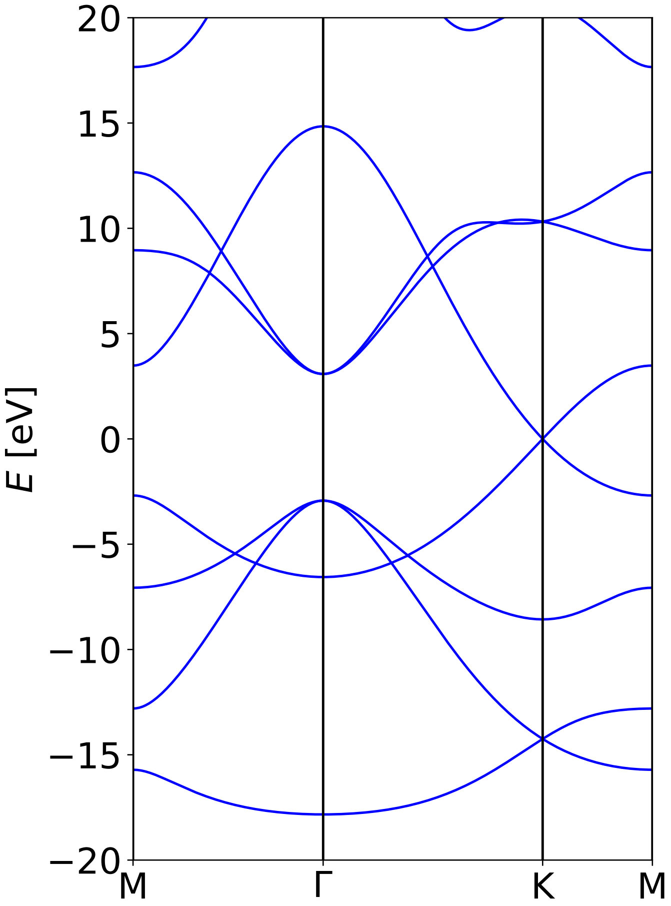

Figure 7.1: Tight-binding band structure of graphene using the parameters of Tab. 7.1

Table 7.1: Parameters of the tight-binding model in of graphene in eV taken from Ref. [189].

$V_s = -6.769$	$W_s = 0.212$
$V_{sp} = -5.580$	$W_{sp} = 0.102$
$V_{p\sigma} = -5.037$	$W_{p\sigma} = 0.146$
$V_{p\pi} = -3.033$	$W_{p\pi} = 0.129$
$\epsilon_s = -8.868$	

matrix elements for the s orbital are all zero, the matrix elements for the three p orbitals are given by Eq. (3.37). Note that the local blocks will also acquire terms like $H_{AA}^{\uparrow\downarrow}$ that couple the two spin species. Furthermore, since the SOC has non-vanishing matrix elements between p_z and p_x, p_y, the σ and π orbitals are coupled as well. Therefore, including the SOC, both the spin and the orbital block structure are destroyed.

For a description of the transport properties of graphene-like structures, it is sufficient to study only the Dirac cone stemming from the p_z orbitals. From Eq. (3.37) it is clear that the p_z matrix elements of the local $\boldsymbol{l} \cdot \boldsymbol{s}$ operator vanish. Hence, when only the p_z orbitals are considered, the local SOC is quenched, just as the case of e_g orbitals discussed in Sec. 3.3. However, a non-local dispersive part of the SOC may persist. It can be shown that in second order perturbation theory, a next-nearest neighbor hopping of the strength

$$\lambda_{\mathrm{SO}} = \frac{|\epsilon_s|}{18V_{sp}^2}\lambda^2 \tag{7.6}$$

exists [192]. It can be visualized as hopping sequences of the form [191]

$$\left|p_{z,A}^{\uparrow}\right\rangle \xrightarrow{\mathrm{SOC}} \left|p_{x,A}^{\downarrow}\right\rangle \xrightarrow{V_{sp}} \left|s_{B}^{\downarrow}\right\rangle \xrightarrow{V_{sp}} \left|p_{x,A}^{\downarrow}\right\rangle \xrightarrow{\mathrm{SOC}} \left|p_{z,A}^{\uparrow}\right\rangle . \tag{7.7}$$

This next-nearest neighbor hopping is purely imaginary. It changes its sign under both spatial inversion and spin inversion and preserves thus time-reversal symmetry.

This second-order SOC on a honeycomb lattice with a nearest neighbor hopping is they key ingredient of the Kane-Mele model [13, 14]. It is responsible for the non-trivial gap opening, making it a quantum spin Hall insulator (see section 4.7.2). The full model also includes an on-site energy difference between A and B sites, and a Rashba coupling, and reads [14]

$$H_{\mathrm{KM}} = -t\sum_{\langle i,j\rangle} c_i^\dagger c_j + \mathrm{i}\lambda_{\mathrm{SO}} \sum_{\langle\langle i,j\rangle\rangle} \nu_{ij} c_i^\dagger \sigma^z c_j + \lambda_\nu \sum_i \xi_i c_i^\dagger c_j + \mathrm{i}\lambda_{\mathrm{R}} \sum_{\langle i,j\rangle} c_i^\dagger (\boldsymbol{\sigma} \times \hat{\boldsymbol{d}}_{ij})_z c_j . \tag{7.8}$$

Here, $c_i^\dagger$ is the creation operator of a spinor $\left(c_{i\uparrow}^\dagger, c_{i\downarrow}^\dagger\right)$, $\langle\cdot\rangle$ denotes nearest neighbors, and $\langle\langle\cdot\rangle\rangle$ next-nearest neighbors. The first term is the tight-binding nearest neighbor hopping term. Since the spinors model the p_z orbitals of a graphene-like structure, the hopping parameter t corresponds to V_π in table 7.1. The second is the intrinsic spin-orbit coupling, leading to the quantum spin Hall topological insulating state as it opens a gap [13, 14, 103]. The third term is a staggered on-site potential. The coefficients ν_{ij} and ξ_i are defined as for the Haldane model (7.1). In fact, these three terms of the Kane-Mele model are equivalent to two time-reversed copies of the Haldane model (one for each spin species). The last term in Eq. (7.8) is the Rashba coupling, where $\hat{\boldsymbol{d}}_{ij}$ denotes a unit vector pointing from site i so site j.

8 Phase diagram of the Kane-Mele-Hubbard Hamiltonian

The content displayed in this chapter was published by the author and his supervisor in Ref. [193], which shows many new results that have been achieved during the PhD studies of the author. However, the foundations of this work were already laid while the master's thesis of the author was written [107], wherefore a detailed declaration of the new content is given here.

The paper analyzes the phase diagram of the KMH model

$$H_{\mathrm{KMH}} = H_{\mathrm{KM}} + U \sum_{i} n_{i\uparrow} n_{i\downarrow}, \tag{8.1}$$

where H_{KM} is given by Eq. (7.8). The Rashba coupling λ_{R} is set to zero, but the on-site energy difference is kept in order to break spatial inversion symmetry. The Green's function is calculated using a two-site dynamical impurity approximation (DIA). The topological properties of the phases were analyzed using the topological Hamiltonian (see Sec. 4.7.4), as well as by calculating the Green's function of a finite-sized ribbon using again a DIA. Furthermore, comparisons to a mean-field approach are made.

The calculation of the topological properties was a main aspect of the author's master's thesis and is fully described therein. The DIA for the bulk is also explained there, but for the results, only an antiferromagnetic Weiss field was used. The second Weiss field enabling unequal electron densities on the two sublattices was first published in the paper [193]. This improvement is important to obtain the phase boundaries shown in Fig. 8.4. The DIA of the ribbon was fully implemented during the PhD studies of the author and the corresponding results were first published in the paper. Mean-field results with the z axis as a decoupling axis are shown already in the master's thesis, the physically more relevant results with an in-plane magnetisation were first shown in the paper.

Since all the physically relevant phase diagrams discussed in the paper (DIA for bulk and ribbon including both Weiss fields, mean-field with physical in-plane decoupling axis) were obtained while the PhD studies of the author and are, hence, not shown in his master's thesis, the paper constitutes an important content of this PhD thesis. Therefore, most parts of the paper are included here just as published [193], in order to allow for a self-contained depiction of the results. However, the sections in [193] entitled "Kane-Mele-Hubbard model" and "Calculation of topological invariants" are left out, since the content is already explained in detail in the author's master's thesis and reviewed in the sections 4.7 and 7.2.

PHYSICAL REVIEW B **94**, 165169 (2016)

Topological insulator on honeycomb lattices and ribbons without inversion symmetry

Robert Triebl* and Markus Aichhorn
Institute of Theoretical and Computational Physics, NAWI Graz, Graz University of Technology, Petersgasse 16, 8010 Graz, Austria

(Received 25 May 2016; published 26 October 2016)

Abstract

We study the Kane-Mele-Hubbard model with an additional inversion-symmetry-breaking term. Using the topological Hamiltonian approach, we calculate the $\mathbb{Z}_2$ invariant of the system as function of spin-orbit coupling, Hubbard interaction U, and inversion-symmetry-breaking on-site potential. The phase diagram calculated in that way shows that, on the one hand, a large term of the latter kind destroys the topological non-trivial state. On the other hand, however, this inversion-symmetry-breaking field can enhance the topological state, since for moderate values the transition from the non-trivial topological to the trivial Mott insulator is pushed to larger values of interaction U. This feature of an enhanced topological state is also found on honeycomb ribbons. With inversion symmetry, the edge of the zigzag ribbon is magnetic for any value of U. This magnetic moment destroys the gapless edge mode. Lifting inversion symmetry allows for a finite region in interaction strength U below which gapless edge modes exist.

8.1 Introduction

Since topological insulators have been theoretically predicted 10 years ago [13, 14], the understanding of topological phases has progressed enormously. Topological Hamiltonians are classified by the tenfold way [194–196], various experiments have been performed showing the practical relevance of the theoretical considerations [10, 16, 197–202], and several groups already succeeded in a next step which is predicting and realizing Weyl semimetals [203–210].

However, the influence of interactions onto the topological classification is still not fully understood. Just recently, new phase transitions in strongly correlated topological insulators have been reported [27, 28]. The most used quantity to characterize topological order, namely the $\mathbb{Z}_2$ invariant introduced by Fu, Kane, and Mele [13, 104, 105, 211], relies on defined Bloch bands and is thus not directly applicable for interacting systems. A generalization is possible using the so-called topological Hamiltonian [115–117], an artificially noninteracting system determined by the Green's function.

The Kane-Mele-Hubbard (KMH) model [13, 14, 212] combines a topological model Hamiltonian with strong interactions and is therefore frequently used to explore correlation effects in topological insulators [12, 212–225]. Within the framework of the topological Hamiltonian, the calculation of the $\mathbb{Z}_2$ invariant is straight forward as long as inversion symmetry is obeyed, since only the time-reversal-invariant momenta (TRIMs) have to be considered [105, 116]. In case of the bare KMH model, it can thus be used since inversion symmetry is respected [12, 219, 220].

Determining the topological phase becomes more difficult if an inversion-symmetry-breaking term such as a staggered on-site potential [13, 224], a Rashba coupling [13, 220], or site-dependent hoppings [217, 223] are included. A possibility to analyze topological phases is to calculate the spin Chern number C_S [103, 217, 223–226]. This approach requires spin to be a good quantum number and has the drawback that due to numerical artifacts a good quantization of C_S is not given close to phase transitions. Another approach is to look directly for gapless edge states and use bulk-boundary correspondence [218, 220–222].

In this paper, we calculate the $\mathbb{Z}_2$ invariant of the KMH model with an inversion-symmetry-breaking on-site potential by combining the topological Hamiltonian with a method introduced by Soluyanov and Vanderbilt [106, 227] that is based on maximally localized Wannier charge centers (WCC) [29]. This enables a precise calculation of invariants without restricting the systems to certain symmetries. Furthermore, we investigate bulk-boundary correspondence by calculating the spectral functions of a zigzag ribbon. We show that bulk-boundary correspondence has to be treated with care in strongly interacting systems since time-reversal symmetry might be lifted locally at the edges due to spontaneous symmetry breaking. The Green's functions in our approach are obtained by a two-site dynamical impurity approximation [228–232].

8.2 Variational cluster approach

The one-electron Green's function is needed to determine the topological Hamiltonian. Since an exact solution of the full many-body problem is not possible, an approximative method has to be chosen. Here we apply the variational cluster approach (VCA) [228, 230], because the Kane-Mele-Hubbard model is known to have an antiferromagnetic moment [12, 212–215, 219, 220] which can efficiently be treated by the VCA with symmetry-breaking Weiss fields [231, 232].

The VCA is based on the self-energy functional approach, which uses the fact that the grand potential of an arbitrary interacting system $H = H_0(\boldsymbol{t}) + H_1(\boldsymbol{U})$ has to be a stationary point of the self-energy functional

$$\Omega_{\boldsymbol{t}}[\Sigma] \equiv \mathrm{Tr}\log\left(-(G_0^{-1} - \Sigma)^{-1}\right) + F[\Sigma], \tag{8.2}$$

where $F[\Sigma]$ denotes the Legendre transform of the Luttinger-Ward functional $\Phi[G]$ [228, 233]. The approximation of this method is to restrict the space of self-energies Σ. This subset $\mathcal{S}$ of self-energies is spanned by all $\Sigma(\boldsymbol{t}')$ that are the exact self-energies of a so-called reference system $H' = H_0(\boldsymbol{t}') + H_1(\boldsymbol{U})$. The interaction parameters $\boldsymbol{U}$ are the same as in the original system, but H and H' can differ in the one-particle parameters. The one-particle parameters $\boldsymbol{t}'$ of the reference system H' are chosen such that the self-energy of the reference system can be calculated exactly. To obtain the approximative physical self-energy $\Sigma \in \mathcal{S}$, a stationary point of $\Omega_{\boldsymbol{t}}[\Sigma(\boldsymbol{t}')]$ has to be found as $\boldsymbol{t}'$ is varied.

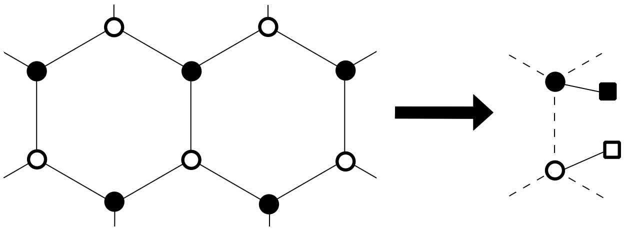

Figure 8.1: The left plot shows the full system, the right the reference system. Full symbols denote sublattice A, open symbols sublattice B. The bath sites (squares) are characterized only by an on-site energy. The impurity sites (circles), on which the Hubbard U is acting, can additionally carry the symmetry-breaking Weiss fields.

The parametrized functional can be reduced to

$$\begin{aligned}\Omega_{\boldsymbol{t}}[\Sigma(\boldsymbol{t}')] &= \Omega'(\boldsymbol{t}') + \operatorname{Tr}\log\left(-\left(G_0^{-1}(\boldsymbol{t}) - \Sigma(\boldsymbol{t}')\right)^{-1}\right) \\ &\quad -\operatorname{Tr}\log\left(-\left(G_0^{-1}(\boldsymbol{t}') - \Sigma(\boldsymbol{t}')\right)^{-1}\right) \qquad (8.3)\end{aligned}$$

and can thus be calculated if the Green's function of the reference system is known. Quite generally, reference systems in the VCA are clusters of finite size, which can be treated by exact diagonalization techniques [228, 230, 231].

In case of the KMH model, several cluster sizes have already been analyzed [218–220]. However, the tiling of the lattice into clusters of finite sizes breaks artificially some symmetries, which can change the topological phase diagram [234]. That is why we choose as a reference system for VCA single-site clusters, which are coupled to one additional bath site by a hopping V. This rather simple approach, called two-site dynamical impurity approximation (DIA) [229], has two advantages. First, despite its simplicity, it gives accurate results for the transition towards an antiferromagnetic insulator for two-dimensional Hubbard models [229]. Second, which is even more important, the lattice symmetries are trivially satisfied. A drawback of this method is the locality of the self-energy. We will show below, however, that for known cases we get very good agreement with existing results obtained by numerically much more expensive methods.

Since the honeycomb lattice has two distinct sites, the unit cell is tiled by two clusters, which are coupled by the noninteracting part of the Hamiltonian, as shown in Fig. 8.1. On-site energies on both impurity and bath site, as well as the connecting hopping between them, give in total three variational parameters per cluster. However, in the inversion-symmetric case ($\lambda_\nu = 0$), the on-site energies are fixed by particle-hole symmetry and only one parameter remains.

In order to capture symmetry breaking necessary for the emerging antiferromagnetic moment, a Weiss field

$$H_{\mathrm{AF}} = \sum_i c_i^\dagger \left(\boldsymbol{h}_i \cdot \boldsymbol{\sigma}\right) c_i \tag{8.4}$$

has to be added [232]. Without any symmetry considerations, these fields on both A and B sites give in total 6 variational parameters. Due to the inversion-symmetry breaking on-site potential λ_ν, a second Weiss field

$$H_\Delta = \Delta \sum_i \xi_i c_i^\dagger c_i \tag{8.5}$$

is used to enable unequal electron densities on the two sublattices. As in Eq. (7.8), $\xi_i = \pm 1$, depending on the sublattice. This Weiss field is basically a renormalisation of λ_ν in the reference system, which is caused by the interplay of the sublattice potential and Hubbard interaction.

The method described so far considers bulk properties. Introducing an edge destroys translational symmetry and influences therefore local magnetization. As known from field theoretical investigations, mean-field approximation gives a finite magnetization on the zigzag edge for every finite interaction strength [213]. This could lead to a breakdown of the bulk-boundary correspondence and may cause problems for calculating topological invariants using the existence of gapless edge states as a proof for nontrivial topology, which has so far been used in some cases of interacting systems without inversion symmetry [218, 220, 222]. Vice versa, a nontrivial topological invariant in the bulk may not result in gapless edge states due to locally broken time-reversal symmetry caused by spontaneous symmetry breaking. Therefore, we additionally implemented the DIA on the zigzag ribbon in order to compare the topological invariants defined by the bulk Green's function to the existence of gapless edge states. The ribbon is translationally invariant in the x direction, whereas the sites along the width of the ribbon are distinct. If a unit cell contains N pairs of A and B sites, $2N$ clusters containing each a bath and an impurity site have to be solved and effectively coupled by the noninteracting part of the Hamiltonian (see Fig. 8.2). In order to keep the number of parameters manageable, the on-site energies and hybridizations are chosen to be constant along the ribbon. To allow for edge magnetization, the antiferromagnetic Weiss fields for each pair of sites A and B is varied independently, only assuming a mirror symmetry $y \mapsto -y$.

8.3 Results

8.3.1 Bulk

As mentioned above, the hopping to the bath sites, the magnetic Weiss fields, and the sublattice potential Weiss field have to be determined in the VCA. For all stationary points, the ferromagnetic part of the Weiss field vanishes, hence only an antiferromagnetic ordering $\boldsymbol{h}_A = -\boldsymbol{h}_B$ is possible. Without spin-orbit coupling, the system has full $SU(2)$ symmetry, so only the absolute value of the Weiss field has to be determined. When spin-orbit coupling is included, only the xy-plane is still degenerate, but

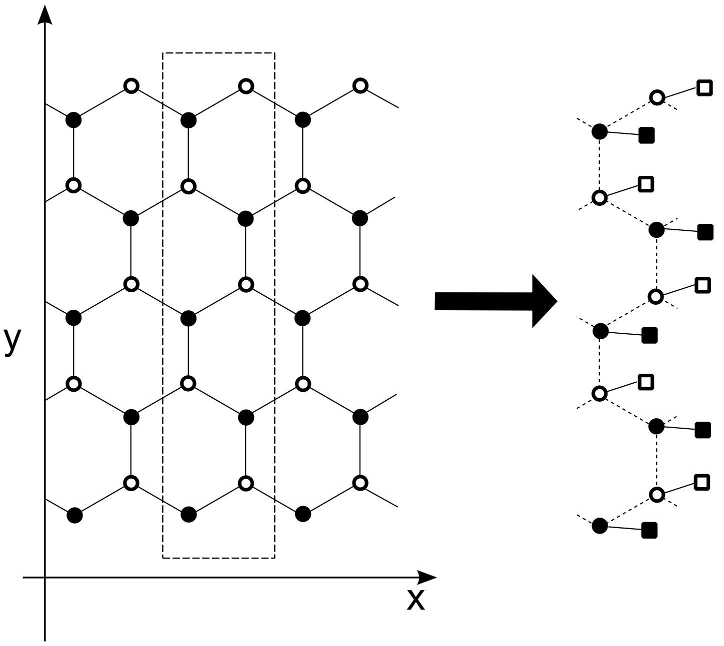

Figure 8.2: Unit cell of the zigzag ribbon and the according reference system. The respective two-site clusters are identical, except for a different AF Weiss field.

the degeneracy of the z direction is lifted. This means that we have to deal with two antiferromagnetic Weiss fields, h_z and h_x. To analyze the direction of the antiferromagnetic moment, we calculate a two-dimensional surface of the self-energy functional $\Omega(h_z, h_x)$, where all other variational parameters are optimized for each set of variables (h_z, h_x). The stationary points, i.e. extrema and saddle points, of this two-dimensional surfaces are physical solutions, where the stable solution is the one with lowest potential Ω. Fig. 8.3 shows the value of the self-energy functional as a function of both in-plane and out-of-plane AF symmetry-breaking field. Depending on the KMH model parameters, up to three different stationary points exist: A saddle point of Ω if $\boldsymbol{h}$ points in z direction; a minimum if it is in the xy plane; the nonmagnetic solution, which can be both maximum or minimum, depending on the parameters. This is consistent with the results of other cluster geometries [218, 220]. The local minimum $\boldsymbol{h} \parallel \hat{z}$ is never the physically realized solution with the lowest grand potential Ω for all sets of parameters considered here. Hence, only one variational quantity is needed for the AF Weiss field, namely the in-plane antiferromagnetic component. As mentioned above, the on-site energy levels of both impurity and bath are fixed by particle hole symmetry and the given chemical potential. Therefore, in total three cluster parameters have to be optimized: The hopping V between impurity and bath, the in-plane antiferromagnetic Weiss field h_x, and the potential difference between the two sublattices Δ.

Directly from the two-site DIA one can distinguish two phases, the antiferromagnetic insulator for large U and the nonmagnetic insulator for small U. The system reduces

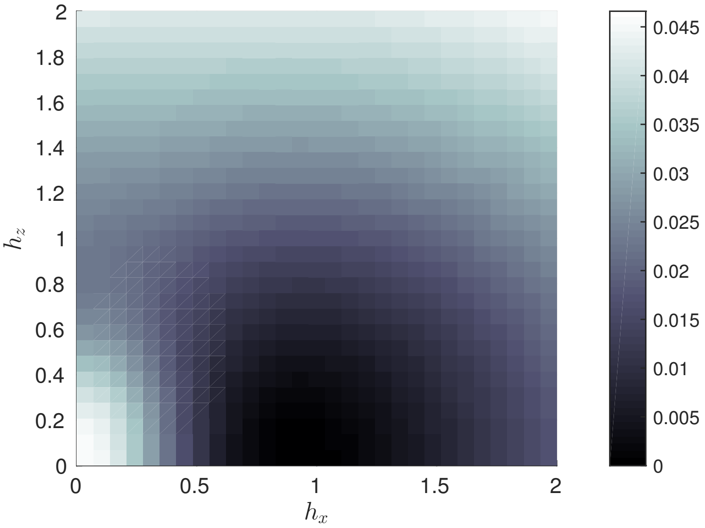

Figure 8.3: Self-energy functional as a function of the antiferromagnetic Weiss fields h_z and h_x for $\lambda_{\mathrm{SO}} = 0.1$, $\lambda_\nu = 0$ and $U = 5$. The hybridization of the bath sites has been optimized for each grid point individually. The global minimum around $h_x \approx 1$ and $h_z = 0$ can clearly be seen.

to the ordinary Hubbard model on the honeycomb lattice if $\lambda_{\mathrm{SO}} = 0$ and $\lambda_\nu = 0$. In this case, the magnetization direction is not important since $SU(2)$ symmetry is not broken. The mean-field critical interaction is $U_{\mathrm{c}} = 2.23$ [212, 235], which is lower as compared to more accurate methods. Quantum Monte Carlo simulations show that it is actually slightly above 4 [12, 214–216, 235]. The two-site DIA considered in this work is expected to give similar results as other variational methods. VCA gives critical interactions between 2.4 and 4, depending on the cluster geometries [218–220], which coincides with our DIA results of $U_{\mathrm{c}} = 3.7$, where we observe a second-order phase transition. With increasing λ_{SO}, all methods show that U_{c} increases as well. Mean-field [212], however, overestimates here the slope in comparison with the more elaborate methods [12, 214–216, 218–220]. The reason for that is analyzed in the Sec. 8.5. Our results show a similar behaviour as VCA with different cluster geometries [220]. To sum up, in the inversion-symmetric case the two-site DIA is in good agreement with other methods. We can therefore expect that the method is suitable to explore the model when inversion symmetry is broken.

Using the topological Hamiltonian defined in Eq. (4.60) in combination with the Soluyanov-Vanderbilt method, information on the topological properties can be obtained in addition to the magnetic ordering. In the noninteracting case, a topological phase transition occurs at $\lambda_\nu = 3\sqrt{3}\lambda_{\mathrm{SO}}$, as known from the original work by Kane and Mele [13, 14]. Including a Hubbard interaction U, the topological Hamiltonian has the same structure as the noninteracting Hamiltonian, as long as the antiferromagnetic moment vanishes. However, both self-energy and staggered on-site Weiss field renormalize

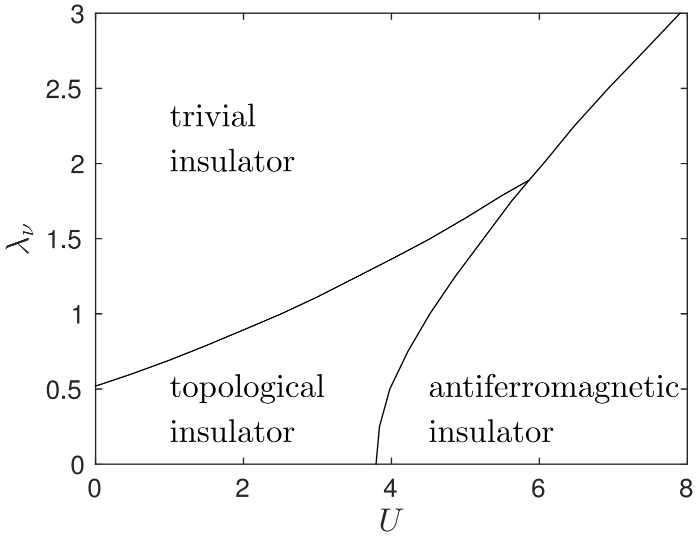

Figure 8.4: Phase diagram of the KMH model obtained from two-site DIA, as a function of the Hubbard interaction and the sublattice potential for a spin-orbit coupling of $\lambda_{\mathrm{SO}} = 0.1$.

the energy scales. The interplay of interaction and on-site energy can be seen as follows: Without interaction, the sublattice with the lower on-site energy has a higher double occupancy. A finite Hubbard U punishes double occupancies, and reduces as a result the double occupancy on the sublattice with lower on-site energy. Hence, the sublattice potential λ_ν is effectively lowered in case of a finite U, stabilizing the topological phase, and shifting the critical λ_ν to higher values. The resulting phase diagram is shown in Fig. 8.4. This stabilization effect is also captured in mean-field, although with quantitative differences [224]. We want to note that we cross-checked the validity of our Wannier charge center (WCC) approach by calculating the spin Chern number C_{S} directly from Eqs. (4.41) and (4.57) for the selected value of $U = 1$. We found perfect quantitative agreement.

This reasoning for the stabilisation of the topological phase is only valid in case of weak interactions where the antiferromagnetic Weiss field is zero. In the strongly interacting regime, the non-vanishing Weiss field causes a time-reversal symmetry breaking term proportional to $\sigma_x \otimes \tau_z$ (σ acts in spin space, τ in sublattice space) in the topological Hamiltonian. As a consequence, the topological invariant in the sense of Fu and Kane [105] is not defined. This can also be seen in the WCC, where the lifted Kramer's degeneracy does not enforce the two WCCs to be identical at half the period of the pumping parameter. Examples of the WCCs are shown in Fig. 8.5. In this regime, not just quantitative, but also qualitative differences compared to a standard Hartree-Fock mean-field arise, as discussed in Sec. 8.5. To sum up, three phases exist for a given spin-orbit coupling: (i) a topological insulator continuously connected to the quantum spin Hall phases of the non-interacting KM-model if both λ_ν and U are small enough; (ii)

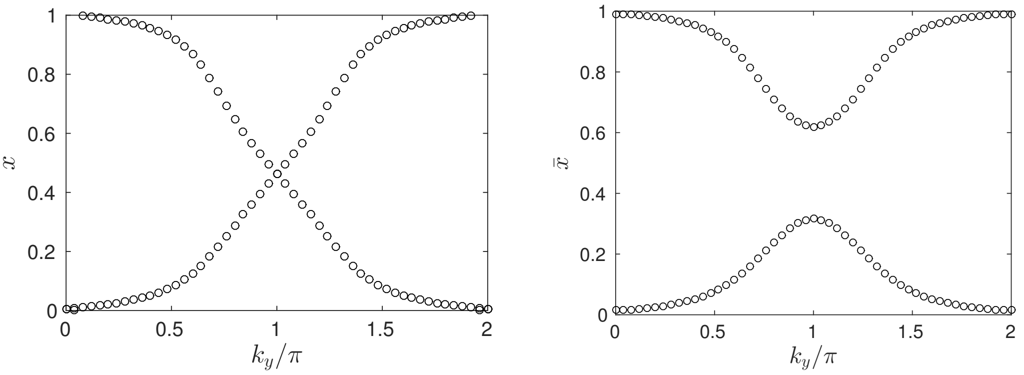

Figure 8.5: Wannier charge centers $\bar{x}(k_y)$ of the topological Hamiltonian for $\lambda_{\mathrm{SO}} = 0.1, \lambda_\nu = 0.25$, and $U = 3$ (left) and $U = 4$ (right).

a trivial band insulator if λ_ν is large; (iii) an antiferromagnetic insulator with in-plane magnetization for large U. The phase boundaries are shown in Fig. 8.4. Interestingly, similar results of an enhanced topological phase have been reported for the Kane-Mele model including long-ranged Coulomb interactions [236]. There, the Coulomb interaction induces charge-density-wave fluctuations, while our model shows static charge ordering through staggered potentials.

8.3.2 Ribbon

In order to analyze the robustness of the topological phases presented in the last section and to investigate the bulk-boundary correspondence, we calculate directly the edge properties on a zigzag ribbon of finite width.

We first consider the inversion-symmetric case, $\lambda_\nu = 0$. Mean-field results have shown different magnetizations at the edge than in the middle of the ribbon [213]. This agrees with our results, and an example of the structure of the Weiss fields across the ribbon profile is shown in the inset of Fig. 8.6. The larger field at the edges decays quickly to the bulk value. The optimized values of both edge and midpoint antiferromagnetic fields as a function of U are shown in Fig. 8.6 for $\lambda_{\mathrm{SO}} = 0.1$. At the edges, any finite U results in a finite antiferromagnetic field. Sites that are not at the edges have a Weiss field comparable to the bulk values. Just below the bulk magnetic transition at $U \approx 3.8$ they become finite, though small, which is a finite-size effect caused by the increasing correlation length as the magnetic transition is approached. The main consequence of the non-vanishing Weiss field is that the finite magnetization at the edges breaks time-reversal symmetry for any U and gaps therefore the edge states. As the interaction is below the critical value for the bulk magnetic transition, topological analysis of the bulk suggests a topological insulator with gapless edge states, but a local symmetry breaking at the edges causes the edge states to gap. This local effect, namely that local time-reversal symmetry breaking by a magnetic field causes states to gap, cannot be captured

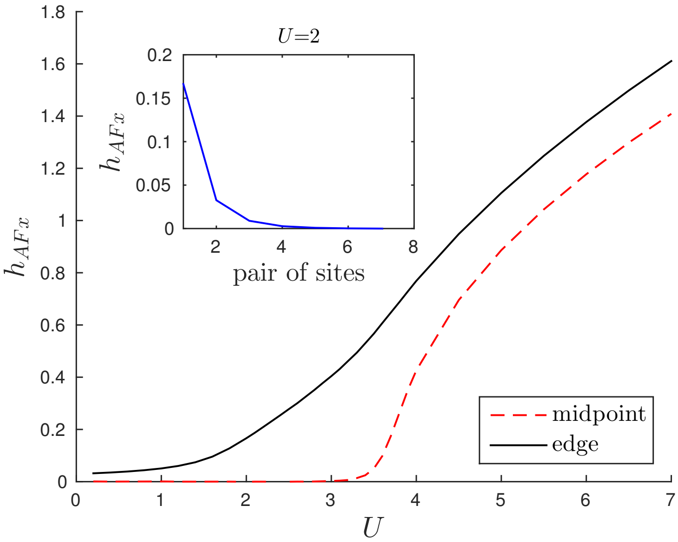

Figure 8.6: Antiferromagnetic Weiss field of the first pair of sites A and B of the ribbon (solid) and in the middle of the ribbon (dashed) as a function of U for $\lambda_{\mathrm{SO}} = 0.1$, $\lambda_\nu = 0$ and $N = 16$ pairs of sites. The inset shows how the moment at the edge decays across the ribbon to the midpoint for $U = 2$.

within a topological invariant of the two-dimensional (2D) system. However, at what point in the phase diagram this local symmetry breaking occurs, depends both on the specific model and also on the edge geometry. For example, for the armchair ribbon, there is a region at small U with vanishing edge magnetization and therefore gapless edge states, even in the inversion-symmetric case $\lambda_\nu = 0$.

In the last paragraph it is demonstrated that gapless edge states are impossible on a zigzag ribbon for any finite U, as long as $\lambda_\nu = 0$. This picture changes if inversion symmetry is broken. From the bulk calculations we know that λ_ν tends to suppress magnetic ordering, where it increases the critical value of interaction U_{c} for the magnetic transition (Fig. 8.4). The same principle is observed looking at the edge magnetization as a function of λ_ν. For given U and λ_{SO}, the Weiss field at the edges changes only marginally as λ_ν is increased, and the edge is magnetic. However, at a critical value λ_ν^{c}, the magnetic moment drops to 0 in a first-order phase transition. This critical value λ_ν^{c} strongly depends on U. For $\lambda_{\mathrm{SO}} = 0.1$, for example, we get $\lambda_\nu^{\mathrm{c}} = 0.006$ as $U = 1$, and it raises by an order of magnitude to $\lambda_\nu^{\mathrm{c}} = 0.07$ for $U = 2$ and to $\lambda_\nu^{\mathrm{c}} = 0.35$ for $U = 3$.

This argument can of course be turned around. Fixing the sublattice potential λ_ν and varying the interaction strength U, one finds a critical value U_{c} for the magnetic transition with finite magnetic moment only for $U > U_{\mathrm{c}}$. This critical value U_{c} raises continuously with increasing sublattice potential λ_ν, starting from $U_{\mathrm{c}} = 0$ at $\lambda_\nu = 0$.

Exemplary spectral functions are shown in Fig. 8.7, where we use spin-orbit coupling strength $\lambda_{\mathrm{SO}} = 0.1$ and interaction strength $U = 2.5$. If the sublattice potential λ_ν is

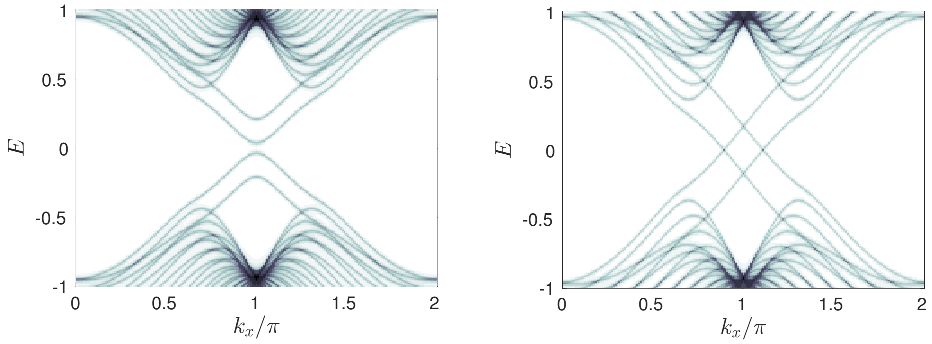

Figure 8.7: Spectral functions of the KMH zigzag ribbon with parameters $U = 2.5$, $\lambda_{\mathrm{SO}} = 0.1$, and $N = 16$. Left panel: $\lambda_\nu = 0.1$ leads to a magnetic solution with a Weiss field of about $h_{\mathrm{AF}x} = 0.4$, gapping the edge states. Right panel: $\lambda_\nu = 0.2$, with a vanishing Weiss field and gapless edge states.

below the critical value, as in the left panel of Fig. 8.7, the edge is magnetic and the edge states are gapped. For $\lambda_\nu > \lambda_\nu^{\mathrm{c}}$ there is no magnetization at the edge, and gapless states occur. We want to stress again that gapless edge states do not occur at any finite U in the inversion-symmetric case. To sum up, an inversion-symmetry-breaking term can stabilize the gapless edge state.

8.4 Conclusion and Discussion

We have investigated the topological properties of the Kane-Mele-Hubbard model, comparing cases with and without inversion symmetry. For the calculation of the topological invariants we apply a combination of the topological Hamiltonian approach and the Wannier charge center method. This approach allowed to calculate the phase diagram of the KMH model in the U-λ_ν plane. The inversion-symmetry-breaking term λ_ν has a two-fold effect. First, for large values the topological order is destroyed and a trivial insulator obtained. Second, in combination with interactions the topological order is enhanced, pushing the phase boundaries towards the antiferromagnetic insulator to larger critical values of U.

This effect can also be seen in the surface properties of the honeycomb lattice. In agreement with previous studies, our calculations on the zigzag-ribbon geometry have shown that with inversion symmetry any finite value of U results in a finite edge magnetization, which in turn produces a finite gap in the edge states. Introducing an inversion-symmetry-breaking field, this critical value U_{c} is shifted to finite values, below which the whole ribbon including the edge is nonmagnetic, and a gapless surface state exists. As a result, one can find gapless edge states on the zigzag ribbon only when inversion symmetry is lifted and the interaction strength U is small enough, such that no ordered magnetic moments can form.

Our study is based on the Kane-Mele Hamiltonian, which was introduced as the low-

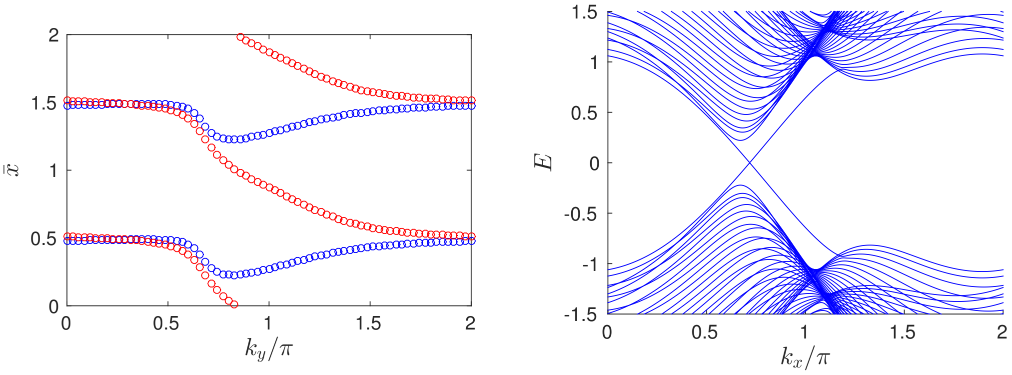

Figure 8.8: Chern insulator phase of the KMH model in mean-field approximation with antiferromagnetic moment in z direction for $U = 3.2$, $\lambda_{\mathrm{SO}} = 0.1$, $\lambda_\nu = 0.4$. The left graph shows Wannier charge centers from the bulk calculations. The blue curve is the WCC of the spin up band, the red curve the WCC of the spin down band, resulting in $C_\uparrow = 0$ and $C_\downarrow = -1$. The right graph shows the bands of a ribbon ($N = 32$) with one spin down, but no spin up edge state.

energy Hamiltonian for graphene. Since the bulk gap in graphene is minute, the effects that we propose here are difficult to see in this material. However, there is increasing interest in artificial honeycomb systems using heavy atoms, such as bismuthene on SiC substrate [190]. Since these systems are grown artificially, it might be possible to modify their structure such that inversion symmetry is broken and the influence of this symmetry breaking on the topological properties can be studied.

8.5 Discussion - Comparison to mean-field

As mentioned in Sec. 8.3.1, the basic structures of the topological Hamiltonian could also be found in a mean-field approximation since the self-energy is diagonal. Usually, the z axis is chosen as the axis of mean-field decomposition [212]. The resulting matrix is then qualitatively different from the topological Hamiltonian of the DIA, since the mean-field magnetic moment points in the z direction. In order to respect that the easy axis is in-plane, we did a mean-field decoupling in the x direction

$$n_{i\uparrow}n_{i\downarrow} \approx \left(\langle n_{i\leftarrow}\rangle n_{i\rightarrow} + \langle n_{i\rightarrow}\rangle n_{i\leftarrow} - \langle n_{i\leftarrow}\rangle\langle n_{i\rightarrow}\rangle\right), \tag{8.6}$$

where $|\rightleftarrows\rangle = 1/\sqrt{2}\,(|\uparrow\rangle \pm |\downarrow\rangle)$. Within this framework, the same phases as in the DIA appear, where the mean-field one-electron Bloch Hamiltonian corresponds to the topological Hamiltonian. The phase boundaries, however, will shift since a bare mean-field approach does not capture quantum dynamics as the DIA.

In case of the Hubbard model on a honeycomb lattice $\lambda_{\mathrm{SO}} = \lambda_\nu = 0$, the magnetization direction is not important since $SU(2)$ symmetry is not broken. The mean-field critical interaction for any quantization axis is $U_\mathrm{c} = 2.23$ [212, 235]. If $\lambda_\mathrm{SO} \neq 0$, the difference between the two mean-field methods is important. Since the in-plane magnetic moment is always favorable, a restriction of the magnetization direction to be out-of-plane requires stronger interactions for the stability of the antiferromagnetic solution. This is the case in a conventional mean-field theory [212, 224], hence, U_c is overestimated in comparison with an in-plane mean-field approach (8.6). Consequently, the slope of the U_c-λ_SO phase boundary is higher if z is used as a quantization axis.

In addition to the magnetic transition considered so far, using Wannier charge centers as an analytical tool allows again to extract topological information. The DIA results are described in the previous sections, showing the phase diagram of three different phases in Fig. 8.4. As mentioned above, the mean-field decoupling in the x direction gives qualitatively the same phases since the MF Bloch Hamiltonian has the same structure as the DIA topological Hamiltonian, but underestimates U_c. New phases appear, however, in the standard Hartree-Fock approach where the z axis is the quantization direction. The Hamiltonian splits into spin up and spin down parts, which are decoupled if neither Rashba coupling nor in-plane magnetization are present. Hence, even though time-reversal symmetry is broken in the presence of an antiferromagnetic moment, a $\mathbb{Z}_2$ invariant can be defined using the spin Chern number $\nu_\mathrm{S} = C_\mathrm{S} \mod 2$, $C_\mathrm{S} = (C_\uparrow - C_\downarrow)/2$ as introduced by Sheng *et al.* [103] (see Sec. 4.7.2). The Chern numbers of the two spin categories are determined with the Wannier charge centers: Because of the conservation of S_z, the two WCC can be labeled by their spin. The Chern number C_S is then given by the difference of the WCCs $\bar{x}_\uparrow$ and $\bar{x}_\downarrow$ as they evolve continuously from 0 to 2π.

In the inversion-symmetric case, the only mean-field parameter that has to be determined self-consistently is the antiferromagnetic moment $M_\mathrm{AF} = \langle n_{A\uparrow}\rangle - \langle n_{B\uparrow}\rangle = \langle n_{B\downarrow}\rangle - \langle n_{A\downarrow}\rangle$. A change of both Chern numbers $C_\uparrow$ and $C_\downarrow$ occurs when the gap closes at a critical moment $M_\mathrm{AF}^\mathrm{c} = 12\sqrt{3}/U$, which follows from diagonalizing the mean-field Bloch Hamiltonian. Since M_AF rises continuously from 0 as U is increased, magnetic and topological transition do not coincide, leading to an antiferromagnetic quantum spin Hall phase between the two transitions.

If additionally inversion symmetry is broken, both on-site energy and occupation of A and B sites are different. Together with the magnetic order, this leads to different M_AF^c for spin up and spin down electrons. If $C_\uparrow = 0$ and $C_\downarrow = 1$ or vice versa, the total Chern number $C = C_\uparrow + C_\downarrow$ is nontrivial. Hence, for a certain parameter range, an antiferromagnetic Chern insulator is realized (see Fig. 8.8). Both Chern insulator and antiferromagnetic quantum spin Hall insulator have also been found recently for cases where the symmetry breaking is not due to an on-site potential, but due to a spin-dependent hopping [225]. These phases are stable since for certain parameter regions the out-of-plane magnetization is energetically favorable.

The topological properties of the Chern insulator are not bound to time-reversal symmetry but related to the spin structure only. The number of edge states is directly determined by the Chern numbers of spin up and spin down electrons. As an example, the bands of a zigzag ribbon in the Chern insulator phase with only one edge state are shown in Fig. 8.8. Hence, bulk boundary correspondence is fully satisfied if the antiferromagnetic moment is in the z direction, but not if it is in-plane.

9 p_x-p_y model of bismuthene

9.1 Introduction

The Kane-Mele model discussed in the last two chapters is a nice toy model to study topological properties on the honeycomb lattice. However, in real materials, the gap induced by SOC will always be below room temperature, since it originates from second order perturbation theory (see Sec. 7.2). Therefore, possible practical applications for example in spintronics are limited. Only the direct, local SOC term $\lambda \boldsymbol{l} \cdot \boldsymbol{s}$ can open a topological gap larger than room temperature. In case of graphene-like structures, this is only possible when the p_x and p_y orbitals have major contributions in the bands around the Fermi energy since the local SOC of the p_z orbitals is quenched, as described in section 7.2. Furthermore, the p_z orbitals do no hybridize with the p_x and p_y orbitals due to the planar structure. Hence, in order to obtain bands around the Fermi energy that are sizably affected by the SOC, the p_z orbitals need to be shifted by some chemical modification of the graphene-like structure. One way proposed by Liu et al. is to passivate a bismuthene layer with hydrogen [191]. Reis et al., on the other hand, realized a large topological band gap by putting a bismuthene layer on a SiC substrate [190].

For a minimal model of such an insulator, the p_z orbitals can be neglected, as they are assumed to be completely filled. Furthermore, the s orbitals are lower in energy and have a smaller band width as compared to graphene (parameters and bands shown in Tab. 7.1 and Fig. 7.1), so that the hybridization between s orbitals and p_x and p_y orbitals is reduced. Therefore, such a system can be modeled by using only the p_x and the p_y orbitals.

9.2 Band structure including spin-orbit coupling

When only the in-plane orbitals p_x and p_y are considered, a finite local SOC persists. However, also here an important part of matrix elements vanishes: From Eq. (3.36), one sees that the p_x, p_y block of both l_x and l_y have no entries. Hence, the spin-orbit operator has in this case the special form $\boldsymbol{l} \cdot \boldsymbol{s} = l_z \otimes s_z$, and is thus diagonal in spin. Even though a local SOC is present, spin remains a good quantum number. Setting the on-site energy of the p_x and p_y elements to zero, the spin-up and spin-down parts of the tight-binding Hamiltonian read [190, 191][1]

$$H_{\uparrow\uparrow/\downarrow\downarrow}(\boldsymbol{k}) = \begin{pmatrix} 0 & \mp\mathrm{i}\lambda/2 & h_{xx} & h_{xy} \\ \pm\mathrm{i}\lambda/2 & 0 & h_{yx} & h_{yy} \\ h_{xx}^* & h_{yx}^* & 0 & \mp\mathrm{i}\lambda/2 \\ h_{xy}^* & h_{yy}^* & \pm\mathrm{i}\lambda/2 & 0 \end{pmatrix}, \tag{9.1}$$

with matrix elements given by (7.5). The spin-coupling parts $H_{\uparrow\downarrow}$ and $H_{\downarrow\uparrow}$ are zero. However, an additional Rashba coupling originating from breaking the mirror symmetry in z direction (e.g. by putting the layer on a substrate) leads to a coupling of the spins. The resulting $\boldsymbol{k}$-dependent matrix elements can be found in the supplementary material of Ref. [190]. The band structure without Rashba coupling is shown in Fig. 9.1. The bandgap stems from the SOC and is of topological nature.

9.3 Introducing interactions

So far, the p_x-p_y model describes a noninteracting topological insulator. Similar to the Kane-Mele-Hubbard Hamiltonian analyzed in chapter 8, one can generalize this model by including an interaction Hamiltonian. The most general Hamiltonian for two p orbitals is a two-band Kanamori Hamiltonian 2.31, with $U' = U - 2J_\mathrm{H}$ (see Sec. 2.2). In chapter 6, the interplay of SOC and correlations is analyzed by means of the correlation strength of a metallic model. Here, the focus is on the topological properties of an insulator. The tools used to do so are DMFT in order to obtain the correlated Green's function, and the topological Hamiltonian (4.60) to describe topological properties. The non-interacting model is the nearest neighbor tight-binding model for bismuthene (9.1) including SOC. Since the DMFT self-energy is independent of the momentum, the topological Hamiltonian is given by

$$H_\mathrm{t}(\boldsymbol{k}) = -G^{-1}(\boldsymbol{k}, \omega = 0) = H(\boldsymbol{k}) - \mu\mathbb{1} + \Sigma(\omega = 0). \tag{9.2}$$

Therefore, the self-energy at zero frequency is the DMFT output relevant for the topology and needs further discussion.

In order to obtain the self-energy, DMFT calculations were performed for $V_{p\sigma} = -2.0\,\mathrm{eV}$, $V_{p\sigma} = -0.3\,\mathrm{eV}$, and different values of λ, U, and J_H at an inverse temperature $\beta = 40\,\mathrm{eV}^{-1}$ using TRIQS [168], DFTTools [33], and the CTHYB solver [169]. For the experimental value $\lambda = 0.870\,\mathrm{eV}$ and test interaction parameters $U = 5\,\mathrm{eV}$ and $J_\mathrm{H} = 0.5\,\mathrm{eV}$, the resulting self-energy is shown in Fig. 9.2. The chosen basis was the cubic basis, since no significant sign problem occurred. However, it is still insightful to switch to the basis where the local Hamiltonian is diagonal. The local Hamiltonian

---

[1] Note that the definition of λ in Ref. [190] corresponds to $\lambda/2$ here.

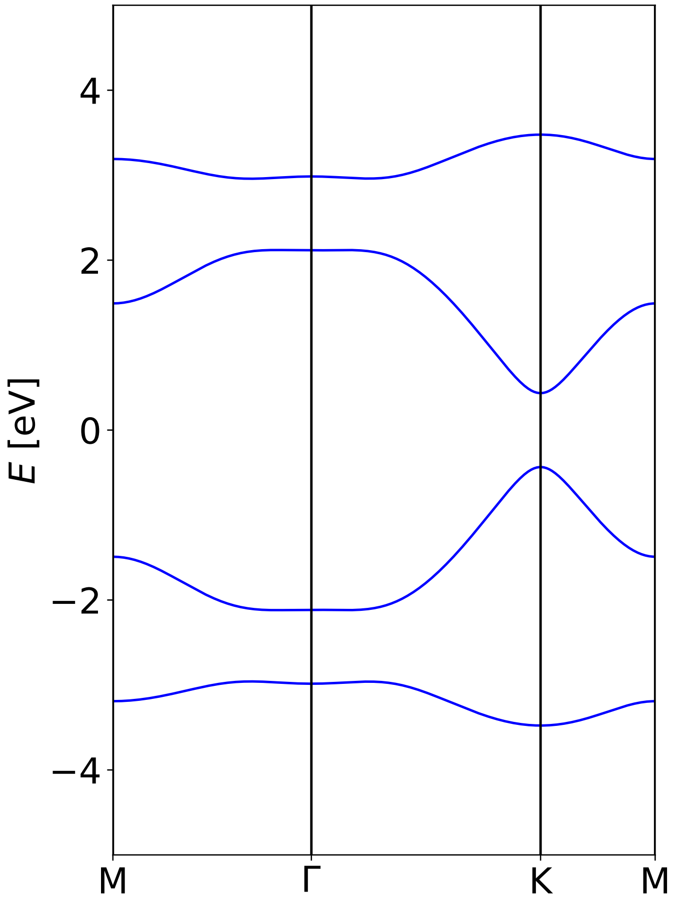

Figure 9.1: Tight-binding band structure of the tight-binding model of bismuthene (9.1) using $V_{p\sigma} = -2.0\,\mathrm{eV}$, $V_{p\sigma} = -0.3\,\mathrm{eV}$, and $\lambda = 0.870\,\mathrm{eV}$.

consists, except for a chemical potential, only of the SOC

$$H_{\text{loc}} = \frac{\lambda}{2}\begin{pmatrix} 0 & -\mathrm{i} & 0 & 0 \\ \mathrm{i} & 0 & 0 & 0 \\ 0 & 0 & 0 & \mathrm{i} \\ 0 & 0 & -\mathrm{i} & 0 \end{pmatrix}. \tag{9.3}$$

The eigenbasis is

$$\begin{aligned} \left|p_\pm^\uparrow\right\rangle &= \frac{1}{\sqrt{2}}\left(\left|p_x^\uparrow\right\rangle \pm \mathrm{i}\left|p_y^\uparrow\right\rangle\right) \\ \left|p_\pm^\downarrow\right\rangle &= \frac{1}{\sqrt{2}}\left(\left|p_x^\downarrow\right\rangle \pm \mathrm{i}\left|p_y^\downarrow\right\rangle\right), \end{aligned} \tag{9.4}$$

where $\left|p_+^\uparrow\right\rangle$ and $\left|p_-^\downarrow\right\rangle$ have the eigenvalue $\lambda/2$, the other two the eigenvalue $-\lambda/2$. In this basis, self-energy of the p_x-p_y model is diagonal. Due to the different sign of λ in the two spin blocks of the local Hamiltonian, $\Sigma_+^\uparrow = \Sigma_-^\downarrow$ and $\Sigma_-^\uparrow = \Sigma_+^\downarrow$ as long as the system is nonmagnetic. One can expand the self-energy matrix in terms of $\boldsymbol{l}\cdot\boldsymbol{s}$ and the unit matrix, similar as in section 6, via

$$\Sigma = \frac{1}{2}\left(\Sigma_+^\uparrow + \Sigma_-^\uparrow\right)\mathbb{1} + \left(\Sigma_+^\uparrow - \Sigma_-^\uparrow\right)\boldsymbol{l}\cdot\boldsymbol{s}. \tag{9.5}$$

Therefore, the strength of the effective SOC is determined by the difference of the two self-energies

$$\lambda_{\text{eff}} = \lambda(\omega) + \Sigma_+^\uparrow(\omega) - \Sigma_-^\uparrow(\omega). \tag{9.6}$$

Using the topological Hamiltonian (9.2) with the self-energy (9.5) and keeping in mind that the parts proportional to the unit matrix have no influence on the topology, the only topological effect of the paramagnetic DMFT calculation is that λ changes to its effective value given by (9.6). The real part of $\Sigma_+^\uparrow - \Sigma_-^\uparrow$ is equivalent to the imaginary part of Σ_{yx} in the cubic basis, which is displayed in the lower panel of Fig. 9.2. One sees that it is positive for all Matsubara frequencies $\mathrm{i}\omega_n$, hence the SOC is enhanced by correlations. This is also true for other sets of parameters that were calculated. Since $\lambda_{\text{eff}}(\omega = 0)$ is the relevant parameter according to the topological Hamiltonian, interactions stabilize the topological phase.

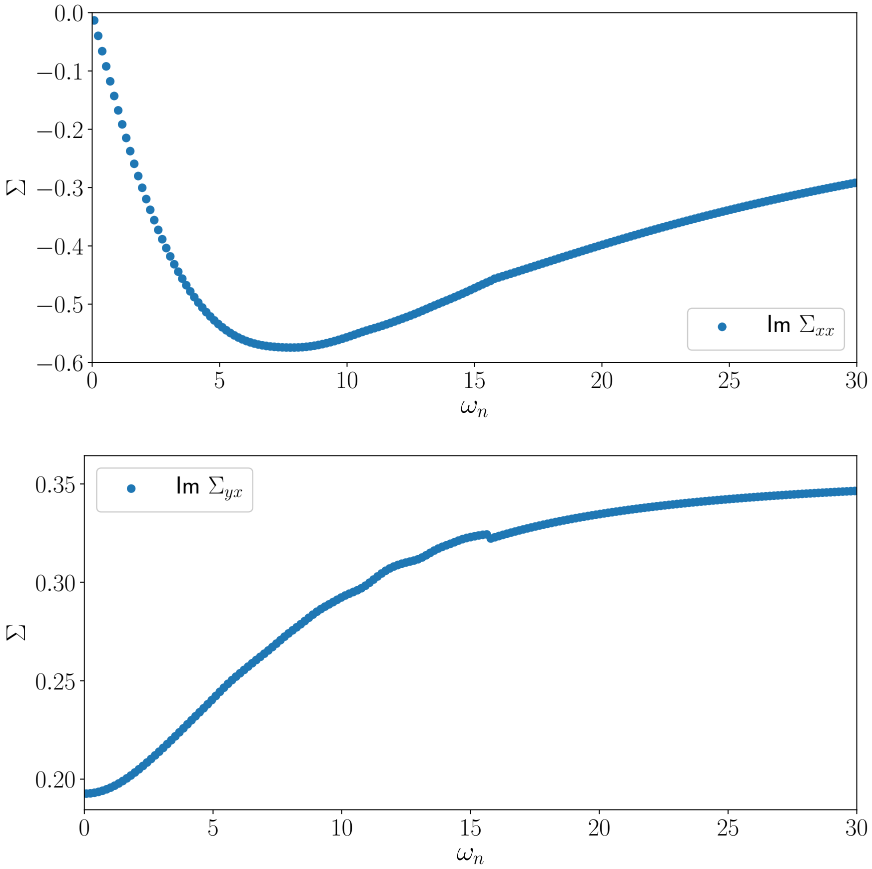

Figure 9.2: Self-energy as a function of Matsubara frequencies ω_n of the tight-binding model of bismuthene (9.1) using $V_{p\sigma} = -2.0\,\mathrm{eV}$, $V_{p\sigma} = -0.3\,\mathrm{eV}$, and $\lambda = 0.870\,\mathrm{eV}$, with a Kanamori interaction using artificial interaction parameters $U = 5\,\mathrm{eV}$ and $J_\mathrm{H} = 0.5\,\mathrm{eV}$. The upper panel shows the imaginary part of the diagonal elements $\mathrm{Im}\Sigma^{\uparrow}_{xx} = \mathrm{Im}\Sigma^{\uparrow}_{yy} = \mathrm{Im}\Sigma^{\downarrow}_{xx} = \mathrm{Im}\Sigma^{\downarrow}_{yy}$, the lower panel the imaginary part of the off-diagonal elements $\mathrm{Im}\Sigma^{\uparrow}_{yx} = -\mathrm{Im}\Sigma^{\uparrow}_{xy} = \mathrm{Im}\Sigma^{\downarrow}_{xy} = -\mathrm{Im}\Sigma^{\downarrow}_{yx}$. The real parts are all constant in $\mathrm{i}\omega_n$.

Bibliography

1. Anderson, P. W. More Is Different. *Science* **177,** 393–396 (1972) (cit. on p. 1).
2. Baibich, M. N., Broto, J. M., Fert, A., Van Dau, F. N., Petroff, F., Etienne, P., Creuzet, G., Friederich, A. & Chazelas, J. Giant Magnetoresistance of (001)Fe/(001)Cr Magnetic Superlattices. *Phys. Rev. Lett.* **61,** 2472–2475 (1988) (cit. on p. 1).
3. Metzner, W. & Vollhardt, D. Correlated Lattice Fermions in $d = \infty$ Dimensions. *Phys. Rev. Lett.* **62,** 324–327 (1989) (cit. on pp. 1, 70).
4. Georges, A. & Kotliar, G. Hubbard model in infinite dimensions. *Phys. Rev. B* **45,** 6479–6483 (1992) (cit. on pp. 1, 17).
5. Georges, A., Kotliar, G., Krauth, W. & Rozenberg, M. J. Dynamical mean-field theory of strongly correlated fermion systems and the limit of infinite dimensions. *Rev. Mod. Phys.* **68,** 13–125 (1996) (cit. on pp. 1, 14, 17, 70).
6. Georges, A. Strongly Correlated Electron Materials: Dynamical Mean-Field Theory and Electronic Structure. *AIP Conference Proceedings* **715,** 3–74 (2004) (cit. on p. 1).
7. Kotliar, G. & Vollhardt, D. Strongly correlated materials: Insights from dynamical mean-field theory. *Physics Today* **57,** 53–59 (2004) (cit. on p. 1).
8. Hohenberg, P. & Kohn, W. Inhomogeneous Electron Gas. *Phys. Rev.* **136,** B864–B871 (1964) (cit. on pp. 1, 4).
9. Kohn, W. & Sham, L. J. Self-Consistent Equations Including Exchange and Correlation Effects. *Phys. Rev.* **140,** A1133–A1138 (1965) (cit. on pp. 1, 4).
10. Hasan, M. Z. & Kane, C. L. Colloquium: Topological insulators. *Rev. Mod. Phys.* **82,** 3045–3067 (2010) (cit. on pp. 2, 49, 100).
11. Ando, Y. Topological Insulator Materials. *Journal of the Physical Society of Japan* **82,** 102001 (2013) (cit. on pp. 2, 44, 49).
12. Hohenadler, M. & Assaad, F. F. Correlation effects in two-dimensional topological insulators. *Journal of Physics: Condensed Matter* **25,** 143201 (2013) (cit. on pp. 2, 49, 100, 101, 105).
13. Kane, C. L. & Mele, E. J. Z_2 Topological Order and the Quantum Spin Hall Effect. *Phys. Rev. Lett.* **95,** 146802 (2005) (cit. on pp. 2, 50, 97, 100, 101, 105).
14. Kane, C. L. & Mele, E. J. Quantum Spin Hall Effect in Graphene. *Phys. Rev. Lett.* **95,** 226801 (2005) (cit. on pp. 2, 50, 97, 100, 105).

15. Bernevig, B. A., Hughes, T. L. & Zhang, S.-C. Quantum Spin Hall Effect and Topological Phase Transition in HgTe Quantum Wells. *Science* **314,** 1757–1761 (2006) (cit. on pp. 2, 50).
16. König, M., Wiedmann, S., Brüne, C., Roth, A., Buhmann, H., Molenkamp, L. W., Qi, X.-L. & Zhang, S.-C. Quantum Spin Hall Insulator State in HgTe Quantum Wells. *Science* **318,** 766–770 (2007) (cit. on pp. 2, 50, 100).
17. Imada, M., Fujimori, A. & Tokura, Y. Metal-insulator transitions. *Rev. Mod. Phys.* **70,** 1039–1263 (1998) (cit. on pp. 2, 67).
18. Jackeli, G. & Khaliullin, G. Mott Insulators in the Strong Spin-Orbit Coupling Limit: From Heisenberg to a Quantum Compass and Kitaev Models. *Phys. Rev. Lett.* **102,** 017205 (2009) (cit. on pp. 2, 67).
19. Chaloupka, J., Jackeli, G. & Khaliullin, G. Kitaev-Heisenberg Model on a Honeycomb Lattice: Possible Exotic Phases in Iridium Oxides $A_2\mathrm{IrO}_3$. *Phys. Rev. Lett.* **105,** 027204 (2010) (cit. on pp. 2, 67).
20. Chen, G., Pereira, R. & Balents, L. Exotic phases induced by strong spin-orbit coupling in ordered double perovskites. *Phys. Rev. B* **82,** 174440 (2010) (cit. on pp. 2, 67).
21. Chen, G. & Balents, L. Spin-orbit coupling in d^2 ordered double perovskites. *Phys. Rev. B* **84,** 094420 (2011) (cit. on pp. 2, 67).
22. Khaliullin, G. Excitonic Magnetism in Van Vlecktype d^4 Mott Insulators. *Phys. Rev. Lett.* **111,** 197201 (2013) (cit. on pp. 2, 67, 70).
23. Chaloupka, J. & Khaliullin, G. Hidden symmetries of the extended Kitaev-Heisenberg model: Implications for the honeycomb-lattice iridates $A_2\mathrm{IrO}_3$. *Phys. Rev. B* **92,** 024413 (2015) (cit. on pp. 2, 67).
24. Kim, B. J., Ohsumi, H., Komesu, T., Sakai, S., Morita, T., Takagi, H. & Arima, T. Phase-Sensitive Observation of a Spin-Orbital Mott State in $\mathrm{Sr_2IrO_4}$. *Science* **323,** 1329–1332 (2009) (cit. on pp. 2, 67).
25. Meng, Z. Y., Kim, Y. B. & Kee, H.-Y. Odd-Parity Triplet Superconducting Phase in Multiorbital Materials with a Strong Spin-Orbit Coupling: Application to Doped $\mathrm{Sr_2IrO_4}$. *Phys. Rev. Lett.* **113,** 177003 (2014) (cit. on pp. 2, 67).
26. Chaloupka, J. & Khaliullin, G. Doping-Induced Ferromagnetism and Possible Triplet Pairing in d^4 Mott Insulators. *Phys. Rev. Lett.* **116,** 017203 (2016) (cit. on pp. 2, 67).
27. Amaricci, A., Budich, J. C., Capone, M., Trauzettel, B. & Sangiovanni, G. First-Order Character and Observable Signatures of Topological Quantum Phase Transitions. *Phys. Rev. Lett.* **114,** 185701 (2015) (cit. on pp. 2, 100).
28. Amaricci, A., Budich, J. C., Capone, M., Trauzettel, B. & Sangiovanni, G. Strong correlation effects on topological quantum phase transitions in three dimensions. *Phys. Rev. B* **93,** 235112 (2016) (cit. on pp. 2, 100).

29. Marzari, N. & Vanderbilt, D. Maximally localized generalized Wannier functions for composite energy bands. *Phys. Rev. B* **56,** 12847–12865 (1997) (cit. on pp. 6, 51, 101).

30. Mostofi, A. A., Yates, J. R., Pizzi, G., Lee, Y.-S., Souza, I., Vanderbilt, D. & Marzari, N. An updated version of wannier90: A tool for obtaining maximally-localised Wannier functions. **185,** 2309–2310 (2014) (cit. on pp. 6, 33).

31. Korotin, Dm., Kozhevnikov, A. V., Skornyakov, S. L., Leonov, I., Binggeli, N., Anisimov, V. I. & Trimarchi, G. Construction and solution of a Wannier-functions based Hamiltonian in the pseudopotential plane-wave framework for strongly correlated materials. *Eur. Phys. J. B* **65,** 91–98 (2008) (cit. on p. 6).

32. Aichhorn, M., Pourovskii, L., Vildosola, V., Ferrero, M., Parcollet, O., Miyake, T., Georges, A. & Biermann, S. Dynamical mean-field theory within an augmented plane-wave framework: Assessing electronic correlations in the iron pnictide LaFeAsO. *Phys. Rev. B* **80,** 085101 (2009) (cit. on pp. 6, 16).

33. Aichhorn, M., Pourovskii, L., Seth, P., Vildosola, V., Zingl, M., Peil, O. E., Deng, X., Mravlje, J., Kraberger, G. J., Martins, C., Ferrero, M. & Parcollet, O. TRIQS/DFTTools: A TRIQS application for ab initio calculations of correlated materials. *Computer Physics Communications* **204,** 200–208 (2016) (cit. on pp. 6, 114).

34. Kraberger, G. *Development of a full matrix ab-initio scheme for materials with strong spin-orbit coupling and Coulomb interactions* PhD thesis (Graz University of Technology, Graz, Austria, 2018) (cit. on pp. 6, 8).

35. Lechermann, F. *Model Hamiltonians and Basic Techniques* in *The LDA+DMFT approach to strongly correlated materials* (Forschungszentrum Jülich GmbH, 2011) (cit. on pp. 7, 10, 11).

36. Aryasetiawan, F., Imada, M., Georges, A., Kotliar, G., Biermann, S. & Lichtenstein, A. I. Frequency-dependent local interactions and low-energy effective models from electronic structure calculations. *Phys. Rev. B* **70,** 195104 (2004) (cit. on p. 8).

37. Aryasetiawan, F., Karlsson, K., Jepsen, O. & Schönberger, U. Calculations of Hubbard U from first-principles. *Phys. Rev. B* **74,** 125106 (2006) (cit. on p. 8).

38. Anisimov, V. I. & Gunnarsson, O. Density-functional calculation of effective Coulomb interactions in metals. *Phys. Rev. B* **43,** 7570–7574 (1991) (cit. on p. 8).

39. Ribic, T., Assmann, E., Tóth, A. & Held, K. Cubic interaction parameters for t_{2g} Wannier orbitals. *Phys. Rev. B* **90,** 165105 (2014) (cit. on p. 8).

40. Sugano, S., Tanabe, Y. & Kamimura, H. *Multiplets of transition-metal ions in crystals* (Academic Press, 1970) (cit. on pp. 8, 9, 11, 14, 28, 31, 69).

41. Electron correlations in narrow energy bands. *Proceedings of the Royal Society of London A: Mathematical, Physical and Engineering Sciences* **276,** 238–257 (1963) (cit. on p. 10).

42. Georges, A., Medici, L. d. & Mravlje, J. Strong Correlations from Hund's Coupling. *Annual Review of Condensed Matter Physics* **4,** 137–178 (2013) (cit. on pp. 11–14, 68, 71, 88, 89).

43. Dworin, L. & Narath, A. Orbital Paramagnetism of Localized Nonmagnetic Impurities in Metals. *Phys. Rev. Lett.* **25,** 1287–1291 (1970) (cit. on p. 12).

44. Anisimov, V. I., Aryasetiawan, F. & Lichtenstein, A. I. First-principles calculations of the electronic structure and spectra of strongly correlated systems: the LDA + U method. *Journal of Physics: Condensed Matter* **9,** 767 (1997) (cit. on p. 17).

45. Lichtenstein, A. I., Katsnelson, M. I. & Kotliar, G. Finite-Temperature Magnetism of Transition Metals: An ab initio Dynamical Mean-Field Theory. *Phys. Rev. Lett.* **87,** 067205 (2001) (cit. on p. 17).

46. Held, K. Electronic structure calculations using dynamical mean field theory. *Advances in Physics* **56,** 829–926 (2007) (cit. on p. 17).

47. Ylvisaker, E. R., Pickett, W. E. & Koepernik, K. Anisotropy and magnetism in the LSDA + U method. *Phys. Rev. B* **79,** 035103 (2009) (cit. on p. 17).

48. Haule, K. Exact Double Counting in Combining the Dynamical Mean Field Theory and the Density Functional Theory. *Phys. Rev. Lett.* **115,** 196403 (2015) (cit. on p. 17).

49. Yosida, K. & Yamada, K. Perturbation Expansion for the Anderson Hamiltonian. *Progress of Theoretical Physics Supplement* **46,** 244–255 (1970) (cit. on p. 17).

50. Yamada, K. Perturbation Expansion for the Anderson Hamiltonian. II. *Progress of Theoretical Physics* **53,** 970–986 (1975) (cit. on p. 17).

51. Yosida, K. & Yamada, K. Perturbation Expansion for the Anderson Hamiltonian. III. *Progress of Theoretical Physics* **53,** 1286–1301 (1975) (cit. on p. 17).

52. Rozenberg, M. J., Kotliar, G. & Zhang, X. Y. Mott-Hubbard transition in infinite dimensions. II. *Phys. Rev. B* **49,** 10181–10193 (1994) (cit. on p. 17).

53. Arsenault, L.-F., Sémon, P. & Tremblay, A.-M. S. Benchmark of a modified iterated perturbation theory approach on the fcc lattice at strong coupling. *Phys. Rev. B* **86,** 085133 (2012) (cit. on p. 17).

54. Dasari, N., Mondal, W. R., Zhang, P., Moreno, J., Jarrell, M. & Vidhyadhiraja, N. S. A multi-orbital iterated perturbation theory for modelHamiltonians and real material-specific calculations of correlated systems. *The European Physical Journal B* **89,** 202 (2016) (cit. on p. 17).

55. Caffarel, M. & Krauth, W. Exact diagonalization approach to correlated fermions in infinite dimensions: Mott transition and superconductivity. *Phys. Rev. Lett.* **72,** 1545–1548 (1994) (cit. on p. 17).

56. García, D. J., Hallberg, K. & Rozenberg, M. J. Dynamical Mean Field Theory with the Density Matrix Renormalization Group. *Phys. Rev. Lett.* **93,** 246403 (2004) (cit. on p. 17).

57. Wolf, F. A., Go, A., McCulloch, I. P., Millis, A. J. & Schollwöck, U. Imaginary-Time Matrix Product State Impurity Solver for Dynamical Mean-Field Theory. *Phys. Rev. X* **5,** 041032 (2015) (cit. on p. 17).

58. Bauernfeind, D., Zingl, M., Triebl, R., Aichhorn, M. & Evertz, H. G. Fork Tensor-Product States: Efficient Multiorbital Real-Time DMFT Solver. *Phys. Rev. X* **7,** 031013 (2017) (cit. on p. 17).

59. Pruschke, T. & Grewe, N. The Anderson model with finite Coulomb repulsion. *Zeitschrift für Physik B Condensed Matter* **74,** 439–449 (1989) (cit. on p. 17).

60. Kotliar, G. & Ruckenstein, A. E. New Functional Integral Approach to Strongly Correlated Fermi Systems: The Gutzwiller Approximation as a Saddle Point. *Phys. Rev. Lett.* **57,** 1362–1365 (1986) (cit. on p. 17).

61. Sakai, O. & Kuramoto, Y. Application of the numerical renormalization group method to the hubbard model in infinite dimensions. *Solid State Communications* **89,** 307–311 (1994) (cit. on p. 17).

62. Hirsch, J. E. & Fye, R. M. Monte Carlo Method for Magnetic Impurities in Metals. *Phys. Rev. Lett.* **56,** 2521–2524 (1986) (cit. on p. 17).

63. Jarrell, M. Hubbard model in infinite dimensions: A quantum Monte Carlo study. *Phys. Rev. Lett.* **69,** 168–171 (1992) (cit. on p. 17).

64. Rozenberg, M. J., Zhang, X. Y. & Kotliar, G. Mott-Hubbard transition in infinite dimensions. *Phys. Rev. Lett.* **69,** 1236–1239 (1992) (cit. on p. 17).

65. Georges, A. & Krauth, W. Numerical solution of the $d=\infty$ Hubbard model: Evidence for a Mott transition. *Phys. Rev. Lett.* **69,** 1240–1243 (1992) (cit. on p. 17).

66. Gull, E., Millis, A. J., Lichtenstein, A. I., Rubtsov, A. N., Troyer, M. & Werner, P. Continuous-time Monte Carlo methods for quantum impurity models. *Rev. Mod. Phys.* **83,** 349–404 (2011) (cit. on pp. 17, 18).

67. Rubtsov, A. N. & Lichtenstein, A. I. Continuous-time quantum Monte Carlo method for fermions: Beyond auxiliary field framework. *Journal of Experimental and Theoretical Physics Letters* **80,** 61–65 (2004) (cit. on p. 18).

68. Werner, P. & Millis, A. J. Hybridization expansion impurity solver: General formulation and application to Kondo lattice and two-orbital models. *Phys. Rev. B* **74,** 155107 (2006) (cit. on pp. 18, 70).

69. Werner, P., Comanac, A., de'Medici, L., Troyer, M. & Millis, A. J. Continuous-Time Solver for Quantum Impurity Models. *Phys. Rev. Lett.* **97,** 076405 (2006) (cit. on p. 18).

70. Gull, E. *Continuous-Time Quantum Monte Carlo Algorithms for Fermions* PhD thesis (ETH Zürich, 2008) (cit. on p. 18).

71. Bjorken, J. D. & Drell, S. D. *Relativistic Quantum Mechanics* (McGraw-Hill Book Company, 1964) (cit. on p. 19).

72. Das, T. P. *Relativistic Quantum Mechanics of Electrons* (Harper & Row, Publishers, 1973) (cit. on p. 20).
73. Martins, C. *Interplay of Spin-Orbit Coupling and Electronic Coulomb Interactions in Strontium Iridate Sr_2IrO_4* PhD thesis (Ecole Polytechnique France, 2010) (cit. on pp. 25, 32).
74. Berestetskii, V., Lifshitz, E. & Pitaevskii, L. *Relativistische Quantentheorie* second. *Lehrbuch der theoretischen Physik* **IVa** (Akademie Verlag, Berlin, 1971) (cit. on p. 25).
75. Montalti, M., Credi, A., Prodi, L. & Gandolfi, M. T. *Handbook of Photochemistry* 3rd ed. (CRC press, 2006) (cit. on pp. 32, 84).
76. Elliott, R. J. Theory of the Effect of Spin-Orbit Coupling on Magnetic Resonance in Some Semiconductors. *Phys. Rev.* **96,** 266–279 (1954) (cit. on p. 32).
77. Dresselhaus, G. Spin-Orbit Coupling Effects in Zinc Blende Structures. *Phys. Rev.* **100,** 580–586 (1955) (cit. on p. 32).
78. Dresselhaus, G., Kip, A. F. & Kittel, C. Spin-Orbit Interaction and the Effective Masses of Holes in Germanium. *Phys. Rev.* **95,** 568–569 (1954) (cit. on p. 32).
79. Parmenter, R. H. Symmetry Properties of the Energy Bands of the Zinc Blende Structure. *Phys. Rev.* **100,** 573–579 (1955) (cit. on p. 32).
80. Bychkov, Y. A. & Rashba, E. I. Oscillatory effects and the magnetic susceptibility of carriers in inversion layers. *Journal of Physics C Solid State Physics* **17,** 6039–6045 (1984) (cit. on p. 32).
81. Blaha, P., Schwarz, K., Madsen, G. K. H., Kvasnicka, D. & Luitz, J. *WIEN2K, An Augmented Plane Wave + Local Orbitals Program for Calculating Crystal Properties* (Karlheinz Schwarz, Techn. Universität Wien, Austria, Wien, Austria, 2001) (cit. on pp. 32, 33).
82. Novák, P. *Calculation of spin-orbit coupling* Institute of Physics (Cukrovarnick 10, 162 53 Praha 6, Czech Republic). (Cit. on p. 33).
83. Kune š, J., Novák, P., Schmid, R., Blaha, P. & Schwarz, K. Electronic structure of fcc Th: Spin-orbit calculation with $6p_{1/2}$ local orbital extension. *Phys. Rev. B* **64,** 153102 (2001) (cit. on p. 33).
84. Koelling, D. D. & Harmon, B. N. A technique for relativistic spin-polarised calculations. *Journal of Physics C: Solid State Physics* **10,** 3107 (1977) (cit. on p. 33).
85. Nakahara, M. *Geometry, Topology and Physics* 2nd ed. (Institute of Physics Publishing, Dirac House, Temple Back, Bristol BS1 6BE, UK, 2003) (cit. on pp. 35–37, 43, 45, 47).
86. Nash, C. & Sen, S. *Topology and Geometry for Physicists* (Academic Press Inc., 1983) (cit. on pp. 35–38, 42).
87. *Winding number — Wikipedia, The Free Encyclopedia* [Online; accessed 6-June-2018]. 2007. URL: `https://en.wikipedia.org/wiki/Winding_number#/media/File:Winding_Number_Around_Point.svg` (cit. on p. 38).

88. Melcher, C. *Mathematical framework for topological solitons in chiral magnetism* in *Topological Matter - Topological Insulators, Skyrmions and Majoranas* (Forschungszentrum Jülich GmbH, 2017) (cit. on pp. 39, 40).

89. Naber, G. L. *Topology, Geometry, and Gauge Fields* (Springer-Verlag New York, Inc., 2000) (cit. on pp. 40, 47).

90. Karin Everschor-Sitte and Matthias Sitte. *Magnetic skyrmion — Wikipedia, The Free Encyclopedia* [Online; accessed 6-June-2018]. 2015. URL: `https://en.wikipedia.org/wiki/Magnetic_skyrmion#/media/File:2skyrmions.PNG` (cit. on p. 41).

91. Skyrme, T. A unified field theory of mesons and baryons. *Nuclear Physics* **31,** 556–569 (1962) (cit. on p. 41).

92. Braun, H.-B. *Topology of static and dynamical spin textures: Skyrmions, vortices and hedgehogs* in *Topological Matter - Topological Insulators, Skyrmions and Majoranas* (Forschungszentrum Jülich GmbH, 2017) (cit. on p. 41).

93. Berry, M. V. Quantal Phase Factors Accompanying Adiabatic Changes. *Proceedings of the Royal Society of London. A. Mathematical and Physical Sciences* **392,** 45–57 (1984) (cit. on p. 44).

94. Mokrousov, Y. *Berry phase in quantum mechanics* in *Topological Matter - Topological Insulators, Skyrmions and Majoranas* (Forschungszentrum Jülich GmbH, 2017) (cit. on pp. 44–46).

95. Hsiang, W.-Y. & Lee, D.-H. Chern-Simons invariant in the Berry phase of a 2×2 Hamiltonian. *Phys. Rev. A* **64,** 052101 (2001) (cit. on p. 48).

96. Qi, X.-L., Wu, Y.-S. & Zhang, S.-C. Topological quantization of the spin Hall effect in two-dimensional paramagnetic semiconductors. *Phys. Rev. B* **74,** 085308 (2006) (cit. on p. 48).

97. Avron, J. E., Seiler, R. & Simon, B. Homotopy and Quantization in Condensed Matter Physics. *Phys. Rev. Lett.* **51,** 51–53 (1983) (cit. on p. 49).

98. Thouless, D. J., Kohmoto, M., Nightingale, M. P. & den Nijs, M. Quantized Hall Conductance in a Two-Dimensional Periodic Potential. *Phys. Rev. Lett.* **49,** 405–408 (1982) (cit. on p. 49).

99. Klitzing, K. v., Dorda, G. & Pepper, M. New Method for High-Accuracy Determination of the Fine-Structure Constant Based on Quantized Hall Resistance. *Phys. Rev. Lett.* **45,** 494–497 (1980) (cit. on p. 49).

100. Kaufmann, R. M., Li, D. & Wehefritz-Kaufmann, B. Notes on topological insulators. *Reviews in Mathematical Physics* **28,** 1630003 (2016) (cit. on pp. 49, 52).

101. Haldane, F. D. M. Model for a Quantum Hall Effect without Landau Levels: Condensed-Matter Realization of the "Parity Anomaly". *Phys. Rev. Lett.* **61,** 2015–2018 (1988) (cit. on pp. 49, 93).

102. Sheng, D. N., Balents, L. & Wang, Z. Phase Diagram for Quantum Hall Bilayers at $\nu = 1$. *Phys. Rev. Lett.* **91,** 116802 (2003) (cit. on p. 49).

103. Sheng, D. N., Weng, Z. Y., Sheng, L. & Haldane, F. D. M. Quantum Spin-Hall Effect and Topologically Invariant Chern Numbers. *Phys. Rev. Lett.* **97,** 036808 (2006) (cit. on pp. 49, 97, 101, 111).

104. Fu, L. & Kane, C. L. Time reversal polarization and a Z_2 adiabatic spin pump. *Phys. Rev. B* **74,** 195312 (2006) (cit. on pp. 50, 100).

105. Fu, L. & Kane, C. L. Topological insulators with inversion symmetry. *Phys. Rev. B* **76,** 045302 (2007) (cit. on pp. 51, 100, 101, 106).

106. Soluyanov, A. A. & Vanderbilt, D. Computing topological invariants without inversion symmetry. *Phys. Rev. B* **83,** 235401 (2011) (cit. on pp. 51, 101).

107. Triebl, R. *Wannier charge centers and the calculation of topological invarians: Application to the Kane-Mele-Hubbard model* MA thesis (Graz University of Technology, Graz, Austria, 2015) (cit. on pp. 51, 93, 99).

108. Qi, X.-L., Hughes, T. L. & Zhang, S.-C. Topological field theory of time-reversal invariant insulators. *Phys. Rev. B* **78,** 195424 (2008) (cit. on pp. 51–53).

109. Wang, Z., Qi, X.-L. & Zhang, S.-C. Equivalent topological invariants of topological insulators. *New Journal of Physics* **12,** 065007 (2010) (cit. on pp. 52, 53).

110. Niu, Q., Thouless, D. J. & Wu, Y.-S. Quantized Hall conductance as a topological invariant. *Phys. Rev. B* **31,** 3372–3377 (1985) (cit. on p. 53).

111. Gurarie, V. Single-particle Green's functions and interacting topological insulators. *Phys. Rev. B* **83,** 085426 (2011) (cit. on p. 53).

112. Volovik, G. E. *The Universe in a Helium Droplet* 305–373 (Oxford University Press, 2003) (cit. on p. 53).

113. Volovik, G. E. Momentum space topology of fermion zero modes brane. *Journal of Experimental and Theoretical Physics Letters* **75,** 55–58 (2002) (cit. on p. 53).

114. Wang, Z., Qi, X.-L. & Zhang, S.-C. Topological Order Parameters for Interacting Topological Insulators. *Phys. Rev. Lett.* **105,** 256803 (2010) (cit. on p. 53).

115. Wang, Z. & Zhang, S.-C. Simplified Topological Invariants for Interacting Insulators. *Phys. Rev. X* **2,** 031008 (2012) (cit. on pp. 53, 100).

116. Wang, Z., Qi, X.-L. & Zhang, S.-C. Topological invariants for interacting topological insulators with inversion symmetry. *Phys. Rev. B* **85,** 165126 (2012) (cit. on pp. 53, 100, 101).

117. Wang, Z. & Yan, B. Topological Hamiltonian as an exact tool for topological invariants. *Journal of Physics: Condensed Matter* **25,** 155601 (2013) (cit. on pp. 53, 54, 100).

118. Ferris-Prabhu, A. V. & Withers, D. H. Numerical analytic continuation using Padé approximants. *J. Comput. Phys.* **13,** 94–99 (1973) (cit. on p. 56).

119. Tomczak, J. M., Casula, M., Miyake, T., Aryasetiawan, F. & Biermann, S. Combined GW and dynamical mean-field theory: Dynamical screening effects in transition metal oxides. *Europhys. Lett.* **100,** 67001 (2012) (cit. on p. 56).

120. Beach, K. S. D., Gooding, R. J. & Marsiglio, F. Reliable Padé analytical continuation method based on a high-accuracy symbolic computation algorithm. *Phys. Rev. B* **61,** 5147–5157 (2000) (cit. on p. 56).

121. Silver, R. N., Sivia, D. S. & Gubernatis, J. E. Maximum-entropy method for analytic continuation of quantum Monte Carlo data. *Phys. Rev. B* **41,** 2380 (1990) (cit. on p. 56).

122. Gubernatis, J. E., Jarrell, M., Silver, R. N. & Sivia, D. S. Quantum Monte Carlo simulations and maximum entropy: Dynamics from imaginary-time data. *Phys. Rev. B* **44,** 6011–6029 (1991) (cit. on p. 56).

123. Gull, S. F. & Skilling, J. Maximum entropy method in image processing. *IEE Proc.-F* **131,** 646–659 (1984) (cit. on p. 56).

124. Bao, F., Tang, Y., Summers, M., Zhang, G., Webster, C., Scarola, V. & Maier, T. A. Fast and efficient stochastic optimization for analytic continuation. *Phys. Rev. B* **94,** 125149 (2016) (cit. on p. 56).

125. Sandvik, A. W. Stochastic method for analytic continuation of quantum Monte Carlo data. *Phys. Rev. B* **57,** 10287–10290 (1998) (cit. on p. 56).

126. Beach, K. S. D. Identifying the maximum entropy method as a special limit of stochastic analytic continuation. *arXiv preprint arXiv:cond-mat/0403055* (2004) (cit. on p. 56).

127. Mishchenko, A. S., Prokof'ev, N. V., Sakamoto, A. & Svistunov, B. V. Diagrammatic quantum Monte Carlo study of the Fröhlich polaron. *Phys. Rev. B* **62,** 6317–6336 (2000) (cit. on p. 56).

128. Fuchs, S., Pruschke, T. & Jarrell, M. Analytic continuation of quantum Monte Carlo data by stochastic analytical inference. *Phys. Rev. E* **81,** 056701 (2010) (cit. on p. 56).

129. Sandvik, A. W. Constrained sampling method for analytic continuation. *Phys. Rev. E* **94,** 063308 (2016) (cit. on p. 56).

130. Kraberger, G. J., Triebl, R., Zingl, M. & Aichhorn, M. Maximum entropy formalism for the analytic continuation of matrix-valued Green's functions. *Phys. Rev. B* **96,** 155128 (2017) (cit. on pp. 56, 61).

131. Maisinger, K., Hobson, M. P. & Lasenby, A. N. A maximum entropy method for reconstructing interferometer maps of fluctuations in the cosmic microwave background radiation. *Mon. Not. R. Astron. Soc.* **290,** 313–326 (1997) (cit. on pp. 56, 61).

132. Hobson, M. P. & Lasenby, A. N. The entropic prior for distributions with positive and negative values. *Mon. Not. R. Astron. Soc.* **298,** 905–908 (1998) (cit. on pp. 56, 59, 61, 64).

133. Skilling, J. *Classic Maximum Entropy* in *Maximum Entropy and Bayesian Methods* (ed Skilling, J.) 45–52 (Kluwer Academic Publishers, Dortrecht, 1989) (cit. on pp. 56–58).

134. Skellam, J. G. The Frequency Distribution of the Difference Between Two Poisson Variates Belonging to Different Populations. *Journal of the Royal Statistical Society* **109,** 296–296 (1946) (cit. on p. 59).

135. Laue, E., Skilling, J. & Staunton, J. Maximum entropy reconstruction of spectra containing antiphase peaks. *Journal of Magnetic Resonance (1969)* **63,** 418–424 (1985) (cit. on p. 60).

136. Sibisi, S. *Quantified Maxent: An NMR Application* in *Maximum Entropy and Bayesian Methods* (ed Fougère, P. F.) 351–358 (Kluwer Academic Publishers, Dordrecht, 1990) (cit. on p. 60).

137. Bryan, R. K. *Solving oversampled data problems by Maximum Entropy* in *Maximum Entropy and Bayesian Methods* (ed Fougère, P. F.) 221–232 (Kluwer Academic Publishers, Dordrecht, 1990) (cit. on pp. 61, 62).

138. Gull, S. F. *Developements in Maximum Entropy Data Analysis* in *Maximum Entropy and Bayesian Methods* (ed Skilling, J.) 53–71 (Kluwer Academic Publishers, Dortrecht, 1989) (cit. on pp. 63, 64).

139. Zhou, Y., Kanoda, K. & Ng, T.-K. Quantum spin liquid states. *Rev. Mod. Phys.* **89,** 025003 (2017) (cit. on p. 67).

140. Nussinov, Z. & van den Brink, J. Compass and Kitaev models – Theory and Physical Motivations. *arXiv preprint arXiv:1303.5922.* (2013) (cit. on p. 67).

141. Meetei, O. N., Cole, W. S., Randeria, M. & Trivedi, N. Novel magnetic state in d^4 Mott insulators. *Phys. Rev. B* **91,** 054412 (2015) (cit. on p. 67).

142. Plumb, K. W., Clancy, J. P., Sandilands, L. J., Shankar, V. V., Hu, Y. F., Burch, K. S., Kee, H.-Y. & Kim, Y.-J. $\alpha-\mathrm{RuCl}_3$. *Phys. Rev. B* **90,** 041112 (2014) (cit. on p. 67).

143. Winter, S. M., Li, Y., Jeschke, H. O. & Valentí, R. Challenges in design of Kitaev materials: Magnetic interactions from competing energy scales. *Phys. Rev. B* **93,** 214431 (2016) (cit. on p. 67).

144. Zhang, G., Gorelov, E., Sarvestani, E. & Pavarini, E. Fermi Surface of $\mathrm{Sr_2RuO_4}$: Spin-Orbit and Anisotropic Coulomb Interaction Effects. *Phys. Rev. Lett.* **116,** 106402 (2016) (cit. on pp. 67, 68, 90).

145. Kim, M., Mravlje, J., Ferrero, M., Parcollet, O. & Georges, A. Spin-Orbit Coupling and Electronic Correlations in $\mathrm{Sr_2RuO_4}$. *Phys. Rev. Lett.* **120,** 126401 (2018) (cit. on pp. 67, 68, 86, 90).

146. Kim, B., Khmelevskyi, S., Mazin, I., Agterberg, D. & Franchini, C. Anisotropy of magnetic interactions and symmetry of the order parameter in unconventional superconductor $\mathrm{Sr_2RuO_4}$. *npj Quantum Materials* **2,** 37 (2017) (cit. on p. 67).

147. Mackenzie, A. P., Scaffidi, T., Hicks, C. W. & Maeno, Y. Even odder after twenty-three years: the superconducting order parameter puzzle of Sr2RuO4. *npj Quantum Materials* **2,** 40 (2017) (cit. on p. 67).

148. Haule, K. & Kotliar, G. Coherence incoherence crossover in the normal state of iron oxypnictides and importance of Hund's rule coupling. *New J. Phys.* **11,** 025021 (2009) (cit. on pp. 68, 77).

149. De'Medici, L., Mravlje, J. & Georges, A. Janus-Faced Influence of Hund's Rule Coupling in Strongly Correlated Materials. *Phys. Rev. Lett.* **107.** (2011) (cit. on pp. 68, 77, 80, 81).

150. Werner, P., Gull, E., Troyer, M. & Millis, A. J. Spin Freezing Transition and Non-Fermi-Liquid Self-Energy in a Three-Orbital Model. *Phys. Rev. Lett.* **101,** 166405 (2008) (cit. on p. 68).

151. Yin, Z. P., Haule, K. & Kotliar, G. Fractional power-law behavior and its origin in iron-chalcogenide and ruthenate superconductors: Insights from first-principles calculations. *Phys. Rev. B* **86,** 195141 (2012) (cit. on p. 68).

152. Aron, C. & Kotliar, G. Analytic theory of Hund's metals: A renormalization group perspective. *Phys. Rev. B* **91,** 041110 (2015) (cit. on p. 68).

153. Stadler, K. M., Yin, Z. P., von Delft, J., Kotliar, G. & Weichselbaum, A. Dynamical Mean-Field Theory Plus Numerical Renormalization-Group Study of Spin-Orbital Separation in a Three-Band Hund Metal. *Phys. Rev. Lett.* **115,** 136401 (2015) (cit. on p. 68).

154. Horvat, A., Zitko, R. & Mravlje, J. Low-energy physics of three-orbital impurity model with Kanamori interaction. *Phys. Rev. B* **94,** 165140 (2016) (cit. on p. 68).

155. Ishida, H. & Liebsch, A. Fermi-liquid, non-Fermi-liquid, and Mott phases in iron pnictides and cuprates. *Phys. Rev. B* **81,** 054513 (2010) (cit. on pp. 68, 79).

156. Misawa, T., Nakamura, K. & Imada, M. Ab Initio. *Phys. Rev. Lett.* **108,** 177007 (2012) (cit. on pp. 68, 79).

157. De'Medici, L., Giovannetti, G. & Capone, M. Selective Mott Physics as a Key to Iron Superconductors. *Phys. Rev. Lett.* **112,** 177001 (2014) (cit. on pp. 68, 79).

158. Fanfarillo, L. & Bascones, E. Electronic correlations in Hund metals. *Phys. Rev. B* **92,** 075136 (2015) (cit. on pp. 68, 79).

159. Sato, T., Shirakawa, T. & Yunoki, S. Spin-orbit-induced exotic insulators in a three-orbital Hubbard model with $(t_{2g})^5$ electrons. *Phys. Rev. B* **91,** 125122 (2015) (cit. on pp. 68, 70).

160. Sato, T., Shirakawa, T. & Yunoki, S. Spin-Orbital Entangled Excitonic Insulators in $(t_{2g})^4$ Correlated Electron Systems. *arXiv preprint arXiv:1603.01800.* (2016) (2016) (cit. on pp. 68, 70).

161. Kim, M. Signatures of spin-orbital states of ${t_{2g}}^2$ system in optical conductivity: RVO$_3$ ($R =$ Y and La). *Phys. Rev. B* **97,** 155141 (2018) (cit. on p. 68).

162. Liu, G.-Q., Antonov, V. N., Jepsen, O. & Andersen., O. K. Coulomb-Enhanced Spin-Orbit Splitting: The Missing Piece in the Sr$_2$RhO$_4$ Puzzle. *Phys. Rev. Lett.* **101,** 026408 (2008) (cit. on p. 68).

163. Bünemann, J., Linneweber, T., Löw, U., Anders, F. B. & Gebhard, F. Interplay of Coulomb interaction and spin-orbit coupling. *Phys. Rev. B* **94,** 035116 (2016) (cit. on pp. 68, 90).

164. Behrmann, M., Piefke, C. & Lechermann, F. Multiorbital physics in Fermi liquids prone to magnetic order. *Phys. Rev. B* **86,** 045130 (2012) (cit. on p. 68).

165. Horvat, A., Žitko, R. & Mravlje, J. Spin-orbit coupling in three-orbital Kanamori impurity model and its relevance for transition-metal oxides. *Phys. Rev. B* **96,** 085122 (2017) (cit. on pp. 68, 81).

166. Kim, A. J., Jeschke, H. O., Werner, P. & Valentí, R. J freezing and Hund's Rules in Spin-Orbit-Coupled Multiorbital Hubbard Models. *Phys. Rev. Lett.* **118,** 086401 (2017) (cit. on pp. 69, 70, 72, 84).

167. Martins, C., Aichhorn, M. & Biermann, S. Coulomb correlations in 4d and 5d oxides from first principles—or how spin–orbit materials choose their effective orbital degeneracies. *Journal of Physics: Condensed Matter* **29,** 263001 (2017) (cit. on pp. 69, 84).

168. Parcollet, O., Ferrero, M., Ayral, T., Hafermann, H., Krivenko, I., Messio, L. & Seth, P. TRIQS: A toolbox for research on interacting quantum systems. *Computer Physics Communications* **196,** 398–415 (2015) (cit. on pp. 70, 114).

169. Seth, P., Krivenko, I., Ferrero, M. & Parcollet, O. "TRIQS/CTHYB: A continuous-time quantum Monte Carlo hybridisation expansion solver for quantum impurity problems ". *Comput. Phys. Commun.* **200,** 274–284 (2016) (cit. on pp. 70, 114).

170. Kaushal, N., Herbrych, J., Nocera, A., Alvarez, G., Moreo, A., Reboredo, F. A. & Dagotto, E. Density matrix renormalization group study of a three-orbital Hubbard model with spin-orbit coupling in one dimension. *Phys. Rev. B* **96,** 155111 (2017) (cit. on p. 70).

171. Kuneř, J. Excitonic condensation in systems of strongly correlated electrons. *Journal of Physics: Condensed Matter* **27,** 333201 (2015) (cit. on p. 70).

172. Akbari, A. & Khaliullin, G. Magnetic excitations in a spin-orbit-coupled d^4 Mott insulator on the square lattice. *Phys. Rev. B* **90,** 035137 (2014) (cit. on p. 70).

173. Du, L., Huang, L. & Dai, X. Metal-insulator transition in three-band Hubbard model with strong spin-orbit interaction. *The European Physical Journal B* **86,** 94 (2013) (cit. on p. 70).

174. Werner, P. & Millis, A. J. High-Spin to Low-Spin and Orbital Polarization Transitions in Multiorbital Mott Systems. *Phys. Rev. Lett.* **99.** (2007) (cit. on p. 72).

175. Werner, P., Gull, E. & Millis, A. J. Metal-insulator phase diagram and orbital selectivity in three-orbital models with rotationally invariant Hund coupling. *Phys. Rev. B* **79.** (2009) (cit. on p. 72).

176. Kita, T., Ohashi, T. & Kawakami, N. Mott transition in three-orbital Hubbard model with orbital splitting. *Phys. Rev. B* **84.** (2011) (cit. on p. 72).

177. Kita, T., Ohashi, T. & Kawakami, N. Orbital-Selective Mott Transition in Multi-orbital Hubbard Model with Orbital Degeneracy Lifting. *Journal of the Physical Society of Japan* **80,** SA142 (2011) (cit. on p. 72).

178. Jarrell, M. & Gubernatis, J. Bayesian inference and the analytic continuation of imaginary-time quantum Monte Carlo data. *Physics Reports* **269,** 133–195 (1996) (cit. on p. 83).

179. Von der Linden, W., Preuss, R. & Dose, V. *The Prior-Predictive Value: A Paradigm of Nasty Multi-Dimensional Integrals* in *Maximum Entropy and Bayesian Methods* (eds von der Linden, W., Dose, V., Fischer, R. & Preuss, R.) 319–326 (Kluwer Academic Publishers, Dortrecht, 1999) (cit. on p. 83).

180. Skilling, J. *Fundamentals of MaxEnt in data analysis* in *Maximum Entropy in Action* (eds Buck, B. & Macaulay, V. A.) 19–40 (Clarendon Press, Oxford, 1991) (cit. on p. 83).

181. Martins, C., Aichhorn, M., Vaugier, L. & Biermann, S. Reduced Effective Spin-Orbital Degeneracy and Spin-Orbital Ordering in Paramagnetic Transition-Metal Oxides: Sr_2IrO_4 versus Sr_2RhO_4. *Phys. Rev. Lett.* **107,** 266404 (2011) (cit. on p. 84).

182. Lee, K.-W. & Pickett, W. E. Orbital-quenching–induced magnetism in Ba 2 NaOsO 6. *EPL (Europhysics Letters)* **80,** 37008 (2007) (cit. on p. 84).

183. Giovannetti, G. The influence of Coulomb Correlations and Spin-Orbit Coupling in the electronic structure of double perovskites Sr2XOsO6 (X=Sc, Mg). *arXiv preprint arXiv:1611.06482.* (2016) (cit. on pp. 84, 86).

184. Ikeda, S.-I., Shirakawa, N., Bando, H. & Ootuka, Y. Orbital-Degenerate Paramagnetic Metal Sr_2MoO_4: An Electronic Analogue to Sr_2RuO_4. *Journal of the Physical Society of Japan* **69,** 3162–3165 (2000) (cit. on p. 86).

185. Nagai, I., Shirakawa, N., Ikeda, S.-i., Iwasaki, R., Nishimura, H. & Kosaka, M. Highest conductivity oxide $SrMoO_3$ grown by a floating-zone method under ultralow oxygen partial pressure. *Applied Physics Letters* **87,** 024105 (2005) (cit. on p. 86).

186. Wadati, H., Mravlje, J., Yoshimatsu, K., Kumigashira, H., Oshima, M., Sugiyama, T., Ikenaga, E., Fujimori, A., Georges, A., Radetinac, A., Takahashi, K. S., Kawasaki, M. & Tokura, Y. Photoemission and DMFT study of electronic correlations in $SrMoO_3$: Effects of Hund's rule coupling and possible plasmonic sideband. *Phys. Rev. B* **90,** 205131 (2014) (cit. on p. 86).

187. Du, L., Sheng, X., Weng, H. & Dai, X. The electronic structure of $NaIrO_3$, Mott insulator or band insulator? *EPL (Europhysics Letters)* **101,** 27003 (2013) (cit. on p. 86).

188. Gharekhanlou, B. & Khorasani, S. *An overview of tight-binding method for two-dimensional carbon structure* in *Graphene: Properties, Synthesis, and Applications* (ed Xu, Z.) (Nova Science Publishers, 2012). (Cit. on pp. 94, 95).

189. Saito, R., Dresselhaus, G. & Dresselhaus, M. S. *Physical Properties of Carbon Nanotubes* (Imperial College Press, 203 Electrical Engineering Building, Imperial College, London SW7 2BT, UK, 1998) (cit. on pp. 95, 96).

190. Reis, F., Li, G., Dudy, L., Bauernfeind, M., Glass, S., Hanke, W., Thomale, R., Schäfer, J. & Claessen, R. Bismuthene on a SiC substrate: A candidate for a high-temperature quantum spin Hall material. *Science* **357,** 287–290 (2017) (cit. on pp. 95, 110, 113, 114).

191. Liu, C.-C., Guan, S., Song, Z., Yang, S. A., Yang, J. & Yao, Y. Low-energy effective Hamiltonian for giant-gap quantum spin Hall insulators in honeycomb X-hydride/halide ($X = \mathrm{N} - \mathrm{Bi}$) monolayers. *Phys. Rev. B* **90,** 085431 (2014) (cit. on pp. 95, 97, 113, 114).

192. Min, H., Hill, J. E., Sinitsyn, N. A., Sahu, B. R., Kleinman, L. & MacDonald, A. H. Intrinsic and Rashba spin-orbit interactions in graphene sheets. *Phys. Rev. B* **74,** 165310 (2006) (cit. on p. 97).

193. Triebl, R. & Aichhorn, M. Topological insulator on honeycomb lattices and ribbons without inversion symmetry. *Phys. Rev. B* **94,** 165169 (2016) (cit. on p. 99).

194. Kitaev, A. *Periodic table for topological insulators and superconductors* in *AIP Conference Proceedings* **1134** (2009), 22–30. (Cit. on p. 100).

195. Schnyder, A. P., Ryu, S., Furusaki, A. & Ludwig, A. W. W. Classification of topological insulators and superconductors in three spatial dimensions. *Phys. Rev. B* **78,** 195125 (2008) (cit. on p. 100).

196. Ryu, S., Schnyder, A. P., Furusaki, A. & Ludwig, A. W. W. Topological insulators and superconductors: tenfold way and dimensional hierarchy. *New Journal of Physics* **12,** 065010 (2010) (cit. on p. 100).

197. Roth, A., Brüne, C., Buhmann, H., Molenkamp, L. W., Maciejko, J., Qi, X.-L. & Zhang, S.-C. Nonlocal Transport in the Quantum Spin Hall State. *Science* **325,** 294–297 (2009) (cit. on p. 100).

198. Hsieh, D., Qian, D., Wray, L., Xia, Y., Hor, Y. S., Cava, R. J. & Hasan, M. Z. A topological Dirac insulator in a quantum spin Hall phase. *Nature* **452,** 970–974 (2008) (cit. on p. 100).

199. Zhang, H., Liu, C.-X., Qi, X.-L., Dai, X., Fang, Z. & Zhang, S.-C. Topological insulators in $\mathrm{Bi_2Se_3}$, $\mathrm{Bi_2Te_3}$ and $\mathrm{Sb_2Te_3}$ with a single Dirac cone on the surface. *Nature Physics* **5,** 438–442 (2009) (cit. on p. 100).

200. Hsieh, D., Xia, Y., Wray, L., Qian, D., Pal, A., Dil, J. H., Osterwalder, J., Meier, F., Bihlmayer, G., Kane, C. L., Hor, Y. S., Cava, R. J. & Hasan, M. Z. Observation of Unconventional Quantum Spin Textures in Topological Insulators. *Science* **323,** 919–922 (2009) (cit. on p. 100).

201. Nishide, A., Taskin, A. A., Takeichi, Y., Okuda, T., Kakizaki, A., Hirahara, T., Nakatsuji, K., Komori, F., Ando, Y. & Matsuda, I. Direct mapping of the spin-filtered surface bands of a three-dimensional quantum spin Hall insulator. *Phys. Rev. B* **81,** 041309 (2010) (cit. on p. 100).

202. Xia, Y., Qian, D., Hsieh, D., Wray, L., Pal, A., Lin, H., Bansil, A., Grauer, D., Hor, Y. S., Cava, R. J. & Hasan, M. Z. Observation of a large-gap topological-insulator class with a single Dirac cone on the surface. *Nature Physics* **5,** 398–402 (2009) (cit. on p. 100).

203. Fang, Z., Nagaosa, N., Takahashi, K. S., Asamitsu, A., Mathieu, R., Ogasawara, T., Yamada, H., Kawasaki, M., Tokura, Y. & Terakura, K. The Anomalous Hall Effect and Magnetic Monopoles in Momentum Space. *Science* **302,** 92–95 (2003) (cit. on p. 100).

204. Wan, X., Turner, A. M., Vishwanath, A. & Savrasov, S. Y. Topological semimetal and Fermi-arc surface states in the electronic structure of pyrochlore iridates. *Phys. Rev. B* **83,** 205101 (2011) (cit. on p. 100).

205. Xu, G., Weng, H., Wang, Z., Dai, X. & Fang, Z. Chern Semimetal and the Quantized Anomalous Hall Effect in $HgCr_2Se_4$. *Phys. Rev. Lett.* **107,** 186806 (2011) (cit. on p. 100).

206. Huang, S.-M., Xu, S.-Y., Belopolski, I., Lee, C.-C., Chang, G., Wang, B., Alidoust, N., Bian, G., Neupane, M., Zhang, C., Jia, S., Bansil, A., Lin, H. & Hasan, M. Z. A Weyl Fermion semimetal with surface Fermi arcs in the transition metal monopnictide TaAs class. *Nature Communications* **6,** 7373 (2015) (cit. on p. 100).

207. Yang, L. X., Liu, Z. K., Sun, Y., Peng, H., Yang, H. F., Zhang, T., Zhou, B., Zhang, Y., Guo, Y. F., Rahn, M., Prabhakaran, D., Hussain, Z., Mo, S.-K., Felser, C., Yan, B. & Chen, Y. L. Weyl semimetal phase in the non-centrosymmetric compound TaAs. *Nature Physics* **11,** 728–732 (2015) (cit. on p. 100).

208. Xu, S.-Y., Alidoust, N., Belopolski, I., Yuan, Z., Bian, G., Chang, T.-R., Zheng, H., Strocov, V. N., Sanchez, D. S., Chang, G., Zhang, C., Mou, D., Wu, Y., Huang, L., Lee, C.-C., Huang, S.-M., Wang, B., Bansil, A., Jeng, H.-T., Neupert, T., Kaminski, A., Lin, H., Jia, S. & Zahid Hasan, M. Discovery of a Weyl fermion state with Fermi arcs in niobium arsenide. *Nature Physics* **11,** 748–754 (2015) (cit. on p. 100).

209. Weng, H., Fang, C., Fang, Z., Bernevig, B. A. & Dai, X. Weyl Semimetal Phase in Noncentrosymmetric Transition-Metal Monophosphides. *Phys. Rev. X* **5,** 011029 (2015) (cit. on p. 100).

210. Lv, B. Q., Weng, H. M., Fu, B. B., Wang, X. P., Miao, H., Ma, J., Richard, P., Huang, X. C., Zhao, L. X., Chen, G. F., Fang, Z., Dai, X., Qian, T. & Ding, H. Experimental Discovery of Weyl Semimetal TaAs. *Phys. Rev. X* **5,** 031013 (2015) (cit. on p. 100).

211. Fu, L., Kane, C. L. & Mele, E. J. Topological Insulators in Three Dimensions. *Phys. Rev. Lett.* **98,** 106803 (2007) (cit. on p. 100).

212. Rachel, S. & Le Hur, K. Topological insulators and Mott physics from the Hubbard interaction. *Phys. Rev. B* **82,** 075106 (2010) (cit. on pp. 100, 101, 105, 110, 111).

213. Lee, D.-H. Effects of Interaction on Quantum Spin Hall Insulators. *Phys. Rev. Lett.* **107,** 166806 (2011) (cit. on pp. 100, 101, 103, 107).

214. Hohenadler, M., Lang, T. C. & Assaad, F. F. Correlation Effects in Quantum Spin-Hall Insulators: A Quantum Monte Carlo Study. *Phys. Rev. Lett.* **106,** 100403 (2011) (cit. on pp. 100, 101, 105).

215. Hohenadler, M., Meng, Z. Y., Lang, T. C., Wessel, S., Muramatsu, A. & Assaad, F. F. Quantum phase transitions in the Kane-Mele-Hubbard model. *Phys. Rev. B* **85,** 115132 (2012) (cit. on pp. 100, 101, 105).

216. Assaad, F. F., Bercx, M. & Hohenadler, M. Topological Invariant and Quantum Spin Models from Magnetic Fluxes in Correlated Topological Insulators. *Phys. Rev. X* **3,** 011015 (2013) (cit. on pp. 100, 105).

217. Hung, H.-H., Chua, V., Wang, L. & Fiete, G. A. Interaction effects on topological phase transitions via numerically exact quantum Monte Carlo calculations. *Phys. Rev. B* **89,** 235104 (2014) (cit. on pp. 100, 101).

218. Yu, S.-L., Xie, X. C. & Li, J.-X. Mott Physics and Topological Phase Transition in Correlated Dirac Fermions. *Phys. Rev. Lett.* **107,** 010401 (2011) (cit. on pp. 100–105).

219. Budich, J. C., Thomale, R., Li, G., Laubach, M. & Zhang, S.-C. Fluctuation-induced topological quantum phase transitions in quantum spin-Hall and anomalous-Hall insulators. *Phys. Rev. B* **86,** 201407 (2012) (cit. on pp. 100–102, 105).

220. Laubach, M., Reuther, J., Thomale, R. & Rachel, S. Rashba spin-orbit coupling in the Kane-Mele-Hubbard model. *Phys. Rev. B* **90,** 165136 (2014) (cit. on pp. 100–105).

221. Wu, W., Rachel, S., Liu, W.-M. & Le Hur, K. Quantum spin Hall insulators with interactions and lattice anisotropy. *Phys. Rev. B* **85,** 205102 (2012) (cit. on pp. 100, 101).

222. Grandi, F., Manghi, F., Corradini, O., Bertoni, C. M. & Bonini, A. Topological invariants in interacting quantum spin Hall: a cluster perturbation theory approach. *New Journal of Physics* **17,** 023004 (2015) (cit. on pp. 100, 101, 103).

223. Chen, Y.-H., Hung, H.-H., Su, G., Fiete, G. A. & Ting, C. S. Cellular dynamical mean-field theory study of an interacting topological honeycomb lattice model at finite temperature. *Phys. Rev. B* **91,** 045122 (2015) (cit. on pp. 100, 101).

224. Lai, H.-H. & Hung, H.-H. Effects of short-ranged interactions on the Kane-Mele model without discrete particle-hole symmetry. *Phys. Rev. B* **89,** 165135 (2014) (cit. on pp. 100, 101, 106, 111).

225. Miyakoshi, S. & Ohta, Y. Coexistence of magnetic and topological phases in the asymmetric Kane-Mele-Hubbard model. *Journal of Physics: Conference Series* **592,** 012129 (2015) (cit. on pp. 100, 101, 111).

226. Yoshida, T., Fujimoto, S. & Kawakami, N. Correlation effects on a topological insulator at finite temperatures. *Phys. Rev. B* **85,** 125113 (2012) (cit. on p. 101).

227. Soluyanov, A. A. & Vanderbilt, D. Wannier representation of $\mathbb{Z}_2$ topological insulators. *Phys. Rev. B* **83,** 035108 (2011) (cit. on p. 101).

228. Potthoff, M. Self-energy-functional approach to systems of correlated electrons. *Eur. Phys. J. B* **32,** 429–436 (2003) (cit. on pp. 101, 102).

229. Potthoff, M. Self-energy-functional approach: Analytical results and the Mott-Hubbard transition. *The European Physical Journal B - Condensed Matter and Complex Systems* **36,** 335–348 (2003) (cit. on pp. 101, 102).

230. Potthoff, M., Aichhorn, M. & Dahnken, C. Variational Cluster Approach to Correlated Electron Systems in Low Dimensions. *Phys. Rev. Lett.* **91,** 206402 (2003) (cit. on pp. 101, 102).

231. Aichhorn, M., Arrigoni, E., Potthoff, M. & Hanke, W. Variational cluster approach to the Hubbard model: Phase-separation tendency and finite-size effects. *Phys. Rev. B* **74,** 235117 (2006) (cit. on pp. 101, 102).

232. Dahnken, C., Aichhorn, M., Hanke, W., Arrigoni, E. & Potthoff, M. Variational cluster approach to spontaneous symmetry breaking: The itinerant antiferromagnet in two dimensions. *Phys. Rev. B* **70,** 245110 (2004) (cit. on pp. 101, 103).

233. Luttinger, J. M. & Ward, J. C. Ground-State Energy of a Many-Fermion System. II. *Phys. Rev.* **118,** 1417–1427 (1960) (cit. on p. 101).

234. Varney, C. N., Sun, K., Rigol, M. & Galitski, V. Topological phase transitions for interacting finite systems. *Phys. Rev. B* **84,** 241105 (2011) (cit. on p. 102).

235. Sorella, S. & Tosatti, E. Semi-Metal-Insulator Transition of the Hubbard Model in the Honeycomb Lattice. *EPL (Europhysics Letters)* **19,** 699 (1992) (cit. on pp. 105, 111).

236. Hohenadler, M., Parisen Toldin, F., Herbut, I. F. & Assaad, F. F. Phase diagram of the Kane-Mele-Coulomb model. *Phys. Rev. B* **90,** 085146 (2014) (cit. on p. 107).